

**UNIVERSIDADE DE SÃO PAULO
INSTITUTO DE FÍSICA DE SÃO CARLOS**

Denis Ricardo Candido

**Blurring the boundaries between topological and
non-topological physical phenomena in dots**

São Carlos

2018

Denis Ricardo Candido

**Blurring the boundaries between topological and
non-topological physical phenomena in dots**

Thesis presented to the Graduate Program
in Physics at the Instituto de Física de São
Carlos, Universidade de São Paulo, to obtain
the degree of Doctor in Science.

Concentration area: Basic Physics

Advisor: Prof. Dr. José Carlos Egues

Corrected version
(Original version available on the Program Unit)

São Carlos
2018

I AUTHORIZE THE REPRODUCTION AND DISSEMINATION OF TOTAL OR PARTIAL COPIES OF THIS DOCUMENT, BY CONVENCIONAL OR ELECTRONIC MEDIA FOR STUDY OR RESEARCH PURPOSE, SINCE IT IS REFERENCED.

Candido, Denis Ricardo

Blurring the boundaries between topological and non-topological physical phenomena in dots / Denis Ricardo Candido; advisor José Carlos Egues - revised version -- São Carlos 2018.

155 p.

Thesis (Doctorate - Graduate Program in Física Básica) - Instituto de Física de São Carlos, Universidade de São Paulo - Brasil , 2018.

1. InAsBi. 2. 2D topological insulators. 3. Cylindrical BHZ quantum dots. 4. Protected trivial helical edge states. 5. Conductance calculation. I. Egues, José Carlos, advisor. II. Title.

To my family, wife and friends who supported me all these years.

ACKNOWLEDGEMENTS

I would like to thank my father Lázaro Alfredo Candido, my mother Rita de Cassia Antunes Candido, my sister Mariana Antunes Candido, my brother Caio Eduardo Candido, my grandparents Wagner Antunes and Vera Dellai Antunes and my dog Loba Candido for the best support and love I received during these years. In addition, a special thanks goes to my wife Bárbara Silva Correia for her love, support, patience, encouragement and help in many aspects of life.

I thank Prof. Dr. José Carlos Egues for his supervision and guidance during my PhD degree. I have been lucky to have a supervisor who cared not only about results, but also about having a solid physics background. Apart from being a good advisor from the physical point of view, he was also a great teacher by showing how science must be taken seriously in Brazil. Also, I would like to thank Egues for providing me the opportunity to attend many international conferences and also to interact with many internationally renowned groups (Switzerland, Germany, USA). During these opportunities, we were able to start two different international collaborations which evolved into two different works, both presented here.

I thank Prof. Ewelina M. Hankiewicz for the hospitality during my stay at the University of Würzburg and for all the valuable physics discussion during this time. I also thank Prof. Michael Flatté from the University of Iowa for all the valuable physics discussions during the preparation of this work and also for helping supporting my travel to the APS March Meeting in 2018.

I am also grateful to the group members during these years: Adonai, Gerson, Jiyong Fu, João, Marco, Poliana and Vernek, for the nice and rich physics discussion. Special thank to Poliana for the invitation to the group, and also for all the help and assistance she gave me during the time we overlapped. I also thank her for the careful reading and checking of this thesis work, as well as for the many physics discussions about the results presented here.

I'd like to thank my friends at IFSC: Carlos, Cesar, Tiago and Paulo, for the opportunity to interact socially and scientifically throughout these years. In addition, I thank the people at IFSC from their help and dedication. Specially Neusa, Silvio, Ricardo, Sonia, Jessica, Paulo, Italo and Maria Cristina.

I would to thank CNPq, UFRN/MEC, FAPESP, PRP-USP/Q-NANO and the Center for Emergent Materials, an NSF MRSEC under Award No. DMR-1420451 for financial support. I also acknowledge the kind hospitality at the International Institute of Physics (IIP/UFRN), where part of this work was done.

*“what we observe is not nature in itself but nature
exposed to our method of questioning.”*

Werner Heisenberg

ABSTRACT

CANDIDO, D. R. **Blurring the boundaries between topological and non-topological physical phenomena in dots.** 2018. 155p. Thesis (Doctor in Science) - Instituto de Física de São Carlos, Universidade de São Paulo, São Carlos, 2018.

In this thesis, we investigate the electronic structure and transport properties of topologically trivial and non-trivial cylindrical quantum dots (QDs) defined by further confining $\text{InAs}_{1-x}\text{Bi}_x/\text{AlSb}$ quantum wells (QWs). First we predict that common III-V $\text{InAs}_{0.85}\text{Bi}_{0.15}/\text{AlSb}$ QWs can become 2D topological insulators (TIs) for well thicknesses $d_c > 6.9$ nm with a topologically non-trivial gap of about 30 meV ($> k_B T$), which can enable room temperature TI applications. Furthermore, we investigate the cylindrical QDs defined from these Bi-based wells by additional confinement, both in the topologically trivial ($d < d_c$) and non-trivial ($d > d_c$) regimes. Surprisingly, we find that topologically trivial and non-trivial QDs have similar transport properties in stark contrast with their 2D counterparts (i.e., a strip). More specifically, through detailed calculations, which involve an analytical solution of the quantum-dot eigenvalue problem, we demonstrate that both trivial and non-trivial cylindrical QDs possess edge-like states, i.e., helical spin-angular-momentum-locked quantum states protected against non-magnetic elastic scattering. Interestingly, our trivial QDs exhibit these geometrically robust helical states, similarly to topologically non-trivial QDs, over a wide range of system parameters (e.g., dot radius). We also calculate the circulating currents for the topologically trivial and non-trivial QDs and find no substantial differences. However, we note that ordinary III-V or II-VI cylindrical QDs (i.e., QDs not formed from a BHZ model + confinement) do not feature robust edge-like helical states. We further consider topologically trivial and non-trivial QDs with four edge-like states and calculate their two-terminal conductance \mathcal{G} via a standard Green-function approach. For both trivial and non-trivial QDs we find that \mathcal{G} shows a double-peak resonance at $2e^2/h$ as a function of the dot radius R and gate voltage V_g controlling the dot energy levels. On the other hand, both trivial and non-trivial QDs can have edge-like and bulk state Kramers pairs coexisting at the same energy within the bulk part of their discrete spectra. In this case, \mathcal{G} displays a single-peak resonance at $2e^2/h$ as the four levels (two edge states and two bulk states now) become degenerate at some particular parameter values $R = R_c$ and $V_g = V_{gc}$ for both topologically trivial and non-trivial QDs. We also extend our investigation to HgTe-based QDs and find similar results.

Keywords: InAsBi. 2D topological insulators. Cylindrical BHZ quantum dots. Protected trivial helical edge states. Conductance calculation.

RESUMO

CANDIDO, D. R. **Borrando a fronteira entre fenômenos físicos topológicos e não topológicos em poços quânticos**. 2018. 155p. Tese (Doutorado em Ciências) - Instituto de Física de São Carlos, Universidade de São Paulo, São Carlos, 2018.

Nesta tese investigamos a estrutura eletrônica e as propriedades de transporte de pontos quânticos cilíndricos topologicamente triviais e não-triviais, definidos por confinamento de poços quânticos (QWs) $\text{InAs}_{1-x}\text{Bi}_x/\text{AlSb}$. Primeiramente, nós prevemos que os QWs usuais baseados em $\text{InAs}_{1-x}\text{Bi}_x/\text{AlSb}$ podem se tornar isolantes topológicos 2D para largura de poço $d_c > 6.9$ nm, com um gap topologicamente não-trivial de aproximadamente 30 meV ($> k_B T$), o que pode permitir aplicações em temperatura ambiente. Além disso, investigamos pontos quânticos cilíndricos definidos a partir de confinamento desses poços contendo Bi, em ambos os regimes trivial ($d < d_c$) e não-trivial ($d > d_c$). Surpreendentemente, descobrimos que os pontos quânticos topologicamente triviais e não triviais têm propriedades de transporte semelhantes, um resultado em grande contraste com as suas versões semi-infinitas, como por exemplo uma fita. Mais especificamente, através de cálculos detalhados, que envolvem uma solução analítica do problema de autovalores dos pontos quânticos, demonstramos que pontos quânticos cilíndricos triviais e não-triviais possuem estados de borda semelhantes, isto é, estados quânticos helicoidais protegidos contra espalhamento elástico não magnético. Curiosamente, nossos pontos quânticos triviais exibem estados helicoidais geometricamente robustos, similarmente aos pontos quânticos topologicamente não-triviais, em uma ampla faixa de parâmetros do sistema, como por exemplo, o raio do ponto quântico. Nós também calculamos as correntes circulantes para os pontos quânticos topologicamente triviais e não-triviais e não encontramos diferenças substanciais entre elas. No entanto, notamos que os pontos quânticos cilíndricos feitos de materiais ordinários III-V ou II-VI (isto é, pontos quânticos não descritos pelo Hamiltoniano BHZ com confinamento) não apresentam estados helicoidais robustos. Consideramos ainda pontos quânticos triviais e não-triviais com quatro estados de borda e calculamos sua condutância entre dois terminais \mathcal{G} através de uma abordagem padrão das funções de Green. Para os pontos quânticos triviais e não-triviais, encontramos que \mathcal{G} mostra uma ressonância de pico duplo em $2e^2/h$ como função do raio do ponto quântico R e da tensão V_g que controla os níveis de energia do ponto quântico. Por outro lado, tanto os pontos quânticos triviais como os não-triviais podem ter pares de Kramers localizados na borda (“edge”) e em todo seu volume (“bulk”) coexistindo em uma mesma janela de energia na região dos estados de valência. Nesse caso, \mathcal{G} exhibe uma ressonância de pico único em $2e^2/h$, já que os quatro níveis (dois estados de borda e dois estados de volume “bulk”) se tornam degenerados para alguns valores de parâmetros particulares $R = R_c$ e $V_g = V_{gc}$, em pontos quânticos

topologicamente triviais e não triviais. Nós também estendemos nossa investigação para os pontos quânticos de HgTe onde encontramos resultados similares.

Palavras-chave: InAsBi. Isolantes topológicos 2D. Pontos quânticos de BHZ cilíndricos. Estados de borda triviais protegidos. Cálculo da condutância.

LIST OF FIGURES

<p>Figure 1 – a) Schematic representation of the IQHE with one chiral edge state (either spin up or down). b) Same as a) for the QSHE with its two helical edge states. c) In the IQHE, the backscattering is not possible since for each interface there are only states (either spin up or down) going in one direction. d) Differently from Fig. 1c), in the QSHE we find helical edge states with spin-momentum locking traveling in both directions. However, here the elastic backscattering off non-magnetic impurities is protected by time reversal symmetry as we need to flip the spin to move in the opposite direction.</p>	24
<p>Figure 2 – Evolution of the s and p atomic orbitals from one atom into the conduction and valence bands of a crystal without spin-orbit coupling. $s^+(s^-)$ represents the new s-bonding (anti-bonding) orbitals arising from the hybridization of the s orbitals, while $p^+(p^-)$ represents the new p-bonding (anti-bonding) orbitals arising from the hybridization of the p orbitals. $\Gamma_1(s^+)$ ($\Gamma_5(p^+)$) represents the valence band from the s^+ (p^+) bonding orbitals and $\Gamma_1(s^-)$ ($\Gamma_5(p^-)$) represents the conduction band from the s^- (p^-) bonding orbitals. E_f represents the Fermi energy of the crystal.</p>	28
<p>Figure 3 – Sketchy of the evolution of the simplified CdTe band structure as the relativistic terms (Darwin term, relativistic mass correction and spin-orbit coupling) are included subsequently. The final band structure profile shows a normal band ordering corresponding to the Γ_6 band above the Γ_8 bands.</p>	29
<p>Figure 4 – Similar to Fig. 3 but for the simplified HgTe band structure with its large atomic number. We emphasize that the mass-correction terms significantly change the conduction band bottom which ultimately produces a band inversion upon the inclusion of the spin-orbit interaction. Note that the inverted band ordering corresponding to the Γ_6 band below the Γ_8 bands.</p>	30
<p>Figure 5 – The sphere and the ellipsoid are topologically equivalent (both with no holes, i.e., $g = 0$) as they can be deformed into each other by using only smooth deformations. We also show the torus and the coffee mug, which are topologically equivalent (both with one hole, i.e., $g = 1$). A non-smooth deformation as for example tearing does change the number of holes, thus connecting two topologically distinct objects.</p>	31

Figure 6 – a) Different energy dispersions within the same topological phase as they are all connected to themselves through adiabatic deformations. b) Different energy dispersion with different topological phase as they are connected only through a gap closing (topological phase transition).	32
Figure 7 – a) Interface of two different materials with different topological phases and the edge states appearance in the interface between them (blue and red arrows). b) Bulk and edge state energy dispersions related to a).	33
Figure 8 – a) Schematic HgTe/CdTe quantum well with thickness d . b) Spin degenerate (\pm) HgTe/CdTe quantum well energy subbands as a function of the QW thickness d at $k_x = k_y = 0$. Here we see the subband inversion at $d = d_c$ between the E_1 and HH_1 .	35
Figure 9 – a) Schematic $\varepsilon_{\mathbf{k}}$ band (gray solid curve) and the localized E_d energy level (red solid curve) with $V = 0$, i.e., no interaction with each other. b) Schematic plot of the energies $E_{\pm}(\mathbf{k})$ arising from the BAC model Eq. (3.15) with $V \neq 0$.	42
Figure 10 – Schematic conduction $\varepsilon_{c\mathbf{k}}$ and valence $\varepsilon_{v\mathbf{k}}$ bands (gray solid curves) and the localized E_d energy level resonant in the conduction band (red solid curve) with $V = 0$, i.e., no interaction with each other. b) Schematic plot of the energies $E_{\pm}(\mathbf{k})$ (Eq. 3.21) with $V \neq 0$. E'_g (E_g) represents the fundamental energy gap with (without) the resonant E_d energy level.	44
Figure 11 – a) InAs Γ_6 , Γ_7 and Γ_8 energy bands (gray solid lines) around the Γ point with the localized Bi energy levels (red energy lines). b) InAs $_{1-x}$ Bi $_x$ dispersion using the VBAC theory in Eq. (3.21) where we clearly see the gap reduction when the Bi energy levels are take into account. Here we sketch the interaction of Bi with only one of the Γ_8 bands for clarity.	46
Figure 12 – InAs $_{1-x}$ Bi $_x$ fundamental energy gap as a function of x (Bi % concentration). The solid black line represents the experimental data for $x < 0.05$ while the dashed black line correspond to its extrapolation for $x > 0.05$. The solid red (blue) curve represents the predicted energy gap using VBAC (VCA) theory.	47
Figure 13 – Symmetric InAs $_{0.85}$ Bi $_{0.15}$ /AlSb QW subbands at $k_x = k_y = 0$ as a function of the well thickness d . The blue (red) colors represent the major Γ_6 (Γ_8) composition. The circle indicates the topological phase transition arising from the subband inversion between $ E_1\pm\rangle$ and $ HH_1\pm\rangle$ at $d_c \approx 6.9$ nm.	48
Figure 14 – a) Even (circles) and odd (triangles) energy levels as functions of j_z for the topologically non-trivial InAs $_{0.85}$ Bi $_{0.15}$ QD with QD radius $R = 100$ nm. b) Same as in a) for $R = 60$ nm. The black arrows denote (forbidden) transitions between spin up (blue) and spin down (red) states.	66

- Figure 15 – a) Topologically non-trivial InAs_{0.85}Bi_{0.15} QD ($R = 100$ nm) modulus square of the spin + wave function $|\psi_{j_z, n}^+(r, \theta)|^2$ (4.38) for the energy levels with even m grouped by the ellipses in Figure 14a). b) Modulus square of the spin + wave function $|\psi_{j_z, n}^+(r, \theta)|^2$ for $j_z^e = -\frac{25}{2}$. c) Same as b) for $j_z^e = \frac{3}{2}$. d) Same as b) for $j_z^e = \frac{27}{2}$. The color bar represents the strength of the probability density and scale from 0 (light blue) to $4 \times 10^{-4} \text{ nm}^{-2}$ (dark blue). 67
- Figure 16 – Same as Fig. 15a) for the QD energy levels with even m grouped by the ellipses in Fig. 14b). b) Same as Fig. 15b) for $j_z^e = -\frac{13}{2}$. c) Same as b) for $j_z^e = \frac{3}{2}$. d) Same as b) for $j_z^e = \frac{27}{2}$ 68
- Figure 17 – a) Same as Fig. 14a) for the trivial InAs_{0.85}Bi_{0.15} QD with QD radius $R = 100$ nm. b) Same as a) for $R = 60$ nm. 70
- Figure 18 – a) Modulus square of the spin + wave function $|\psi_{j_z, n}^+(r, \theta)|^2$ (4.38) for the highest valence states (even states grouped by the lower ellipses in Figs. 17a) with $E_{j_z} < 0$) from $j_z^e = -\frac{25}{2}$ to $j_z^e = \frac{27}{2}$. b) $|\psi_{j_z, n}^+(r, \theta)|^2$ (4.38) for lowest conduction states (even states grouped by the upper ellipses in Figs. 17a) with $E_{j_z} > 0$) from $j_z^e = -\frac{21}{2}$ to $j_z^e = \frac{23}{2}$. c) Same as a) for the even states grouped by the lower ellipses in Figs. 17b) with $E_{j_z} < 0$. d) Same as b) even states grouped by the lower ellipses in Figs. 17b) with $E_{j_z} > 0$ 71
- Figure 19 – a) Trivial InAs_{0.85}Bi_{0.15} QD energy levels as functions of j_z with QD radius $R = 30$ nm. b) $|\psi_{j_z, n}^+(r, \theta)|^2$ of the edge states grouped by the ellipse in Fig. 19a). The black triangles $j_z^o = \pm 1/2$ states represent the bulk-like states that merge with the edge states in Fig. 20. 72
- Figure 20 – Eigenenergies of the spin + trivial edge states $j_z^e = 3/2$, $j_z^o = 5/2$, $j_z^e = 7/2$ and $j_z^e = 9/2$ within the gray area of Figure 19a) and their nearest bulk valence level $j_z^o = 1/2$ as a function of QD radius R . The red points indicate the crossing points where the number of the protected trivial edge states is decreased by one as they become degenerate or start coexisting with bulk states. 73
- Figure 21 – a) Even (circles) and odd (triangles) energy levels as functions of j_z for the trivial InAs_{0.85}Bi_{0.15} QD with QD radius $R = 30$ nm. b) Modulus square of the spin + wave function for edge grouped by the ellipse. . . 76
- Figure 22 – QD energy levels as functions of j_z for a topological QD with $R = 40$ nm and b) the spin up circulating current Eq. (4.51) for the three levels represented by the pentagon ($j_z = -7/2$), star ($j_z = 3/2$) and square ($j_z = 13/2$). The horizontal lines here represent the soft-wall QW barriers. 81

Figure 23 – Spin-up envelope circulating current Eq. (4.53) for the three levels represented by the pentagon ($j_z = -7/2$), star ($j_z = 3/2$) and square ($j_z = 13/2$) in Figure 22. Here the circulating currents were plotted with an amplification of 15 times.	82
Figure 24 – Same as Fig. 22 for the trivial QD with $R = 40$ nm with the spin up circulating current for the pentagon ($j_z = -3/2$), star ($j_z = 3/2$) and square ($j_z = 9/2$) levels.	83
Figure 25 – Spin-up envelope circulating current Eq. (4.53) for the three levels represented by the pentagon ($j_z = -3/2$), star ($j_z = 3/2$) and square ($j_z = 9/2$) in Figure 22. Here the circulating currents were plotted with an amplification of 20 times.	84
Figure 26 – Spin up circulating currents for the topologically non-trivial QD with $R = 40$ nm for a) $j_z = 3/2$ and b) $j_z = 5/2$. Same as a) and b) for the topologically trivial QD with $R = 40$ nm for c) $j_z = 3/2$ and d) $j_z = 5/2$. The horizontal lines here represent the soft-wall QW barriers.	85
Figure 27 – a) Topologically trivial HgTe/CdTe QD energy levels for $R = 30$ nm. b) $ \psi_{j_z,n}^+(r, \theta) ^2$ of the edge states grouped by the ellipse.	86
Figure 28 – a) Topologically non-trivial InAs _{0.85} Bi _{0.15} QD energy levels as functions of j_z for the soft ($M_O = 2$ eV) and hard wall case ($M_O \rightarrow \infty$) for $R = 60$ nm. b) Same as a) for the soft wall $M_O = 15$ eV case. The faded (solid) colors represent the soft wall (hard wall) case. The black arrows denote the transitions between the spin down and up states of the BHZ blocks, red and blue symbols, respectively.	87
Figure 29 – a) Topologically trivial InAs _{0.85} Bi _{0.15} QD energy levels as functions of j_z for the soft ($M_O = 2$ eV) and hard wall case ($M_O \rightarrow \infty$) for $R = 60$ nm. b) Same as a) for the soft wall $M_O = 15$ eV case. The faded (solid) colors represent the soft wall (hard wall) case. The arrows denote the forbidden transitions between the spin down and up states of the BHZ blocks, red and blue symbols, respectively.	88
Figure 30 – Schematic figure for the spin up Hamiltonian with levels $\varepsilon_1, \varepsilon_3$ coupled to each other through t_{13} and coupled to left and right leads through $V_{k_L}^{1,3}$ and $V_{k_R}^{1,3}$	90

Figure 31 – a) Schematic $\text{In}_{0.85}\text{As}_{0.15}\text{Bi}$ QD Hamiltonian for the four topologically protected edge states $j_z = \pm 5/2$ and $j_z = \pm 7/2$ coupled to left (L) and right (R) leads. b) Topological $\text{In}_{0.85}\text{As}_{0.15}\text{Bi}$ QD energy levels as a function of j_z for $R = 30$ nm [The green triangles represent the $j_z = \pm 5/2$ and $j_z = \pm 7/2$ energy levels considered in the conductance calculation]. c) QD conductance calculation \mathcal{G} at $T = 0$ K for the $j_z = \pm 5/2, \pm 7/2$ as a function of the QD radius R and the gate potential V_g . QD conductance \mathcal{G} at $T = 0$ K for d) $R = 30$ nm, e) $R = 48.8$ nm and f) $R = 70$ nm.	95
Figure 32 – $\text{In}_{0.85}\text{As}_{0.15}\text{Bi}$ QD conductance calculation \mathcal{G} (black curve), \mathcal{G}_{DOS} (blue curve) and \mathcal{G}_{INT} (red curve) Eq. (6.27) with $R = 30$ nm [Fig. 31d)] as a function of V_g . The blue curve represents the DOS contribution of the total conductance \mathcal{G} (always positive) while the red curve represents the interference contribution.	96
Figure 33 – a) Schematic $\text{In}_{0.85}\text{As}_{0.15}\text{Bi}$ QD Hamiltonian for the four geometrically protected trivial edge states $j_z = \pm 5/2$ and $j_z = \pm 7/2$ coupled to left (L) and right (R) leads. b) Trivial $\text{In}_{0.85}\text{As}_{0.15}\text{Bi}$ QD energy levels as a function of j_z for $R = 30$ nm [The green triangles represent the $j_z = \pm 5/2$ and $j_z = \pm 7/2$ energy levels considered in the conductance calculation]. c) QD conductance calculation \mathcal{G} at $T = 0$ K for the $j_z = \pm 5/2, \pm 7/2$ as a function of the QD radius R and the gate potential V_g . QD conductance \mathcal{G} at $T = 0$ K for d) $R = 30$ nm, e) $R = 48.8$ nm and f) $R = 70$ nm.	98
Figure 34 – Schematic $\text{In}_{0.85}\text{As}_{0.15}\text{Bi}$ QD Hamiltonian for the edge states $j_z = \pm 9/2$ and the bulk state $j_z = \pm 1/2$ coupled to left (L) and right (R) leads. b) Trivial $\text{In}_{0.85}\text{As}_{0.15}\text{Bi}$ QD energy levels as a function of j_z for $R = 30$ nm [The green triangles represent the $j_z = \pm 9/2$ and $j_z = \pm 1/2$ energy levels considered in the conductance calculation]. c) QD conductance calculation \mathcal{G} at $T = 0$ K for the $j_z = \pm 9/2, \pm 1/2$ as a function of the QD radius R and the gate potential V_g . QD conductance \mathcal{G} at $T = 0$ K for d) $R = 30$ nm, e) $R = 48.8$ nm and f) $R = 70$ nm.	100
Figure 35 – Few spin + non-trivial edge states with their nearest bulk valence level $j_z^o = 1/2$ as a function of QD radius R . The red points indicate the degenerate crossing points where the number of the protected trivial edge states is decreased by one.	101

LIST OF TABLES

Table 1 – Effective BHZ parameters for $\text{InAs}_{0.85}\text{Bi}_{0.15}/\text{AlSb}$ QW with different well thickness, 6 and 8 nm.	48
-----------------------------------------------------------------------------------------------------------------------------------------------	----

CONTENTS

1	INTRODUCTION	23
2	INTRODUCTION TO TOPOLOGICAL INSULATORS	27
2.1	Crystals and Band Theory	27
2.2	Topology and Topological Insulators	29
2.3	Bernevig-Hughes-Zhang (BHZ) Model	32
3	<i>InAs</i>_{1-<i>x</i>}<i>Bi</i>_{<i>x</i>}: A NEW TOPOLOGICAL INSULATOR PROPOSAL	39
3.1	Virtual crystal approximation (VCA)	39
3.2	Valence Band Anti-Crossing (VBAC) theory	39
3.2.1	Periodic Anderson model	41
3.2.2	Dilute alloy case	42
3.3	InAs alloyed with Bi atoms	45
3.3.1	Virtual crystal approximation - InAsBi	45
3.3.2	Valence band anti-crossing theory - InAsBi	46
3.4	Symmetric AISb/<i>InAs</i>_{0.85}<i>Bi</i>_{0.15}/AISb quantum well grown on a GaSb substrate	47
4	BHZ QUANTUM DOTS	51
4.1	Cylindrical BHZ Quantum Dots	51
4.2	Energies and wave functions	52
4.2.1	Hard-Wall case	55
4.3	QD cylindrical symmetries and their good quantum numbers	55
4.3.1	Effective Inversion Symmetry	57
4.3.2	Total Angular Momentum	58
4.3.3	Time Reversal Symmetry	59
4.4	Circulating current densities	60
4.4.1	QD circulating currents	61
4.4.2	Helical states	63
5	RESULTS: ENERGY, WAVE-FUNCTION AND CIRCULATING CURRENT	65
5.1	Energy levels and wave functions	65
5.1.1	Topologically non-trivial <i>InAs</i> _{0.85} <i>Bi</i> _{0.15} QD	65
5.1.2	Topologically trivial <i>InAs</i> _{0.85} <i>Bi</i> _{0.15} QD	69
5.1.3	Topologically trivial <i>InAs</i> _{0.85} <i>Bi</i> _{0.15} QD in the presence of BIA	74
5.1.4	Ordinary InAs QD	74

5.1.5	Ordinary InAs QD in the presence of C_1 - H_1 mixing	77
5.1.6	Ordinary InAs QD in the presence of spin orbit Rashba term	78
5.1.7	Ordinary InAs QD in the presence of bulk inversion asymmetry term (BIA)	79
5.2	Circulating current densities	80
5.2.1	Topologically non-trivial $\text{InAs}_{0.85}\text{Bi}_{0.15}$ QD	80
5.2.2	Topologically trivial $\text{InAs}_{0.85}\text{Bi}_{0.15}$ QD	82
5.3	HgTe/CdTe QD	84
5.4	Stability of the protected trivial helical edge states under the soft wall confinement	85
5.4.1	Soft-wall confinement	85
6	CONDUCTANCE CALCULATION	89
6.1	QD Hamiltonian and its Green function	89
6.2	Conductance	91
6.3	Results	94
6.3.1	Conductance results for topologically trivial and non-trivial edge states	95
6.3.2	Conductance results for the coexistence of edge-like and bulk-like states	98
7	CONCLUSION	103
	REFERENCES	105
	ANNEX	113
	ANNEX A – SUBMITTED ARTICLES	115
	ANNEX B – SUBMITTED ARTICLES	145

1 INTRODUCTION AND OUTLINE

In the last decades, topological states of quantum matter have been investigated deeply in condensed matter physics. This field has increased and developed very fast because of the precise theoretical predictions and the possibility of different applications. The field started with the Integer Quantum Hall Effect¹ (IQHE) and its robust quantized longitudinal conductance arising from its exotic dissipationless transport along the edges. Later on, the discovery of topological insulators (TI)^{2,3} brought about another revolution in the field. Apart from realizing novel phases of matter, these TI materials can be used in many applications like spintronics and low-power electronics,⁴⁻⁶ and can even serve as a platform to realize another exotic phases of matter like Majorana fermions⁷⁻¹¹ envisioned as candidates for building robust topological qubits.^{4,5,7,8} Additionally, the classification of topological states of matter was also extended to include gapless systems. These so-called topological semimetals host exotic quasi-particles such as Weyl and 2D/3D Dirac massless fermions¹² - neither of them observed as fundamental particles in nature so far.

Topological insulators are a new class of insulators having the unusual property of being insulators in bulk with gapless helical* edge states localized near their edges (2D TIs) or surfaces (3D TIs). The defining property of these edge/surface states is the locking between spin and momentum, i.e., the spin of the electron determines their propagation direction as they are locked to each other [See Fig. 1b) in which spin up (down) moves counterclockwise (clockwise)]. One of the most important features of these edge states, is that their propagation direction is protected against non-magnetic elastic backscattering by time reversal symmetry, which leads to dissipationless transport through the edges, similarly to the Integer Quantum Hall Effect (IQHE)¹ Figs. 1a) and c). In other words, each time that an edge state electron meets a non-magnetic impurity, it never scatters backward. Instead, it goes around this impurity [Fig. 1d)] with no dissipation produced. Additionally, these helical edge states are robust as they are guaranteed to exist by the topology of the system. This means that their existence does not depend on fine tuning of the geometrical parameters of the Hamiltonian (unless they change the topological phase or indices) or on the geometry of the interface. As a consequence, TIs have attracted the attention of the scientific community since they may improve electronic transport and enable novel applications. Topological Insulators are also referred to as quantum spin hall insulators which can give rise to the Quantum Spin Hall Effect (QSHE)^{2,3} when one considers a finite geometry [Fig. 1b)] and the Fermi level within the gap. The QSHE can be interpreted as two copy of the IQHE with opposite spins and opposite propagation

* Helical here means that the spin up and down have opposite propagation direction, see Fig. 1b)

directions in the absence of the magnetic field [Fig. 1b)].

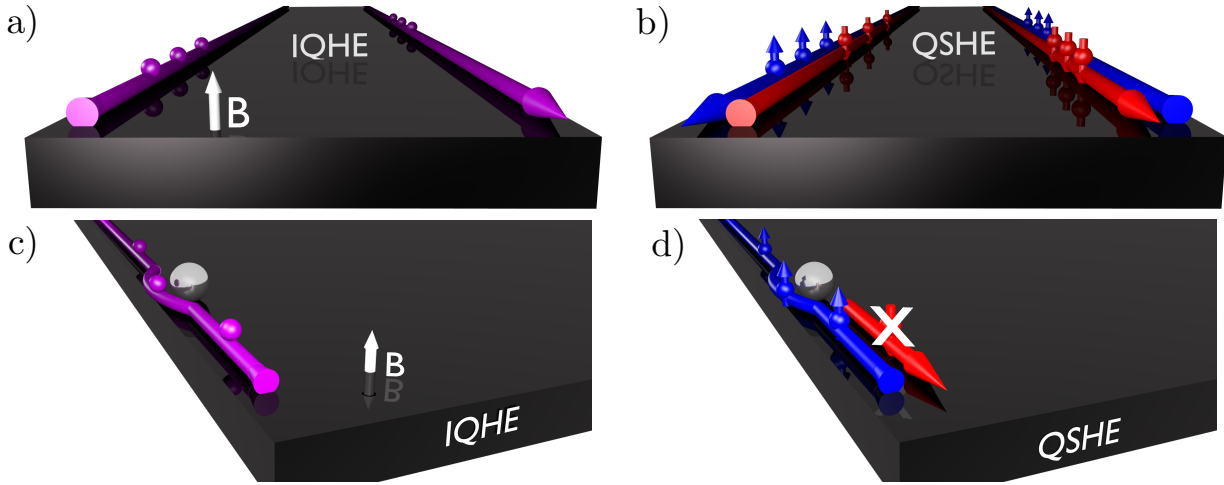


Figure 1 – a) Schematic representation of the IQHE with one chiral edge state (either spin up or down). b) Same as a) for the QSHE with its two helical edge states. c) In the IQHE, the backscattering is not possible since for each interface there are only states (either spin up or down) going in one direction. d) Differently from Fig. 1c), in the QSHE we find helical edge states with spin-momentum locking traveling in both directions. However, here the elastic backscattering off non-magnetic impurities is protected by time reversal symmetry as we need to flip the spin to move in the opposite direction.

Source: By the author

The first 2D TI was proposed by Kane and Mele² based on the spin-orbit interaction in graphene. Independently, Bernevig and Zhang³ also proposed a QSHE in semiconductors based on the spin-orbit interaction induced by strain gradient. However, no of these proposals has yet been realized because of the small spin-orbit interaction in graphene systems and the experimental difficulty when dealing with strain gradients. Later on, Bernevig, Hughes and Zhang proposed a topological phase transition in HgTe/CdTe QWs controlled by the thickness of the QW.¹³ In 2007, König et. al., realized for the first time the 2D HgTe/CdTe TI and measured their quantized conductance following from the QSHE. In 2008, Liu¹⁴ proposed another 2D TI based on the usual InAs/GaSb QW, followed also by the experimental realization through conductance calculations¹⁵ (We emphasize this result is still controversial as similar results were also found in the trivial regime). The 2D TI proposal was also extended for III–V double wells with just electrons.¹⁶ Later on, the concepts of TIs was also extended to 3D system^{17,18} and subsequently probe experimentally using ARPES.^{19–21}

To understand the concepts and the ingredients behind TIs, in Chapter 2 of this thesis we briefly introduce this field making connections with band theory, semiconductors, topology and topological phases. We also derive in detail the effective Bernevig-Hughes-

Zhang (BHZ) Hamiltonian that describes the band structure around the topological phase transition of 2D TIs (e.g., HgTe/CdTe).

Despite the fact that 2D and 3D TIs have already been realized experimentally, it is important to emphasize that only a few groups managed to obtain experimental evidence of 2D TIs.^{6,22} This is due to most proposals relying on materials systems (e.g., HgTe/CdTe) that are instable, difficult to grow and to reproduce. Therefore, it is important to find alternative 2D TI proposals using standard and stable materials, more easily synthesized from the point of view of growth and micro-fabrication.

Motivated by the above issue, we present in Chapter 3 a *new 2D TI proposal* based on the ordinary InAs material alloyed with Bi, which contains a large inverted gap ~ 30 meV possibly supporting practical applications at room temperature. Our new proposal consists of a symmetric InAs_{0.85}Bi_{0.15}/AlSb QW grown on a GaSb substrate. For the InAs_{1-x}Bi_x, we use an extrapolation of its experimental linear gap reduction as a function of x , which is explained using Band Anti-Crossing theory for low Bi concentration. We then solve numerically the InAs_{0.85}Bi_{0.15}/AlSb QW Hamiltonian[†] and find an inversion between the conduction E_1 and valence HH_1 subbands for a quantum well thickness $d = 6.9$ nm, similar to the 2D TI HgTe/CdTe QWs. We also derive the corresponding effective BHZ Hamiltonian describing the physics around this topological phase transition.

More recently, cylindrical quantum dots (QDs) made out of TI materials have also been investigated.²³⁻³⁴ They are artificial atoms and have discrete energy levels with bound electronic states. TI QDs have received great attention in the last decade as a consequence of their potential applications in quantum spintronics, electronic devices, diode lasers, solar cells, single electron transistors and other quantum technologies.²³⁻³⁴ Therefore, it became important to perform electronic structure and transport calculations in TI QDs. Now, a natural and fair question would be “is it possible to find the same features of topologically non-trivial QDs in topologically trivial QDs or ordinary QDs?”. To answer this question, in Chapter 4 we define BHZ QDs – topologically trivial or non-trivial – by introducing a cylindrical confining potential in the BHZ Hamiltonian. Then, we solve the corresponding BHZ QD eigenvalues problem analytically for the soft and hard wall confinements using the modified Bessel functions. For the hard wall case, we find analytical closed forms for the wave functions and circulating currents, together with a transcendental equation determining all the QD energy levels.

In Chapter 5 we thus present numerical results for the BHZ QDs for our InAs_{0.85}Bi_{0.15} QW TI proposal in both topologically trivial and non-trivial regimes. We show that InAs_{0.85}Bi_{0.15} QD in the non-trivial topological regime has counter propagating discrete helical edge states protected against elastic scattering within the energy gap. Most impor-

[†] this part of the work is done in collaboration with Prof. Michael Flatté from the University of Iowa

tantly, we report the first appearance of *helical edge states in topologically trivial* cylindrical BHZ QDs. Surprisingly, these trivial edge states are found to be *geometrically protected* against elastic scattering for a large range of the QD radius, thus showing the possibility of having the same features as those of a topologically non-trivial BHZ QD in a trivial one. We have also calculated the circulating currents for parameters spanning both the topologically trivial and non-trivial regimes, finding no substantial differences.

Although our electronic structure calculations showed an equivalence between trivial and non-trivial BHZ QDs, we could ask whether there should be further differences in a more detailed transport calculations. In order to answer this question, in Chapter 6 we perform a two-terminal conductance calculation within linear response at zero temperature ($T = 0$ K) as a means of finding possible quantities distinguishing the topologically trivial from the non-trivial helical edge states. We use a standard Green functions calculation to determine the dependence of the conductance as a function of the QD radius R and gate V_g controlling the QD energy levels with respect to the Fermi energy of the terminals (leads). For a conduction energy window with four protected helical edge states, we show that both topologically trivial and non-trivial BHZ QDs always present a double peak at $2e^2/h$ as a function of V_g for a fixed R . On the other hand, when both edge and bulk states coexist and lie in the conduction window, both topologically trivial and non-trivial BHZ QDs show a single conductance peak at $2e^2/h$ when the levels are degenerate.

Hence, we conclude that topological and non-topological edge states are also equivalent from the stand point of a quantum transport calculations. Therefore, our findings *blur the boundaries between topological and non-topological physical phenomena in small systems such as BHZ QDs*.

We summarize our findings in Chapter 7 together with possible extensions and perspectives for future developments.

2 INTRODUCTION TO TOPOLOGICAL INSULATORS

2.1 Crystals and Band Theory

In condensed matter physics, crystals are defined as a periodic arrangement of atoms extended in the vector space \mathbb{R}^1 , \mathbb{R}^2 or \mathbb{R}^3 . Their spatial positions are mathematically defined by the Bravais lattice together with the atomic basis. On the other hand, crystals can also be described in terms of their unit cells, which when stacked over all the dimension, originates the crystal. In general, the atoms crystallize in different types of unit cells giving rise to different crystal phases such as the Diamond, Zincblende and Wurtzite.³⁵ The crystal phases are defined by their symmetry under translations, rotations, reflections and improper rotations.^{36,37}

Similarly to the atoms, where the electrons can only occupy discrete energy levels, electrons in crystals are just allowed to occupy the quasi-continuum energy bands. Their energy bands are separated from each other by energy gaps which are prohibited energy regions for the electrons. The origin of the bands can be understood through the hybridization of the atomic orbitals between the different crystal atoms, also known as tight-binding approximation or Linear Combination of Atomic Orbitals (LCAO).^{35,38,39} When the spatial separation between two atoms becomes comparable to the lattice constant of the crystal ($3-7 \text{ \AA}$) their wave functions start to overlap yielding bonding and anti-bonding states. As a consequence of these overlaps through the whole crystal, the bonding and anti-bonding states are broadened into bands which have a range of allowed energy values, instead of just discrete levels (See Fig. 2).^{35,38,39} The bands that are occupied by electrons form the valence bands and the empty ones form the conduction bands. If our material has the highest full filled valence band separated by gap from an empty conduction band, the crystal is an insulator. On the other hand, if we have a partially filled band or an overlap between a valence and a conduction band, then our crystal is a metal. Semimetals are usually employed for a metal with a slight overlap of bands and semiconductors are insulators with a small gap $< 2 \text{ eV}$.

Usually, the most of II-V and III-V semiconductors crystallizes in the tetrahedrally bonded Zincblende phase e.g., GaAs, InAs, InSb, AlAs, CdTe, HgTe and InBi. For these materials, the valence electrons responsible for the crystal bonds are mainly³⁹ sp , i.e., the electrons with s and p orbitals (Fig. 2). Therefore, s and p orbitals of two different atoms hybridize and create new bonding (+) and anti-bonding (-) s^\pm and p^\pm orbitals (Fig. 2). Now, when these two new orbitals s^\pm and p^\pm hybridize with the other many atom orbitals of the crystal, bands are created. The $\Gamma_1(s^+)$ ($\Gamma_1(s^-)$) bands are made from the bonding s^+ (anti-bonding s^-) orbitals while $\Gamma_5(p^+)$ ($\Gamma_5(p^-)$) bands are made from the bonding p^+ (anti-bonding p^-) orbitals (Fig. 2).

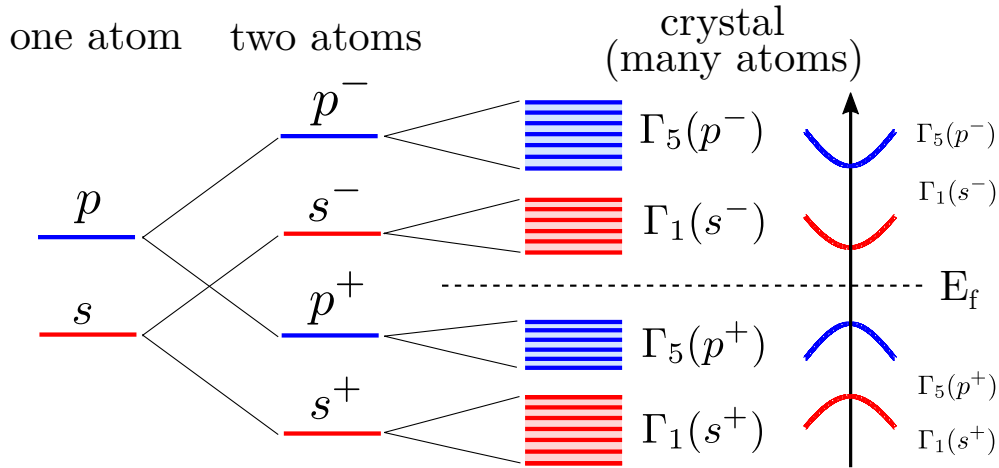


Figure 2 – Evolution of the s and p atomic orbitals from one atom into the conduction and valence bands of a crystal without spin-orbit coupling. $s^+(s^-)$ represents the new s-bonding (anti-bonding) orbitals arising from the hybridization of the s orbitals, while $p^+(p^-)$ represents the new p-bonding (anti-bonding) orbitals arising from the hybridization of the p orbitals. $\Gamma_1(s^+)$ ($\Gamma_5(p^+)$) represents the valence band from the s^+ (p^+) bonding orbitals and $\Gamma_1(s^-)$ ($\Gamma_5(p^-)$) represents the conduction band from the s^- (p^-) bonding orbitals. E_f represents the Fermi energy of the crystal.

Source: By the author

Although the tight-binding or LCAO picture (illustrated by Fig. 2) describes qualitatively well the formation of bands, the above description made by us fails on the details. For instance, in Fig. 2 we only considered the bands as originated from the hybridization of the atomic orbitals. If we now include the relativistic energy corrections from the Darwin term,^{37,40–43} the relativistic mass correction^{37,42,44,45} and the spin-orbit coupling,^{37,40–42,46} the energy bands change considerably. In Fig. 3, we show the evolution of the CdTe bands where all of these terms were taken into account gradually.^{47,48} We see in Fig. 3 that while the Darwin and the relativistic mass correction terms produce just a shift in the spectrum, the spin-orbit coupling splits the Γ_5 bands into Γ_8 and Γ_7 , with energy difference of Δ in between. For most of the II-V and III-V compounds, e.g., GaAs, InAs, InSb, AlAs, CdTe, the lowest conduction band is Γ_6 , arising mostly from the hybridization of the anti-bonding s^- orbitals while the highest valence bands is Γ_8 , arising mostly from the bonding p^+ orbitals.

On the other hand, materials with large atomic numbers and large spin orbit coupling, e.g., HgTe and InBi, have a different ordering of the bands. In Fig. 4 we show the evolution of the HgTe bands^{47,48} in the presence of the Darwin term, relativistic mass correction and spin-orbit coupling. Differently from Fig. 3, here the band ordering has changed. Instead of having Γ_6 as lowest conduction band, now we have a Γ_8 conduction

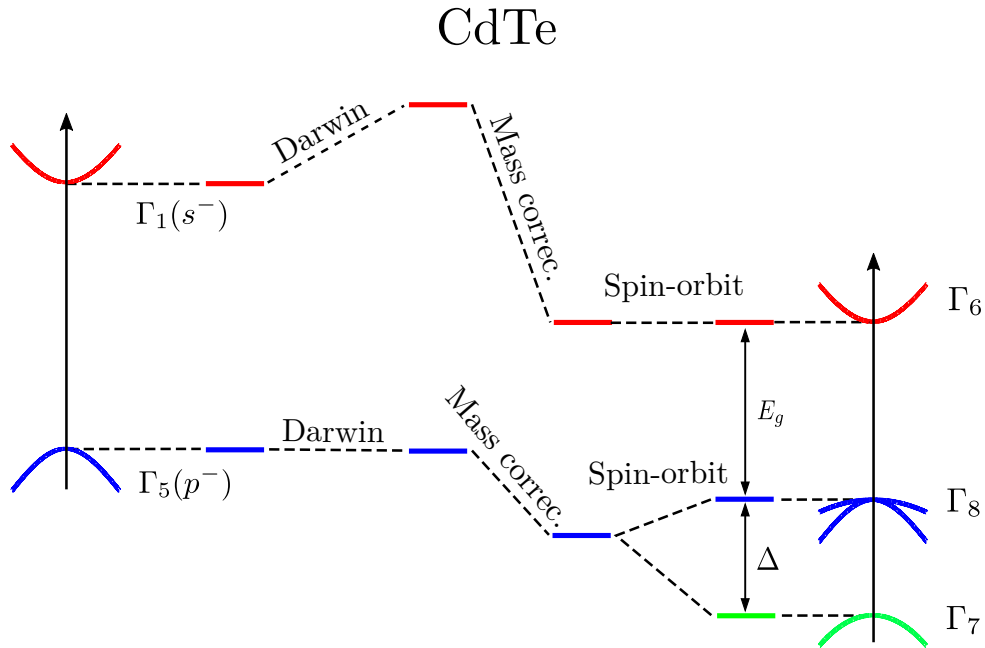


Figure 3 – Sketchy of the evolution of the simplified CdTe band structure as the relativistic terms (Darwin term, relativistic mass correction and spin-orbit coupling) are included subsequently. The final band structure profile shows a normal band ordering corresponding to the Γ_6 band above the Γ_8 bands.

Source: By the author

band*. The reason behind this distinct band ordering is attributed to the large atomic mass of Hg, i.e., ~ 2 times that of the Cd. In this case, the mass correction and the Darwin terms become larger and significantly lower the energy of the conduction band bottom, as can be seen in Fig. 4[†]. By turning on the spin-orbit coupling, we see that the Γ_8 bands now lie above the Γ_6 , characterizing a band inversion.

As we will in the next section, this band inversion is an important ingredient to have a topological insulator. Therefore, it becomes important to introduce the concepts of topology and topological insulators.

2.2 Topology and Topological Insulators

To start talking about topological insulator (TIs), we first introduce the concept of topology. Topology is a field of mathematics that studies the shape of surfaces.⁴⁹ The topology of a surface is usually characterized by integer numbers, which is said to be preserved under smooth deformation such as bending and/or compressing, but not gluing

* We emphasize that differently from the CdTe (Fig. 3), HgTe is a semimetal.

† Since the spin-orbit coupling is stronger in the Te atoms, the Δ value does not have a substantial change between HgTe and CdTe^{47,48}

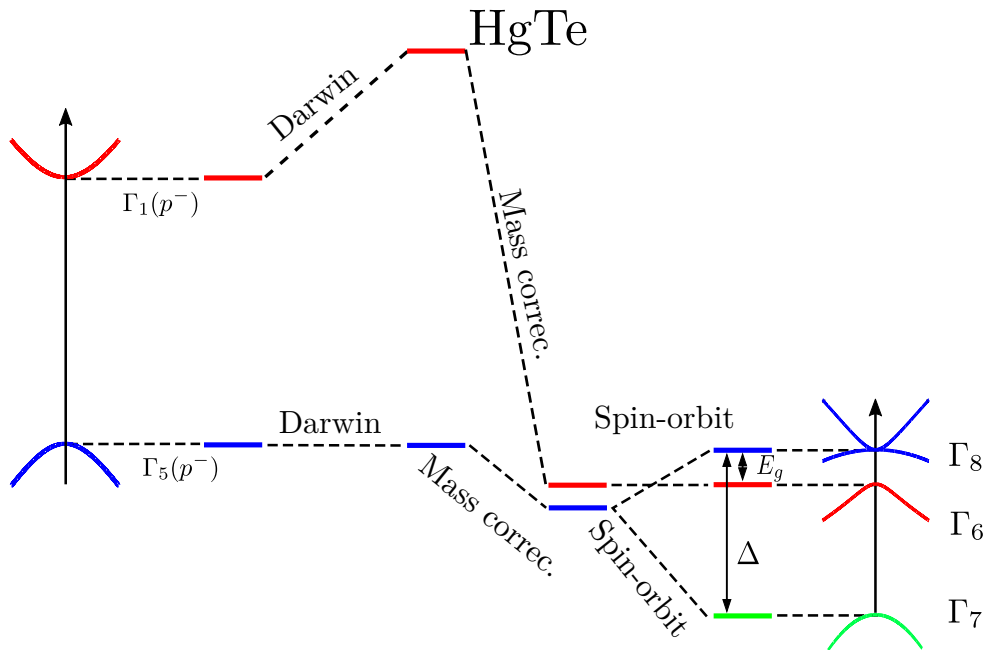


Figure 4 – Similar to Fig. 3 but for the simplified HgTe band structure with its large atomic number. We emphasize that the mass-correction terms significantly change the conduction band bottom which ultimately produces a band inversion upon the inclusion of the spin-orbit interaction. Note that the inverted band ordering corresponding to the Γ_6 band below the Γ_8 bands.

Source: By the author

or tearing. For two dimension surfaces, the topology is characterized by the genus[‡] g , which represents the number of the holes of the surface. In Fig. 5, the sphere (torus) with the topological number $g = 0$ ($g = 1$) can be smoothly deformed into an ellipsoid (coffee mug) which also has $g = 0$ ($g = 1$) and thus, they are said to be topologically equivalent. On the other hand, it is impossible to smoothly deform the sphere into a torus since they differ in the number of holes. The sphere and the torus are said to be topologically distinct since their integer number g cannot change smoothly from 0 to 1. On the other hand, we see that by tearing the torus, which is a non smooth deformation, we can change the topology of the object as the number of holes can be changed from 1 to 0.

Moving now to the physical part, we can ask how the topology can be used to classify different phases of insulators. Similar to the process described in Fig. 5, different insulators are said to be topologically equivalent if their energy spectra can be changed into each other by smooth changes in their Hamiltonians [Fig. 6a)]. Smooth here means that the changes should be made adiabatically, i.e., by preserving then the time scale $\tau \sim \frac{\hbar}{E_g}$ ^{50,51} with \hbar the reduced Planck constant and E_g the energy gap between the filled

[‡] The Gauss-Bonnet theorem⁴⁹ states that the integral of the Gaussian curvature over a closed surface is a topological invariant number, \mathcal{N} , related to g through $\mathcal{N} = 2(1 - g)$.

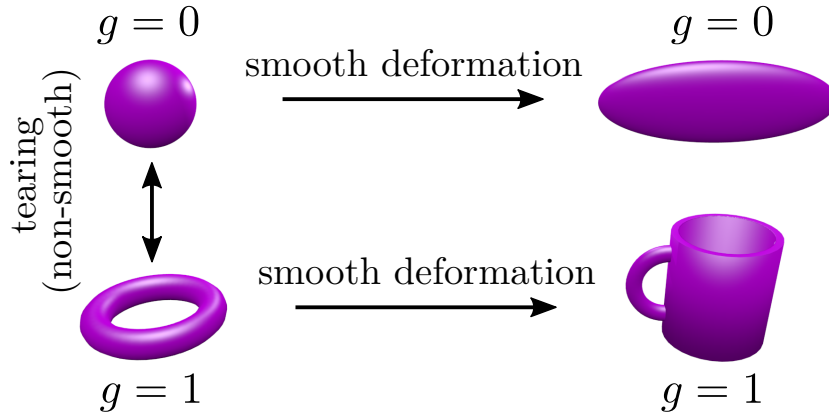


Figure 5 – The sphere and the ellipsoid are topologically equivalent (both with no holes, i.e., $g = 0$) as they can be deformed into each other by using only smooth deformations. We also show the torus and the coffee mug, which are topologically equivalent (both with one hole, i.e., $g = 1$). A non-smooth deformation as for example tearing does change the number of holes, thus connecting two topologically distinct objects.

Source: By the author

valence band and the nearest empty conduction band. Therefore, we state that different insulators are topologically equivalent if we can adiabatically connect their energy bands without closing the energy gap E_g [Fig. 6a)].^{4,5,51,52} Hence, in order to have a topological difference between insulators, we must have a topological phase transition defined as a transition where the gap closes and reopens with inverted bands.^{4,5,51,52} In Fig. 6b), we show an insulator evolving from one topological phase to another through a gap closing process (topological phase transition). As a consequence, we can also state that insulators with different band ordering have different topological phases, which is essentially the case of the HgTe and CdTe (Figs. 3 and 4)[§].

Although we have already explained how to identify different topological insulator phases and also noticed that HgTe (strained) and CdTe have different topological phases, we still do not know how to topologically classify each of them. Usually, the topological phases of an insulator are classified as trivial and non-trivial.⁵³ We can mathematically define their topological classification via topological quantities such as Chern number,⁵⁴ Berry phase,⁵⁵ TKNN invariants,⁵⁶ \mathcal{Z}_2 ,^{4,17} etc, depending on the symmetry of the Hamiltonian.⁵³ We define TIs as the materials with a non-trivial topological phase, corresponding to the topological indices different from zero, while the normal insulators with a trivial topological

[§] To be precise, HgTe cannot be classified with a topological insulator phase since it is a semimetal. However, by applying uniaxial strain we can open a gap¹⁷ at the Fermi energy thus transforming the HgTe in insulator with inverted bands.

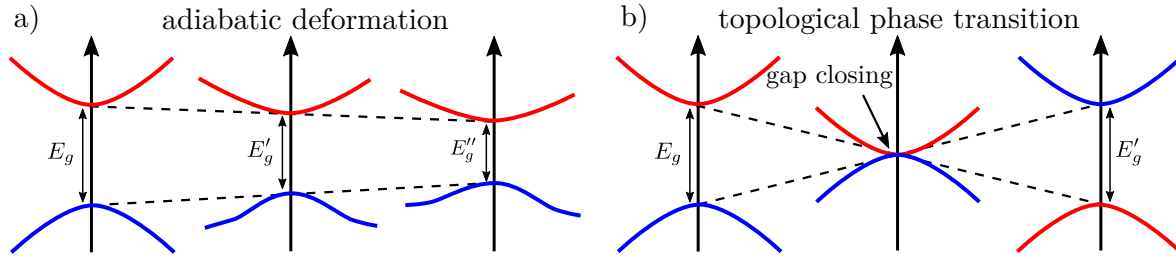


Figure 6 – a) Different energy dispersions within the same topological phase as they are all connected to themselves through adiabatic deformations. b) Different energy dispersion with different topological phase as they are connected only through a gap closing (topological phase transition).

Source: By the author

phase corresponding to the topological indices equals to zero.

An important result arises when we make an interface along some spatial coordinate by joining two materials A and B with distinct topological phases (indices), i.e., a TI and a normal insulator. For the sake of the concreteness, let us imagine that material A slowly changes its bands as a function of the spatial coordinate till the end of material B. Therefore, somewhere along this way the energy gap has to close since materials A and B have different band ordering (topological phases) [Fig. 7a)]. As a consequence, we find low energy states that connect the conduction to the valence band as the system has to be gapless at the interface. We call these states as edge states as they have to live where the gap closes, i.e., at the interface between materials A and B [Fig. 7b)]. This result is formally described by the bulk-boundary correspondence theorem^{4,5,51–53,57–59} which relates the number of low energy states localized in the interface and connecting the conduction and the valence bands with the difference on the topological indices of the materials A and B.

In the next section we derive in details the effective Hamiltonian for 2D TIs that describes accurately the band structure around a topological phase transition. As we will see, this Hamiltonian will be used many times during this thesis.

2.3 Bernevig-Hughes-Zhang (BHZ) Model

In this subsection we derive the Bernevig-Hughes-Zhang (BHZ) effective model¹³ that describes the low-energy physics of a HgTe/CdTe quantum well, the first 2D Topological Insulator (TI) discovered in nature.^{13,22}

Materials such as HgTe and CdTe crystallize in Zincblende structure. A well known method used to describe the physics of this system is the $\mathbf{k} \cdot \mathbf{p}$ method (or envelope function approximation for heterostructures),^{41,46,60–64} a semi-empirical method that uses

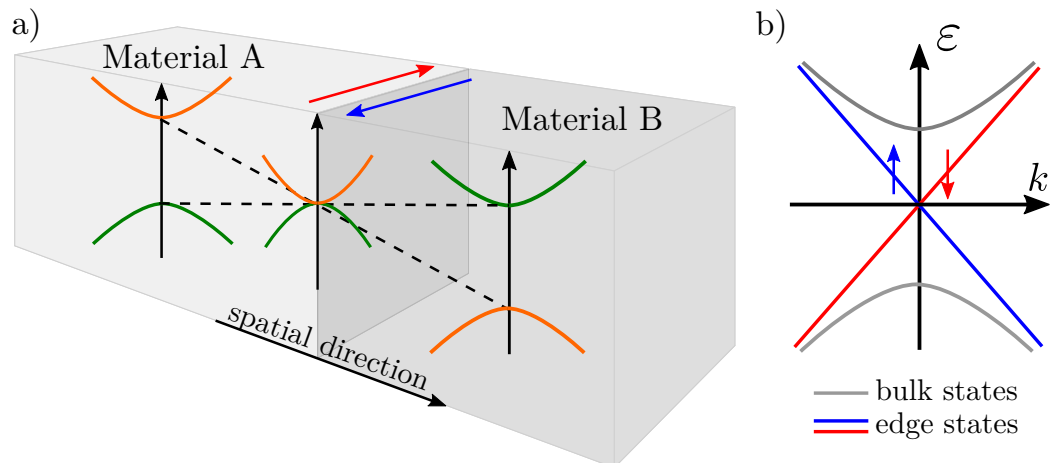


Figure 7 – a) Interface of two different materials with different topological phases and the edge states appearance in the interface between them (blue and red arrows). b) Bulk and edge state energy dispersions related to a).

Source: By the author

parameters obtained from experimental results and/or ab-initio calculations. This method was extensively derived and studied in my Master thesis,⁶⁵ thus showing the committee with this approach.

The starting point to derive the BHZ model for 2D TIs is the extended Kane Hamiltonian^{41,66} for QWs given by Eq. (2.1). This Hamiltonian describes the band structures around the Γ point ($k_x = k_y = 0$) arising from the confinement of lowest conduction band $|\Gamma_6, \frac{1}{2}, \pm\frac{1}{2}\rangle$ and the other three highest valence bands $|\Gamma_8, \frac{3}{2}, \pm\frac{1}{2}\rangle$, $|\Gamma_8, \frac{3}{2}, \pm\frac{3}{2}\rangle$ and $|\Gamma_7, \frac{1}{2}, \pm\frac{1}{2}\rangle$. This basis set is also known as the total angular momentum basis^{41,67} as they are eigenstates of the z-component of the total angular momentum J_z , i.e., $J_z |\Gamma_i, j, j_z\rangle = \hbar j_z |\Gamma_i, j, j_z\rangle$.

In the original derivation, the authors have excluded the $|\Gamma_7, \frac{1}{2}, \pm\frac{1}{2}\rangle$ split-off bands due to their small contribution to the relevant envelope functions.^{13,68} Here, however we will derive the BHZ model by taking into account the influence of also the $|\Gamma_7, \frac{1}{2}, \pm\frac{1}{2}\rangle$

bands.

$$\mathcal{H}_{|AM\rangle}^{8 \times 8} = \begin{pmatrix} T & 0 & -\frac{1}{\sqrt{2}}Pk_+ & \sqrt{\frac{2}{3}}P\hat{k}_z & \frac{1}{\sqrt{6}}Pk_- & 0 & -\frac{1}{\sqrt{3}}P\hat{k}_z & -\frac{1}{\sqrt{3}}Pk_- \\ 0 & T & 0 & -\frac{1}{\sqrt{6}}Pk_+ & \sqrt{\frac{2}{3}}P\hat{k}_z & \frac{1}{\sqrt{2}}Pk_- & -\frac{1}{\sqrt{3}}Pk_+ & \frac{1}{\sqrt{3}}P\hat{k}_z \\ -\frac{1}{\sqrt{2}}Pk_- & 0 & U+V & -\bar{S}_- & R & 0 & \frac{1}{\sqrt{2}}\bar{S}_- & -\sqrt{2}R \\ \sqrt{\frac{2}{3}}P\hat{k}_z & -\frac{1}{\sqrt{6}}Pk_- & -\bar{S}_-^\dagger & U-V & C & R & \sqrt{2}V & -\sqrt{\frac{3}{2}}\bar{S}_- \\ \frac{1}{\sqrt{6}}Pk_+ & \sqrt{\frac{2}{3}}P\hat{k}_z & R^\dagger & C^\dagger & U-V & \bar{S}_+^\dagger & -\sqrt{\frac{3}{2}}\bar{S}_+ & -\sqrt{2}V \\ 0 & \frac{1}{\sqrt{2}}Pk_+ & 0 & R^\dagger & \bar{S}_+ & U+V & \sqrt{2}R^\dagger & \frac{1}{\sqrt{2}}\bar{S}_+ \\ -\frac{1}{\sqrt{3}}P\hat{k}_z & -\frac{1}{\sqrt{3}}Pk_- & \frac{1}{\sqrt{2}}\bar{S}_-^\dagger & \sqrt{2}V & -\sqrt{\frac{3}{2}}\bar{S}_+^\dagger & \sqrt{2}R & U-\Delta & C \\ -\frac{1}{\sqrt{3}}Pk_+ & \frac{1}{\sqrt{3}}P\hat{k}_z & -\sqrt{2}R^\dagger & -\sqrt{\frac{3}{2}}\bar{S}_-^\dagger & -\sqrt{2}V & \frac{1}{\sqrt{2}}\bar{S}_+^\dagger & C^\dagger & U-\Delta \end{pmatrix} \quad (2.1)$$

$$T = E_c(z) + \frac{\hbar^2}{2m_0}A'k_{\parallel}^2 + \frac{\hbar^2}{2m_0}\hat{k}_z A' \hat{k}_z, \quad (2.2)$$

$$U = E_v(z) - \frac{\hbar^2}{2m_0}(\gamma_1 k_{\parallel}^2 + \hat{k}_z \gamma_1 \hat{k}_z), \quad (2.3)$$

$$V = -\frac{\hbar^2}{2m_0}(\gamma_2 k_{\parallel}^2 - 2\hat{k}_z \gamma_2 \hat{k}_z), \quad (2.4)$$

$$R = -\frac{\hbar^2}{2m_0}\sqrt{3}(\mu k_+^2 - \bar{\gamma} k_-^2), \quad (2.5)$$

$$\bar{S}_{\pm} = -\frac{\hbar^2}{2m_0}\sqrt{3}k_{\pm} \left(\{\gamma_3, \hat{k}_z\} + [\kappa, \hat{k}_z] \right), \quad (2.6)$$

$$C = \frac{\hbar^2}{m_0}k_- [\kappa, \hat{k}_z], \quad (2.7)$$

$$\bar{\gamma} = (\gamma_3 + \gamma_2)/2, \quad (2.8)$$

$$\mu = (\gamma_3 - \gamma_2)/2. \quad (2.9)$$

In the above Hamiltonian, all the parameters depend on axis z as we have a QW heterostructure along this direction. E_c and E_v correspond to the conduction and valence energies at $k_x = k_y = 0$ of the $|\Gamma_6\rangle$ and $|\Gamma_8\rangle$ bands, respectively, and Δ quantifies the split-off energy separation [see Figs. 3 and 4]. The notation $[A, B] = AB - BA$ denotes the commutator between the A and B operators while $\{A, B\} = AB + BA$ denotes their anti-commutator. P is the Kane parameter, m_0 is the free electron mass, γ_i are the Luttinger parameters⁶⁴ which together with κ and A' accounts for the influence of

remote bands up to second order in \mathbf{k} . Here for simplicity we will make the the axial approximation[¶], i.e., we take $\mu = 0$, and $\gamma_3 = \gamma_2 = \bar{\gamma}$, which results in an isotropic band structure in k_x, k_y plane.

Having established the Hamiltonian of our systems we now proceed with our perturbative approach. We first split the Hamiltonian in an unperturbed plus a perturbative term. The unperturbed Hamiltonian is chosen as the Hamiltonian in Eq. (2.1) at $k_x = k_y = 0$, and the perturbative part is simply the rest, i.e.,

$$\mathcal{H}_{|AM\rangle}^{8\times 8}(k_x, k_y) = \overbrace{\mathcal{H}_{|AM\rangle}^{8\times 8}(k_x = 0, k_y = 0)}^{\text{unperturbed}} + \overbrace{\mathcal{H}'_{|AM\rangle}(k_x, k_y)}^{\text{perturbation}}. \quad (2.10)$$

We then solve the unperturbed part for, e.g., HgTe/CdTe QW for concreteness with thickness d Fig. 8a) and parameters given in Ref. 71. In Fig. 8b) we plot the subband QW energies as a function of the thickness d . As we already discussed, here we find an inversion of the E_1^\pm and HH_1^\pm subbands at $d_c \sim 6.8$ nm, characterizing a topological phase transition.^{4-6,13}

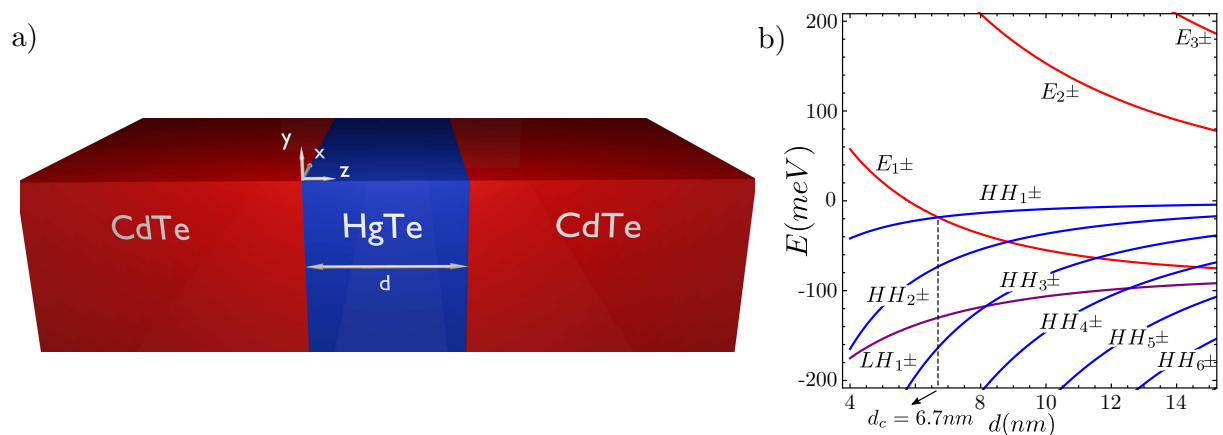


Figure 8 – a) Schematic HgTe/CdTe quantum well with thickness d . b) Spin degenerate (\pm) HgTe/CdTe quantum well energy subbands as a function of the QW thickness d at $k_x = k_y = 0$. Here we see the subband inversion at $d = d_c$ between the E_1 and HH_1 .

Source: By the author

The idea of the BHZ model is to describe the E_1 and HH_1 subband inversion via an effective low-energy model so that we focus on the relevant E_1 and HH_1 subbands.

[¶] In the total QW Hamiltonian (2.1), the term that breaks the axial symmetry is proportional to $\gamma_2 - \gamma_3$. For most of semiconductors this term is a small quantity as compared to the terms proportional to γ_1 and γ_2 .^{69,70}

The total wave function of the lowest E_1 and HH_1 subband states from Eq. (2.1) can be written within the envelope function approximation (EFA)^{38,60,61} as

$$|E_{1\pm}\rangle = f_1^\pm(z) \left| \Gamma_6, \frac{1}{2}, \pm \frac{1}{2} \right\rangle + f_4^\pm(z) \left| \Gamma_8, \frac{3}{2}, \pm \frac{1}{2} \right\rangle + f_7^\pm(z) \left| \Gamma_7, \frac{1}{2}, \pm \frac{1}{2} \right\rangle \quad (2.11)$$

$$|HH_{1\pm}\rangle = f_3^\pm(z) \left| \Gamma_8, \frac{3}{2}, \pm \frac{3}{2} \right\rangle, \quad (2.12)$$

where $f_i^\pm(z)$ with $i = 1, \dots, 8$ denote the eight components of the QW envelope wavefunctions arising from the confinement. We now project the Hamiltonian Eq. (2.1) in the basis set $|E_{1+}\rangle, |HH_{1+}\rangle, |E_{1-}\rangle, |HH_{1-}\rangle$, creating an effective electronic Hamiltonian of this 4×4 subspace given by

$$\mathcal{H}_{BHZ}(k_x, k_y) = \begin{pmatrix} \epsilon(\mathbf{k}) + M(\mathbf{k}) & Ak_+ & 0 & 0 \\ Ak_- & \epsilon(\mathbf{k}) - M(\mathbf{k}) & 0 & 0 \\ 0 & 0 & \epsilon(\mathbf{k}) + M(\mathbf{k}) & -Ak_- \\ 0 & 0 & -A^*k_+ & \epsilon(\mathbf{k}) - M(\mathbf{k}) \end{pmatrix}, \quad (2.13)$$

where $M(\mathbf{k}) = M - B\mathbf{k}^2$, $\epsilon(\mathbf{k}) = C - D\mathbf{k}^2$ and $\mathbf{k}^2 = k_x^2 + k_y^2$. The BHZ parameters C and M represent respectively the middle gap and the half of the gap size, i.e.,

$$C = \frac{E_{E_{1\pm}} + E_{HH_{1\pm}}}{2}, \quad (2.14)$$

$$M = \frac{E_{E_{1\pm}} - E_{HH_{1\pm}}}{2}, \quad (2.15)$$

while B , D and A are defined as

$$B = \frac{\langle HH_{1\pm} | \mathcal{H}'_{|AM}\rangle | HH_{1\pm}\rangle - \langle E_{1\pm} | \mathcal{H}'_{|AM}\rangle | E_{1\pm}\rangle}{2\mathbf{k}^2}, \quad (2.16)$$

$$D = \frac{-\langle HH_{1\pm} | \mathcal{H}'_{|AM}\rangle | HH_{1\pm}\rangle - \langle E_{1\pm} | \mathcal{H}'_{|AM}\rangle | E_{1\pm}\rangle}{2\mathbf{k}^2}, \quad (2.17)$$

$$A = \pm \frac{\langle E_{1\pm} | \mathcal{H}'_{|AM}\rangle | HH_{1\pm}\rangle}{k_\pm}. \quad (2.18)$$

The block diagonal form of the BHZ Hamiltonian Eq. (2.13) here happens as a consequence of the two-fold degeneracy of the 8×8 Kane Hamiltonian Eq. (2.1) in the absence of

the Bulk inversion asymmetry terms (BIA)^{36,41,72} and the structural inversion asymmetry (SIA).^{41,67,73}

Although a lot of authors claim that the \pm signs of the BHZ model represent the real *spin*, this is not a precise information. To emphasize this point we analyze the dependence of the BHZ basis states ($|E_1\pm\rangle$ and $|HH_1\pm\rangle$) explicitly writing the BHZ basis in terms of their spin up $|\uparrow\rangle$ and spin down $|\downarrow\rangle$ components. For the $|HH_1\pm\rangle$ state we have

$$|HH_1+\rangle = \frac{f_3^+(z)}{\sqrt{2}} |X + iY\rangle |\uparrow\rangle, \quad |HH_1-\rangle = -\frac{f_3^-(z)}{\sqrt{2}} |X + iY\rangle |\downarrow\rangle, \quad (2.19)$$

which shows that the \pm signs in the $|HH_1\pm\rangle$ states do represent spin up and spin down states (along the growth direction z). On the other hand, for the $|E_1\pm\rangle$ states we have

$$|E_1+\rangle = f_1^+(z) |S\rangle |\uparrow\rangle + \frac{f_4^+(z)}{\sqrt{6}} |X + iY\rangle |\downarrow\rangle - \sqrt{\frac{2}{3}} f_7^+(z) |Z\rangle |\uparrow\rangle, \quad (2.20)$$

$$|E_1-\rangle = f_1^-(z) |S\rangle |\downarrow\rangle - \frac{f_4^-(z)}{\sqrt{6}} |X - iY\rangle |\uparrow\rangle - \sqrt{\frac{2}{3}} f_7^-(z) |Z\rangle |\downarrow\rangle, \quad (2.21)$$

which clearly show that due to the middle terms of the above equations, the $|E_1\pm\rangle$ states cannot be considered as purely spin up or down. Therefore, as a general solution of the BHZ Hamiltonian Eq. (2.13) should be a linear combination of $|E_1\pm\rangle$ and $|H_1\pm\rangle$, the spin indices up and down $|\uparrow\rangle$ and $|\downarrow\rangle$ are not good quantum numbers. Interestingly, the calculated expectation value of $\frac{\hbar}{2}\sigma_z$ for states arising from the confinement⁷⁴ yields $\approx \frac{\hbar}{2}$, showing, however, that it is a good approximation to treat the \pm subspace with \uparrow, \downarrow .

In the next chapter we propose a new 2D TI based on the addition of Bi in the InAs QWs. Similarly to the HgTe/CdTe QWs 2D TI, the thickness of the well also controls the topological phase transition in our proposal. We calculate the corresponding BHZ parameters of our proposal.

3 $InAs_{1-x}Bi_x$: A NEW TOPOLOGICAL INSULATOR PROPOSAL

In this chapter we predict that the symmetric AlSb/InAs_{1-x}Bi_x/AlSb quantum well (QW) becomes a new 2D topological insulator for $x = 0.15$ and for well widths $d > 6.9$ nm. Its large inverted topological gap ~ 30 meV has the advantage of enabling applications at room temperature. This prediction is achieved combining experimental data^{75–77} explained by the Valence Band Anti-Crossing (VBAC) theory^{78–83} and finding numerically the QW energy subbands.

3.1 Virtual crystal approximation (VCA)

A simple and first approximation to predict the values of some physical parameter, \mathcal{X} (e.g., fundamental band gap, effective mass, lattice constant, etc), of a semiconductor alloy $A_xB_{1-x}C$, where AC and BC are crystalline compounds, is to assume that the parameters scale linearly between their bulk values for $x = 0$ and $x = 1$, i.e.,

$$\mathcal{X}(A_xB_{1-x}C) = x\mathcal{X}(AC) + (1-x)\mathcal{X}(BC). \quad (3.1)$$

This is also known as virtual crystal approximation (VCA).⁷¹ For some quantities such as the lattice constant, it yields very accurate results.⁷¹ However, the fundamental band gaps of alloy semiconductors do not always obey the linear trend in Eq. (3.1) with concentration x .^{71,84,85} In this case, we need to consider some “bowing terms”, i.e., higher order in x terms, to obtain, for example, the correct fundamental gap of GaAs_{1-x}N_x^{86–89} and ZnSe_{1-x}Te_x.^{84,85} Usually, a bowing term b for the fundamental gap appears as

$$E_g(A_xB_{1-x}C) = xE_g(AC) + (1-x)E_g(BC) - bx(1-x). \quad (3.2)$$

The origin of the bowing term was studied in some works⁹⁰ and shown that Eq. (3.2) could be derived by considering the effect of the alloy as disorder via perturbation theory. So that the VCA approximation just works when the bowing parameter b is much smaller than the fundamental energy gap E_g and at low alloy concentrations.

3.2 Valence Band Anti-Crossing (VBAC) theory

There are many theories that explain the origin of the bowing term in the fundamental gap of allowed semiconductors.^{90–97} Here, however, we will focus only on the two-level band anti-crossing theory (BAC),^{78,79} also known as valence/conduction band

anti-crossing theory (VBAC/CBAC).^{80–83} We emphasize that this theory describes accurately many experimental results in literature such as the N-induced enhancement of the effective mass,^{98,99} change of the fundamental gap from indirect to direct in GaP_{1-x}N_x¹⁰⁰ and fundamental band gap reduction of the GaSb_xAs_{1-x}, GaBi_xAs_{1-x} and GaAs_{1-x}N_x alloys.^{80–82}

Within BAC theory, the extended crystal band states hybridize with the localized impurities states, randomly placed in the crystal. The interaction is modeled using an anti-crossing two level system. Formally, the whole BAC theory is derived^{80,81} using the many-impurity Anderson model,¹⁰¹ which deal with a continuum spectrum coupled to discrete levels. In our case, the continuum spectrum corresponds to the crystal band structure while the discrete impurity levels correspond to the alloy atoms energy levels. In the following paragraphs we derive the equations of the BAC theory.

First, we start with the many-impurity Anderson model, which has the Hamiltonian^{80,81}

$$\mathcal{H} = \sum_{\mathbf{k}} \varepsilon_{\mathbf{k}} c_{\mathbf{k}}^{\dagger} c_{\mathbf{k}} + \sum_{\mathbf{i}} E_d d_{\mathbf{i}}^{\dagger} d_{\mathbf{i}} + \frac{1}{\sqrt{N}} \sum_{\mathbf{i}, \mathbf{k}} e^{i\mathbf{k}\mathbf{i}} V_{\mathbf{k}\mathbf{i}} c_{\mathbf{k}}^{\dagger} d_{\mathbf{i}} + h.c.. \quad (3.3)$$

The first term in Eq. (3.3) describes electrons in a band of the crystal “A” with wave vector \mathbf{k} and energy $\varepsilon_{\mathbf{k}}$. The second term represents the contribution of the localized impurities “D” at the i^{th} -site with energy E_d and vector coordinate \mathbf{i} . The last term describes the coupling of the localized electron states with the extended electrons of the band crystal, and N denotes the number of primitive cells in the crystal. Therefore, we say Eq. (3.3) represents the Hamiltonian of the crystal AD_{*x*} where the impurities D represent the alloy atoms in the original crystal A and x represents the number of alloy atoms per unit cell.

To solve our Hamiltonian Eq. (3.3), we will use the Green function approach.^{102–105} The retarded Green functions for the band electron and for the electron on the site \mathbf{i} are defined using the Zubarev notation¹⁰⁶ as, respectively,

$$G_{\mathbf{k}, \mathbf{k}}(t) \equiv \langle \langle c_{\mathbf{k}}(t), c_{\mathbf{k}}^{\dagger}(0) \rangle \rangle = \frac{1}{i\hbar} \theta(t) \langle \{ c_{\mathbf{k}}(t), c_{\mathbf{k}}^{\dagger}(0) \} \rangle, \quad (3.4)$$

$$G_{\mathbf{i}, \mathbf{i}}(t) \equiv \langle \langle d_{\mathbf{i}}(t), d_{\mathbf{i}}^{\dagger}(0) \rangle \rangle = \frac{1}{i\hbar} \theta(t) \langle \{ d_{\mathbf{i}}(t), d_{\mathbf{i}}^{\dagger}(0) \} \rangle, \quad (3.5)$$

where $\theta(t)$ is the Heavside function, $b(t) = e^{i\mathcal{H}t} b e^{-i\mathcal{H}t} \{ \dots \}$ is the anti-commutator and $\langle a \rangle$ represents the canonical ensemble average or a expectation value calculated at $T = 0$ K. The Fourier transform of Eqs. (3.4) and (3.5) reads

$$G_{\mathbf{k},\mathbf{k}}(E) \equiv \langle\langle c_{\mathbf{k}}, c_{\mathbf{k}}^\dagger \rangle\rangle = \int_{-\infty}^{\infty} dt G_{\mathbf{k},\mathbf{k}}(t) e^{i(\frac{E}{\hbar} + i0^+)t}, \quad (3.6)$$

$$G_{i,i}(E) \equiv \langle\langle d_i, d_i^\dagger \rangle\rangle = \int_{-\infty}^{\infty} dt G_{i,i}(t) e^{i(\frac{E}{\hbar} + i0^+)t}. \quad (3.7)$$

The Fourier transform of the Heisenberg equation, $i\hbar\partial_t A(t) = [A(t), H]$, yields the equations of motion for the retarded Greens function. Defining $G_{i,i}^{(0)}(E) = (E - E_d + i\eta)^{-1}$ and $G_{\mathbf{k},\mathbf{k}}^{(0)}(E) = (E - \varepsilon_{\mathbf{k}} + i\eta)^{-1}$, we obtain

$$G_{\mathbf{k},\mathbf{k}'}(E) = \delta_{\mathbf{k}\mathbf{k}'} G_{\mathbf{k},\mathbf{k}}^{(0)}(E) + \frac{G_{\mathbf{k},\mathbf{k}}^{(0)}(E) G_{i,i}^{(0)}(E)}{N} \sum_{i,\mathbf{k}''} e^{i(\mathbf{k}-\mathbf{k}'')i} V_{\mathbf{k}i} V_{\mathbf{k}''i} G_{\mathbf{k}'',\mathbf{k}'}(E). \quad (3.8)$$

Now we assume that $V_{\mathbf{k}i}$ depends weakly on the position and momentum, so we can assume it as constant i.e., $V_{\mathbf{k}i} = V$, yielding

$$G_{\mathbf{k},\mathbf{k}'}(E) = \delta_{\mathbf{k}\mathbf{k}'} G_{\mathbf{k},\mathbf{k}}^{(0)}(E) + \frac{V^2}{N} G_{\mathbf{k},\mathbf{k}}^{(0)}(E) G_{i,i}^{(0)}(E) \sum_{i,\mathbf{k}''} e^{i(\mathbf{k}-\mathbf{k}'')i} G_{\mathbf{k}'',\mathbf{k}'}(E) \quad (3.9)$$

3.2.1 Periodic Anderson model

First we solve the periodic Anderson model, where we have one localized state (impurity) per unit cell ($x = 1$) yielding the crystal AD. In this case, we have $\frac{1}{N} \sum_i e^{i(\mathbf{k}-\mathbf{k}'')i} = \delta(\mathbf{k} - \mathbf{k}'')$, and thus, Eq. (3.9) has the following closed form

$$G_{\mathbf{k},\mathbf{k}'}(E) = \delta_{\mathbf{k}\mathbf{k}'} G_{\mathbf{k},\mathbf{k}}^{(0)}(E) + V^2 G_{\mathbf{k},\mathbf{k}}^{(0)}(E) G_{i,i}^{(0)}(E) \sum_{\mathbf{k}''} \delta(\mathbf{k} - \mathbf{k}'') G_{\mathbf{k}'',\mathbf{k}'}(E), \quad (3.10)$$

$$= \delta_{\mathbf{k}\mathbf{k}'} G_{\mathbf{k},\mathbf{k}}^{(0)}(E) + V^2 G_{\mathbf{k},\mathbf{k}}^{(0)}(E) G_{i,i}^{(0)}(E) G_{\mathbf{k},\mathbf{k}'}(E), \quad (3.11)$$

$$\rightarrow G_{\mathbf{k},\mathbf{k}'}(E) = \frac{\delta_{\mathbf{k}\mathbf{k}'} G_{\mathbf{k},\mathbf{k}}^{(0)}(E)}{1 - V^2 G_{\mathbf{k},\mathbf{k}}^{(0)}(E) G_{i,i}^{(0)}(E)}. \quad (3.12)$$

Recalling the definitions of $G_{\mathbf{k},\mathbf{k}}^{(0)}(E)$ and $G_{i,i}^{(0)}(E)$, we obtain the diagonal Green's function

$$G_{\mathbf{k},\mathbf{k}}(E) = \frac{1}{(E - \varepsilon_{\mathbf{k}}) - \frac{V^2}{(E - E_d)}}. \quad (3.13)$$

The new energy dispersions of our system are thus obtained from the poles of $G_{\mathbf{k},\mathbf{k}}(E)$, which are equivalent to the eigenenergies of the two-level system below

$$\begin{vmatrix} \varepsilon_{\mathbf{k}} - E(\mathbf{k}) & V \\ V & E_d - E(\mathbf{k}) \end{vmatrix} = 0, \quad (3.14)$$

yielding

$$E_{\pm}(\mathbf{k}) = \frac{1}{2} \left[\varepsilon_{\mathbf{k}} + E_d \pm \sqrt{(\varepsilon_{\mathbf{k}} - E_d)^2 + 4V^2} \right]. \quad (3.15)$$

The above equation is understood as a result of the hybridization through the term V between the localized levels E_d and the crystal band state $\varepsilon_{\mathbf{k}}$, yielding two new energy dispersions arising from the anti-crossing between the old energies $\varepsilon_{\mathbf{k}}$ and E_d (see Fig. 9). This result is equivalent to the first proposal of the BAC model,⁷⁸ which at that time was not properly derived by the authors.

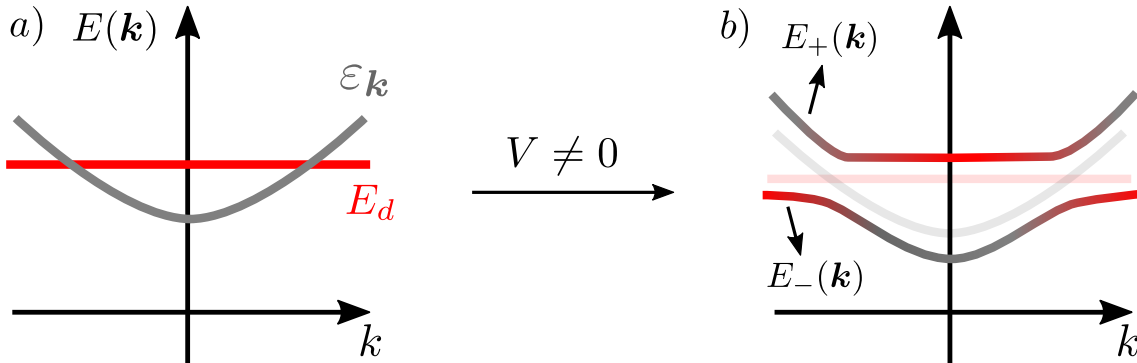


Figure 9 – a) Schematic $\varepsilon_{\mathbf{k}}$ band (gray solid curve) and the localized E_d energy level (red solid curve) with $V = 0$, i.e., no interaction with each other. b) Schematic plot of the energies $E_{\pm}(\mathbf{k})$ arising from the BAC model Eq. (3.15) with $V \neq 0$.

Source: By the author

3.2.2 Dilute alloy case

Now we consider the dilute alloy (impurity) crystal case AD_x , where the number of impurities per unit cell, x , obeys $x \ll 1$. The alloy atoms (impurities) in this case are assumed as randomly distributed in the whole crystal, so we can use the coherent potential approximation (CPA)^{107–109} where we neglect the correlations between the alloy atoms. By neglecting the correlations between different impurity positions we can use the configurational averaging to still treat our crystal as periodic, keeping then \mathbf{k} as a good

quantum number. Within the CPA approach, the $G_{\mathbf{k},\mathbf{k}}(E)$ Green function is given by^{80,81}

$$G_{\mathbf{k},\mathbf{k}}(E) = \frac{1}{E - \varepsilon_{\mathbf{k}} - \frac{xV^2 G_{i,i}^{(0)}(E)}{1 - \frac{V^2}{N} G_{i,i}^{(0)}(E) \sum_{\mathbf{k}} G_{\mathbf{k},\mathbf{k}}(E)}}. \quad (3.16)$$

It is clear that the $G_{\mathbf{k},\mathbf{k}}$ does not have a closed since we find $G_{\mathbf{k},\mathbf{k}}$ in the denominator of Eq. (3.16). Thus, in order to find an analytical closed expression for $G_{\mathbf{k},\mathbf{k}}(E)$ we approximate $\frac{1}{N} \sum_{\mathbf{k}} G_{\mathbf{k},\mathbf{k}} \approx \frac{1}{N} \sum_{\mathbf{k}} G_{\mathbf{k},\mathbf{k}}^{(0)}$ and use the wide band limit (WBL)^{103,110,111} approximation*. These two approximations yield

$$\frac{1}{N} \sum_{\mathbf{k}} G_{\mathbf{k},\mathbf{k}}(E) \approx \int d\varepsilon_{\mathbf{k}} \frac{\rho_0(E)}{E - \varepsilon_{\mathbf{k}} + i\eta} = -i\pi\rho_0(E), \quad (3.17)$$

where $\rho_0(E)$ is the density of states of the band $\varepsilon_{\mathbf{k}}$ for $x = 0$. Using Eq. (3.17) in Eq. (3.16), we obtain

$$G_{\mathbf{k},\mathbf{k}}(E) = \frac{1}{E - \varepsilon_{\mathbf{k}} - \frac{xV^2 G_{i,i}^{(0)}(E)}{1 + i\pi\rho_0(E)V^2 G_{i,i}^{(0)}(E)}} \quad (3.18)$$

$$= \frac{E - E_d + i\pi\rho_0(E)V^2}{(E - \varepsilon_{\mathbf{k}})(E - E_d + i\pi\rho_0(E)V^2) - xV^2} \quad (3.19)$$

The poles of the above Green's function can also be thought of as given by the energies of the following two-level system,

$$\begin{vmatrix} \varepsilon_{\mathbf{k}} - E(\mathbf{k}) & V\sqrt{x} \\ V\sqrt{x} & E_d + i\Gamma_d - E(\mathbf{k}) \end{vmatrix} = 0, \quad (3.20)$$

where $\Gamma_d = \pi V^2 \rho_0(E)$ corresponds to the broadening of the discrete levels E_d . If we take $\Gamma_d = 0$, we obtain similar energies as compared to Eq. (3.14), given by

$$E_{\pm}(\mathbf{k}) = \frac{1}{2} \left[\varepsilon_{\mathbf{k}} + E_d \pm \sqrt{(\varepsilon_{\mathbf{k}} - E_d)^2 + 4xV^2} \right], \quad (3.21)$$

where we recover completely Eq. (3.14) for $x = 1$. The form $V\sqrt{x}$ indicates that this effective coupling between the impurity levels and energy bands increase with alloy concentration. The broadening here appears as a consequence of the discrete levels coupled

* Within the WBL, the density of states of the crystal is assumed to have an energy range much larger than the characteristic energies of our system thus yielding a pure imaginary value of Eq. (3.17) - See Sec. 6.2 for details.

to the continuum, which broadens the energy levels of our system. The latter is also used to access information about the broadening of the optical transitions. We emphasize that the E_d and V energy parameters are determined by fitting the experimental data. From now on we refer to Eq. (3.21) as the Valence (Conduction) Band Anti-crossing VBAC (CBAC) equations if E_d lies in the valence (conduction) band.

Similarly to the BAC model, here we see using Eq. (3.21) that the inclusion of the alloy atoms with their discrete energy levels E_d produces two new energy dispersions given by $E_{\pm}(\mathbf{k})$. The origin of these two new energy dispersion is also a consequence of the anti-crossing repulsion between E_d and $\varepsilon_{\mathbf{k}}$ through the interaction of two level states. In order to understand physically the consequence of the appearance of the new two $E_{\pm}(\mathbf{k})$ energy bands, we assume that the energy level E_d lies in the conduction band $\varepsilon_{c\mathbf{k}}$, for example, and that the valence band $\varepsilon_{v\mathbf{k}}$ is far away in energy from both E_d and $\varepsilon_{c\mathbf{k}}$, so that we can ignore its influence on both E_d and $\varepsilon_{\mathbf{k}}$ (Fig. 10). For this case we see through Eq. (3.21) that we obtain an effective reduction of the fundamental gap as the repulsion between E_d and $\varepsilon_{\mathbf{k}}$ shifts $E_-(\mathbf{k})$ downward (represented schematically in Figure 10). As we already mentioned in the beginning of this chapter, the gap reduction has been reported many times in literature and is explained using Eq. (3.21).^{80–82,84–89} We emphasize that the VCA does not provide a correct prediction for this gap reduction^{80–82}

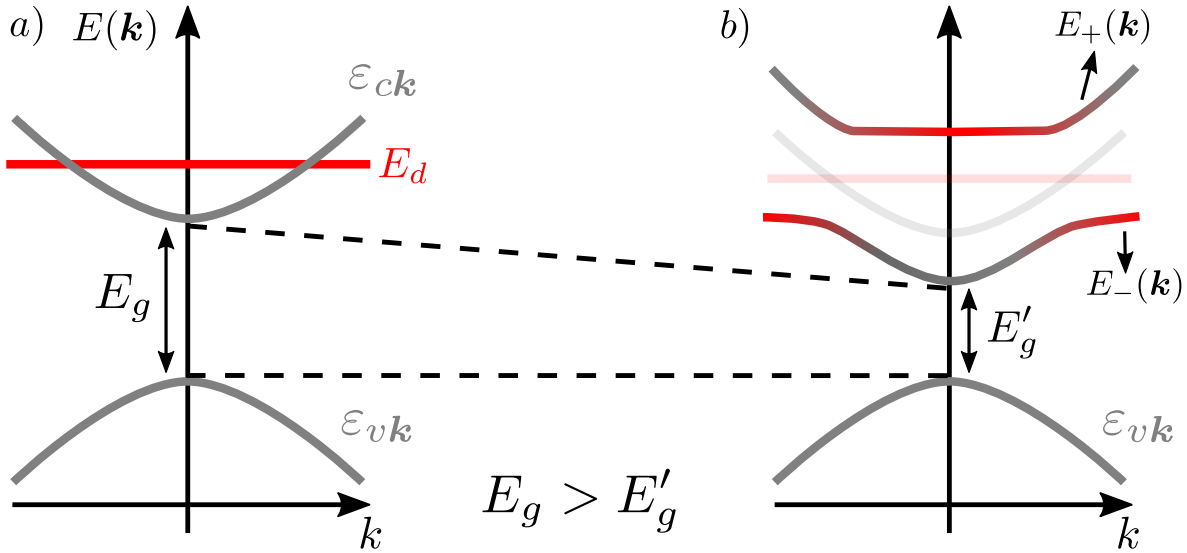


Figure 10 – Schematic conduction $\varepsilon_{c\mathbf{k}}$ and valence $\varepsilon_{v\mathbf{k}}$ bands (gray solid curves) and the localized E_d energy level resonant in the conduction band (red solid curve) with $V = 0$, i.e., no interaction with each other. b) Schematic plot of the energies $E_{\pm}(\mathbf{k})$ (Eq. 3.21) with $V \neq 0$. E'_g (E_g) represents the fundamental energy gap with (without) the resonant E_d energy level.

Source: By the author

Besides the shifts in the spectrum and its consequent gap reduction, Eq. (3.21)

also yields a change in the effective mass of the bands. Assuming a parabolic dispersion $\varepsilon_{\mathbf{k}} = \frac{\hbar^2 \mathbf{k}^2}{2m^*}$ in Eq. (3.21), we find the new effective masses given by

$$m_{\pm}^* = \frac{\hbar^2 k}{dE_{\pm}/dk|_{k=0}} = \frac{m^*}{\frac{1}{2} \pm \frac{\varepsilon_{\mathbf{k}=\mathbf{0}} - E_d}{2\sqrt{(\varepsilon_{\mathbf{k}=\mathbf{0}} - E_d)^2 + 4xV^2}}}, \quad (3.22)$$

which explain the mentioned enhancement of the effective mass ($m_-^* > m^*$) of the lowest conduction band E_- induced by the addition of Nitrogen as an alloy in GaAs.^{98,99}

3.3 InAs alloyed with Bi atoms

As we have already discussed in the previous chapter, the band inversion at the Γ point is the most important ingredient defining topological insulators. Motivated by the large reduction in the fundamental gap of GaAs when it is alloyed with Bi⁸² or N,^{80,81} here we investigate the InAs ordinary III-V material alloyed with Bi for a possible band inversion.

Bi atoms have the same number of valence states as the host InAs. Then, we refer to Bi as an isovalent impurity; hence there is no excess electrons or holes in the system. As we discussed in the last section, we can use the VBAC (CBAC) results to predict a reduction of the fundamental gap depending on where E_d lies. In contrast to the case described by Figure 10, where we have the resonant level in the conduction band, Bi has discrete levels (E_{Bi} and $E_{Bi,SO}$) in the InAs-valence bands (Γ_8 and Γ_7) as shown in Fig. 11. Therefore, we expect a repulsion between the valence bands and the discrete Bi energy levels yielding a reduction of the gap due to this upper shift of the valence band (see Fig. 11). In Fig. 11b) we have drawn the interaction of Bi with just one Γ_8 band in order to present the idea of the gap reduction through VBAC in a cleaner way.

3.3.1 Virtual crystal approximation - InAsBi

The first attempt to determine the fundamental gap of our $\text{InAs}_{1-x}\text{Bi}_x$ is to use the VCA where we have the fundamental gap of $\text{InAs}_{1-x}\text{Bi}_x$ given by

$$E_g^{\text{InAs}_{1-x}\text{Bi}_x} = (1-x)E_g^{\text{InAs}} + xE_g^{\text{InBi}}. \quad (3.23)$$

Using the results in literature $E_g^{\text{InAs}} = 417 \text{ meV}$ ⁷¹ and $E_g^{\text{InBi}} = -1610 \text{ meV}$,^{112,113} we find $E_g^{\text{InAs}_{1-x}\text{Bi}_x} = 417 \text{ meV} - 2040x \text{ meV}$ (blue curve in Figure 12). VCA thus gives a gap reduction of 20.4 meV per Bi percentage and a gapless bulk condition at $x \approx 0.21$. On the other hand, experiments show a reduction in the $\text{InAs}_{1-x}\text{Bi}_x$ gap of $\approx 55 \text{ meV}$ per Bi percentage^{75,76,82} for $x < 0.05$ (solid black line). An extrapolation of this curve (dashed

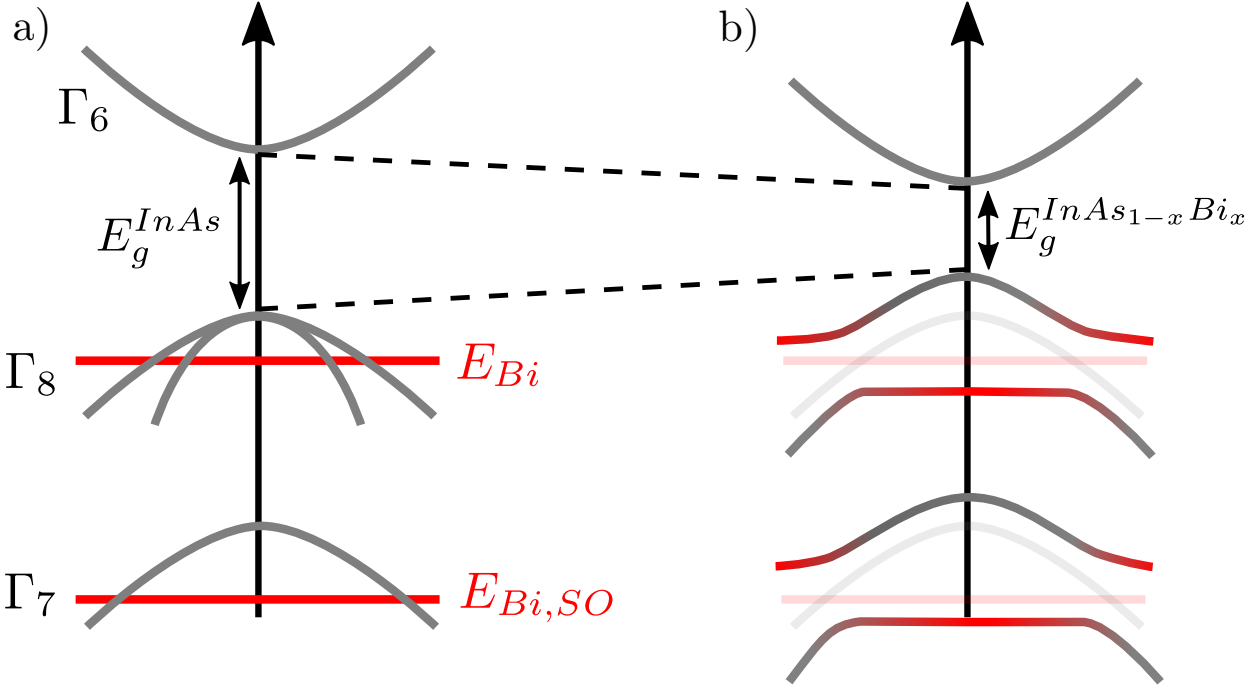


Figure 11 – a) InAs Γ_6 , Γ_7 and Γ_8 energy bands (gray solid lines) around the Γ point with the localized Bi energy levels (red energy lines). b) InAs $_{1-x}$ Bi $_x$ dispersion using the VBAC theory in Eq. (3.21) where we clearly see the gap reduction when the Bi energy levels are taken into account. Here we sketch the interaction of Bi with only one of the Γ_8 bands for clarity.

Source: By the author

black line) leads to a gapless bulk condition at $x \approx 0.076$. This thus shows that the VCA cannot describe accurately the gap of our ordinary InAs alloyed with Bi.

3.3.2 Valence band anti-crossing theory - InAsBi

In order to obtain the correct experimental behavior of the InAs $_{1-x}$ Bi $_x$ fundamental gap as a function of x , we now use the VBAC theory. Within this theory, the fundamental gap is given by the difference at $\mathbf{k} = \mathbf{0}$ between the lowest conduction band $E_c^{InAs_{1-x}Bi_x}$ and the highest valence band $E_+(\mathbf{k})$ of Eq. (3.21), i.e.,

$$E_g^{InAs_{1-x}Bi_x} = E_c^{InAs_{1-x}Bi_x} - E_+(\mathbf{k} = \mathbf{0}). \quad (3.24)$$

As for the lowest conduction band $E_c^{InAs_{1-x}Bi_x}$, we use the VCA which gives $E_c^{InAs_{1-x}Bi_x} = (1-x)E_g^{InAs} + x(E_g^{InBi} + VBO)$, where $VBO = 940$ meV is the valence band offset parameter between InAs and InBi.⁸³ Here we take $E_d = E_{Bi} = -400$ meV^{82,83} and $V = -1643$ meV as a fit parameter in order to yield approximately the 55 meV experimental gap reduction per Bi percentage for $x < 0.05$. In Fig. 12 we plot $E_g^{InAs_{1-x}Bi_x}$ given by Eq. (3.24) as a

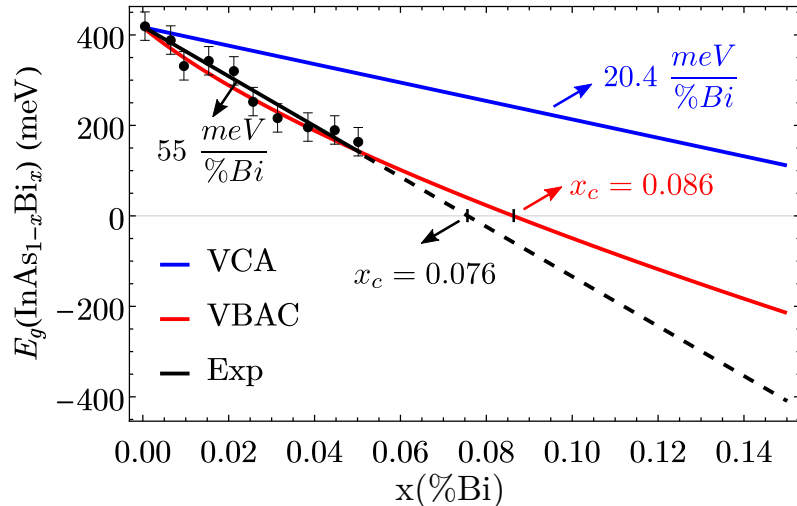


Figure 12 – $\text{InAs}_{1-x}\text{Bi}_x$ fundamental energy gap as a function of x (Bi % concentration). The solid black line represents the experimental data for $x < 0.05$ while the dashed black line correspond to its extrapolation for $x > 0.05$. The solid red (blue) curve represents the predicted energy gap using VBAC (VCA) theory.

Source: By the author

function of x (red solid curve), where we find the gapless bulk condition at $x_c = 0.086$. In contrast to the VCA, using the VBAC results (solid red curve) we find a good agreement with the experimental data (solid black curve). Additionally, we obtain a band inversion between Γ_6 and Γ_8 for $x > 0.086$. We will see in the next section that this bulk inversion band leads to an inversion of the quantum well subbands, characterizing then a topological phase transition.

3.4 Symmetric $\text{AlSb}/\text{InAs}_{0.85}\text{Bi}_{0.15}/\text{AlSb}$ quantum well grown on a GaSb substrate

In this section all the presented results were obtained in collaboration with Prof. Michael Flatté from University of Iowa.

As we discussed in the previous section, the repulsion between the valence bands and the discrete Bi energy level yields a upper shift in the valence bands. The lowest conduction and the highest valence bands swap for $x > 0.083$ within the VBAC model and for $x > 0.076$ within the linear extrapolation of the experimental results. Here we take $x = 0.15$ to guarantee this inversion. We solve then the symmetric $\text{AlSb}/\text{InAs}_{0.85}\text{Bi}_{0.15}/\text{AlSb}$ quantum well Hamiltonian grown on a GaSb substrate using a superlattice electronic structure theory within a fourteen bulk band basis.¹¹⁴ We emphasize that as we are only interested here in the subband gap value, we have considerer the $\text{InAs}_{0.85}\text{Bi}_{0.15}$ bulk material with the same parameters as InAs ¹¹⁴ apart from the lattice constant and the fundamental gap E_g were taken, respectively, as 6.15 \AA and -457.3 meV . For the value of the lattice

Table 1 – Effective BHZ parameters for $\text{InAs}_{0.85}\text{Bi}_{0.15}/\text{AlSb}$ QW with different well thickness, 6 and 8 nm.

$d(\text{nm})$	$A(\text{meV}\cdot\text{nm})$	$B(\text{meV}\cdot\text{nm}^2)$	$C(\text{meV})$	$D(\text{meV}\cdot\text{nm}^2)$	$M(\text{meV})$
6	543.2	-201.7	0	-180	16.1
8	488.0	-339.3	0	-300	-15.5

Source: By the author

constant we used the VCA expression $a_0(\text{InAs}_{1-x}\text{Bi}_x) = (1-x)a_0(\text{InAs}) + xa_0(\text{InBi})$ with $a_0(\text{InAs}) = 6.058\text{\AA}$ and $a_0(\text{InBi}) = 6.686\text{\AA}$, while for the fundamental energy gap we used the extrapolation of the experimental linear trend ($55\text{meV}/\%\text{-Bi}$) at $x = 0.15^\dagger$.

A more detailed investigation should also account for the changes in the effective masses through Eq. (3.22) as well as the changes in the spin orbit splitting through the inclusion of the discrete $E_{Bi,SO}$ level resonant with the Γ_7 bands. Since we know that Bi atoms have a strong spin orbit coupling, we expect an enhancement of the Rashba and Dresselhaus spin orbit coupling under their addition in InAs. We plan to address this issue in a future work in collaboration with the Iowa group.

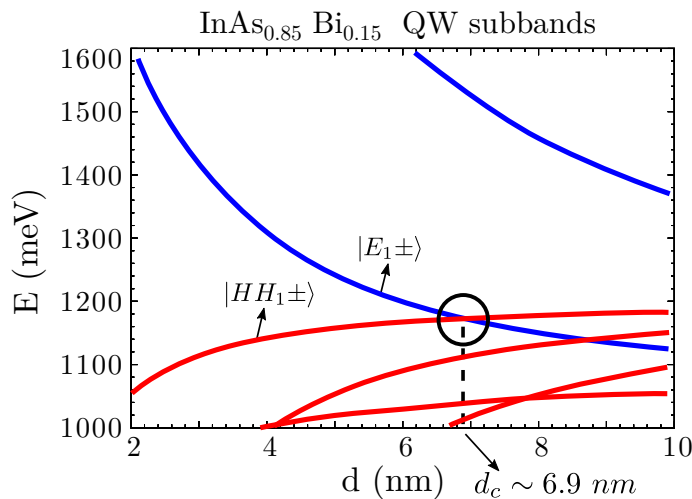


Figure 13 – Symmetric $\text{InAs}_{0.85}\text{Bi}_{0.15}/\text{AlSb}$ QW subbands at $k_x = k_y = 0$ as a function of the well thickness d . The blue (red) colors represent the major Γ_6 (Γ_8) composition. The circle indicates the topological phase transition arising from the subband inversion between $|E_1\pm\rangle$ and $|HH_1\pm\rangle$ at $d_c \approx 6.9$ nm.

Source: By the author

In Fig. 13 we plot the QW energy subbands at $\mathbf{k} = \mathbf{0}$ as a function of the well thickness d . The subband crossing between the lowest conduction subband $|E_1\pm\rangle$ and the

[†] We emphasize the same value of the fundamental gap of the $\text{InAs}_{0.85}\text{Bi}_{0.15}$ can also be obtained for $x = 0.2$ within the VBAC prediction (solid red line).

highest valence subband $|HH_1\pm\rangle$ at the critical well thickness $d_c = 6.9$ nm represents a topological phase transition between an ordinary insulator ($d < d_c$) and a 2D TI ($d > d_c$) as already discussed in the previous chapter. An important feature of our 2D TI proposal is that the magnitude of the inverted gap for $d \approx 8$ nm is around 30 meV which enables room temperature applications since $30 \text{ meV} \gg k_B T$ for $T \approx 300\text{K}$. Using the QW envelope functions corresponding to the QW energy subbands Fig. 13 we also determine the BHZ parameters A , B , C , D and M , defined in Sec. 2.3, for well thickness $d = 6$ nm and $d = 8$ nm. These values are given in Table 1.

We emphasize that our proposal is relevant for the community since it does not deal with the less conventional HgTe/CdTe QWs and thus should stimulate experimental research groups working on III-V semiconductors to investigate Bi-based 2D TIs, thus making them more readily available. Additionally, our 2D TI proposal opens a new avenue in the discovery of new TIs using the idea behind the VBAC theory. For instance, we expect the same kind of TI prediction in other materials such as the $\text{InAs}_{1-y-x}\text{Sb}_y\text{Bi}_x$, in which a gap reduction of 46meV/%-Bi has similarly been reported.⁷⁶ In these compounds, our proposal can be very promising since different groups have reported a small energy gap ~ 100 meV^{115,116} for the bulk $\text{InAs}_{0.55}\text{Sb}_{0.45}$. Therefore, we expect that the incorporation of only a few Bi percentage be necessary to have a subband inversion similar to Fig. 13. Further calculations will also be performed to explore in detail the $\text{InAs}_{1-y-x}\text{Sb}_y\text{Bi}_x$ proposal for a new 2D TI.

In the next chapter, we use our new InAsBi 2D TI proposal to define BHZ quantum dots in both topologically trivial and non-trivial regimes. The BHZ QDs are defined by an additional in plane cylindrical confinement. We find analytical formulas for the wave functions and circulating currents and a transcendental equations determining all the discrete QD energy levels.

4 BHZ QUANTUM DOTS

In this chapter we define our BHZ QDs via a further cylindrical confinement on InAs_{0.85}Bi_{0.15}/AlSb QWs, predicted to be a 2D TI for well thickness $d > 6.9$ nm in the previous chapter. More specifically, we add a confining potential to the effective BHZ model for InAs_{0.85}Bi_{0.15}/AlSb QW and impose both soft and hard walls boundary condition. Using the modified Bessel functions, we find analytical expressions for the wave functions and circulating currents and a transcendental equation determining all the discrete energies of our BHZ QDs.

4.1 Cylindrical BHZ Quantum Dots

To define our QDs we use the 2D BHZ Hamiltonian Eq. (2.13) confined by the cylindrical soft-wall potential

$$V_c(r) = \begin{pmatrix} V(r)\sigma_z & 0 \\ 0 & V(r)\sigma_z \end{pmatrix}, \quad V(r) = \begin{cases} 0 & r < R \\ M_O - M > 0 & r > R \end{cases} \quad (4.1)$$

with equal strength barrier heights $M_O > 0$ for the conduction $|E_{1\pm}\rangle$ and valence $|HH_{1\pm}\rangle$ subbands. The parameter R defines the QD radius. Thus, the total QD Hamiltonian is given by

$$\mathcal{H}_{QD} = \mathcal{H}_{BHZ}(-i\partial_x, -i\partial_y) + V_c(r). \quad (4.2)$$

For such a confined system, the wave vectors k_x and k_y are no longer good quantum numbers and are replaced by $k_x \rightarrow -i\partial_x$ and $k_y \rightarrow -i\partial_y$. Due to the cylindrical (or axial) symmetry of the BHZ Hamiltonian Eq. (2.13) and the soft-wall confinement, it is convenient to use the polar coordinates $x = r \cos \theta$ and $y = r \sin \theta$ in Eq. (4.2). The change in the coordinate system amounts to the following replacements,

$$-i\partial_x \pm \partial_y \rightarrow -i e^{\pm i\theta} \left(\frac{\partial}{\partial r} \pm \frac{1}{r} \frac{\partial}{\partial \theta} \right), \quad (4.3)$$

$$-\partial_x^2 - \partial_y^2 \rightarrow - \left(\partial_r^2 + \frac{1}{r} \partial_r + \frac{1}{r^2} \partial_\theta^2 \right), \quad (4.4)$$

yielding

$$\mathcal{H}_{QD} = \begin{bmatrix} \mathcal{H}_{QD}^+ & 0 \\ 0 & \mathcal{H}_{QD}^- \end{bmatrix}, \quad (4.5)$$

with

$$\mathcal{H}_{QD}^\pm = \begin{bmatrix} C_+ + V(r) + D_+ \left(\partial_r^2 + \frac{1}{r} \partial_r + \frac{1}{r^2} \partial_\theta^2 \right) & \mp iA e^{\pm i\theta} \left(\frac{\partial}{\partial r} \pm i \frac{1}{r} \frac{\partial}{\partial \theta} \right) \\ \mp iA e^{\mp i\theta} \left(\frac{\partial}{\partial r} \mp i \frac{1}{r} \frac{\partial}{\partial \theta} \right) & C_- - V(r) + D_- \left(\partial_r^2 + \frac{1}{r} \partial_r + \frac{1}{r^2} \partial_\theta^2 \right) \end{bmatrix}, \quad (4.6)$$

where $D_\pm = D \pm B$ and $C_\pm = C \pm M$.

4.2 Energies and wave functions

Here we determine the energies and wave functions of our QD Hamiltonian Eq. (4.5), i.e., we solve $\mathcal{H}_{QD}\psi(r, \theta) = E\psi(r, \theta)$. Since we have a block diagonal Hamiltonian with the two blocks connected through Time Reversal Symmetry,^{4,5} we first solve one block and then we use the TRS operator to find the corresponding solution for the other block. For the upper block, we choose the following ansatz

$$\psi_m^+(r, \theta) = \begin{pmatrix} p R_1(r) e^{im\theta} \\ q R_2(r) e^{im'\theta} \end{pmatrix}, \quad (4.7)$$

where $m, m' \in \mathbb{Z}$ in order to obey the 2π periodicity of the θ coordinate, i.e., $\psi_m^+(r, \theta) = \psi_m^+(r, \theta + 2\pi)$ (single-valuedness) and p, q are constants. We now solve the Schrödinger equation,

$$\mathcal{H}_{QD}^+ \psi_m^+(r, \theta) = E^+ \psi_m^+(r, \theta), \quad (4.8)$$

yielding

$$\begin{bmatrix} D_+ \left(\partial_r^2 + \frac{1}{r} \partial_r - \frac{m^2}{r^2} - \frac{E^+ - C_+}{D_+} \right) p R_1(r) e^{im\theta} - iA \left(\partial_r - \frac{m'}{r} \right) q R_2(r) e^{i(m'+1)\theta} \\ -iA \left(\partial_r + \frac{m}{r} \right) p R_1(r) e^{i(m-1)\theta} + D_- \left(\partial_r^2 + \frac{1}{r} \partial_r - \frac{m'^2}{r^2} - \frac{E^+ - C_-}{D_-} \right) q R_2(r) e^{im'\theta} \end{bmatrix} = \begin{bmatrix} 0 \\ 0 \end{bmatrix}. \quad (4.9)$$

We see from the above equation that the integers m and m' should always be constrained

by $m = m' + 1^*$ since the above equation has to be satisfied for any θ . For $m' = m - 1$ Eq. (4.9) thus reads

$$\begin{bmatrix} D_+ \left(\partial_r^2 + \frac{1}{r} \partial_r - \frac{(m+1)^2}{r^2} - \frac{E^+ - C_+}{D_+} \right) & -iA \left(\partial_r - \frac{m}{r} \right) \\ -iA \left(\partial_r + \frac{m+1}{r} \right) & D_- \left(\partial_r^2 + \frac{1}{r} \partial_r - \frac{m^2}{r^2} - \frac{E^+ - C_-}{D_-} \right) \end{bmatrix} \begin{bmatrix} p R_1(r) \\ q R_2(r) \end{bmatrix} = \begin{bmatrix} 0 \\ 0 \end{bmatrix}. \quad (4.10)$$

For the inner QD region, $r < R$, the above equation has its solution expressed in terms of the $I_m(\lambda r)$ modified Bessel functions regularized at $r = 0$ (first kind),¹¹⁷ i.e.,

$$\psi_m^{+,r < R}(r, \theta) = \sum_{\tau=\pm} p_{m,\tau}^+ \begin{bmatrix} I_{m+1}(\lambda_\tau r) e^{i(m+1)\theta} \\ \frac{D_+ \lambda_\tau^2 - E^+ + C_+}{iA \lambda_\tau} I_m(\lambda_\tau r) e^{im\theta} \end{bmatrix}, \quad (4.11)$$

where $\lambda_\pm^2 = -F \pm \sqrt{F^2 - Q^2}$ with $F = \frac{1}{2} \left(\frac{A^2}{(D+B)(D-B)} - \frac{E^+ - C - M}{D+B} - \frac{E^+ - C + M}{D-B} \right)$ and $Q^2 = \left(\frac{E^+ - C + M}{D-B} \right) \left(\frac{E^+ - C - M}{D+B} \right)$. In contrast, for the outer region, $r > R$, the solution is written in terms of the $K_m(\lambda r)$ modified Bessel function regularized at $r \rightarrow \infty$ (second kind),¹¹⁷

$$\psi_m^{+,r > R}(r, \theta) = \sum_{\tau=\pm} r_{m,\tau}^+ \begin{bmatrix} K_{m+1}(\lambda_\tau r) e^{i(m+1)\theta} \\ \frac{D_+ (\lambda_\tau^O)^2 - E^+ + C_+}{-iA \lambda_\tau^O} K_m(\lambda_\tau r) e^{im\theta} \end{bmatrix}, \quad (4.12)$$

with $\lambda_\tau^O = \lambda_\tau (M \rightarrow M^O)$.

In order to find the quantized energies of our QD, we need to impose the continuity of the wave function at $r = R$ and the continuity of its derivative in the radial direction at $r = R$, yielding

$$\psi_m^{+,r < R}(r = R, \theta) = \psi_m^{+,r > R}(r = R, \theta), \quad (4.13)$$

$$\partial_r \psi_m^{+,r < R}(r = R, \theta) = \partial_r \psi_m^{+,r > R}(r = R, \theta). \quad (4.14)$$

The above equations are satisfied for $\forall \theta$ and we chose $\theta = 0$ for simplicity. We combine the above equations in the following linear matrix equation

$$\begin{pmatrix} I_{m+1}(\lambda_+ R) & I_{m+1}(\lambda_- R) & K_{m+1}(\lambda_+^O R) & K_{m+1}(\lambda_-^O R) \\ R_{m,+}^+ I_m(\lambda_+ R) & R_{m,-}^+ I_m(\lambda_- R) & -R_{m,+}^{O,+} K_m(\lambda_+^O R) & -R_{m,-}^{O,+} K_m(\lambda_-^O R) \\ \partial_r I_{m+1}(\lambda_+ R) & \partial_r I_{m+1}(\lambda_- R) & \partial_r K_{m+1}(\lambda_+^O R) & \partial_r K_{m+1}(\lambda_-^O R) \\ R_{m,+}^+ \partial_r I_m(\lambda_+ R) & R_{m,-}^+ \partial_r I_m(\lambda_- R) & -R_{m,+}^{O,+} \partial_r K_m(\lambda_+^O R) & -R_{m,-}^{O,+} \partial_r K_m(\lambda_-^O R) \end{pmatrix} \begin{pmatrix} p_{m,+}^+ \\ p_{m,-}^+ \\ -r_{m,+}^+ \\ -r_{m,-}^+ \end{pmatrix} = 0, \quad (4.15)$$

* As we will comment later, this constraint follows from the \hbar difference between the angular momentum of the Bloch functions of $|E_1+\rangle$ and $|HH_1+\rangle$.

with $R_{m,\tau}^+ = \frac{(D_+\lambda_\tau^2 - E^+ + C_+)}{iA(\lambda_\tau)}$ and $R_{m,\tau}^{O,+} = R_{m,\tau}^+(M \rightarrow M_O)$. For each integer value of m , the non-trivial solution of the above linear system (4.15) is given by its determinant equals to zero, yielding an infinite number of quantized energy levels $\{E_{m,n}^+\}$, where $n = 1, 2, 3, \dots$ ($n = -1, -2, -3, \dots$) corresponding to the positive (negative) energies of Eq. (4.8). From now on, we will include the index n in all the following energies and wave functions. The corresponding wave functions are then obtained from each $E_{m,n}$ by solving the above linear system together with the normalization condition for the wave function.

As for the lower BHZ block, we apply the TRS operator $\Theta = -i\sigma_y \otimes \mathbf{1}_{2 \times 2} \mathcal{K}^{4,5}$ (where \mathcal{K} is the complex conjugate) in the upper block wave functions (4.11) and (4.12), giving [†]

$$\Theta \psi_{m,n}^+(r, \theta) = \psi_{-m,n}^-(r, \theta). \quad (4.16)$$

Using now the fact that $I_n(\lambda r) = I_{-n}(\lambda r)$ for $n \in \mathbb{Z}$, we find

$$\psi_{m,n}^{-,r < R}(r, \theta) = \sum_{\tau=\pm} p_{m,n,\tau}^- \left[\begin{array}{c} I_{m-1}(\lambda_\tau r) e^{i(m-1)\theta} \\ \frac{D_+\lambda_\tau^2 - E_{m,n}^+ + C_+}{-iA\lambda_\tau} I_m(\lambda_\tau r) e^{im\theta} \end{array} \right], \quad (4.17)$$

and

$$\psi_{m,n}^{-,r > R}(r, \theta) = \sum_{\tau=\pm} r_{m,n,\tau}^- \left[\begin{array}{c} K_{m-1}(\lambda_\tau r) e^{i(m-1)\theta} \\ \frac{D_+(\lambda_\tau^O)^2 - E_{m,n}^+ + C_+}{iA\lambda_\tau^O} K_m(\lambda_\tau r) e^{im\theta} \end{array} \right]. \quad (4.18)$$

By applying the boundary conditions (4.13) and (4.14) in the above wave functions, we obtain

$$\left(\begin{array}{cccc} I_{m-1}(\lambda_+ R) & I_{m-1}(\lambda_- R) & K_{m-1}(\lambda_+^O R) & K_{m-1}(\lambda_-^O R) \\ R_{m,n,+}^- I_m(\lambda_+ R) & R_{m,n,-}^- I_m(\lambda_- R) & -R_{m,n,+}^{O,-} K_m(\lambda_+^O R) & -R_{m,n,-}^{O,-} K_m(\lambda_-^O R) \\ \partial_r I_{m-1}(\lambda_+ R) & \partial_r I_{m-1}(\lambda_- R) & \partial_r K_{m-1}(\lambda_+^O R) & \partial_r K_{m-1}(\lambda_-^O R) \\ R_{m,n,+}^- \partial_r I_m(\lambda_+ R) & R_{m,n,-}^- \partial_r I_m(\lambda_- R) & -R_{m,n,+}^{O,-} \partial_r K_m(\lambda_+^O R) & -R_{m,n,-}^{O,-} \partial_r K_m(\lambda_-^O R) \end{array} \right) \left(\begin{array}{c} p_{m,n,+}^- \\ p_{m,n,-}^- \\ -r_{m,n,+}^- \\ -r_{m,n,-}^- \end{array} \right) = 0, \quad (4.19)$$

with $R_{m,\tau}^{O,-} = \frac{(D_+\lambda_\tau^2 - E^- + C_+)}{-iA(\lambda_\tau)}$ and $R_{m,\tau}^{O,-} = R_{m,\tau}^-(M \rightarrow M_O)$. As a consequence of the TRS,

[†] Although the upper block wave functions (4.11) and (4.12) were written as 2×1 vectors, we recall that they stem from the block diagonal 4×4 Hamiltonian (4.5) and therefore are given by $\psi_m^+ = \begin{pmatrix} 1 \\ 0 \end{pmatrix} \otimes \psi_m^+$ within the total Hamiltonian subspace.

the energies arising from the non-trivial solution of the above linear system are connected to the ones of Eq. (4.15) by $E_{m,n}^- = \Theta E_{-m,n}^+$

4.2.1 Hard-Wall case

In this section we study the hard-wall case, which represents a BHZ QD confined by an impenetrable radial barrier potential. This case can be obtained from Eqs. (4.15) and (4.19) by taking the limit $M_O \rightarrow \infty$, yielding for the BHZ blocks (\pm)

$$\begin{pmatrix} I_{m\pm 1}(\lambda_+ R) & I_{m\pm 1}(\lambda_- R) \\ R_{m,+}^\pm I_m(\lambda_+ R) & R_{m,-}^\pm I_m(\lambda_- R) \end{pmatrix} \begin{pmatrix} p_{m,n,+}^\pm \\ p_{m,n,-}^\pm \end{pmatrix} = 0. \quad (4.20)$$

The non-trivial solution of the above linear system thus gives the following transcendental equation for the eigenenergies

$$\frac{\lambda_-^2 \left(E_{m,n}^\pm \right) - \frac{E_{m,n}^\pm - C - M}{D+B} I_{m\pm 1} \left[\lambda_+ \left(E_{m,n}^\pm \right) R \right]}{\lambda_- \left(E_{m,n}^\pm \right)} \frac{I_{m\pm 1} \left[\lambda_+ \left(E_{m,n}^\pm \right) R \right]}{I_{m\pm 1} \left[\lambda_- \left(E_{m,n}^\pm \right) R \right]} = \frac{\lambda_+^2 \left(E_{m,n}^\pm \right) - \frac{E_{m,n}^\pm - C - M}{D+B} I_m \left[\lambda_+ \left(E_{m,n}^\pm \right) R \right]}{\lambda_+ \left(E_{m,n}^\pm \right)} \frac{I_m \left[\lambda_+ \left(E_{m,n}^\pm \right) R \right]}{I_m \left[\lambda_- \left(E_{m,n}^\pm \right) R \right]}, \quad (4.21)$$

with

$$p_{m,n,+}^\pm = -p_{m,n,-}^\pm. \quad (4.22)$$

The energy dependence in (4.21) is written explicitly in the argument of λ_τ . The wave functions are then obtained through Eqs. (4.11), (4.12), (4.17), (4.18), using the $M_O \rightarrow \infty$ limit and $p_{m,n,+}^\pm = -p_{m,n,-}^\pm$, and read

$$\psi_{m,n}^\pm(r, \theta) = p_{m,n}^\pm \left[\begin{array}{c} \left(I_{m\pm 1}(\lambda_+ r) - \frac{I_{m\pm 1}(\lambda_+ R)}{I_{m\pm 1}(\lambda_- R)} I_{m\pm 1}(\lambda_- r) \right) e^{i(m\pm 1)\theta} \\ \frac{D_+ \left(\lambda_+^2 - \frac{E_{m,n}^\pm - C_+}{D_+} \right)}{\pm i A \lambda_+} \left(I_m(\lambda_+ r) - \frac{I_m(\lambda_+ R)}{I_m(\lambda_- R)} I_m(\lambda_- r) \right) e^{im\theta} \end{array} \right], \quad (4.23)$$

which satisfy $\psi_{m,n}^\pm(r = R, \theta) = 0$ for $\forall \theta$ through Eq. (4.21). We emphasize that the \pm signs in Eqs. (4.21) and (4.23) correspond, respectively, to the \pm BHZ blocks subspaces.

4.3 QD cylindrical symmetries and their good quantum numbers

By recalling Noether's first theorem,¹¹⁸ we know that for each symmetry present in the Hamiltonian there is a corresponding conserved quantity in time. The most common

example is the time invariance that leads to the energy conservation. Starting from the Schrödinger equation

$$-i\hbar \frac{\partial \psi}{\partial t} = \mathcal{H}\psi, \quad (4.24)$$

we would like to know whether the unitary \mathcal{U} spinor transformation operator defined as $\psi' = \mathcal{U}\psi$ is a possible symmetry of our Hamiltonian. To find the condition for such a symmetry, we substitute $\psi = \mathcal{U}^{-1}\psi'$ in the above equation, yielding

$$-i\hbar \frac{\partial(\mathcal{U}^{-1}\psi')}{\partial t} = \mathcal{H}\mathcal{U}^{-1}\psi' \rightarrow -i\hbar \frac{\partial\psi'}{\partial t} = \mathcal{U}\mathcal{H}\mathcal{U}^{-1}\psi', \quad (4.25)$$

for $\frac{\partial\mathcal{U}}{\partial t} = 0$ (assuming a time-independent U). Thus, we see that for

$$\mathcal{H} = \mathcal{U}\mathcal{H}\mathcal{U}^{-1} \rightarrow [\mathcal{H}, \mathcal{U}] = 0, \quad (4.26)$$

the unitary transformation operator \mathcal{U} maps Eq. (4.25) into Eq. (4.24) and thus it can be considered as a symmetry of the Hamiltonian. It is also very common to say the Hamiltonian is symmetric and invariant under \mathcal{U} . A practical and important consequence of a invariant Hamiltonian under \mathcal{U} is the existence of a common eigenstate basis $\{\psi\}$ between \mathcal{H} and \mathcal{U} . The proof is simple and it is shown below. By applying the commutator of Eq. (4.26) on a particular Hamiltonian eigenstate ψ_h such that $\mathcal{H}\psi_h = h\psi_h$, we obtain

$$[\mathcal{H}, \mathcal{U}] \psi_h = 0, \quad (4.27)$$

$$\rightarrow \mathcal{H}(\mathcal{U}\psi_h) = h(\mathcal{U}\psi_h). \quad (4.28)$$

Thus, if $\mathcal{U}\psi_h$ is eigenstate of \mathcal{H} with eigenvalue h , $\mathcal{U}\psi_h$ must be proportional to ψ_h , yielding

$$\mathcal{U}\psi_h = u\psi_h, \quad (4.29)$$

with u the corresponding eigenvalue of \mathcal{U} . Therefore, the wave functions (eigenvectors) should be labeled by the quantum numbers h and u yielding $\psi_{u,h}$. Since our Hamiltonian remains the same (no external perturbations) as time evolves, the quantum numbers h and u are also called as good quantum numbers. In the following subsections we will discuss the QD symmetries and the corresponding labels for them in the final QD wave function Eqs. (4.15) and (4.23).

4.3.1 Effective Inversion Symmetry

The initial 8×8 $\mathbf{k} \cdot \mathbf{p}$ Hamiltonian Eq. (2.1) used to derive the effective BHZ Hamiltonian Eq. (2.13) does not contain the bulk inversion asymmetry (BIA) terms arising from the lack of inversion symmetry ($\mathbf{r} \rightarrow -\mathbf{r}$) in the ZB unit cell.^{41,63} As a consequence, we say the BHZ Hamiltonian preserves effectively the bulk inversion symmetry \mathcal{I} .^{17,73} The word “effectively” is placed here to emphasize that although the BIA terms were not taken into account in the $\mathbf{k} \cdot \mathbf{p}$ Hamiltonian, our basis function ($|\Gamma_6, \frac{1}{2}, \pm \frac{1}{2}\rangle$, $|\Gamma_8, \frac{3}{2}, \pm \frac{1}{2}\rangle$, $|\Gamma_8, \frac{3}{2}, \pm \frac{3}{2}\rangle$ and $|\Gamma_7, \frac{1}{2}, \pm \frac{1}{2}\rangle$) are still composed of ZB Bloch functions at the Γ point, which do not have a well defined parity. Using the compatibility relation^{37,119,120} between the ZB and diamond irreducible representation at the Γ point together with the parities of the QW envelope functions of Eqs. (2.11) and (2.12), we obtain the inversion operator written in the BHZ basis Eqs. (2.11) and (2.12) as⁷³

$$\mathcal{I}_{BHZ} = \begin{pmatrix} -1 & 0 & 0 & 0 \\ 0 & 1 & 0 & 0 \\ 0 & 0 & -1 & 0 \\ 0 & 0 & 0 & 1 \end{pmatrix}. \quad (4.30)$$

In polar coordinates, the inversion operation ($\mathbf{r} \rightarrow -\mathbf{r}$) is represented by $(r, \theta) \rightarrow (r, \theta + \pi)$. Since our QD confinement potential $V_c(r)$ is also invariant under spatial inversion, the total QD Hamiltonian (4.2) remains invariant, i.e.,

$$\begin{aligned} [\mathcal{H}_{QD}(r, \theta) + V_c(r), \mathcal{I}] &= 0, \\ \mathcal{I}_{BHZ} \mathcal{H}_{QD}(\mathcal{I}r, \mathcal{I}\theta) \mathcal{I}_{BHZ}^{-1} - \mathcal{H}_{QD}(r, \theta) &= 0 \\ \mathcal{I}_{BHZ} \mathcal{H}_{QD}(r, \theta + \pi) \mathcal{I}_{BHZ}^{-1} - \mathcal{H}_{QD}(r, \theta) &= 0 \end{aligned} \quad (4.31)$$

As a consequence, parity is a good quantum number used then to label the total wave function. Therefore, the inversion symmetry \mathcal{I} applied to the final wave function Eq. (4.23) yields

$$\mathcal{I}\psi_{m,n}^{\pm}(r, \theta) = \mathcal{I}_{BHZ}\psi_{m,n}^{\pm}(r, \theta + \pi) \quad (4.32)$$

$$= (-1)^m \psi_{m,n}^{\pm}(r, \theta), \quad (4.33)$$

showing that the parity is fully connected to the label m , i.e., for even (odd) m we have an even (odd) total wave function.

4.3.2 Total Angular Momentum

As we have pointed out in Sec. (2.3), the initial $8 \times 8 \mathbf{k} \cdot \mathbf{p}$ Hamiltonian (2.1) used in BHZ Hamiltonian derivation was assumed as good approximation (see Sec. 2.3) to have axial symmetry, i.e, it is symmetrical by any rotation of θ around the z axis (QW growth direction). As a result of this assumption, the BHZ Hamiltonian also holds symmetric under the axial symmetry. Furthermore, the introduced QD confinement potential was also assumed purely radial dependent, preserving then the axial symmetry. Therefore, the projection of the total angular momentum on the z axis, $\mathcal{J}_z = L_z + J_z$, where $L_z = -i\hbar\partial_\theta$ is the z -component of the envelope function orbital angular momentum and J_z is the z -component of the Bloch function total angular momentum

$$J_z = \hbar \begin{pmatrix} \frac{1}{2} & 0 & 0 & 0 \\ 0 & \frac{3}{2} & 0 & 0 \\ 0 & 0 & -\frac{1}{2} & 0 \\ 0 & 0 & 0 & -\frac{3}{2} \end{pmatrix}, \quad (4.34)$$

commutes with the total QD Hamiltonian (4.2),

$$[\mathcal{H}_{QD}(r, \theta) + V_c(r), \mathcal{J}_z] = 0. \quad (4.35)$$

Accordingly, the above leads to the conserved quantity j_z – the total angular momentum, which includes the orbital angular momentum of the envelope functions plus the orbital angular momentum of the Bloch functions and the spin angular momentum. Upon applying \mathcal{J}_z to the total wave function, we find

$$\begin{aligned} \mathcal{J}_z \psi_{m,n}^\pm(r, \theta) &= p_{m,n}^\pm (-i\hbar\partial_\theta + J_z) \left[\frac{\left(I_{m\pm 1}(\lambda_+ r) - \frac{I_{m\pm 1}(\lambda_+ R)}{I_{m\pm 1}(\lambda_- R)} I_{m\pm 1}(\lambda_- r) \right) e^{i(m\pm 1)\theta}}{D_+ \left(\lambda_+^2 - \frac{E - C_+}{D_+} \right) \pm iA\lambda_+} \left(I_m(\lambda_+ r) - \frac{I_m(\lambda_+ R)}{I_m(\lambda_- R)} I_m(\lambda_- r) \right) e^{im\theta} \right], \\ &= \left(m \pm \frac{3}{2} \right) \hbar \psi_{m,n}^\pm(r, \theta), \end{aligned} \quad (4.36)$$

$$= \hbar j_z \psi_{m,n}^\pm(r, \theta), \quad (4.37)$$

where j_z can assume only half-integer values $j_z = \pm\frac{1}{2}, \pm\frac{3}{2}, \pm\frac{5}{2}, \dots$. The above result can also be obtained individually for each (upper + and lower –) components of the BHZ QD Hamiltonian thus leading to a better physical understanding. For instance, for the BHZ \pm upper (lower) wave function component, the envelope angular momentum and the Bloch function angular momentum read, respectively, $L_z e^{i(m\pm 1)\theta} = \hbar(m \pm 1) e^{i(m\pm 1)\theta}$, ($L_z e^{im\theta} = \hbar m e^{im\theta}$) and $J_z |E_1 \pm\rangle = \pm\frac{\hbar}{2} |E_1 \pm\rangle$ ($J_z |HH_1 \pm\rangle = \pm\frac{3\hbar}{2} |HH_1 \pm\rangle$). Hence, we

have $j_z = m \pm \frac{3}{2}$ for both upper and lower wave function components. We thus make the substitution $m = j_z - \frac{3}{2}$ ($m = j_z + \frac{3}{2}$) for the spin up (down) in Eq. (4.23), yielding the following total wave function

$$\psi_{j_z, n}^{\pm}(r, \theta) = p_{j_z, n}^{\pm} \left[\begin{array}{c} \left(I_{j_z \mp \frac{1}{2}}(\lambda_+ r) - \frac{I_{j_z \mp \frac{1}{2}}(\lambda_+ R)}{I_{j_z \mp \frac{1}{2}}(\lambda_- R)} I_{j_z \mp \frac{1}{2}}(\lambda_- r) \right) e^{i(j_z \mp \frac{1}{2})\theta} \\ \frac{D_+ \left(\lambda_+^2 - \frac{E-C_{\pm}}{D_+} \right)}{\pm i A \lambda_+} \left(I_{j_z \mp \frac{3}{2}}(\lambda_+ r) - \frac{I_{j_z \mp \frac{3}{2}}(\lambda_+ R)}{I_{j_z \mp \frac{3}{2}}(\lambda_- R)} I_{j_z \mp \frac{3}{2}}(\lambda_- r) \right) e^{i(j_z \mp \frac{3}{2})\theta} \end{array} \right], \quad (4.38)$$

where we emphasize that the parameters λ_{\pm} depend on the energy, i.e., $\lambda_{\pm} = \lambda_{\pm}(E_{j_z, n}^{\sigma})$. As for the energy transcendental equation we have

$$\frac{\lambda_-^2 \left(E_{j_z, n}^{\pm} \right) - \frac{E_{j_z, n}^{\pm} - C - M}{D_+ B} I_{j_z \mp \frac{1}{2}, n} \left[\lambda_+ \left(E_{j_z, n}^{\pm} \right) R \right]}{\lambda_- \left(E_{j_z, n}^{\pm} \right) I_{j_z \mp \frac{1}{2}, n} \left[\lambda_- \left(E_{j_z, n}^{\pm} \right) R \right]} = \frac{\lambda_+^2 \left(E_{j_z, n}^{\pm} \right) - \frac{E_{j_z, n}^{\pm} - C - M}{D_+ B} I_{j_z \mp \frac{3}{2}, n} \left[\lambda_+ \left(E_{j_z, n}^{\pm} \right) R \right]}{\lambda_+ \left(E_{j_z, n}^{\pm} \right) I_{j_z \mp \frac{3}{2}, n} \left[\lambda_- \left(E_{j_z, n}^{\pm} \right) R \right]}, \quad (4.39)$$

while, for the energies arising from the soft wall confinement Eqs. 4.15 and 4.19, we have

$$A_{4 \times 4} \begin{pmatrix} p_{j_z, n, +}^{\pm} \\ p_{j_z, n, -}^{\pm} \\ -r_{j_z, n, +}^{\pm} \\ -r_{j_z, n, -}^{\pm} \end{pmatrix} = 0, \quad (4.40)$$

where

$$A_{4 \times 4} = \begin{pmatrix} I_{j_z \mp \frac{1}{2}}(\lambda_+ R) & I_{j_z \mp \frac{1}{2}}(\lambda_- R) & K_{j_z \mp \frac{1}{2}}(\lambda_+^O R) & K_{j_z \mp \frac{1}{2}}(\lambda_-^O R) \\ R_{j_z, n, +}^{\pm} I_{j_z \mp \frac{3}{2}}(\lambda_+ R) & R_{j_z, n, -}^{\pm} I_{j_z \mp \frac{3}{2}}(\lambda_- R) & -R_{j_z, n, +}^{O, \pm} K_{j_z \mp \frac{3}{2}}(\lambda_+^O R) & -R_{j_z, n, -}^{O, \pm} K_{j_z \mp \frac{3}{2}}(\lambda_-^O R) \\ \partial_r I_{j_z \mp \frac{1}{2}}(\lambda_+ R) & \partial_r I_{j_z \mp \frac{1}{2}}(\lambda_- R) & \partial_r K_{j_z \mp \frac{1}{2}}(\lambda_+^O R) & \partial_r K_{j_z \mp \frac{1}{2}}(\lambda_-^O R) \\ R_{j_z, n, +}^{\pm} \partial_r I_{j_z \mp \frac{3}{2}}(\lambda_+ R) & R_{j_z, n, -}^{\pm} \partial_r I_{j_z \mp \frac{3}{2}}(\lambda_- R) & -R_{j_z, n, +}^{O, \pm} \partial_r I_{j_z \mp \frac{3}{2}}(\lambda_+^O R) & -R_{j_z, n, -}^{O, \pm} \partial_r I_{j_z \mp \frac{3}{2}}(\lambda_-^O R) \end{pmatrix}. \quad (4.41)$$

4.3.3 Time Reversal Symmetry

The TRS operator ($t \rightarrow -t$) \mathcal{T} is written in the BHZ basis as $\Theta = -i\sigma_y \otimes \mathbf{1}_{2 \times 2} \mathcal{K}$ where \mathcal{K} is the complex conjugate operator. Due to the absence of magnetic and time dependent fields in our problem, TRS is an operator that commutes with the total QD Hamiltonian Eq. (4.2),

$$\begin{aligned}
[\mathcal{H}_{QD}(r, \theta) + V_c(r), \mathcal{T}] &= 0, \\
\Theta \mathcal{H}_{QD}(\mathcal{T}r, \mathcal{T}\theta) \Theta^{-1} - \mathcal{H}_{QD}(r, \theta) &= 0, \\
\Theta \mathcal{H}_{QD}(r, \theta) \Theta^{-1} - \mathcal{H}_{QD}(r, \theta) &= 0,
\end{aligned} \tag{4.42}$$

yielding the conservation of the \pm quantity labeling the “spin” subspaces in the BHZ model (i.e., its two 2x2 blocks) and in the total wave function.

4.4 Circulating current densities

In this section we derive expressions for the circulating current densities $\mathbf{j}(\mathbf{r})$ for the QD states found in the last section. Differently from the BHZ model confined only in one dimension, in which the group velocity contains the information about the propagation direction of the states, QDs do not have an energy dispersion. As a consequence, we cannot associate a group velocity to their states. Then it becomes important to calculate their circulating current densities in order to obtain information about the electronic propagation within the QD.

Our derivation is based on Refs. ^{69,70} The circulating current associated with a particular QD state $\psi_{j_z, n}^\sigma(\mathbf{r})$ (4.38) is defined by

$$\mathbf{j}_{j_z, n}^\sigma(\mathbf{r}) = \frac{e\hbar}{m_0} \text{Im} \left[\psi_{j_z, n}^{\sigma\dagger}(\mathbf{r}) \nabla \psi_{j_z, n}^\sigma(\mathbf{r}) \right], \tag{4.43}$$

where $\sigma = \pm$ are the two possible BHZ subspaces, $e < 0$ is the electronic charge, m_0 the free electron mass and \hbar the reduced Planck’s constant. Here the total QD wave function $\psi_{j_z, n}^\sigma(\mathbf{r})$ is written within the EFA ^{38,60,61} as

$$\psi_{j_z, n}^\sigma(\mathbf{r}) = \sum_i F_{i, j_z, n}^\sigma(r, \theta, z) u_i(\mathbf{r}), \tag{4.44}$$

where $u_i(\mathbf{r})$ is the Bloch function at the Γ point of the i -band (See Tab. 1) and $F_{i, j_z, n}^\sigma(r, \theta, z)$ is its respective envelope function due to the 3D heterostructure quantum confinement. By substituting Eq. (4.44) into Eq. (4.43), we obtain

$$\begin{aligned}
\mathbf{j}_{j_z, n}^\sigma(\mathbf{r}) &= \frac{e\hbar}{m_0} \sum_{i, l} \text{Im} \left[F_{l, j_z, n}^{\sigma*}(r, \theta, z) F_{i, j_z, n}^\sigma(r, \theta, z) u_l^*(\mathbf{r}) \nabla u_i(\mathbf{r}) \right. \\
&\quad \left. + F_{l, j_z, n}^{\sigma*}(r, \theta, z) \nabla F_{i, j_z, n}^\sigma(r, \theta, z) u_l^*(\mathbf{r}) u_i(\mathbf{r}) \right].
\end{aligned} \tag{4.45}$$

Now, using the EFA where the envelope functions are assumed as constants inside the unit-cell, we take in Eq. (4.45) the average over the unit-cell volume (V_s),^{38,60,61} $\frac{1}{V_s} \int_{V_s} d\mathbf{r}$, in order to remove the Bloch function dependence, reading

$$\begin{aligned} \langle \mathbf{j}_{j_z, n}^\sigma \rangle(\mathbf{r}) &= \frac{1}{V_s} \int_{V_s} d\mathbf{r} \mathbf{j}_{j_z, n}^\sigma(\mathbf{r}) \\ &= \frac{e\hbar}{m_0} \sum_{i,l} \text{Im} \left[F_{l,j_z, n}^{\sigma*}(r, \theta, z) F_{i,j_z, n}^\sigma(r, \theta, z) \langle u_l | \nabla | u_i \rangle \right. \\ &\quad \left. + F_{l,j_z, n}^{\sigma*}(r, \theta, z) \nabla F_{i,j_z, n}^\sigma(r, \theta, z) \delta_{li} \right], \end{aligned} \quad (4.46)$$

where we have used the $\langle u_l | \mathbf{A} | u_i \rangle = \frac{1}{V_s} \int_{V_s} d\mathbf{r} u_l^*(\mathbf{r}) \mathbf{A} u_i(\mathbf{r})$. In Eq. (4.46), the first term stems from the periodic Bloch functions $u_{i,l}(\mathbf{r})$ and it is known as the ‘‘Bloch velocity’’ contribution to the average current, while the second term is the ‘‘envelope velocity’’ contribution as it stems from the envelope functions $F_{i,j_z, n}^\sigma(r, z, \theta)$.

4.4.1 QD circulating currents

To find the circulating currents for our problem we must first write our total QD wave functions explicitly as functions of the Bloch functions as shown in Eq. (4.44). For practical reasons, here we focus on the hard wall case. The total wave function Eq. (4.23) is then written as

$$\psi_{j_z, n}^\pm(r, \theta) = \frac{N}{\sqrt{2\pi}} \left[I_{E_1}^{j_z \mp \frac{1}{2}, n}(r) e^{i(j_z \mp \frac{1}{2})\theta}, \quad \pm i I_{HH_1}^{j_z \mp \frac{3}{2}, n}(r) e^{i(j_z \mp \frac{3}{2})\theta} \right]^T, \quad (4.47)$$

with

$$I_{E_1}^{j_z \mp \frac{1}{2}, n}(r) = I_{j_z \mp \frac{1}{2}, n} \left(\lambda_+ \left(E_{j_z, n}^\pm \right) r \right) - \frac{I_{j_z \mp \frac{1}{2}, n} \left(\lambda_+ \left(E_{j_z, n}^\pm \right) R \right)}{I_{j_z \mp \frac{1}{2}, n} \left(\lambda_- \left(E_{j_z, n}^\pm \right) R \right)} I_{j_z \mp \frac{1}{2}, n} \left(\lambda_- \left(E_{j_z, n}^\pm \right) r \right), \quad (4.48)$$

and

$$\begin{aligned} I_{HH_1}^{j_z \mp \frac{3}{2}, n}(r) &= \frac{D_+ \lambda_+^2 \left(E_{j_z, n}^\pm \right) - E_{j_z, n}^\pm + C_+}{\pm i A \lambda_+ \left(E_{j_z, n}^\pm \right)} \\ &\quad \times \left(I_{j_z \mp \frac{3}{2}, n} \left(\lambda_+ \left(E_{j_z, n}^\pm \right) r \right) - \frac{I_{j_z \mp \frac{3}{2}, n} \left(\lambda_+ \left(E_{j_z, n}^\pm \right) R \right)}{I_{j_z \mp \frac{3}{2}, n} \left(\lambda_- \left(E_{j_z, n}^\pm \right) R \right)} I_{j_z \mp \frac{3}{2}, n} \left(\lambda_- \left(E_{j_z, n}^\pm \right) r \right) \right), \end{aligned} \quad (4.49)$$

where N is the normalization factor. We know the above wave function was found within the BHZ model which has the usual basis $|E_1+\rangle$, $|HH_1+\rangle$, $|E_1-\rangle$ and $|HH_1-\rangle$ (See Sec. 2). Thus, Eq. (4.47) can be also written as

$$\begin{aligned} \psi_{j_z, n}^\pm = & \frac{N}{\sqrt{2\pi}} \left[I_{E_1}^{j_z \mp \frac{1}{2}, n}(r) e^{i(j_z \mp \frac{1}{2})\theta} \left(f_1^\pm(z) \left| \Gamma_6, \pm \frac{1}{2} \right\rangle + f_4^\pm(z) \left| \Gamma_8, \pm \frac{1}{2} \right\rangle + f_7^\pm(z) \left| \Gamma_7, \pm \frac{1}{2} \right\rangle \right) \right. \\ & \left. \pm i I_{HH_1}^{j_z \mp \frac{3}{2}, n}(r) e^{i(j_z \mp \frac{3}{2})\theta} f_3^\pm(z) \left| \Gamma_8, \pm \frac{3}{2} \right\rangle \right]^T. \end{aligned} \quad (4.50)$$

By making the proper identifications, we obtain for the total QD circulating current,

$$\langle \mathbf{j}_{j_z, n}^\pm \rangle(\mathbf{r}) = \langle \mathbf{j}_{j_z, n}^\pm \rangle_b(\mathbf{r}) + \langle \mathbf{j}_{j_z, n}^\pm \rangle_e(\mathbf{r}), \quad (4.51)$$

where we define the ‘‘Bloch velocity’’ and ‘‘Envelope velocity’’ contributions as, respectively,

$$\langle \mathbf{j}_{j_z, n}^\pm \rangle_b = \pm e N^2 \frac{P}{\pi \hbar \sqrt{2}} |f_1^\pm(z)| |f_3^\pm(z)| I_{E_1}^{j_z \mp \frac{1}{2}, n}(r) I_{HH_1}^{j_z \mp \frac{3}{2}, n}(r) \hat{\theta}, \quad (4.52)$$

and

$$\begin{aligned} \langle \mathbf{j}_{j_z, n}^\pm \rangle_e = & \frac{\hbar e N^2}{2\pi r m_0} \left\{ \left(j_z \mp \frac{1}{2} \right) \left[|f_1^\pm(z)|^2 + |f_4^\pm(z)|^2 + |f_7^\pm(z)|^2 \right] \left| I_{E_1}^{j_z \mp \frac{1}{2}, n}(r) \right|^2 \right. \\ & \left. + \left(j_z \mp \frac{3}{2} \right) |f_3^\pm(z)|^2 \left| I_{HH_1}^{j_z \mp \frac{3}{2}, n}(r) \right|^2 \right\} \hat{\theta}, \end{aligned} \quad (4.53)$$

where P is the Kane parameter^{63, 121, 122} coupling the conduction and valence bands.

The motivation to call the currents as ‘‘circulating’’ comes from the fact that the current within our QD has just the $\hat{\theta}$ vector dependence, thus circulating in a loop around our cylindrical QD rim. The restriction of the current direction along $\hat{\theta}$ can be understood through the following argument: all our confined QD levels must have their energies below the AlSb QW barriers in the z direction as well as below the barrier in r direction Eq. (4.1). Thus, for $\langle \mathbf{j} \rangle(r, \theta, z) = \hat{r} j_r(r, \theta, z) + \hat{\theta} j_\theta(r, \theta, z) + \hat{z} j_z(r, \theta, z)$, we must have $j_r(r, \theta, z) = j_z(r, \theta, z) = 0$ in order to just allow for ‘‘bound states’’, i.e.,

$$\langle \mathbf{j} \rangle(\mathbf{r}) = \hat{\theta} j_\theta(r, z), \quad (4.54)$$

where the θ dependence in j_θ is absent due to the cylindrical symmetry of our QD. The

absence of the θ dependence can also be understood by recalling that $\nabla \cdot \mathbf{j} = \frac{\hat{\theta}}{r} \partial_\theta j_\theta(r, \theta, z) = 0$, thus yielding $\mathbf{j} = \hat{\theta} j_\theta(r, z)$.

We can understand the Bloch velocity contribution by recalling that $\langle \mathbf{j}_{j_z, n}^\sigma \rangle_b \propto \sum_{i,j} a_{ij} \langle u_i | \nabla | u_j \rangle$. Since we are dealing with Zincblend crystals, this current is only non-zero for the matrix elements between conduction and valence bands (Group theory result). Thus, for the spin + state, Eq. (4.50), we can only have

$$\begin{aligned} \langle \mathbf{j}_{j_z, n}^+ \rangle_b &\propto a_{13} \left\langle \Gamma_6, +\frac{1}{2} \left| \nabla \right| \Gamma_8, +\frac{3}{2} \right\rangle + a_{14} \left\langle \Gamma_6, +\frac{1}{2} \left| \nabla \right| \Gamma_8, +\frac{1}{2} \right\rangle + a_{17} \left\langle \Gamma_6, +\frac{1}{2} \left| \nabla \right| \Gamma_7, +\frac{1}{2} \right\rangle \\ &\quad + c.c. \end{aligned} \quad (4.55)$$

However, using the fact that $\langle \mathbf{j}_{j_z, n}^+ \rangle_b \propto \hat{\theta}$, we can eliminate the last two terms by recalling that $\langle \Gamma_6, \frac{1}{2} | \nabla | \Gamma_8, \frac{1}{2} \rangle, \langle \Gamma_6, \frac{1}{2} | \nabla | \Gamma_7, \frac{1}{2} \rangle \propto i\hat{z}P$ where P is the Kane parameter. As a result, the circulating current due to the Bloch velocity comes fully from the $\langle \Gamma_6, +\frac{1}{2} | \nabla | \Gamma_8, +\frac{3}{2} \rangle$ matrix element, justifying then the form of Eq. (4.52).

As for the circulating current expression due to the $\langle \mathbf{j}_{j_z, n}^\sigma \rangle_e$ envelope velocity, the argument is similar. However, for it we have $\langle \mathbf{j}_{j_z, n}^\sigma \rangle_e \propto \sum_i F_i(r, \theta, z) \nabla F_i(r, \theta, z)$. Again, by using the fact that our current must be in the $\hat{\theta}$ direction we reduce it to $\langle \mathbf{j}_{j_z, n}^\sigma \rangle_e \propto \sum_i F_i(r, \theta, z) \frac{\hat{\theta}}{r} \partial_\theta F_i(r, \theta, z)$, i.e., the $\langle \mathbf{j}_{j_z, n}^\sigma \rangle_e$ is proportional to the angular momentum ($L_z = -i\hbar \partial_\theta$) of the envelope functions. By recalling that for spin + states, $F_{i=1,4,7}(r, \theta, z) \propto e^{i(j_z - \frac{1}{2})\theta}$ 4.50 and $F_{i=3}(r, \theta, z) \propto e^{i(j_z - \frac{3}{2})\theta}$ 4.50, we thus find

$$\langle \mathbf{j}_{j_z, n}^+ \rangle_e \propto \frac{1}{r} \left[a \left(j_z - \frac{1}{2} \right) + b \left(j_z - \frac{3}{2} \right) \right] \hat{\theta}, \quad (4.56)$$

which maps onto Eq. (4.53).

4.4.2 Helical states

Using the $I_m(r) = I_{-m}(r)$ (for $m \in \mathbb{Z}$) property of the modified Bessel function we find for Eqs. (4.48) and (4.49), $I_{E_1}^{j_z \mp \frac{1}{2}, n}(r) = I_{E_1}^{-j_z \pm \frac{1}{2}, n}(r)$ and $I_{HH_1}^{j_z \mp \frac{3}{2}, n}(r) = I_{HH_1}^{-j_z \pm \frac{3}{2}, n}(r)$, respectively. By using this result in the total circulating current formula Eqs. (4.51), (4.52) and (4.53), we find

$$\langle \mathbf{j}_{j_z, n}^\pm \rangle(\mathbf{r}) = -\langle \mathbf{j}_{-j_z, n}^\mp \rangle(\mathbf{r}). \quad (4.57)$$

From the above we see that the currents of QD states with opposite j_z and spin (\pm)

propagate in opposite angular directions, which is essentially the helical condition for two QD states. As we will see later on, this relation will be important in the analysis of the circulating current results.

In the next chapter we present numerical results for the cylindrical InAsBi BHZ QDs in both topologically trivial and non-trivial regimes. We plot their discrete energy levels, wave functions and circulating currents. For both regimes of the BHZ QDs we find *geometrically protected helical edge states* within a large energy range, showing thus an equivalent behavior between trivial and non-trivial BHZ QDs. We show this feature is particular of trivial BHZ QDs, being absent in the ordinary InAs QDs.

5 RESULTS: ENERGY, WAVE-FUNCTION AND CIRCULATING CURRENT

Here we use the analytical formulas derived in the previous chapter and show results for the energy levels, wave functions and circulating currents for the i) topologically non-trivial $\text{InAs}_{0.85}\text{Bi}_{0.15}$ QD, ii) topologically trivial $\text{InAs}_{0.85}\text{Bi}_{0.15}$ QD, and iii) ordinary InAs QD. All of these QDs arise from the cylindrical hard-wall confinement of the $\text{InAs}_{1-x}\text{Bi}_x/\text{AlSb}$ QW with $x = 0.15$ and thickness $d = 8$ nm, $x = 0.15$ and thickness $d = 6$ nm, and $x = 0$ and thickness $d = 6$ nm, respectively. Surprisingly, we find in the trivial regime *geometrically protected helical edge states* with spin-angular-momentum locking similar to the topologically non-trivial QDs. These trivial edge states have similar circulating current densities when compared to the ones arising in the topologically non-trivial regime, thus showing a physical equivalence between them. Additionally, we show that this feature holds for the HgTe/CdTe QDs and for realistic soft wall QD confinement.

5.1 Energy levels and wave functions

5.1.1 Topologically non-trivial $\text{InAs}_{0.85}\text{Bi}_{0.15}$ QD

In Figure 14 we plot the energy levels as a function of the z component of the total angular momentum j_z for the topologically non-trivial $\text{InAs}_{0.85}\text{Bi}_{0.15}$ QD. We choose to plot the energies for the hard-wall boundary condition (Sec. 4.2.1) determined via Eq. (4.39). We use two different radius sizes ($R = 60$ nm and $R = 100$ nm) as a matter of comparison. As for the effective BHZ parameters, we use the parameters corresponding to the $\text{InAs}_{0.85}\text{Bi}_{0.15}/\text{AlSb}$ QW with thickness $d = 8$ nm, given in Table 1.

The blue and red symbols denote, respectively, the spin $+$ and $-$ subspaces of the BHZ Hamiltonian discussed in Sec. 2.3, while the circles (triangles) denote the even (odd) parity of the total wave function Eq. (4.23). In contrast to the confined BHZ model with one or two interfaces,^{4,5} in which the edge and bulk dispersions are continuous, here we obtain only discrete energy levels arising from the 3D quantum dot confinement. Some of these energy levels lie within the bulk gap region (gray area) between the conduction and valence levels and correspond to the edge states as shown in Figs. 15 and 16. As a direct consequence of a discrete version of Kramers theorem [Eq. (4.16)], for each energy level $E_{j_z, n}^\sigma$ there is also its Kramers partner with the same energy but opposite j_z and σ . Therefore, it is impossible to scatter elastically through a time reversal symmetric impurity potential from all the $E_{j_z, n}^\sigma$ energy states within the bulk gap (gray region) to its Kramers partner with opposite j_z and σ , i.e.,

$$[V_{imp}(r), \Theta] = 0 \quad \rightarrow \quad \langle \psi_{j_z, n}^\sigma | V_{imp}(r) | \psi_{-j_z, n}^{-\sigma} \rangle = 0. \quad (5.1)$$

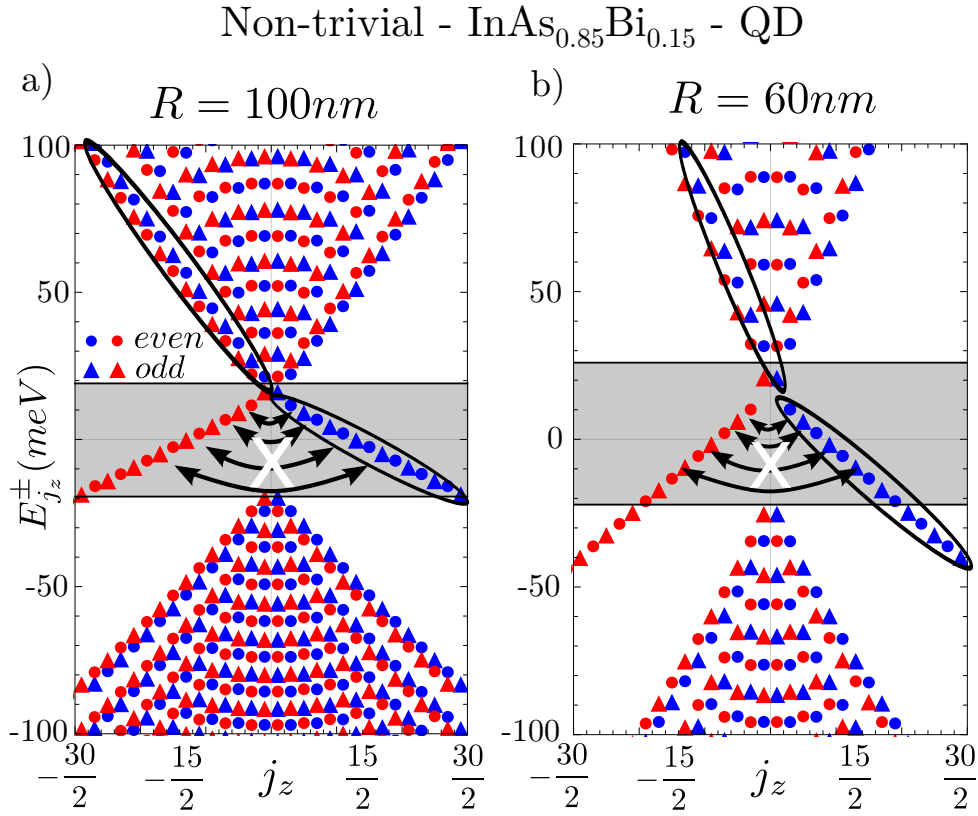


Figure 14 – a) Even (circles) and odd (triangles) energy levels as functions of j_z for the topologically non-trivial InAs_{0.85}Bi_{0.15} QD with QD radius $R = 100$ nm. b) Same as in a) for $R = 60$ nm. The black arrows denote (forbidden) transitions between spin up (blue) and spin down (red) states.

Source: By the author

These forbidden transitions are represented in Fig. 14 by the black arrows with the white cross symbol. Differently from the usual plot of the energy dispersion for 2D TIs^{4,5} and the energy levels for TI QDs,^{23–27,27–34} where the “Dirac point” (spin degeneracy of the energies in momentum) is near the mid gap,^{23,24} here we find our “Dirac point” near the conduction levels. This fact can be understood through the 2D TI energy dispersion formula for the edge states of one interface,⁷² which yields $C - \frac{D}{B}M$ at zero wave vector. Using the proper parameters from Table 1, we find a Dirac point placed at $\sim C + |M|$, very near the bottom of the conduction states. Regarding the QD energy levels for the two different QD radii ($R = 60$ nm and $R = 100$ nm), we see that the smaller the QD radius is, the larger the energy quantization is, thus increasing the energy separation between two consecutive energy levels, $E_{j_z+\frac{1}{2},n}^{\sigma} - E_{j_z,n}^{\sigma}$, as can be seen in Figures 14a) and 14b). The continuous bulk and edge energy dispersion for one interface are reached by taking

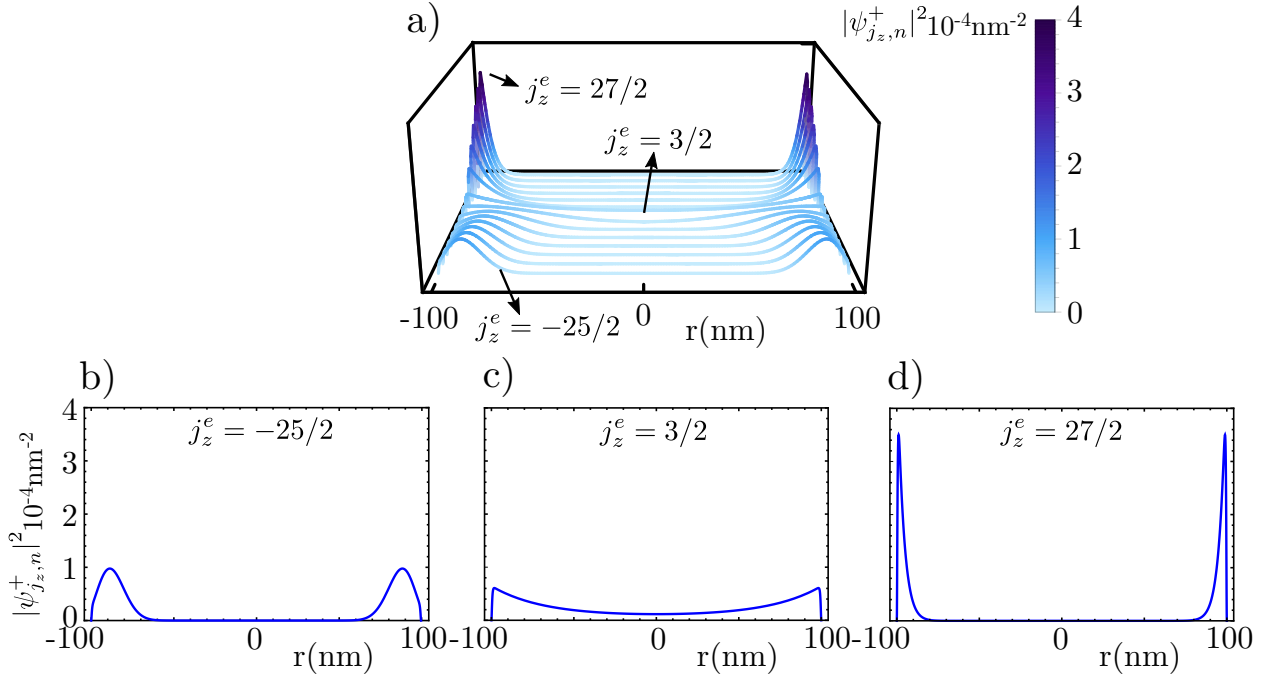


Figure 15 – a) Topologically non-trivial InAs_{0.85}Bi_{0.15} QD ($R = 100$ nm) modulus square of the spin + wave function $|\psi_{j_z, n}^+(r, \theta)|^2$ (4.38) for the energy levels with even m grouped by the ellipses in Figure 14a). b) Modulus square of the spin + wave function $|\psi_{j_z, n}^+(r, \theta)|^2$ for $j_z^e = -\frac{25}{2}$. c) Same as b) for $j_z^e = \frac{3}{2}$. d) Same as b) for $j_z^e = \frac{27}{2}$. The color bar represents the strength of the probability density and scale from 0 (light blue) to $4 \times 10^{-4} \text{ nm}^{-2}$ (dark blue).

Source: By the author

the $R \rightarrow \infty$ limit, yielding $\lim_{R \rightarrow \infty} (E_{j_z + \frac{1}{2}, n}^+ - E_{j_z, n}^+) = 0$ thus recovering the continuum limit of the 2D energy dispersions. The k wave vector is recovered by using $\Delta k \sim \frac{(j_z + 1) - j_z}{R}$, which after the limit $\lim_{R \rightarrow \infty}$ also gives a continuum wave vector.

We plot in Fig. 15 and 16 the modulus square of the spin + wave functions $|\psi_{j_z, n}^+(r, \theta)|^2$ (4.38) for the grouped energy levels with even m (j_z^e) in Figure 14a) and 14b). Here we have introduced the superscript e (o) in $j_z^{e(o)}$ to identify the states that are even (odd) with respect to the spatial inversion [See Eq. (4.33)]. We emphasize that we focus only on the spin + wave function part since the spin – part is straightforwardly obtained using $\Theta \psi_{j_z, n}^+ = \psi_{-j_z, n}^-$, yielding

$$|\psi_{-j_z, n}^-|^2 = \Theta \Theta^\dagger |\psi_{j_z, n}^+|^2 = |\psi_{j_z, n}^+|^2. \quad (5.2)$$

In Figure 15a) we see that the electronic energy levels lying within the bulk gap region (gray area) clearly show they are edge states with the only exception for the even $j_z^e = \frac{3}{2}$ state which extends within the whole QD [Figure 15c)]. More interestingly, we can see

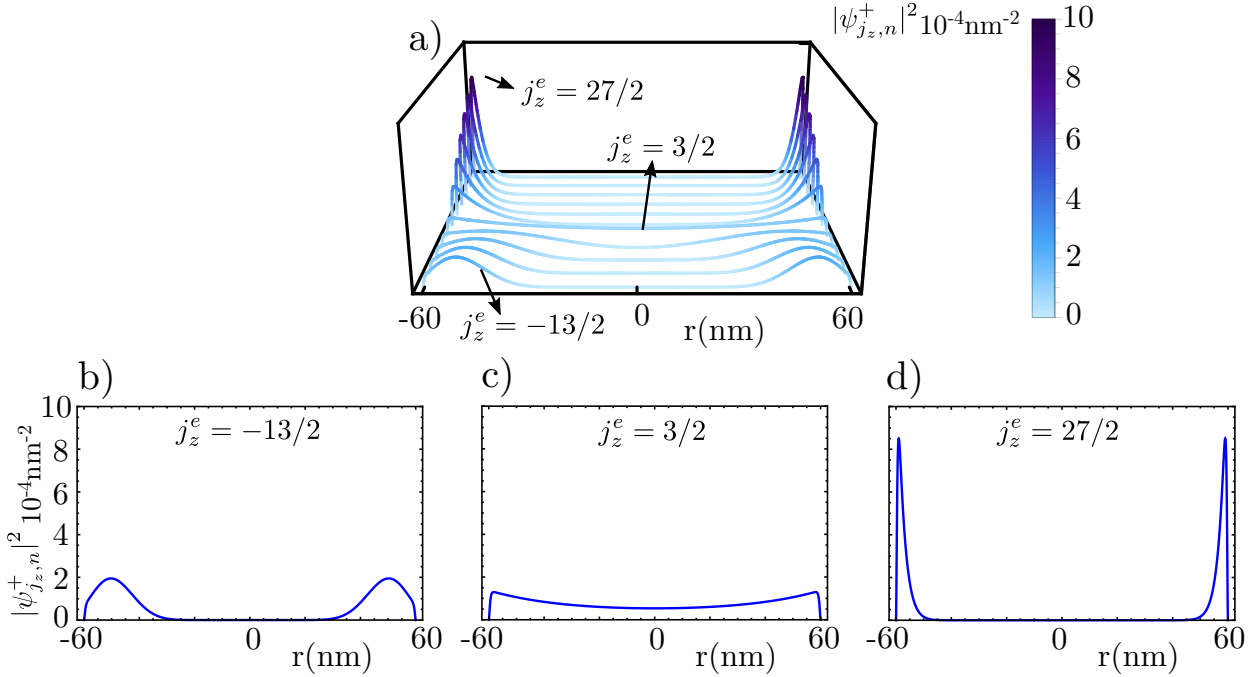


Figure 16 – Same as Fig. 15a) for the QD energy levels with even m grouped by the ellipses in Fig. 14b). b) Same as Fig. 15b) for $j_z^e = -\frac{13}{2}$. c) Same as b) for $j_z^e = \frac{3}{2}$. d) Same as b) for $j_z^e = \frac{27}{2}$.

Source: By the author

that unlike the strip confinement case, here the edge states do not start losing their edge character when merging with the conduction/valence levels. Instead, they become more and more localized as we can see in Figure 15a) for $j_z < 0$. This fact together with the extended wave function for $j_z^e = \frac{3}{2}$ is understood through the “centrifugal (CF) potential” or force. From Eq. (4.10) it is possible to see that the CF potential associated to the spin + BHZ Hamiltonian is given by

$$V_{CF, j_z}^+ = \begin{bmatrix} -(D+B) \frac{(j_z - \frac{1}{2})^2}{r^2} & 0 \\ 0 & -(D-B) \frac{(j_z - \frac{3}{2})^2}{r^2} \end{bmatrix}, \quad (5.3)$$

with its CF force given by $F_{CF}^+ = -\frac{\partial V_{CF, j_z}^+}{\partial r}$. The CF potential (5.3) clearly shows that the larger j_z is the stronger the centrifugal potential becomes in the middle of the QD, thus localizing the electrons (or pushing them to lie) near the QD edge. Additionally, for the extended state $j_z^e = \frac{3}{2}$ [Figure 15c)], we find no CF potential (or force) in the $|HH_1+\rangle$ subspace*. Hence, we have its radial envelope function component extended within the whole QD, which is clearly seen in Figure 15c). Although the edge states within the bulk

* $|HH_1+\rangle$ is the most relevant subspace of the $j_z^e = \frac{3}{2}$ state [within the gray area of Figure 15c)] since its energy is near the conduction levels.

energy region ($j_z < 0$) are more localized near the edge as we increase the absolute value of j_z , their wave function profile [Figure 15b)] are still different when compared to the edge states lying inside the bulk gap region ($j_z > 0$) [Figure 15d)], showing clearly the bulk influence.

Now, if we weakly couple our QD to source and drain leads and tune their respective chemical potential values so as to have a conduction window within the gray area of Figures 14a) and 14b), we can restrict the quantum transport through just the edge states, which are dissipationless and protected by TRS against elastic back-scattering[†].

The analysis and discussion of the wave functions for the InAs_{0.85}Bi_{0.15} non-trivial QD with $R = 60$ nm (Fig. 16) is similar as for the $R = 100$ nm case (Fig. 15).

5.1.2 Topologically trivial InAs_{0.85}Bi_{0.15} QD

In Figure 17, we plot the energy levels as functions of j_z , for the hard-wall boundary condition (Sec. 4.2.1) [determined via Eq. (4.39)] for the topologically trivial InAs_{0.85}Bi_{0.15} QD. We use two different QD radii sizes $R = 60$ nm and $R = 100$ nm and effective BHZ parameters corresponding to the InAs_{0.85}Bi_{0.15}/AlSb QW with thickness $d = 6$ nm given in Table 1.

As expected for a QD in the topologically trivial regime, here we clearly find a gapped region represented by the gray area in Figure 17. The lowest spin \pm conduction levels happen at $j_z^o = \pm\frac{1}{2}$ ($m = \mp 1$). As we have already discussed in Sec. 4.3, this happens because the j_z of the upper spin \pm wave function component [Eq. (4.23)] is the sum of the $(m \pm 1)\hbar$ envelope function angular momentum with the $\pm\frac{\hbar}{2}$ angular momentum arising from $|E_1\pm\rangle$ [See Eq. (2.11)], while for the lower \pm wave function component [Eq. (4.23)] it is the sum of the $m\hbar$ envelope function angular momentum with the $\pm\frac{3\hbar}{2}$ angular momentum arising from $|HH_1\pm\rangle$ [See Eq. (2.12)].

On the other hand, the highest spin \pm valence levels happen at $j_z^e = \pm\frac{3}{2}$ ($m = 0$) which for the upper spin \pm wave function component [Eq. (4.23)] correspond to the sum of the $(m \pm 1)\hbar$ envelope function angular momentum with $\pm\frac{\hbar}{2}$ angular momentum arising from $|E_1\pm\rangle$ [See Eq. (2.11)], while for the lower spin \pm wave function component [Eq. (4.23)] correspond to the sum of the $m\hbar$ envelope function angular momentum with the $\pm\frac{3\hbar}{2}$ angular momentum arising from $|HH_1\pm\rangle$ [See Eq. (2.12)].

The above results can also be understood considering the lowest $j_z^e = \pm\frac{1}{2}$ QD conduction states as arising approximately only from the periodic $|\Gamma_6, \pm\frac{1}{2}\rangle$ bulk conduction band (arising from s-orbitals) multiplied by the envelope function with the lowest angular momentum ($m = 0$), thus yielding $j_z^o = \pm\frac{1}{2}$. As for the highest $j_z^e = \pm\frac{3}{2}$ QD valence states, we understand them by considering them as being purely due to the periodic $|\Gamma_8, \pm\frac{3}{2}\rangle$

[†] Absence of elastic back-scattering here means it is impossible to scatter elastically from a spin + state with j_z to a spin - with $-j_z$.

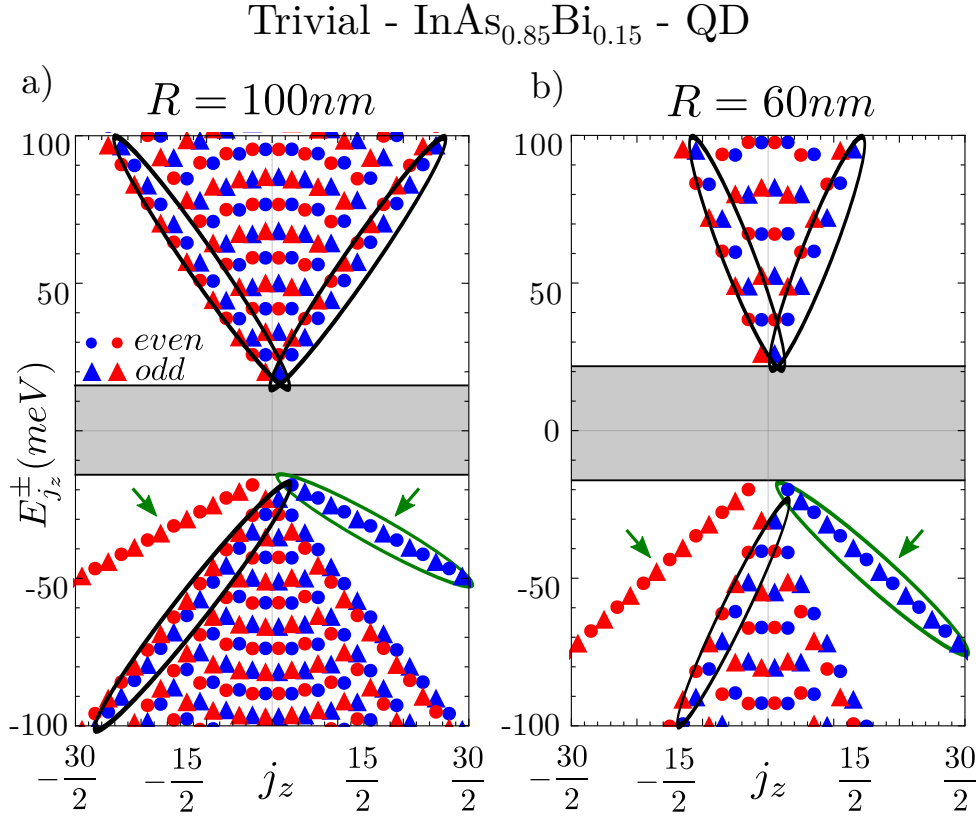


Figure 17 – a) Same as Fig. 14a) for the trivial InAs_{0.85}Bi_{0.15} QD with QD radius $R = 100$ nm. b) Same as a) for $R = 60$ nm.

Source: By the author

bulk valence band (arising from p-orbitals) multiplied by the lowest angular momentum envelope function ($m = 0$), thus yielding $j_z^e = \pm\frac{3}{2}$.

In Figures 17a) and 17b) we see a peculiarity in the energy levels represented by the two branches that are deviating from the other valence levels (pointed out by the dark green arrows and grouped by the dark green ellipses). In order to investigate and compare these deviating energy states with the others, we plot in Figures 18a) and 18c) the wave function of the highest spin + valence the states from $j_z^e = -\frac{25}{2}$ to $j_z^e = \frac{27}{2}$ for $R = 100$ nm [even states grouped by the ellipses in Fig. 17a) with $E_{j_z} < 0$] and from $j_z^e = -\frac{13}{2}$ to $j_z^e = \frac{27}{2}$ for $R = 60$ nm [even states grouped by the ellipses in Fig. 17b) with $E_{j_z} < 0$]. Interestingly and differently from all the results for topologically trivial QDs in the literature,^{23–27,27–34} here we find the appearance of trivial edge states in the valence levels. The wave functions corresponding to the branch energy levels ($\frac{3}{2} \leq j_z^e \leq \frac{27}{2}$) [even states grouped by the dark green ellipses in Figs. 17a) and b)] show here the same wave function profile as the topologically non-trivial QD edge states lying within the gap of Figures 15a) and 16a), respectively.

Although the edge states can appear in trivial cylindrical QDs due to the CF

potential, which is the case for the lowest even conduction states in Figs. 18b) and 18d) [even levels grouped by the upper ellipses in Figs. 17a) and b) with $E_{j_z} > 0$], we emphasize that their wave function profiles are different from the topological edge states [Figures 15 and 16] because they do not have sharp ends near the rim of the QD. For this reason, we will call as trivial edge states just the states corresponding to the valence branch energy levels ($\frac{3}{2} \leq j_z^e \leq \frac{27}{2}$) [states grouped by the lower green ellipses in Figs. 17a) and b)] which have similar wave function profile as compared to the topological edge states, i.e., wave functions with a sharp ends near $r = R$. As for the others, we will call them as valence or conduction bulk states (or levels).

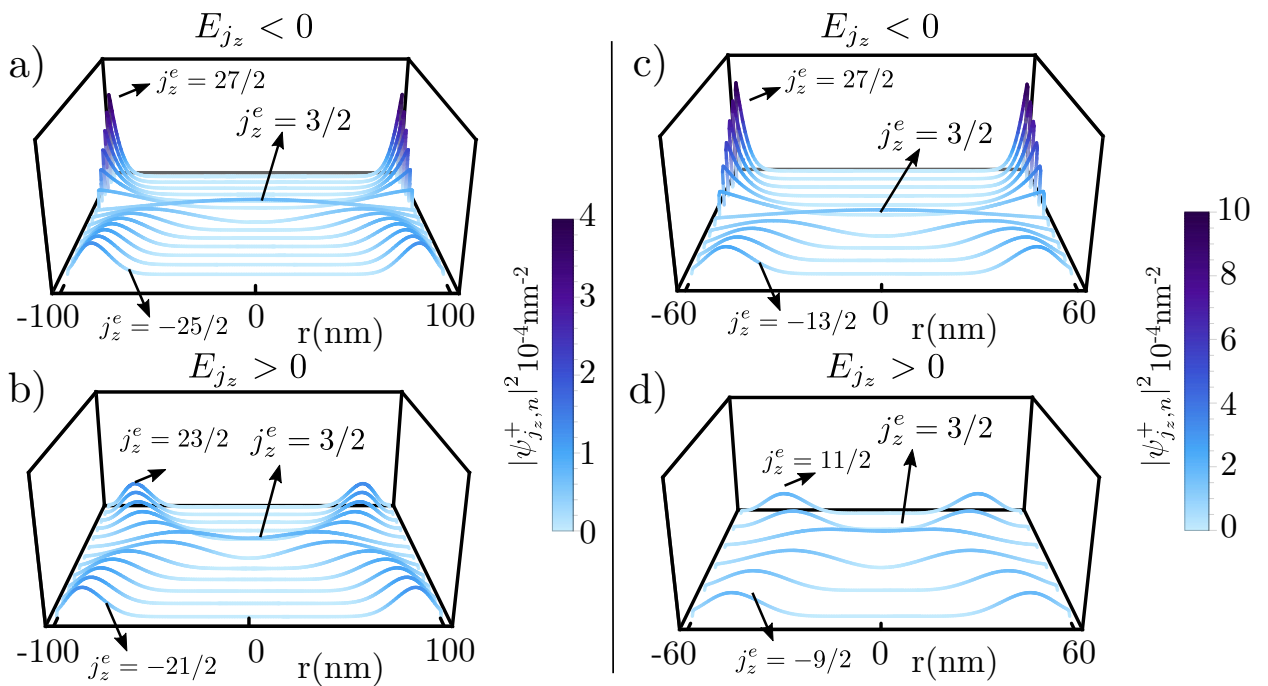


Figure 18 – a) Modulus square of the spin + wave function $|\psi_{j_z,n}^+(r, \theta)|^2$ (4.38) for the highest valence states (even states grouped by the lower ellipses in Figs. 17a) with $E_{j_z} < 0$) from $j_z^e = -\frac{25}{2}$ to $j_z^e = \frac{27}{2}$. b) $|\psi_{j_z,n}^+(r, \theta)|^2$ (4.38) for lowest conduction states (even states grouped by the upper ellipses in Figs. 17a) with $E_{j_z} > 0$) from $j_z^e = -\frac{21}{2}$ to $j_z^e = \frac{23}{2}$. c) Same as a) for the even states grouped by the lower ellipses in Figs. 17b) with $E_{j_z} < 0$. d) Same as b) even states grouped by the lower ellipses in Figs. 17b) with $E_{j_z} > 0$.

Source: By the author

In contrast to the topologically non-trivial edge states lying within the gap energy region, here our trivial edge states are not isolated from the other valence levels. As a consequence, the elastic backscattering between these trivial edge states (deviating branch states) and the others valence bulk levels becomes possible. Thus, although we find trivial edge states with a similar wave function profiles as those of the non-trivial edge states,

here they are not protected. As we see next, we can still make this states robust over a wide range of dot radii (geometric protection).

We know that wave function profile of the trivial edge states is more localized near the QD edge ($r = R$) as compared to the bulk valence wave functions. Thus the energies of the latter are more sensitive to the QD size than the energies of trivial edge states. As a consequence, we can decrease the size of our QD in order to push the bulk valence energy levels far away from the trivial edge states energy levels.

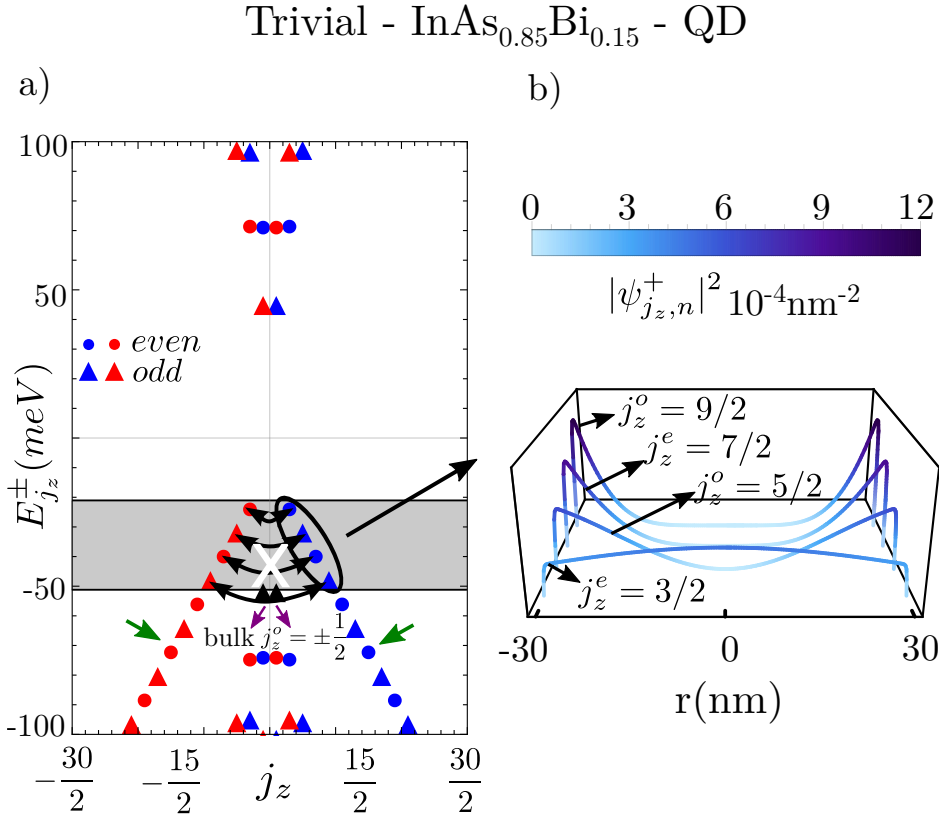


Figure 19 – a) Trivial InAs_{0.85}Bi_{0.15} QD energy levels as functions of j_z with QD radius $R = 30$ nm. b) $|\psi_{j_z, n}^+(r, \theta)|^2$ of the edge states grouped by the ellipse in Fig. 19a). The black triangles $j_z^o = \pm 1/2$ states represent the bulk-like states that merge with the edge states in Fig. 20.

Source: By the author

In Figure 19 we plot the energy levels for the topologically trivial InAs_{0.85}Bi_{0.15} QD with radius $R = 30$ nm, where there are still two branches deviating from the other valence levels (pointed out by the dark green arrows). Surprisingly, we find within the gray area trivial spin resolved single Kramers pairs with spin angular-momentum locking, i.e., for each edge state inside the gray areas with energy $E_{j_z, n}^\sigma$, we find its Kramer partner with same energy but opposite j_z and σ . In summary, we show that inside the gray area of Figures 14 and 19, both topologically trivial and non-trivial QDs contain the same features

concerning the existence and protection of the edge states, showing thus a qualitative equivalence between both regimes in QDs. The only difference is that in the trivial QD, the edge states lie outside the original bulk gap in the 2D BHZ model. Therefore, similarly to the topological QDs, here it is also possible to restrict the quantum transport through just edge states with TRS protection against elastic backscattering (we investigate this possibility in detail in Chapter 5).

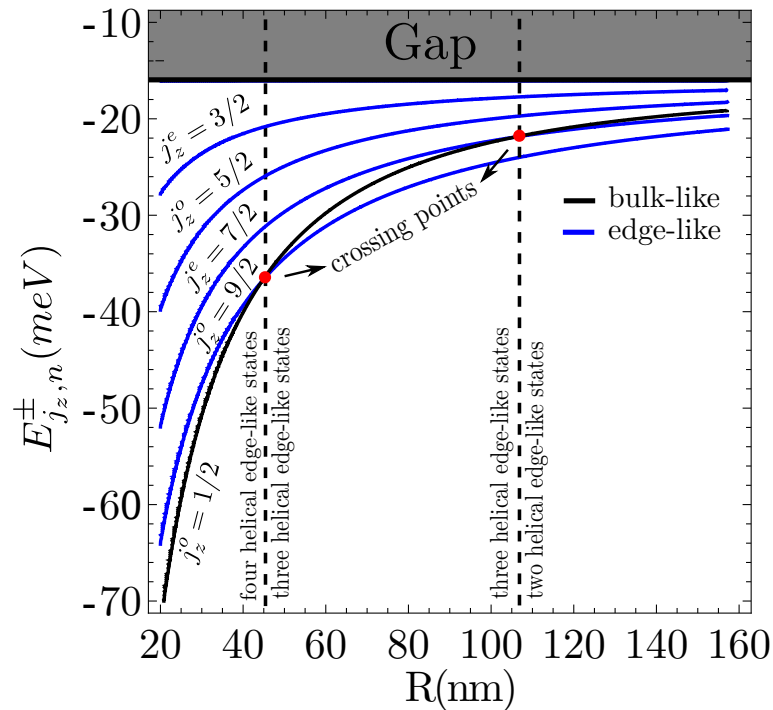


Figure 20 – Eigenenergies of the spin + trivial edge states $j_z^e = 3/2$, $j_z^e = 5/2$, $j_z^e = 7/2$ and $j_z^e = 9/2$ within the gray area of Figure 19a) and their nearest bulk valence level $j_z^o = 1/2$ as a function of QD radius R . The red points indicate the crossing points where the number of the protected trivial edge states is decreased by one as they become degenerate or start coexisting with bulk states.

Source: By the author

While in the topologically non-trivial QD, the edge states are protected by the non-trivial topology of the system, in the topologically trivial QD the edge states are geometrically protected by the small radius of the QD confinement. The latter prevents the coexistence of the bulk-like and edge-like valence states within the gray area in Figure 19 for QD radii $R < 44$ nm. Due to the different sensitivity of the bulk-like wave functions and the edge-like states, as we increase the radius $R > 44$ nm, the nearest bulk valence state in energy, $j_z^o = \frac{1}{2}$, goes inside the gray area and cross the edge-like energy levels at $R_{c1} = 44$ nm and $R_{c2} = 106$ nm [see crossing points (red dots) in Figure 19], allowing now for possible scatterings within our defined gray area. As a result, the number of

protected trivial edge states is effectively reduced by one at $R = R_{c1}$ and $R = R_{c2}$. This is clearly seen in Figure 20 where we plot the energy levels of the spin $+j_z^e = 3/2$, $j_z^o = 5/2$, $j_z^e = 7/2$ and $j_z^o = 9/2$ edge states within the gray area of Figure 19a), together with their nearest bulk valence level $j_z^o = 1/2$ outside the gray area as a function of the QD radius. Although at both of these points, the number of the protected edge states is decreased our features remain the same for a reasonably energy window.

5.1.3 Topologically trivial InAs_{0.85}Bi_{0.15} QD in the presence of BIA

In Zincblende structures, the lack of bulk inversion symmetry allows for the appearance of BIA (bulk inversion asymmetry) terms. Here we investigate our protected helical edge states in trivial InAs_{0.85}Bi_{0.15} QD [Fig. 19] in the presence of these terms. As we already discussed in Sec. 11, the BIA term here should be very important since Bi-based compounds have larger spin-orbit interaction, thus possibly enhancing the strength of the BIA terms. In leading order, the BHZ Hamiltonian with BIA reads^{5,51,72}

$$\mathcal{H}_{InAsBi}^{BIA} = C - D\mathbf{k}^2 + \begin{bmatrix} M - B\mathbf{k}^2 & Ak_+ & 0 & -\Delta_{BIA} \\ Ak_- & -M + B\mathbf{k}^2 & \Delta_{BIA} & 0 \\ 0 & \Delta_{BIA} & M - B\mathbf{k}^2 & -Ak_- \\ -\Delta_{BIA} & 0 & -Ak_+ & -M + B\mathbf{k}^2 \end{bmatrix}, \quad (5.4)$$

with eigenenergies given by⁷²

$$E_{BHZ}^{\pm, s=\pm}(\mathbf{k}, \Delta_{BIA}) = C - D\mathbf{k}^2 \pm \sqrt{(A|\mathbf{k}| + s\Delta)^2 + (M - B\mathbf{k}^2)^2}. \quad (5.5)$$

Using the parameters on Tab. 1, assuming $|\mathbf{k}| \approx \frac{1}{R}$ with $R = 30$ nm, and $\Delta_{BIA} = 4$ meV (twice the value of HgTe/CdTe?) we estimate the energy shift in, e.g., the valence levels, as

$$E_{BHZ}^{-, s=\pm}\left(\frac{1}{R}, \Delta_{BIA}\right) - E_{BHZ}^{-, s=\pm}\left(\frac{1}{R}, \Delta_{BIA} = 0\right) \approx 2meV, \quad (5.6)$$

leading to small energy level shift as compared to the QD energy separation. A similar estimate also holds for the topological InAs_{0.85}Bi_{0.15} QD. Therefore, we expect that the inclusion of the BIA terms does not destroy the protected trivial helical edge states in Figure 19.

5.1.4 Ordinary InAs QD

In order to check whether the protected trivial helical edge states are present or not in ordinary large gap QDs, here we investigate the energy levels and their corresponding

wave function profiles for the ordinary InAs QD. As opposed to the topologically trivial and non-trivial InAsBi QWs, the ordinary InAs/AlSb QW with its large subband gap can be treated approximately using decoupled parabolic dispersions with realistic effective masses. The respective Hamiltonian for the spin degenerate lowest conduction $|C_{1\pm}\rangle$ (with energy E_{C_1}), and the highest valence $|H_{1\pm}\rangle$ (with energy E_{H_1}) subbands reads

$$\mathcal{H}_{InAs} = \begin{bmatrix} \frac{\hbar^2}{2m_{C_1}} \mathbf{k}^2 + E_{C_1} & 0 & 0 & 0 \\ 0 & \frac{\hbar^2}{2m_{H_1}} \mathbf{k}^2 - E_{H_1} & 0 & 0 \\ 0 & 0 & \frac{\hbar^2}{2m_{C_1}} \mathbf{k}^2 + E_{C_1} & 0 \\ 0 & 0 & 0 & \frac{\hbar^2}{2m_{H_1}} \mathbf{k}^2 - E_{H_1} \end{bmatrix}. \quad (5.7)$$

Realistic $\mathbf{k} \cdot \mathbf{p}$ calculations¹¹⁴ for the InAs/AlSb QW with well thickness $d = 6$ nm yield $E_{C_1} = 200.7$ meV, $E_{H_1} = 200.7$ meV, $m_{C_1} = 0.0473m_0$ and $m_{H_1} = -0.2163m_0$. The wave function solutions of Eq. (5.7) for the hard-wall case read

$$\psi_{j_z, n}^{C_{1\pm}}(r, \theta) = p_{j_z, n} I_{j_z \mp \frac{1}{2}}(\lambda_{C_1} r) e^{i(j_z \mp \frac{1}{2})\theta}, \quad (5.8)$$

$$\psi_{j_z, n}^{H_{1\pm}}(r, \theta) = q_{j_z, n} I_{j_z \mp \frac{3}{2}}(\lambda_{H_1} r) e^{i(j_z \mp \frac{3}{2})\theta}, \quad (5.9)$$

with $\lambda_{C_1} = \sqrt{\frac{E_{C_{1\pm}} - E_{C_1}}{-\frac{\hbar^2}{2m_{C_1}}}}$, $\lambda_{HH_1} = \sqrt{\frac{E_{H_{1\pm}} + E_{H_1}}{-\frac{\hbar^2}{2m_{H_1}}}}$ and $p_{j_z, n}$, $q_{j_z, n}$ as being the normalization factors. By imposing that the above wave functions vanish at $r = R$, we obtain the energy levels

$$E_{j_z, n}^{C_{1\pm}} = E_{C_1} + \frac{\hbar^2}{2m_{C_1}} \left(\frac{\alpha_{j_z \mp \frac{1}{2}}^n}{R} \right)^2, \quad (5.10)$$

$$E_{j_z, n}^{H_{1\pm}} = -E_{H_1} + \frac{\hbar^2}{2m_{H_1}} \left(\frac{\alpha_{j_z \mp \frac{3}{2}}^n}{R} \right)^2, \quad (5.11)$$

where $\alpha_{j_z \mp \frac{1}{2}}^n$ and $\alpha_{j_z \mp \frac{3}{2}}^n$ are the n^{th} -zeros of the modified Bessel function of order $j_z \mp \frac{1}{2}$ and $j_z \mp \frac{3}{2}$, respectively.

As a direct consequence of the solutions for parabolic dispersions, Eqs. (5.8) and (5.9), here we have the appearance of the following extra degeneracy (in addition to the Kramers degeneracy) of the energy levels arising from $I_{j_z \mp \frac{1}{2}}(\lambda r) = I_{-j_z \pm \frac{1}{2}}(\lambda r)$ and $I_{j_z \mp \frac{3}{2}}(\lambda r) = I_{-j_z \pm \frac{3}{2}}(\lambda r)$, i.e.,

$$E_{j_z \mp \frac{1}{2}, n}^{C_1 \pm} = E_{-j_z \pm \frac{1}{2}, n}^{C_1 \pm}, \quad (5.12)$$

$$E_{j_z \mp \frac{3}{2}, n}^{H_1 \pm} = E_{-j_z \pm \frac{3}{2}, n}^{H_1 \pm}. \quad (5.13)$$

Using now the TRS energy degeneracy $E_{j_z, n}^{\pm} = E_{-j_z, n}^{\mp}$, we find for each j_z level ($j_z \neq \pm \frac{1}{2}$ for $C_1 \pm$ and $j_z \neq \pm \frac{3}{2}$ for $H_1 \pm$) the following 4-fold degeneracy of the ordinary InAs QD energy levels

$$E_{j_z \mp \frac{1}{2}, n}^{C_1 \pm} = E_{-(j_z \mp \frac{1}{2}), n}^{C_1 \mp} = E_{-j_z \pm \frac{1}{2}, n}^{C_1 \pm} = E_{-(-j_z \pm \frac{1}{2}), n}^{C_1 \mp}, \quad (5.14)$$

$$E_{j_z \mp \frac{3}{2}, n}^{H_1 \pm} = E_{-(j_z \mp \frac{3}{2}), n}^{H_1 \mp} = E_{-j_z \pm \frac{3}{2}, n}^{H_1 \pm} = E_{-(-j_z \pm \frac{3}{2}), n}^{H_1 \mp}. \quad (5.15)$$

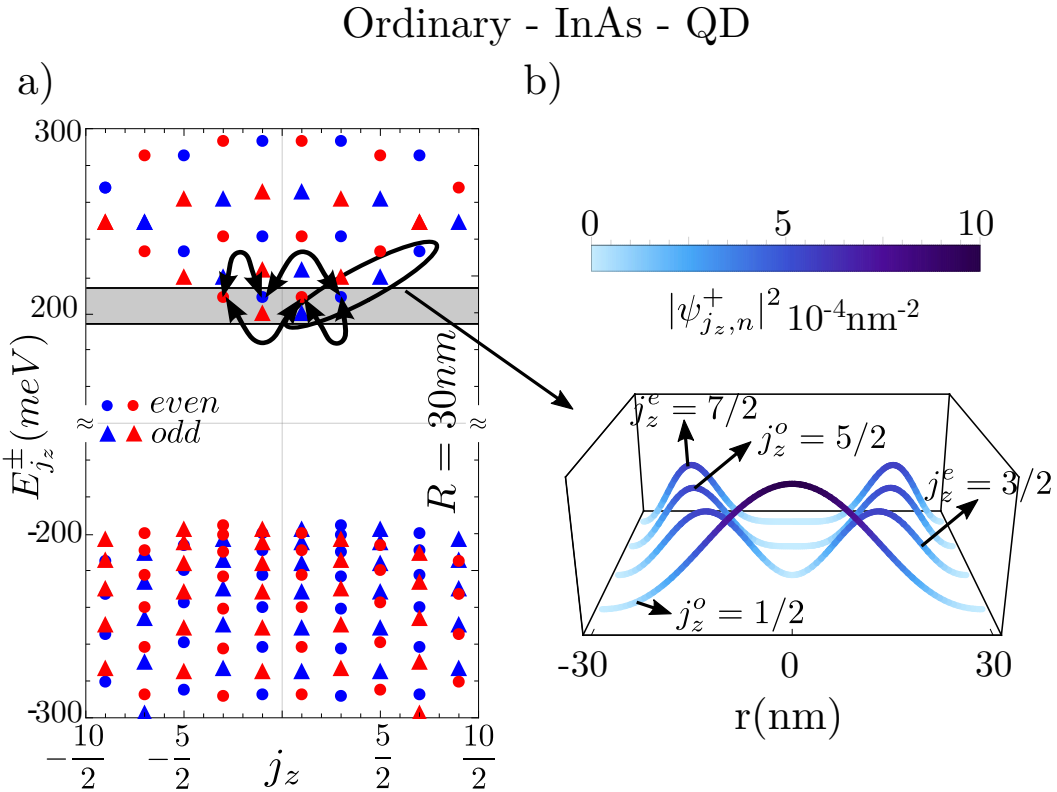


Figure 21 – a) Even (circles) and odd (triangles) energy levels as functions of j_z for the trivial $\text{InAs}_{0.85}\text{Bi}_{0.15}$ QD with QD radius $R = 30$ nm. b) Modulus square of the spin + wave function for edge grouped by the ellipse.

Source: By the author

This inherent degeneracy of the InAs QD levels (not present in the BHZ QDs) can be seen in Fig. 21 where we plot the energy levels Eqs. (5.10) and (5.11) with the probability densities $|\psi_{j_z, n}^+(r, \theta)|^2$ Eqs. (5.8) and (5.9) for states grouped by the ellipse in Fig. 21. In contrast to the degenerate Kramers pairs energy levels, which cannot be scattered into each other due to the TRS protection Eq. (5.1), here the new degenerate levels Eqs. (5.12) and (5.13) are allowed to scatter into each other (curved black arrows in Fig. 21) thus effectively destroying the whole protection of the 4-fold states. Additionally, the helical character in the ordinary InAs QD is also absent since the degenerate states in Eqs. (5.12) and (5.13) have circulating currents with opposite propagating directions. As for the almost flat valence levels in Fig. 21 as function of j_z , the reason lies in the large effective mass of the heavy-hole states.

We emphasize that even by including higher order \mathbf{k} -terms like \mathbf{k}^4 and \mathbf{k}^6 in the diagonal of Eq. (5.7), we still do not find protected trivial helical edge states. This can be understood by noting that a Hamiltonian even in \mathbf{k} will always produce degenerate conduction (valence) levels with respect to the j_z of the lowest conduction level (highest valence level). Thus, in order to break this degeneracy arising from a Hamiltonian even in \mathbf{k} , we need to include in the Hamiltonian large odd terms in \mathbf{k} . This situation occurs in particular for the topologically trivial InAs_{0.85}Bi_{0.15} QD (described by the BHZ Hamiltonian), where the linear terms in \mathbf{k} , Ak_{\pm} , dominate all the other terms, thus breaking the degeneracy and yielding a very asymmetric spectrum with respect to the j_z of the highest valence state Fig. 19. Therefore, we see that the two-level structure of the BHZ Hamiltonian with its large linear term is an important ingredient to find the protected trivial helical edge states.

5.1.5 Ordinary InAs QD in the presence of C_1 - H_1 mixing

In order to investigate the stability of the ordinary InAs QD results, here we include the mixing between the $|C_1 \pm\rangle$ and $|H_1 \pm\rangle$ subbands in the effective InAs/AlSb QW Hamiltonian allowed by $\mathbf{k} \cdot \mathbf{p}$ theory.^{63,122} This coupling is modelled through the $\pm A'k_{\pm}$ terms in the Hamiltonian

$$\mathcal{H}_{InAs}^{C_1-H_1} = \begin{bmatrix} \frac{\hbar^2}{2m_{C_1}} \mathbf{k}^2 + E_{C_1} & A'k_+ & 0 & 0 \\ A'k_- & \frac{\hbar^2}{2m_{H_1}} \mathbf{k}^2 - E_{H_1} & 0 & 0 \\ 0 & 0 & \frac{\hbar^2}{2m_{C_1}} \mathbf{k}^2 + E_{C_1} & -A'k_- \\ 0 & 0 & -A'k_+ & \frac{\hbar^2}{2m_{H_1}} \mathbf{k}^2 - E_{H_1} \end{bmatrix}. \quad (5.16)$$

The new energies thus read

$$E_{\pm} = \frac{E_{C_1} + E_{H_1}}{2} + \frac{\hbar^2}{4} \left(\frac{1}{m_{C_1}} + \frac{1}{m_{H_1}} \right) \mathbf{k}^2 \pm \sqrt{\left[\frac{E_{C_1} - E_{H_1}}{2} + \frac{\hbar^2}{4} \left(\frac{1}{m_{C_1}} - \frac{1}{m_{H_1}} \right) \mathbf{k}^2 \right]^2 + (A'\mathbf{k})^2}. \quad (5.17)$$

Here we estimate the QD energies by making $|\mathbf{k}| \approx \frac{1}{R}$ in the above formula (the QD radius is a reasonable assumption for $|\mathbf{k}|$) which using leading order perturbative expansion yields the following energy change due to the $|C_1 \pm\rangle - |H_1 \pm\rangle$ mixing.

$$\Delta E_{C_1-H_1}^{mix} \approx \frac{\left(\frac{A'}{R}\right)^2}{E_{C_1} - E_{H_1}}. \quad (5.18)$$

Using $E_{C_1} - E_{H_1} = 401.4$ meV, $A' \approx 300$ meV.nm (Tab. 1) and $R = 30$ nm, we obtain

$$\Delta E_{C_1-H_1}^{mix} \approx 1 \text{ meV}, \quad (5.19)$$

which is much smaller as compared to the energy separation of two conduction QD levels Fig. 21 and thus should not change the main feature of it.

We emphasize that although we have linear terms in \mathbf{k} in the Hamiltonian (5.16), the degeneracies here are just lifted to within ~ 1 meV as the linear terms are not large as compared to the rest of the Hamiltonian for the lowest energy states (this is in contrast with the BHZ model for which the linear terms are relevant).

5.1.6 Ordinary InAs QD in the presence of spin orbit Rashba term

Although we have performed our calculations by only considering symmetric InAs/AlSb QWs, we can estimate the shift in the QD energy due to spin-orbit interaction (linear Rashba term^{41,67}) arising from a possible structural inversion asymmetry (SIA). For the sake of simplicity, we only consider the Rashba term within the electron subspace. For this case, our Hamiltonian reads

$$\mathcal{H}_{InAs}^{Rashba} = \begin{bmatrix} \frac{\hbar^2}{2m_{C_1}} \mathbf{k}^2 + E_{C_1} & 0 & -i\alpha k_- & 0 \\ 0 & \frac{\hbar^2}{2m_{H_1}} \mathbf{k}^2 - E_{H_1} & 0 & 0 \\ i\alpha k_+ & 0 & \frac{\hbar^2}{2m_{C_1}} \mathbf{k}^2 + E_{C_1} & 0 \\ 0 & 0 & 0 & \frac{\hbar^2}{2m_{H_1}} \mathbf{k}^2 - E_{H_1} \end{bmatrix}. \quad (5.20)$$

The new conduction energies are given by

$$E_{C_1, SIA}^{\pm} = E_{C_1} + \frac{\hbar^2 \mathbf{k}^2}{2m_{C_1}} \pm \alpha |\mathbf{k}|. \quad (5.21)$$

Using the realistic $\alpha = 28 \text{ meV}\cdot\text{nm}$ ¹²³ and again making $|\mathbf{k}| \approx \frac{1}{R}$ with $R = 30 \text{ nm}$, we obtain the QD energy level shift due the Rashba spin orbit coupling

$$\Delta E_{C_1, SIA} \approx \frac{\alpha}{R} \rightarrow \Delta E_{C_1, R} \approx 0.9 \text{ meV}, \quad (5.22)$$

which is also small as compared to the energy separation of two conduction QD energy levels [c.f., Eq. (5.19)].

5.1.7 Ordinary InAs QD in the presence of bulk inversion asymmetry term (BIA)

Here we investigate the influence of the BIA terms in the ordinary InAs QD arising from the lack of the bulk inversion symmetry. We also consider only the BIA terms within the electron subspace. Using the leading order BIA terms^{36,41} in Eq. (5.7) we obtain

$$\mathcal{H}_{InAs}^{BIA} = \begin{bmatrix} \frac{\hbar^2}{2m_{C_1}} \mathbf{k}^2 + E_{C_1} & 0 & -\beta k_+ & 0 \\ 0 & \frac{\hbar^2}{2m_{H_1}} \mathbf{k}^2 - E_{H_1} & 0 & 0 \\ -\beta k_- & 0 & \frac{\hbar^2}{2m_{C_1}} \mathbf{k}^2 + E_{C_1} & 0 \\ 0 & 0 & 0 & \frac{\hbar^2}{2m_{H_1}} \mathbf{k}^2 - E_{H_1} \end{bmatrix}, \quad (5.23)$$

which has eigenvalues

$$E_{C_1, BIA}^{\pm} = E_{C_1} + \frac{\hbar^2 \mathbf{k}^2}{2m_{C_1}} \pm \beta |\mathbf{k}|. \quad (5.24)$$

The linear Dresselhaus parameter for InAs/AlSb QW is typically $\beta \approx 5 \text{ meV}\cdot\text{nm}$.¹²³ Using then $|\mathbf{k}| \approx \frac{1}{R}$ with $R = 30 \text{ nm}$, we obtain the following shift in the QD energy levels

$$\Delta E_{C_1, BIA} \approx \frac{\beta}{R} \rightarrow \Delta E_{C_1} \approx 0.17 \text{ meV}, \quad (5.25)$$

which is also negligible compared to the QD energy level separation.

5.2 Circulating current densities

In this section we investigate the circulating current densities $\langle \mathbf{j}_{j_z, n}^\pm \rangle(\mathbf{r})$ of the QD energy levels for both topologically trivial and non-trivial $\text{InAs}_{0.85}\text{Bi}_{0.15}$ QDs. Most importantly, we investigate and compare whether there are differences or not between the protected trivial and non-trivial helical edge states (within the gray areas) found in the last section in Figs. 19 and 14, respectively.

5.2.1 Topologically non-trivial $\text{InAs}_{0.85}\text{Bi}_{0.15}$ QD

In Fig. 22 we plot the energy levels for the topological QD with $R = 40$ nm together with their respective spin up circulating currents for the levels represented by the pentagon, star and square. Similar to the wave function results, the circulating current of the state within the gap region, $j_z = 13/2$ (square) in Fig. 22 is localized near the edge. Interestingly, although the $j_z = 3/2$ level (star) was not considered as edge state since its wave function is extended through the whole QD, we see that its associated circulating current shows a larger density contribution near the edge. This comes from the fact that the circulating current Eq. (4.52) is proportional to the product of the upper $I_{E_1}^{1, n}(r)$ and lower $I_{HH_1}^{0, n}(r)$ wave function components. While the larger $I_{HH_1}^{0, n}(r)$ component is extended through the whole QD, the $I_{E_1}^{1, n}(r)$ is localized near the edge. As a consequence, the product of both yields a circulating current with large edge character.

Additionally, we also see a circulating current density localized near the edge for the bulk state outside the gray area, $j_z = -7/2$ (pentagon). However, it has a very different profile as compared to the levels within the gray area region (star and square). This stems from the fact that the pentagon is a bulk state under the presence of the centrifugal potential confining arising due to our QD geometry [similarly to the wave function results Figure 16b)]. The highest circulating current density peak is found for the j_z -highest level, $j_z = 13/2$ (square), which is a consequence of its having the most localized edge character.

We showed in Sec. 4.4 that the total circulating current formula is composed of a sum of two different parts. The first term, called the Bloch contribution $\langle \mathbf{j}_{j_z, n}^\pm \rangle_b$ stems from the periodic Bloch functions while the second one, the envelope function contribution $\langle \mathbf{j}_{j_z, n}^\pm \rangle_e$ stems from the total envelope function arising from the 3D heterostructure confinement. Now we use Eqs. (4.52) and (4.53) to obtain a rough estimate of the ratio between them. Using thus $j_z \sim 2$, $P = 0.9055$ eV.nm and $r \sim R = 40$ nm, we find

$$\frac{\langle \mathbf{j}_{j_z, n}^\pm \rangle_b}{\langle \mathbf{j}_{j_z, n}^\pm \rangle_e} \approx \frac{r P}{\sqrt{2} \frac{\hbar^2}{m_0} j_z} \approx 340, \quad (5.26)$$

which shows that the circulating currents are mostly related to the Bloch contribution (in agreement with Ref. 69. The linear dependence on the QD radius in Eq. (5.26) (also in

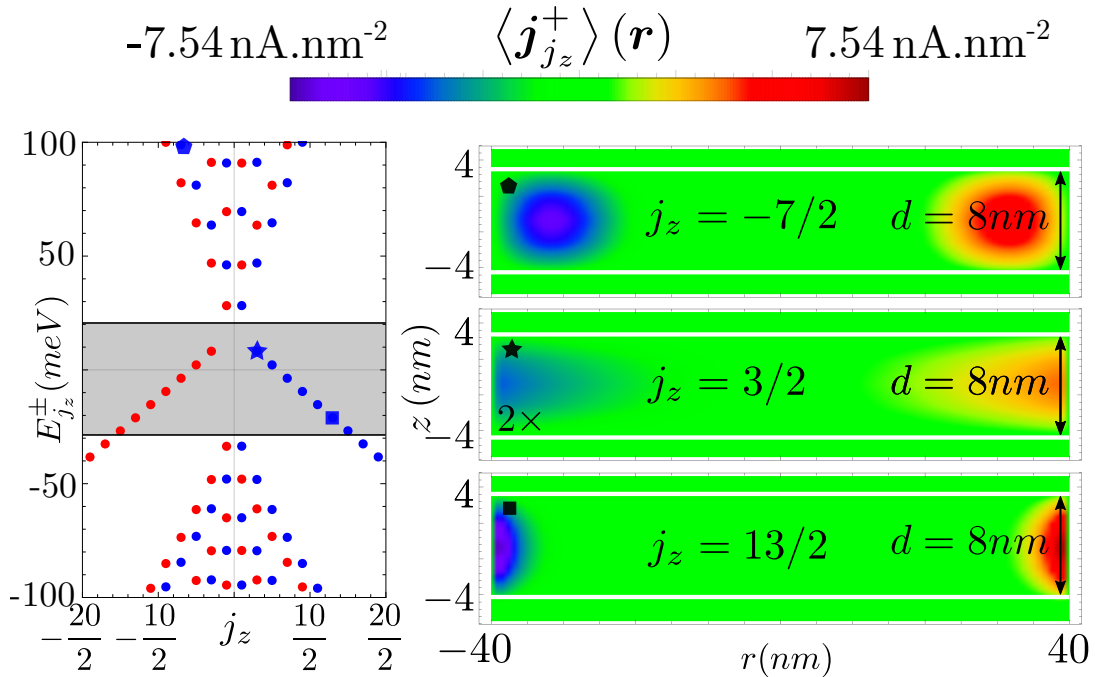


Figure 22 – QD energy levels as functions of j_z for a topological QD with $R = 40$ nm and b) the spin up circulating current Eq. (4.51) for the three levels represented by the pentagon ($j_z = -7/2$), star ($j_z = 3/2$) and square ($j_z = 13/2$). The horizontal lines here represent the soft-wall QW barriers.

Source: By the author

agreement with Ref. 69, refers to the fact that the larger R , the closer our QD approach the bulk material limit, thus leading to a larger Bloch current contribution. On the other hand, the ratio dependence on $\frac{1}{j_z}$ refers to the fact that the larger the angular momentum j_z is, the larger the envelope function angular momentum is, thus yielding a large envelope function contribution

In order to distinguish more precisely the two contributions, we plot in Fig. 23 the envelope function contribution of the total circulating currents, Eq. (4.53), for the pentagon ($j_z = -7/2$), star ($j_z = 3/2$) and square ($j_z = 13/2$) states in Fig. 22. The magnitude of the color bar here is set as the same as the one in Fig. 22. Therefore, in all the plots of Fig. 22 we have multiplied the density plots by a factor of 15 to make easier a comparison with the total circulating currents.

We see in Fig. 23 that the envelope circulating current associated to the pentagon symbol ($j_z = -7/2$) is the only one with opposite angular propagation direction as compared to the total circulating currents in Fig. 22. This is understood through Eq. (4.53) which yields a negative sign for $j_z < 3/2$. As for the current of the star state $j_z = 3/2$, we interestingly find a negligible current contribution which cannot be visualized using the $15\times$ amplification. This fact arises from 1) the spin-up star $j_z = 3/2$ state is almost

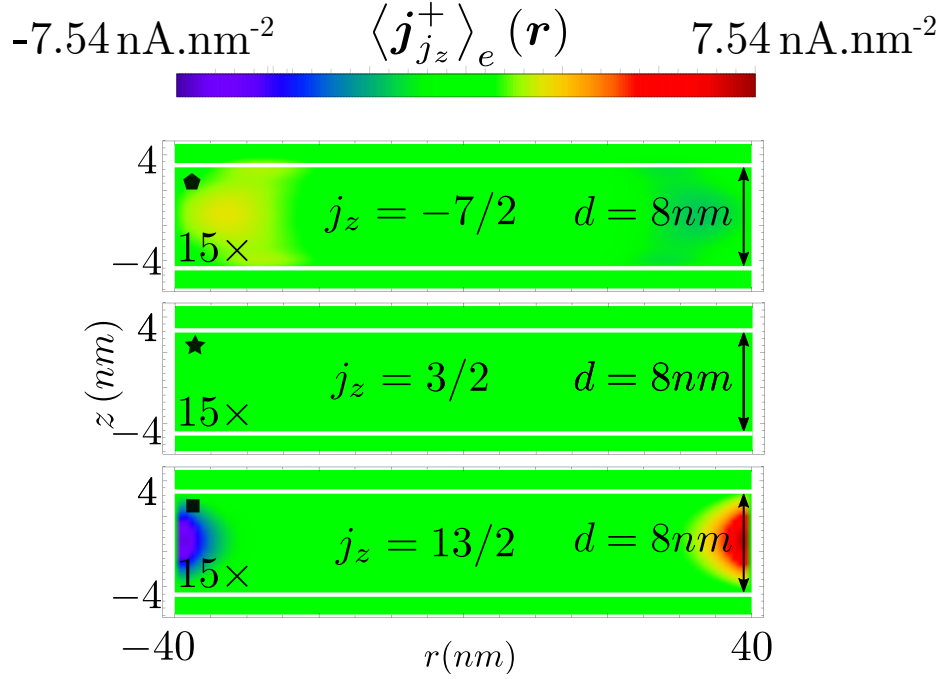


Figure 23 – Spin-up envelope circulating current Eq. (4.53) for the three levels represented by the pentagon ($j_z = -7/2$), star ($j_z = 3/2$) and square ($j_z = 13/2$) in Figure 22. Here the circulating currents were plotted with an amplification of 15 times.

Source: By the author

purely HH_1+ states, so that the $I_{HH_1}^{0,n}(r)$ - HH_1+ wave function component is larger than $I_{E_1}^{1,n}(r)$ - E_1+ wave function component and 2) the star $j_z = 3/2$ spin up state has no circulating current envelope contribution from the HH_1+ subspace. Applying these two facts in Eq. (4.53) we thus understand the negligible envelope circulating current. The $j_z = 13/2$ state represented by the square symbol is the one that shows the largest envelope circulating current contribution, which is attributed to its higher envelope angular momentum.

5.2.2 Topologically trivial $\text{InAs}_{0.85}\text{Bi}_{0.15}$ QD

In Figure 24 we plot the QD energy levels for the trivial QD with $R = 40$ nm together with their respective spin up circulating currents for the levels represented by the pentagon ($j_z = -3/2$), star ($j_z = 3/2$) and square ($j_z = 9/2$). Here we find similar results as compared to the ones of the non-trivial regime, i.e., 1) the bulk state represented by the pentagon shows a current near the edge as a consequence of the centrifugal potential confinement, 2) the star level which has an extended wave function has its circulating current localized near the edge and 3) the square level has the highest circulating current density as a consequence of its highest total angular momentum. Most importantly, we

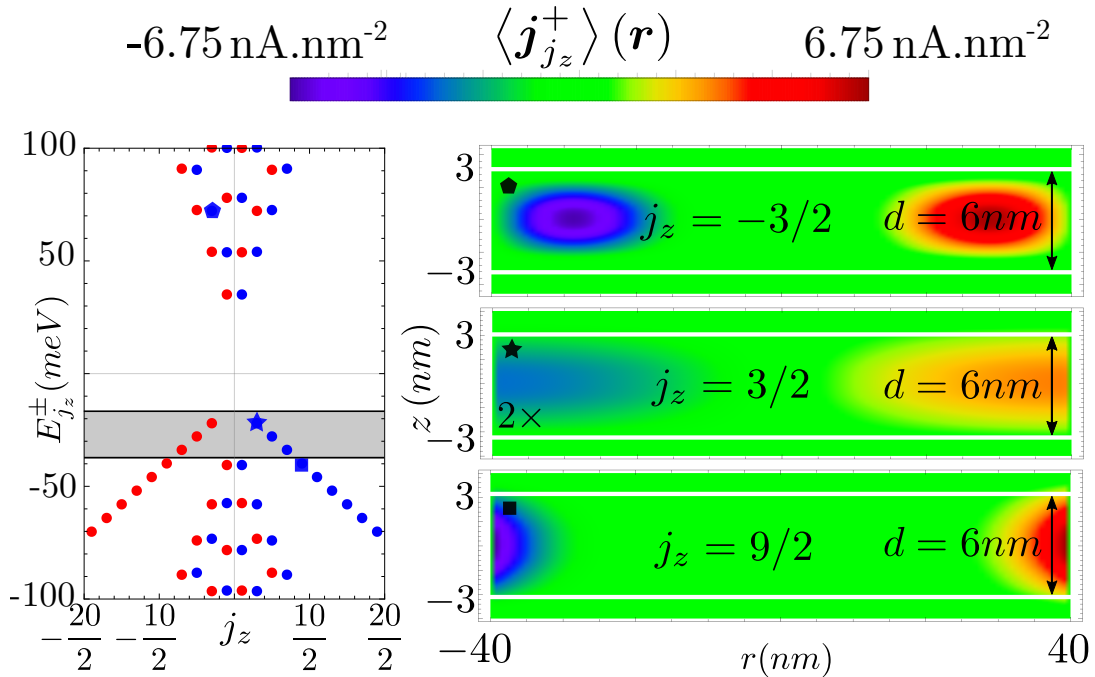


Figure 24 – Same as Fig. 22 for the trivial QD with $R = 40 \text{ nm}$ with the spin up circulating current for the pentagon ($j_z = -3/2$), star ($j_z = 3/2$) and square ($j_z = 9/2$) levels.

Source: By the author

conclude that although the highest $j_z = 3/2$ valence state within the gray areas of Figs 19 and 24 are not edge states as their wave functions are extended through the whole QD, their circulating currents are localized near the edge. Therefore, we can also call the $j_z = 3/2$ state as a protected helical edge state.

The envelope contribution of the total circulating currents, Eq. (4.53), is plotted in Fig. 25 with an amplification factor of 20 in order to scale with Fig. 24. Here, the results are also very similar to the topological QD case. The pentagon state ($j_z = -3/2$) has a circulating current propagating in opposite direction as compared to the total circulating current, which stems from the negative total angular momentum. The negligible envelope contribution of the star state ($j_z = 3/2$) arises from a valence state with zero angular momentum. Finally, the square state ($j_z = 9/2$) has the larger envelope circulating current contribution due to its higher envelope angular momentum.

To compare the circulating currents of the topologically non-trivial helical edge states within the gray area of Fig. 14 with the topologically trivial helical edge states within the gray area of Fig. 19, we plot in Fig. 26 both circulating currents for $R = 40 \text{ nm}$ with $j_z = 3/2$ and $j_z = 5/2$. The highest current density is achieved in the trivial case because of its smaller QW thickness d . Despite this fact we note that both topologically non-trivial and trivial circulating currents for the same QD radius R and j_z are essentially the same.

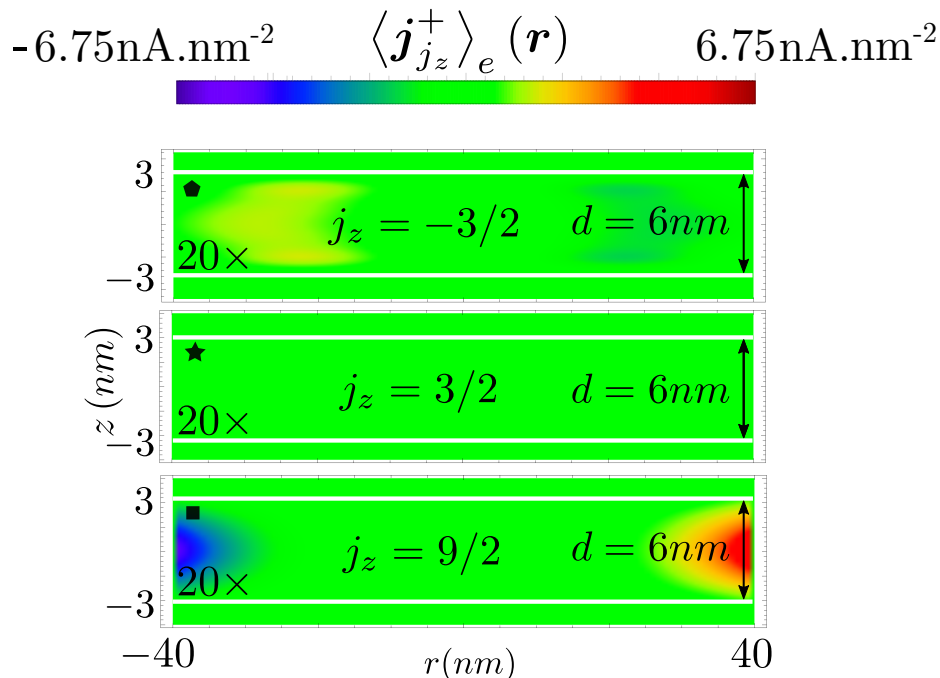


Figure 25 – Spin-up envelope circulating current Eq. (4.53) for the three levels represented by the pentagon ($j_z = -3/2$), star ($j_z = 3/2$) and square ($j_z = 9/2$) in Figure 22. Here the circulating currents were plotted with an amplification of 20 times.

Source: By the author

We have also calculated the integrated current density over half of the cross section of the QD, $I_{j_z, n}^\pm = \int d\mathbf{S} \cdot \langle \mathbf{j}_{j_z, n}^\pm \rangle = \int_0^R dr \int_{-\frac{d}{2}}^{\frac{d}{2}} dz |\langle \mathbf{j}_{j_z, n}^\pm \rangle| \sim 0.17 \mu\text{A}$ for both topologically non-trivial and trivial edge states with a difference of only 2% between them, thus showing no significant difference either. Therefore, we conclude that from the point of view of the circulating currents there are no substantial differences between the topologically non-trivial and trivial protected helical edge states.

5.3 HgTe/CdTe QD

In Figure 27, we make a plot similar to that in Fig. 19 for the trivial HgTe/CdTe QD, for which we have used the BHZ parameters from Ref. 73. As we can see, the feature found here, i.e., the appearance of protected trivial helical edge states, is not a particular result related to our InAs_{0.85}Bi_{0.15} QD. Instead, it also can be found in other systems such as HgTe/CdTe QDs. On the other hand, there are still some differences when Figure 27 is compared with Figure 19. For instance, we see that here the number of the protected trivial helical edge states is decreased by one. We find that the number of the protected trivial helical edge states strongly depends on the BHZ parameters. More specifically, the smaller the difference $|D| - |B|$ with $D < 0$ ($D > 0$) is, the larger the number of protected

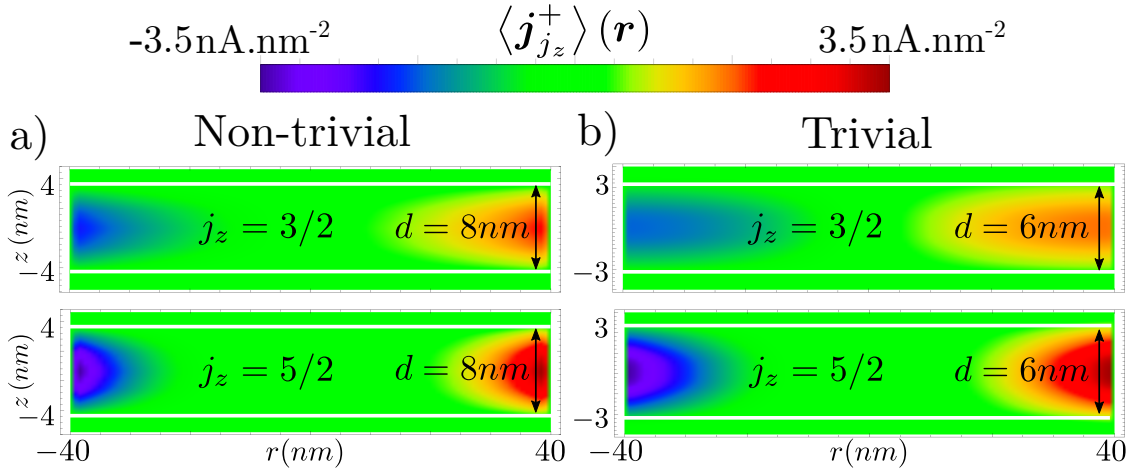


Figure 26 – Spin up circulating currents for the topologically non-trivial QD with $R = 40$ nm for a) $j_z = 3/2$ and b) $j_z = 5/2$. Same as a) and b) for the topologically trivial QD with $R = 40$ nm for c) $j_z = 3/2$ and d) $j_z = 5/2$. The horizontal lines here represent the soft-wall QW barriers.

Source: By the author

helical edge states in the valence (conduction) subspace is.

5.4 Stability of the protected trivial helical edge states under the soft wall confinement

In this section we study the stability of the protected trivial helical edge states under the replacement of the hard wall confinement by the realistic soft wall confinement. As we will see in the following, the inclusion of the soft wall confinement only changes the number of protected helical edge states within the gray area of Fig. 19, thus preserving the main feature of our work.

5.4.1 Soft-wall confinement

Here, using the soft wall confinement we analyze the QD energy levels (given by Eq. 4.40) for both topologically trivial and non-trivial $\text{InAs}_{0.85}\text{Bi}_{0.15}$ QDs and compare them to the ones arising from the hard wall confinement Eq. 4.39. The soft wall barriers can represent QDs defined electrostatically using gates on the QWs^{124–126} or even QDs fully defined by the heterostructure confinement.^{124–126}

In Figure 28 we plot the energy levels using $M_0 = 2$ eV and $M_0 = 15$ eV for the topologically non-trivial $\text{InAs}_{0.85}\text{Bi}_{0.15}$ QD with $R = 60$ nm. The solid blue and red colors represent the hard wall case while the faded colors represent the soft wall case. We see that the energy levels corresponding to the edge states are more sensible to the soft wall confinement than the bulk-like states. Also, while the soft wall energy shift of the edge

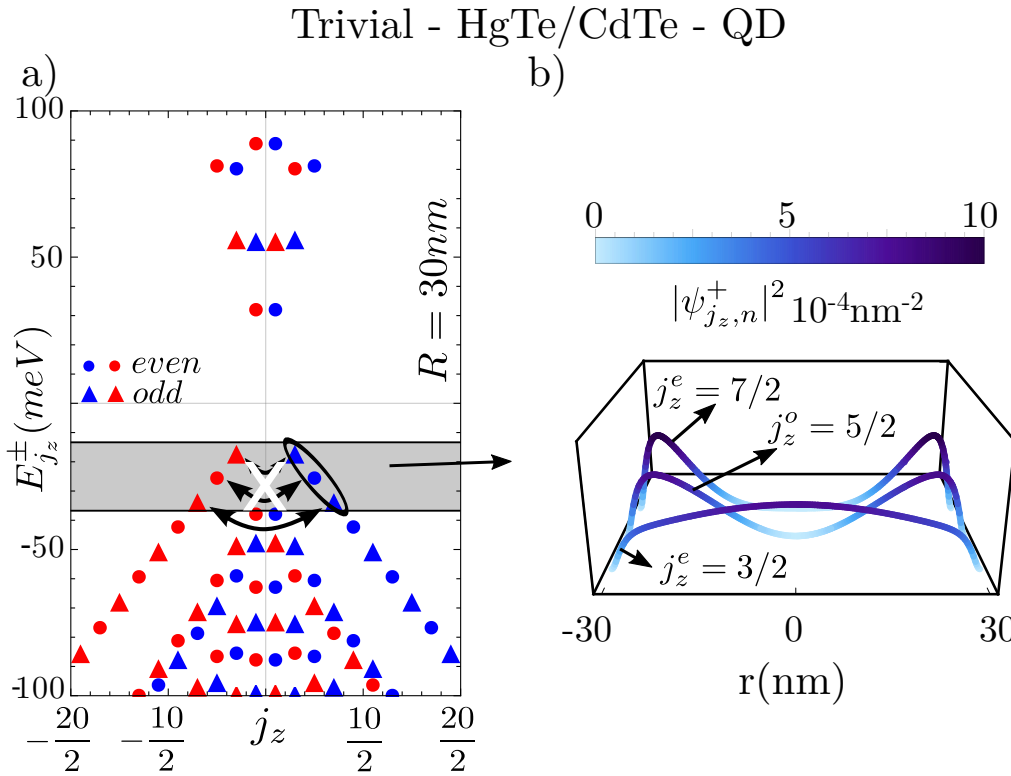


Figure 27 – a) Topologically trivial HgTe/CdTe QD energy levels for $R = 30$ nm. b) $|\psi_{j_z, n}^+(r, \theta)|^2$ of the edge states grouped by the ellipse.

Source: By the author

states is proportional to j_z , for the bulk states we do not find a significant dependence. This fact can be understood by the following argument. When we go from the hard wall to the soft wall confinement, the states start to have a non-null wave function contribution in the soft wall barrier region. Since the wave function of the edge states are more localized near the interface as compared to the bulk states, their wave function contribution arising in the soft wall barrier region will be larger. Thus, using perturbation theory we obtain for the edge states a larger energy correction, and hence a larger shift in the energy levels. As for the dependence on j_z we just need to recall that the larger j_z is the more localized the wave function is.

In Figure 29 we plot the energy levels for the topologically trivial $\text{InAs}_{0.85}\text{Bi}_{0.15}$ QD with $R = 30$ nm using $M_0 = 2$ eV and $M_0 = 15$ eV. As we can see, the presence of the protected trivial helical edge states is not changed by the soft wall potential, showing thus that our results do not depend specifically on the fictitious hard wall confinement. By comparing now Figure 29 with Figure 28 we see that both bulk-like and edge-like states behave similar in the presence of the soft wall confinement (shifts in energy proportional to j_z), showing one more time the equivalence between the topologically trivial and non-trivial

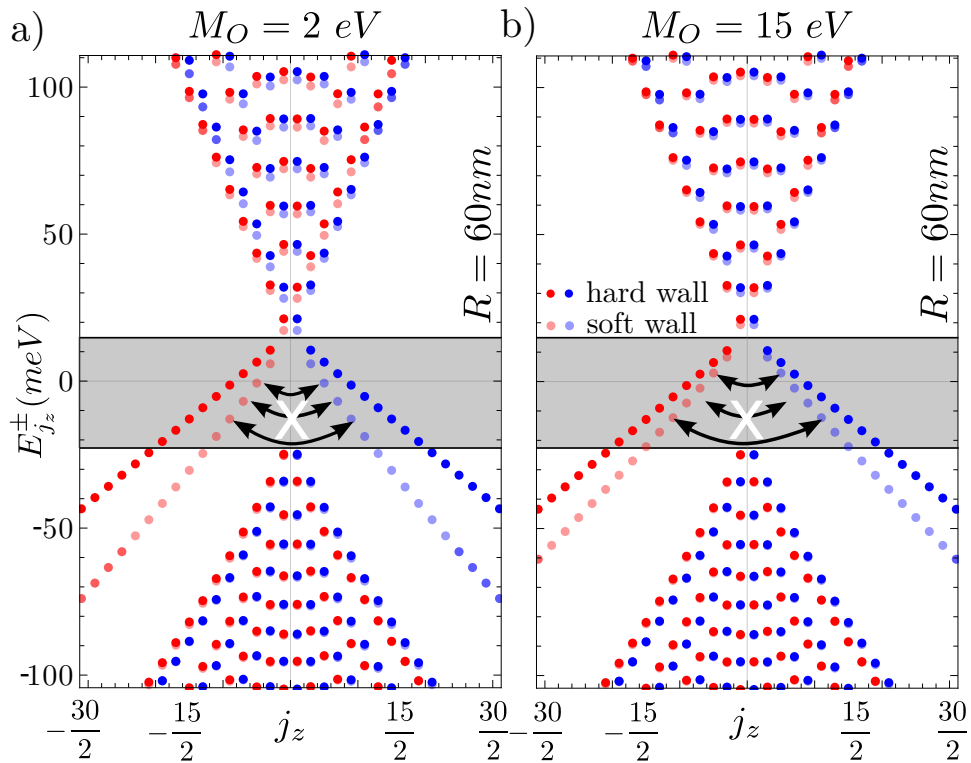


Figure 28 – a) Topologically non-trivial $\text{InAs}_{0.85}\text{Bi}_{0.15}$ QD energy levels as functions of j_z for the soft ($M_O = 2$ eV) and hard wall case ($M_O \rightarrow \infty$) for $R = 60$ nm. b) Same as a) for the soft wall $M_O = 15$ eV case. The faded (solid) colors represent the soft wall (hard wall) case. The black arrows denote the transitions between the spin down and up states of the BHZ blocks, red and blue symbols, respectively.

Source: By the author

protected helical edge states. Moreover, we see that it is possible to fully control the number of trivial helical edge states within the gray area by tuning M_0 through the soft barrier modulated by tunable gates.

In the next chapter we will perform two-terminal QD conductance calculation in both topological regimes using edge states as the conducting energy levels. The idea is to see whether there are differences in the conductance between the topologically trivial and non-trivial edge states, in order to possibly distinguish them from the point of view of transport calculation.

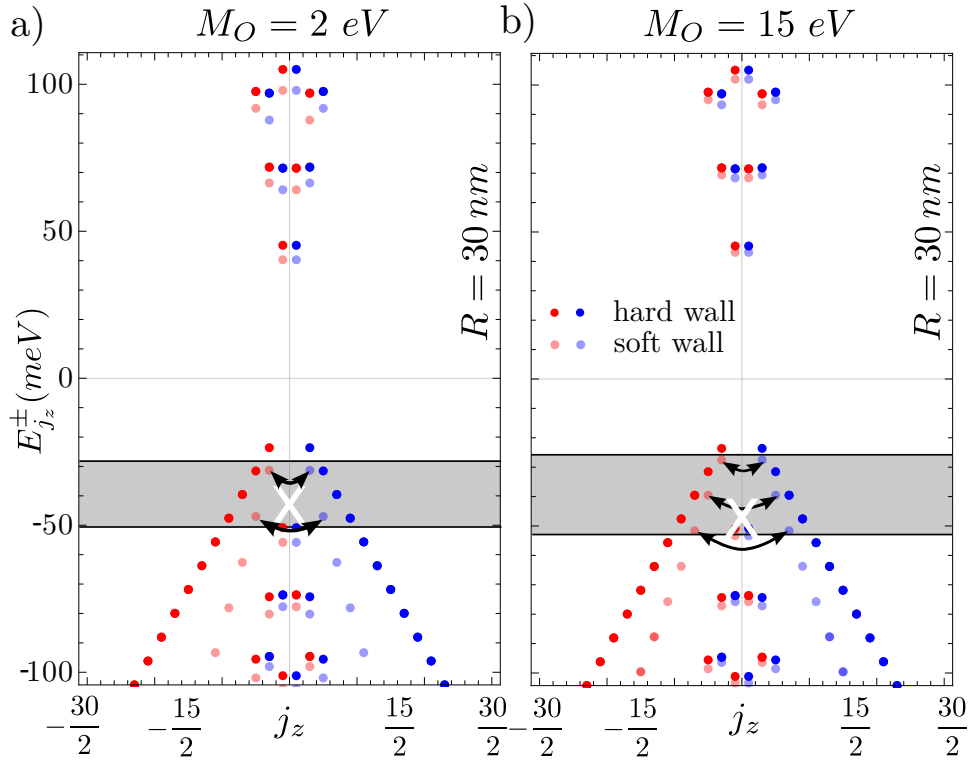


Figure 29 – a) Topologically trivial InAs_{0.85}Bi_{0.15} QD energy levels as functions of j_z for the soft ($M_O = 2$ eV) and hard wall case ($M_O \rightarrow \infty$) for $R = 60$ nm. b) Same as a) for the soft wall $M_O = 15$ eV case. The faded (solid) colors represent the soft wall (hard wall) case. The arrows denote the forbidden transitions between the spin down and up states of the BHZ blocks, red and blue symbols, respectively.

Source: By the author

6 CONDUCTANCE CALCULATION

In this chapter, we couple our non-interacting QDs to left and right leads and calculate the conductance \mathcal{G} using the Green function formalism within linear response at $T = 0$ K.^{110,111,127–129} The idea here is to check if it is possible through our conductance calculation to make experimental predictions for \mathcal{G} via which one can distinguish the geometrically protected trivial helical edge states from the topological non-trivial ones. As we find in this chapter, the calculation of \mathcal{G} involving only the protected edge states (trivial and non-trivial) shows equivalent two-peak resonance profiles as a function of the QD radius and the gate V_g controlling the QD energy levels with respect to the Fermi level of the leads. This implies that conductance measurements should not be able to distinguish trivial and non-trivial BHZ QDs.

6.1 QD Hamiltonian and its Green function

In this section we derive the Green functions for our non-interacting BHZ QD coupled to left (L) and right (R) leads.^{110,111,127–129} We consider a BHZ QD (either trivial or non-trivial) with only four levels given by two Kramers pairs tunned within the conduction window by external gates. We denote them by $|1\rangle = |n, j_z, +\rangle$, $|2\rangle = |n, -j_z, -\rangle$, $|3\rangle = |n', j'_z, +\rangle$ and $|4\rangle = |n', -j'_z, -\rangle$ [obtained from Eq. (4.38)] with $\varepsilon_1 = \varepsilon_2$, $\varepsilon_3 = \varepsilon_4$ and $\varepsilon_i = \varepsilon_i(R, V_g)$ [obtained from Eq. (4.39)], with R the QD radius and V_g an additional gate controlling the dot levels with respect to the Fermi energy ε_F of the leads. For this QD, the most general Hamiltonian reads

$$H = \sum_i \varepsilon_i d_i^\dagger d_i + \sum_{\mathbf{k}_\alpha, \alpha, \sigma} \varepsilon_{\mathbf{k}_\alpha \sigma} c_{\mathbf{k}_\alpha \sigma}^\dagger c_{\mathbf{k}_\alpha \sigma} + \sum_{i, \mathbf{k}_\alpha, \alpha, \sigma} V_{\mathbf{k}_\alpha \sigma}^i d_i^\dagger c_{\mathbf{k}_\alpha \sigma} + \sum_{i \neq j} t_{ij} d_j^\dagger d_i + h.c., \quad (6.1)$$

where d_i^\dagger creates an electron in the QD state $|i\rangle$ with energy $\varepsilon_i = \varepsilon_i(R, V_g)$, and the dependence of the QD energy levels on the gate V_g is assumed as $\varepsilon_i(R, V_g) = \varepsilon_i(R) - eV_g$. Additionally, i denotes the set of QD quantum numbers n , j_z , and \pm (or \uparrow, \downarrow *), and $c_{\mathbf{k}_\alpha \sigma}^\dagger$ creates an electron in the lead $\alpha = L, R$ with wave-vector \mathbf{k}_α , energy $\varepsilon_{\mathbf{k}_\alpha \sigma}$ and spin component $\sigma = \uparrow, \downarrow$. $V_{\mathbf{k}_\alpha \sigma}^i$ denotes the dot-lead coupling and t_{ij} denotes the coupling of the dot levels. Since we are assuming QDs invariant by TRS, TRS prevents the elastic scattering between the two states composing a Kramers pairs, so that we have $t_{12} = t_{34} = 0$.

* Due to the mixing between spin up \uparrow and spin down \downarrow components within the $|E_1 \pm\rangle$ subbands, the spin index \uparrow (\downarrow) is not a good quantum number within the BHZ subspace $+$ ($-$). However, we calculate $\langle j_z \pm | s_z | j_z \pm \rangle \simeq \pm \frac{\hbar}{2}$; hence it is an excellent approximation to identify the \pm subspace with \uparrow, \downarrow [See Sec. 2.3]

Although we have numerically calculated the Green functions for the complete Hamiltonian in (6.1), here we will only derive them in the absence of spin-flip processes as it is simpler analytically. We emphasize, however, that the inclusion of spin-flip processes does not yield fundamental differences in the results as these terms are small.³⁸ Therefore, we take $t_{14} = t_{23} = V_{\mathbf{k}_\alpha\uparrow}^{2(4)} = V_{\mathbf{k}_\alpha\downarrow}^{1(3)} = 0$, and the general Hamiltonian in (6.1) assumes the following spin block diagonal form with the spin up Hamiltonian H_\uparrow schematically represented in Fig. 30.

$$\begin{aligned}
 H = & \overbrace{\varepsilon_1 d_1^\dagger d_1 + \varepsilon_3 d_3^\dagger d_3 + \sum_{\mathbf{k}_\alpha\uparrow,\alpha} \varepsilon_{\mathbf{k}_\alpha\uparrow} c_{\mathbf{k}_\alpha\uparrow}^\dagger c_{\mathbf{k}_\alpha\uparrow} + \sum_{\mathbf{k}_\alpha\uparrow,\alpha} \left(V_{\mathbf{k}_\alpha\uparrow}^1 d_1^\dagger c_{\mathbf{k}_\alpha\uparrow} + V_{\mathbf{k}_\alpha\uparrow}^3 d_3^\dagger c_{\mathbf{k}_\alpha\uparrow} \right)}^{=H_\uparrow} + t_{13} d_1^\dagger d_3 + h.c. \\
 & + \overbrace{\varepsilon_2 d_2^\dagger d_2 + \varepsilon_4 d_4^\dagger d_4 + \sum_{\mathbf{k}_\alpha\downarrow,\alpha} \varepsilon_{\mathbf{k}_\alpha\downarrow} c_{\mathbf{k}_\alpha\downarrow}^\dagger c_{\mathbf{k}_\alpha\downarrow} + \sum_{\mathbf{k}_\alpha\downarrow,\alpha} \left(V_{\mathbf{k}_\alpha\downarrow}^2 d_2^\dagger c_{\mathbf{k}_\alpha\downarrow} + V_{\mathbf{k}_\alpha\downarrow}^4 d_4^\dagger c_{\mathbf{k}_\alpha\downarrow} \right)}^{=H_\downarrow} + t_{24} d_2^\dagger d_4 + h.c.,
 \end{aligned} \tag{6.2}$$

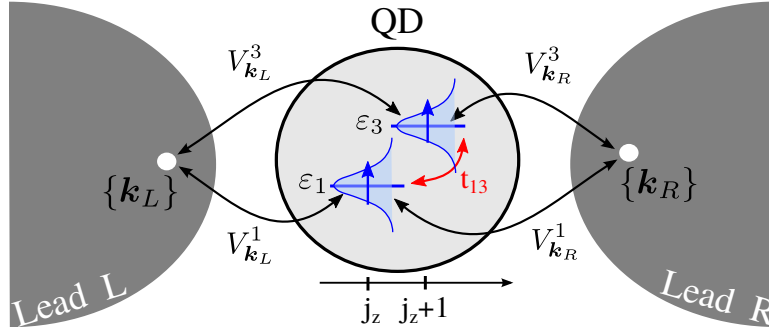


Figure 30 – Schematic figure for the spin up Hamiltonian with levels $\varepsilon_1, \varepsilon_3$ coupled to each other through t_{13} and coupled to left and right leads through $V_{\mathbf{k}_L}^{1,3}$ and $V_{\mathbf{k}_R}^{1,3}$.

Source: By the author

We solve our Hamiltonian H_\uparrow using the Green functions approach^{102–105} discussed in Chapter 3. Introducing the retarded spin up Green function $G_{nn'}(t)$ and its respective Fourier transform $G_{nn'}(E)$,

$$G_{nn'}(t) \equiv \langle\langle d_n, d_{n'}^\dagger \rangle\rangle = \frac{1}{i\hbar} \theta(t) \langle\{d_n(t), d_{n'}^\dagger(0)\}\rangle, \tag{6.3}$$

$$G_{nn'}^r(E) \equiv \langle\langle d_n, d_{n'}^\dagger \rangle\rangle = \int_{-\infty}^{\infty} dt G_{n,n'}(t) e^{i(\frac{E}{\hbar} + i0^+)t}, \tag{6.4}$$

where $n, n' = 1, 3$, we obtain the following equations of motion for the retarded spin up Green functions

$$\begin{pmatrix} E - \varepsilon_1 + i\eta - \sum_\alpha^{11} & 0 & 0 & -\sum_\alpha^{13} - t_{13}^* \\ 0 & E - \varepsilon_3 + i\eta - \sum_\alpha^{33} & -\sum_\alpha^{31} - t_{13} & 0 \\ 0 & -\sum_\alpha^{13} - t_{13}^* & E - \varepsilon_1 + i\eta - \sum_\alpha^{11} & 0 \\ -\sum_\alpha^{31} - t_{13} & 0 & 0 & E - \varepsilon_3 + i\eta - \sum_\alpha^{33} \end{pmatrix} = \begin{pmatrix} 1 \\ 1 \\ 0 \\ 0 \end{pmatrix} \times \left(G_{11}^r(E) \quad G_{33}^r(E) \quad G_{13}^r(E) \quad G_{31}^r(E) \right)^T \quad (6.5)$$

with $\sum_\alpha^{ab} = \sum_{\mathbf{k}_{\alpha}, \alpha} \frac{V_{\mathbf{k}_{\alpha}\uparrow}^a V_{\mathbf{k}_{\alpha}\uparrow}^{b*}}{E - \varepsilon_{\mathbf{k}_{\alpha}\uparrow} + i\eta}$, $\alpha = L, R$ and $a, b = 1, 3$. The solution of the above linear system Eq. (6.5) is given by

$$G_{11}^r(E) = \frac{1}{E - \varepsilon_1 - \sum_\alpha^{11} - \frac{(\sum_\alpha^{13} + t_{13}^*)(\sum_\alpha^{31} + t_{13})}{E - \varepsilon_3 - \sum_\alpha^{33} + i\eta} + i\eta}, \quad (6.6)$$

$$G_{33}^r(E) = \frac{1}{E - \varepsilon_3 - \sum_\alpha^{33} - \frac{(\sum_\alpha^{13} + t_{13}^*)(\sum_\alpha^{31} + t_{13})}{E - \varepsilon_1 - \sum_\alpha^{11} + i\eta} + i\eta}, \quad (6.7)$$

$$G_{13}^r(E) = \frac{\sum_\alpha^{13} + t_{13}^*}{(E - \varepsilon_1 - \sum_\alpha^{11} + i\eta)(E - \varepsilon_3 - \sum_\alpha^{33} + i\eta) - (\sum_\alpha^{13} + t_{13}^*)(\sum_\alpha^{31} + t_{13})}, \quad (6.8)$$

$$G_{31}^r(E) = \frac{\sum_\alpha^{31} + t_{13}}{(E - \varepsilon_1 - \sum_\alpha^{11} + i\eta)(E - \varepsilon_3 - \sum_\alpha^{33} + i\eta) - (\sum_\alpha^{13} + t_{13}^*)(\sum_\alpha^{31} + t_{13})}. \quad (6.9)$$

The importance of calculating the retarded Green functions Eqs. (6.6)–(6.9), is because they are connected to physical quantities such as the eigenenergies of our problem,^{102–105} the local density of states (LDOS),^{102–105} and the conductance.^{102–105, 110, 111, 127–129} In the following section we obtain explicitly these physical quantities. Due to TRS, the Green functions for the spin down Hamiltonian H_\downarrow are given by $G_{22}^r(E) = G_{11}^r(E)$, $G_{44}^r(E) = G_{33}^r(E)$, $G_{24}^r(E) = G_{13}^r(E)$ and $G_{42}^r(E) = G_{31}^r(E)$ since $t_{13} = t_{24}$, $\varepsilon_1 = \varepsilon_2$, $\varepsilon_3 = \varepsilon_4$, $\sum_\alpha^{11} = \sum_\alpha^{22}$, $\sum_\alpha^{13} = \sum_\alpha^{24}$ and $\sum_\alpha^{33} = \sum_\alpha^{44}$.

6.2 Conductance

From the Green functions obtained above (6.6)–(6.9), we calculate the conductance using the result obtained by Meir-Wingreen^{103, 110, 111} assuming: 1) equal left and right density of states in the leads ($\rho_L = \rho_R$) and 2) equal spin-conserving couplings of the QD to left and right leads ($V_{\mathbf{k}_L\uparrow}^a = V_{\mathbf{k}_R\uparrow}^a$) yielding $\Gamma^L = \Gamma^R$. In the absence of spin-flip process, we determine the conductance formula just for one particular spin, and then multiply

the result by a factor of two to take into account both spins. Within the Meir-Wingreen approach, the spin up current in the equilibrium regime reads^{103,110,111}

$$J_{\uparrow} = -\frac{e}{h} \int dE [f_L(E) - f_R(E)] \text{Im} \left[\text{tr} \left\{ \mathbf{\Gamma}^{L(R)}(E) \mathbf{G}^r(E) \right\} \right], \quad (6.10)$$

where $e < 0$ is the electron charge, h is the Planck constant, $f_{L(R)}(E)$ is the Fermi-Dirac distribution of left (right) lead defined here as

$$f_L(E) = \frac{1}{\left(1 + e^{\frac{E - \mu_L}{k_B T}}\right)}, \quad f_R(E) = \frac{1}{\left(1 + e^{\frac{E - \mu_R}{k_B T}}\right)}, \quad (6.11)$$

where k_B is the Boltzmann constant, T is the temperature and $\mu_{L(R)}$ is the chemical potential of the left (right) lead. As for $\mathbf{\Gamma}^{L(R)}(E)$ and $\mathbf{G}^r(E)$, we have $\left(\mathbf{\Gamma}^{L(R)}\right)_{ab}(E) = \Gamma_{ab}^{L(R)}(E) = 2\pi\rho_{L(R)}(E) V_{\mathbf{k}_{L(R)\uparrow}^a} V_{\mathbf{k}_{L(R)\uparrow}^{b*}}$ and $\left(\mathbf{G}^r\right)_{ab}(E) = G_{ab}^r(E)$, or explicitly,

$$\mathbf{\Gamma}^L(E) = 2\pi\rho_L(E) \begin{pmatrix} V_{\mathbf{k}_{L\uparrow}^1} V_{\mathbf{k}_{L\uparrow}^{1*}} & V_{\mathbf{k}_{L\uparrow}^1} V_{\mathbf{k}_{L\uparrow}^{3*}} \\ V_{\mathbf{k}_{L\uparrow}^3} V_{\mathbf{k}_{L\uparrow}^{1*}} & V_{\mathbf{k}_{L\uparrow}^3} V_{\mathbf{k}_{L\uparrow}^{3*}} \end{pmatrix}, \quad \mathbf{G}^r(E) = \begin{pmatrix} G_{11}^r(E) & G_{13}^r(E) \\ G_{31}^r(E) & G_{33}^r(E) \end{pmatrix}. \quad (6.12)$$

Within linear response, i.e., $\mu_L - \mu_R = -eV$ with $eV \ll \mu_{L,R}$, we write

$$f_L(E) - f_R(E) \approx (\mu_L - \mu_R) \left(-\frac{\partial f_0}{\partial E} \right) = (-eV) \left(-\frac{\partial f_0}{\partial E} \right), \quad (6.13)$$

with the equilibrium Fermi function $f_0(E) = 1/(e^{\frac{E - \varepsilon_F}{k_B T}} + 1)$, in which we have taken the chemical potential at $T = 0$ K, i.e., the Fermi energy $\lim_{T \rightarrow 0} \mu = \varepsilon_F$. Therefore, within linear response we have our conductance (6.10) given by

$$\mathcal{G}_{\uparrow} = \left. \frac{dJ_{\uparrow}}{dV} \right|_{V=0} = \frac{e^2}{h} \int dE \text{Im} \left[\text{tr} \left\{ \mathbf{\Gamma}^{L(R)}(E) \mathbf{G}^r(E) \right\} \right] \left(-\frac{\partial f_0}{\partial E} \right), \quad (6.14)$$

which at $T = 0$ K reads

$$\mathcal{G}_{\uparrow} = \frac{e^2}{h} \text{Im} \left[\text{tr} \left\{ \mathbf{\Gamma}^{L(R)}(\varepsilon_F) \mathbf{G}^r(\varepsilon_F) \right\} \right]. \quad (6.15)$$

Hence, the total (spin \uparrow and \downarrow) conductance follows

$$\mathcal{G} = \mathcal{G}_{\uparrow} + \mathcal{G}_{\downarrow} = 2\mathcal{G}_{\uparrow}. \quad (6.16)$$

Now we assume the wide-band limit^{103,110,111} in the leads, i.e., our leads have a constant and uniform 2D density of states with an energy range $\Delta\varepsilon_L$ centered at 0, much larger than the characteristic energies of our quantum dot, i.e., ($\Delta\varepsilon_L \gg E$),

$$\rho_\alpha(E) = \frac{1}{\Delta\varepsilon_L} \Theta\left(\frac{\Delta\varepsilon_L}{2} - E\right) \Theta\left(\frac{\Delta\varepsilon_L}{2} + E\right). \quad (6.17)$$

For practical reasons, we will also assume a k -independent tunneling potential $V_{\mathbf{k}_\alpha}^i = V_\alpha^i$, yielding for \sum_α^{ab} in Eqs. (6.6)-(6.9)

$$\sum_\alpha^{ab} = \sum_{\mathbf{k}_\alpha, \alpha} \frac{V_{\mathbf{k}_\alpha}^a V_{\mathbf{k}_\alpha}^{b*}}{E - \varepsilon_{\mathbf{k}_\alpha} + i\eta} = \sum_\alpha V_\alpha^a V_\alpha^{b*} \sum_{\mathbf{k}_\alpha} \frac{1}{E - \varepsilon_{\mathbf{k}_\alpha} + i\eta}. \quad (6.18)$$

By performing the change $\sum_{\mathbf{k}_\alpha} \rightarrow \frac{L^2}{(2\pi)^2} \int d\mathbf{k}_\alpha$, together with

$$\frac{L^2}{(2\pi)^2} \int d\mathbf{k}_\alpha = \int d\varepsilon_{\mathbf{k}_\alpha} \rho_\alpha(\varepsilon_{\mathbf{k}_\alpha}), \quad (6.19)$$

we obtain

$$\begin{aligned} \sum_\alpha^{ab} &= \sum_\alpha V_\alpha^a V_\alpha^{b*} \int_{-\infty}^{\infty} d\varepsilon_k \frac{\rho_\alpha(\varepsilon_k)}{E - \varepsilon_k + i\eta}, \\ &= \frac{\sum_\alpha V_\alpha^a V_\alpha^{b*}}{\Delta\varepsilon_L} \lim_{\eta \rightarrow 0^+} \left[\int_{-\frac{\Delta\varepsilon_L}{2}}^{\frac{\Delta\varepsilon_L}{2}} d\varepsilon_k \frac{E - \varepsilon_k}{(E - \varepsilon_k)^2 + \eta^2} - i \int_{-\frac{\Delta\varepsilon_L}{2}}^{\frac{\Delta\varepsilon_L}{2}} d\varepsilon_k \frac{\eta}{(E - \varepsilon_k)^2 + \eta^2} \right], \\ &= \frac{\sum_\alpha V_\alpha^a V_\alpha^{b*}}{\Delta\varepsilon_L} \left[-\ln \left| E - \varepsilon_k \right|_{-\frac{\Delta\varepsilon_L}{2}}^{\frac{\Delta\varepsilon_L}{2}} - i\pi \int_{-\frac{\Delta\varepsilon_L}{2}}^{\frac{\Delta\varepsilon_L}{2}} d\varepsilon_k \delta(E - \varepsilon_k) \right], \\ &= \frac{\sum_\alpha V_\alpha^a V_\alpha^{b*}}{\Delta\varepsilon_L} \left[\ln \left| \frac{E + \frac{\Delta\varepsilon_L}{2}}{E - \frac{\Delta\varepsilon_L}{2}} \right| - i\pi \begin{cases} 1 & \text{if } -\frac{\Delta\varepsilon_L}{2} < E < \frac{\Delta\varepsilon_L}{2} \\ 0 & \text{if } |E| > \frac{\Delta\varepsilon_L}{2} \end{cases} \right], \\ &= \frac{\sum_\alpha V_\alpha^a V_\alpha^{b*}}{\Delta\varepsilon_L} \ln \left| \frac{E + \frac{\Delta\varepsilon_L}{2}}{E - \frac{\Delta\varepsilon_L}{2}} \right| - i\pi \frac{\sum_{j,\alpha} V_\alpha^a V_\alpha^{b*}}{\Delta\varepsilon_L} \Theta\left(\frac{\Delta\varepsilon_L}{2} - E\right) \Theta\left(\frac{\Delta\varepsilon_L}{2} + E\right), \\ &= \frac{\sum_\alpha V_\alpha^a V_\alpha^{b*}}{\Delta\varepsilon_L} \ln \left| \frac{E + \frac{\Delta\varepsilon_L}{2}}{E - \frac{\Delta\varepsilon_L}{2}} \right| - i\pi \sum_\alpha \rho_\alpha(E) V_\alpha^a V_\alpha^{b*}. \end{aligned} \quad (6.20)$$

Applying now the wide-band limit $\Delta\varepsilon_L \gg E$,^{103,110,111} the above term is given by the following fully imaginary value

$$\sum_{\alpha}^{a,b} = \sum_{\mathbf{k}_{\alpha}, \alpha} \frac{V_{\mathbf{k}_{\alpha}}^a V_{\mathbf{k}_{\alpha}}^{b*}}{E - \varepsilon_{\mathbf{k}_{\alpha}} + i\eta} \approx \frac{\sum_{\alpha} V_{\alpha}^a V_{\alpha}^{b*}}{\Delta\varepsilon_L} \ln|-1| - i\pi \sum_{\alpha} V_{\alpha}^a V_{\alpha}^{b*} \rho_{\alpha}(E) = -i\pi \sum_{\alpha} V_{\alpha}^a V_{\alpha}^{b*} \rho_{\alpha}(E), \quad (6.21)$$

which is related to the broadening of the α -lead $\Gamma_{ab}^{\alpha} = 2\pi\rho_{\alpha}V_{\alpha}^aV_{\alpha}^{b*}$ by

$$\sum_{\alpha}^{ab} = -i\Gamma_{ab}^{L(R)}. \quad (6.22)$$

Therefore, using Eq. (6.22) in Eq. (6.16), the total conductance through our QD reads,

$$\mathcal{G} = \frac{2e^2}{h} \frac{[\Gamma_{33}^L(\varepsilon_F - \varepsilon_1) + \Gamma_{11}^L(\varepsilon_F - \varepsilon_3) + 2t_{13}\Gamma_{13}^L]^2}{[(\varepsilon_F - \varepsilon_1)(\varepsilon_F - \varepsilon_3) - t_{13}^2]^2 + [\Gamma_{33}^L(\varepsilon_F - \varepsilon_1) + \Gamma_{11}^L(\varepsilon_F - \varepsilon_3) + 2t_{13}\Gamma_{13}^L]^2}, \quad (6.23)$$

where we recall that $\varepsilon_i = \varepsilon_i(R, V_g) = \varepsilon_i(R) - eV_g$.

6.3 Results

Here we present the results for the conductance \mathcal{G} within the linear regime at $T = 0$ K (6.23) for the $\text{In}_{0.85}\text{As}_{0.15}\text{Bi}$ BHZ QD in both topologically trivial and non-trivial regimes. For the hopping t_{13} and the broadening terms $\Gamma_{11}^{L(R)}$, $\Gamma_{13}^{L(R)}$, and $\Gamma_{33}^{L(R)}$, in the Hamiltonian (6.2), a detailed calculation is needed in literature. However, this is beyond the scope of our present work and will be addressed in a future work.

A back of the envelope estimate for the hopping term t_{ij} in Hamiltonian Eq. (6.2) is given by

$$t_{ij} = \int d\theta dr r \psi_i^{\dagger}(r, \theta) V_{\text{pert}} \psi_j(r, \theta), \quad (6.24)$$

where $\psi_i(r, \theta) = \psi_{j_z, n}(r, \theta)$ from (4.38). By taking a typical value for non-magnetic impurities³⁸ $V_{\text{pert}} \approx 1$ meV, we find $t_{13} \approx 1$ meV. On the other hand, the broadening $\Gamma_{ab}^{L(R)}$ of the QD levels due to the coupling with the leads ranges from tens of μeV to meV.^{124–126} Since there is no data for the level broadening of InAsBi BHZ QD, we assume $\Gamma = \Gamma_{11}^{L(R)} = \Gamma_{33}^{L(R)} = \Gamma_{13}^{L(R)} = 4$ meV in our \mathcal{G} calculation. We emphasize however that smaller Γ 's do not change our findings. Instead, they just make the conductance resonances narrower.

6.3.1 Conductance results for topologically trivial and non-trivial edge states

Here, we will show the conductance \mathcal{G} [Eq. (6.23)] results for both topologically trivial and non-trivial $\text{In}_{0.85}\text{As}_{0.15}\text{Bi}$ QD considering only edge states as the conducting states in Eq. 6.1.

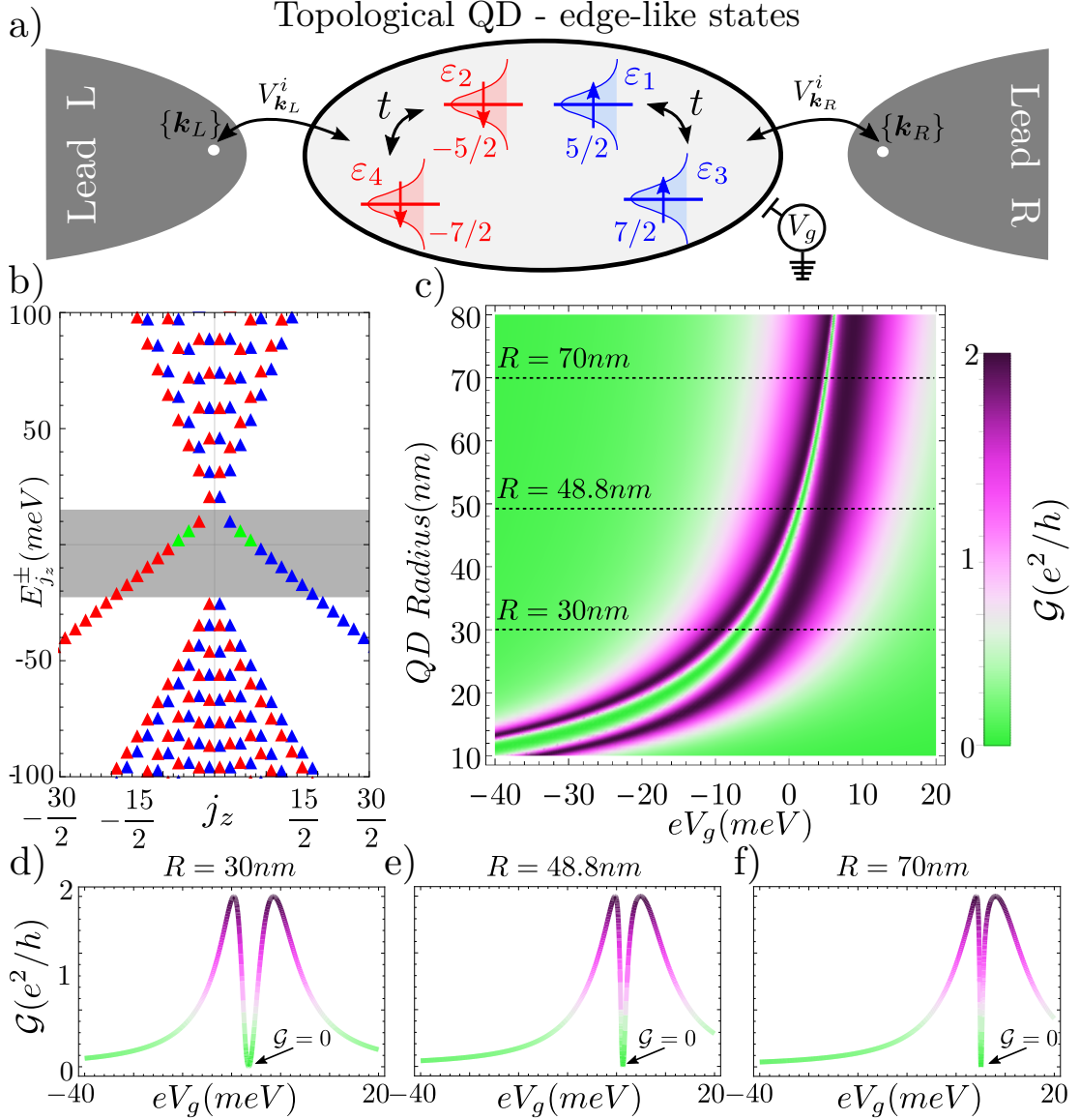


Figure 31 – a) Schematic $\text{In}_{0.85}\text{As}_{0.15}\text{Bi}$ QD Hamiltonian for the four topologically protected edge states $j_z = \pm 5/2$ and $j_z = \pm 7/2$ coupled to left (L) and right (R) leads. b) Topological $\text{In}_{0.85}\text{As}_{0.15}\text{Bi}$ QD energy levels as a function of j_z for $R = 30$ nm [The green triangles represent the $j_z = \pm 5/2$ and $j_z = \pm 7/2$ energy levels considered in the conductance calculation]. c) QD conductance calculation \mathcal{G} at $T = 0$ K for the $j_z = \pm 5/2, \pm 7/2$ as a function of the QD radius R and the gate potential V_g . QD conductance \mathcal{G} at $T = 0$ K for d) $R = 30$ nm, e) $R = 48.8$ nm and f) $R = 70$ nm.

Source: By the author

In Figure 31 we plot the conductance \mathcal{G} [Eq. (6.23)] for the topologically non-trivial

$\text{In}_{0.85}\text{As}_{0.15}\text{Bi}$ QD considering the four levels in Eq. (6.2) as the topological edge states $j_z = \pm 5/2$ and $j_z = \pm 7/2$ within the gap [Fig. 31a)]. These states are represented by the green triangles in Fig. 31b) where we have plotted the QD energy levels for $R = 30$ nm. In Figure 31c) we plot \mathcal{G} as a function of the gate potential V_g and QD radius R varied experimentally through an electrostatic confining potential.¹³⁰ In Figs. 31d), e) and f) we plot \mathcal{G} for three different R 's given by 30 nm, 48.4 nm and 70 nm. For those figures we clearly see a double Lorentzian-like profile with $2e^2/h$ maximum peaks always separated by a dip where the conductance is zero. The two peaks occur approximately at the doubly degenerate ε_1 (ε_3) and ε_2 (ε_4) QD energy levels yielding the $2e^2/h$ conductance peak. As we increase R the energy separation between these two consecutive QD energy levels decreases, thus making the two peaks get closer together. From Eq. (6.23), we see that the $2e^2/h$ maximum peak condition happens exactly when

$$[\varepsilon_F - \varepsilon_1(R, V_g)][\varepsilon_F - \varepsilon_3(R, V_g)] - t_{13}^2 = 0. \quad (6.25)$$

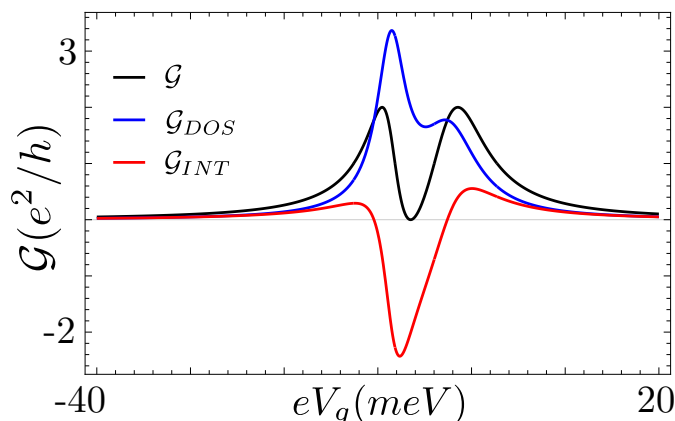


Figure 32 – $\text{In}_{0.85}\text{As}_{0.15}\text{Bi}$ QD conductance calculation \mathcal{G} (black curve), \mathcal{G}_{DOS} (blue curve) and \mathcal{G}_{INT} (red curve) Eq. (6.27) with $R = 30$ nm [Fig. 31d)] as a function of V_g . The blue curve represents the DOS contribution of the total conductance \mathcal{G} (always positive) while the red curve represents the interference contribution.

Source: By the author

This condition represents the situation in which the Fermi energy ε_F corresponds to the poles of Green functions Eqs. (6.6) and (6.7). Therefore, we understand that the \mathcal{G} maximum peak is reached when the Fermi energy is on resonance with the eigenvalues of Hamiltonian (6.2), i.e., the poles of Eqs. (6.6) and (6.7), where the factor of 2 within the $2 \times e^2/h$ maximum peaks represents the two-fold degeneracy of the diagonal QD energy levels.

The dip in the conductance between the two $2e^2/h$ peaks can also be determined analytically and it is achieved by changing both R and V_g in such a way that the numerator of Eq. (6.23) vanishes. This condition happens at

$$\varepsilon_F = \frac{\varepsilon_3(R, V_g)\Gamma_1^L - 2t_{13}\Gamma_{13}^L + \varepsilon_1(R, V_g)\Gamma_3^L}{\Gamma_1^L + \Gamma_3^L}. \quad (6.26)$$

This dip is a consequence of a destructive interference between the spin edge states $|1\rangle$ ($|2\rangle$) and $|3\rangle$ ($|4\rangle$) and can be easily seen by rewriting Eq. (6.23) using the LDOS formula $\rho_i(\varepsilon_F) = -\frac{1}{\pi} \text{Im} \{G_{ii}(\varepsilon_F)\}$, yielding

$$\begin{aligned} \mathcal{G} &= \frac{2e^2}{h} \left\{ \pi\Gamma_1^L \rho_1(\varepsilon_F) + \pi\Gamma_3^L \rho_3(\varepsilon_F) \right\} - \frac{4e^2}{h} \Gamma_{13}^L \text{Im} [G_{13}^r(\varepsilon_F)], \\ &= \mathcal{G}_{DOS} + \mathcal{G}_{INT}. \end{aligned} \quad (6.27)$$

The first term \mathcal{G}_{DOS} in Eq. (6.27) (always positive definite) corresponds to the conductance via the two decoupled QD levels and the second one \mathcal{G}_{INT} represents the interference term^{127–129} as it assumes negative conductance values. In Figure 32, we plot these two components together with the total conductance \mathcal{G} for the topological non-trivial QD with $j_z = \pm 5/2$ and $j_z = \pm 7/2$ [green triangles in Fig. 31b)] for $R = 30$ nm, represented by Fig. 31d). Figure 32 thus shows that while \mathcal{G}_{DOS} gives a positive contribution, \mathcal{G}_{INT} yields a negative one. Additionally, we see in Fig. 32 that \mathcal{G}_{DOS} is not symmetric. This is understood through Eqs. (6.6) and (6.7) where we note that the broadening of the ε_3 energy level is larger than the one of ε_1 as $\varepsilon_3 > \varepsilon_1$. Therefore, as a consequence of the larger broadening of the ε_3 energy level we expect a lower conductance maximum amplitude through it as compared to the maximum conductance amplitude through the ε_1 energy level.

Now we move to the topologically trivial $\text{In}_{0.85}\text{As}_{0.15}\text{Bi}$ QD. In Figure 33 we plot the conductance \mathcal{G} (6.23) for the geometrically protected trivial helical edge states $j_z = \pm 5/2$ and $j_z = \pm 7/2$, represented by the green triangles within the gray area of Fig. 33b). Clearly we find the same features observed in the conductance of the topologically protected helical edge states Fig. 31c), i.e., we observe two $2e^2/h$ maximum conductance peaks evolving as a function of R and V_g separated by a dip. Here the distance between the two peaks also decreases as we increase the QD radius R . The energy peaks and the zero conductance dip are still given respectively by Eqs. (6.25) and (6.26). Surprisingly, we conclude that from the point of view of our quantum transport calculation (considering only trivial/non-trivial edge states) the topologically trivial and non-trivial $\text{In}_{0.85}\text{As}_{0.15}\text{Bi}$ cylindrical QDs are equivalent.

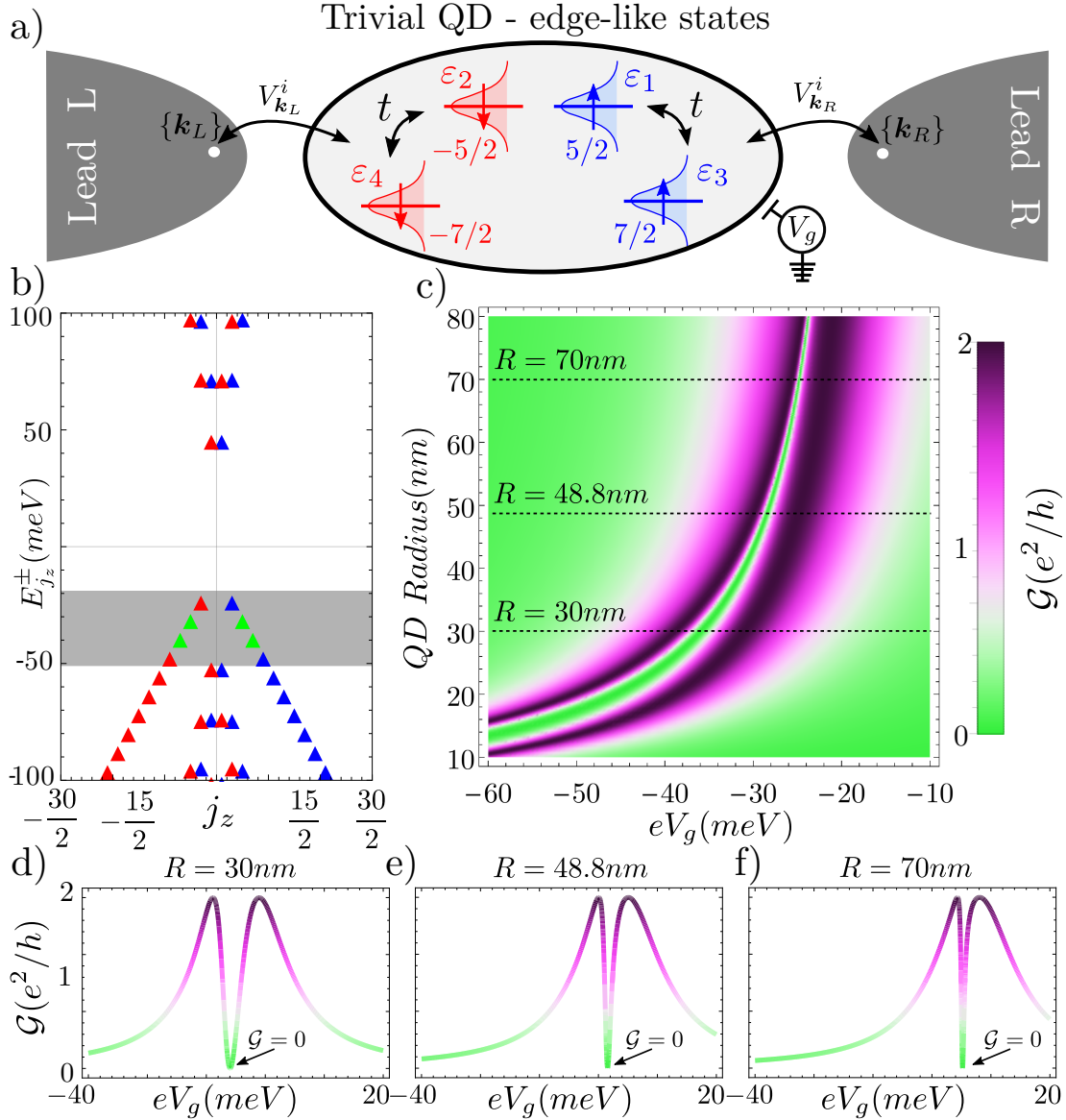


Figure 33 – a) Schematic $\text{In}_{0.85}\text{As}_{0.15}\text{Bi}$ QD Hamiltonian for the four geometrically protected trivial edge states $j_z = \pm 5/2$ and $j_z = \pm 7/2$ coupled to left (L) and right (R) leads. b) Trivial $\text{In}_{0.85}\text{As}_{0.15}\text{Bi}$ QD energy levels as a function of j_z for $R = 30$ nm [The green triangles represent the $j_z = \pm 5/2$ and $j_z = \pm 7/2$ energy levels considered in the conductance calculation]. c) QD conductance calculation \mathcal{G} at $T = 0$ K for the $j_z = \pm 5/2, \pm 7/2$ as a function of the QD radius R and the gate potential V_g . QD conductance \mathcal{G} at $T = 0$ K for d) $R = 30$ nm, e) $R = 48.8$ nm and f) $R = 70$ nm.

Source: By the author

6.3.2 Conductance results for the coexistence of edge-like and bulk-like states

For a certain energy window, bulk and edge states can coexist and even be degenerate in energy (See Fig. 20, for instance). Therefore, it is important to investigate the conductance of trivial and non-trivial $\text{In}_{0.85}\text{As}_{0.15}\text{Bi}$ QD with coexisting bulk and edge

states as the conducting levels in Eq. (6.1).

In Figure 34 we plot the conductance for the trivial $\text{In}_{0.85}\text{As}_{0.15}\text{Bi}$ QD considering the $j_z = \pm 9/2$ edge state and the $j_z = \pm 1/2$ bulk state, both represented by the green triangles in Fig. 34b) which contains the QD energy levels for the trivial $\text{In}_{0.85}\text{As}_{0.15}\text{Bi}$ QD with $R = 30$ nm. As we can see in Fig. 34c), the conductance \mathcal{G} shows a very different pattern as compared to the ones in Figs. 31c) and 33c). Here, \mathcal{G} exhibits a crossover from a $2e^2/h$ double-peak resonance for $R < R_c$ and $V_c < V_{gc}$, to a $2e^2/h$ single-peak at $R = R_c$ and $V_g = V_{gc}$, and back to a $2e^2/h$ double-peak resonance for $R > R_c$ and $V_c > V_{gc}$, represented in Figs. 34d), e) and f).

In order to understand the origin of this crossover, we start with the spin up Hamiltonian H_\uparrow in Eq. (6.2) in the absence of the coupling to the leads, yielding

$$H_{QD} = \begin{pmatrix} d_1^\dagger & d_3^\dagger \end{pmatrix} \begin{pmatrix} \varepsilon_1 & t_{13} \\ t_{13} & \varepsilon_3 \end{pmatrix} \begin{pmatrix} d_1 \\ d_3 \end{pmatrix}. \quad (6.28)$$

The above Hamiltonian has thus the following diagonal form

$$H_{QD} = \begin{pmatrix} d_+^\dagger & d_-^\dagger \end{pmatrix} \begin{pmatrix} \varepsilon_+ & 0 \\ 0 & \varepsilon_- \end{pmatrix} \begin{pmatrix} d_+ \\ d_- \end{pmatrix}, \quad (6.29)$$

where

$$d_+^\dagger = \frac{t_{13} d_1^\dagger + (\varepsilon_+ - \varepsilon_1) d_3^\dagger}{\sqrt{t_{13}^2 + (\varepsilon_+ - \varepsilon_1)^2}}, \quad d_-^\dagger = \frac{t_{13} d_1^\dagger + (\varepsilon_- - \varepsilon_1) d_3^\dagger}{\sqrt{t_{13}^2 + (\varepsilon_- - \varepsilon_1)^2}}, \quad (6.30)$$

and $\varepsilon_\pm = \frac{\varepsilon_1 + \varepsilon_3 \pm \sqrt{(\varepsilon_1 - \varepsilon_3)^2 + 4t_{13}^2}}{2}$. Now we rewrite the Hamiltonian responsible for the coupling of the QD to the leads $H_{Lead-QD}$ [Eq. (6.31)] using the diagonal d_+, d_- operators given by Eq. (6.30), yielding

$$H_{Lead-QD} = \sum_{\mathbf{k}_\alpha, \alpha} \left(V_{\mathbf{k}_\alpha}^1 d_1^\dagger c_{\mathbf{k}_\alpha} + V_{\mathbf{k}_\alpha}^3 d_3^\dagger c_{\mathbf{k}_\alpha} \right) + H.C \quad (6.31)$$

$$= \sum_{\mathbf{k}_\alpha, \alpha} \left[V_{\mathbf{k}_\alpha}^1 (\varepsilon_1 - \varepsilon_+) + t_{13} V_{\mathbf{k}_\alpha}^3 \right] \frac{\sqrt{(\varepsilon_1 - \varepsilon_-)^2 + t_{13}^2}}{(\varepsilon_- - \varepsilon_+) t_{13}} d_-^\dagger c_{\mathbf{k}_\alpha} - \sum_{\mathbf{k}_\alpha, \alpha} \left[V_{\mathbf{k}_\alpha}^1 (\varepsilon_1 - \varepsilon_-) + t_{13} V_{\mathbf{k}_\alpha}^3 \right] \frac{\sqrt{(\varepsilon_1 - \varepsilon_+)^2 + t_{13}^2}}{(\varepsilon_- - \varepsilon_+) t_{13}} d_+^\dagger c_{\mathbf{k}_\alpha} + H.C \quad (6.32)$$

$$= \sum_{\mathbf{k}_\alpha, \alpha} \left(V_{\mathbf{k}_\alpha}^- d_-^\dagger c_{\mathbf{k}_\alpha} + V_{\mathbf{k}_\alpha}^+ d_+^\dagger c_{\mathbf{k}_\alpha} \right) + H.C \quad (6.33)$$

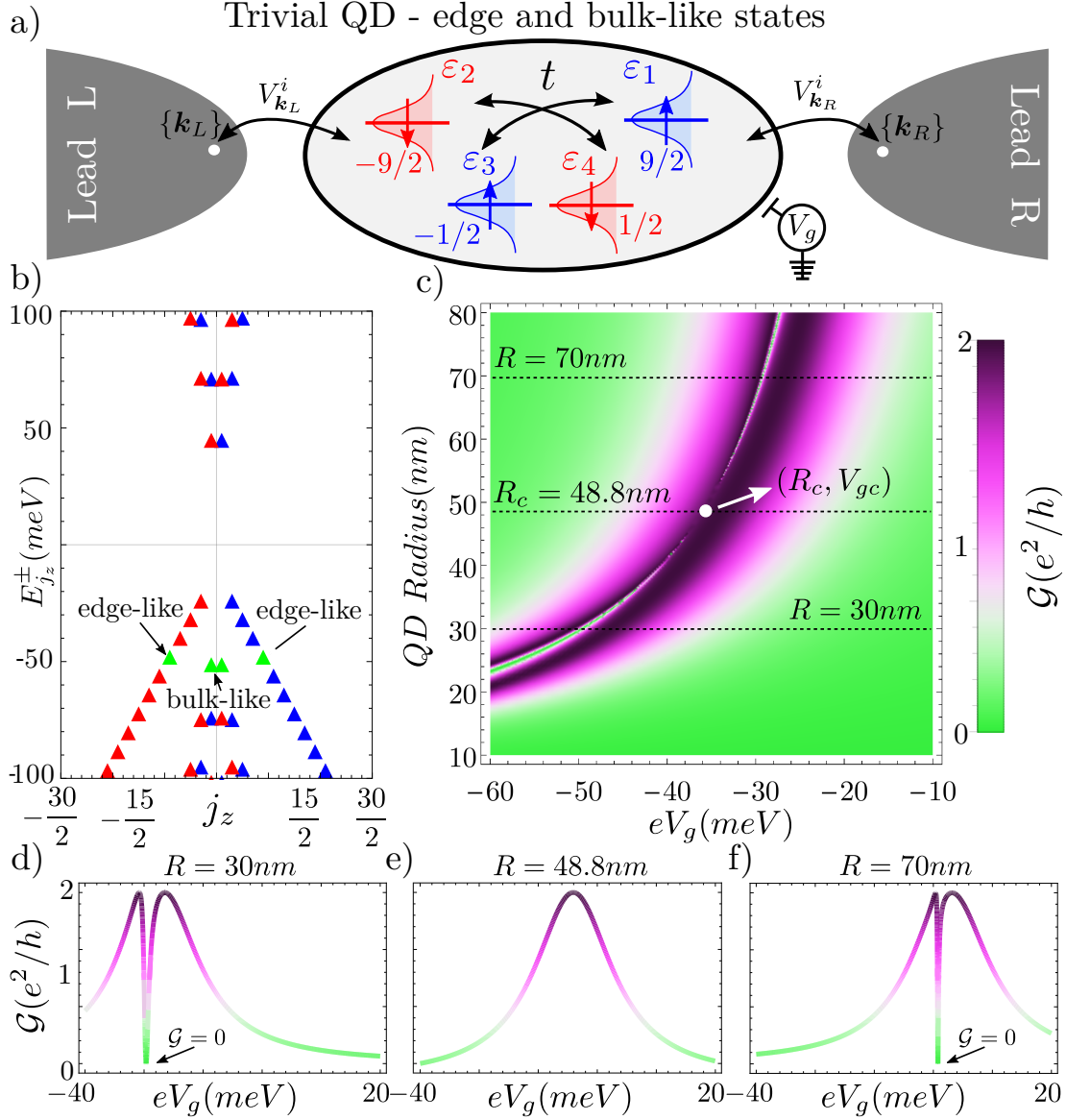


Figure 34 – Schematic $\text{In}_{0.85}\text{As}_{0.15}\text{Bi}$ QD Hamiltonian for the edge states $j_z = \pm 9/2$ and the bulk state $j_z = \pm 1/2$ coupled to left (L) and right (R) leads. b) Trivial $\text{In}_{0.85}\text{As}_{0.15}\text{Bi}$ QD energy levels as a function of j_z for $R = 30$ nm [The green triangles represent the $j_z = \pm 9/2$ and $j_z = \pm 1/2$ energy levels considered in the conductance calculation]. c) QD conductance calculation \mathcal{G} at $T = 0$ K for the $j_z = \pm 9/2, \pm 1/2$ as a function of the QD radius R and the gate potential V_g . QD conductance \mathcal{G} at $T = 0$ K for d) $R = 30$ nm, e) $R = 48.8$ nm and f) $R = 70$ nm.

Source: By the author

Therefore, we note that by tuning the QD radius R and the gate V_g such that

$$\varepsilon_1(R_c, V_{gc}) - \varepsilon_3(R_c, V_{gc}) = t_{13} \left(\frac{V_{k_\alpha}^1}{V_{k_\alpha}^3} - \frac{V_{k_\alpha}^3}{V_{k_\alpha}^1} \right) \quad (6.34)$$

we obtain $V_{\mathbf{k}_\alpha}^1 (\varepsilon_1 - \varepsilon_+) + t_{13} V_{\mathbf{k}_\alpha}^3 = 0$, which decouples the diagonal QD level d_- from the lead. As a consequence, when Eq. (6.34) is satisfied we just see a single $2e^2/h$ peak occurring in the conductance calculation Fig. 34c) at $(R, V_g) = (R_c, V_{gc})$ corresponding to the conductance through only the diagonal d_+ QD energy channel. Since here we are assuming $V_{\mathbf{k}_\alpha}^1 = V_{\mathbf{k}_\alpha}^3$, the above condition is achieved when the two different Kramers pairs become degenerate in energy, i.e., $\varepsilon_1(R_c, V_{gc}) = \varepsilon_3(R_c, V_{gc})$.

We emphasize that the same feature of Fig. 34c), i.e., the $2e^2/h$ single-peak also happens when considering bulk and edge energy levels in the topologically non-trivial InAsBi QD conductance calculation. This can be seen from Fig. 35 where different edge and bulk states become degenerate as a function of the QD radius R .

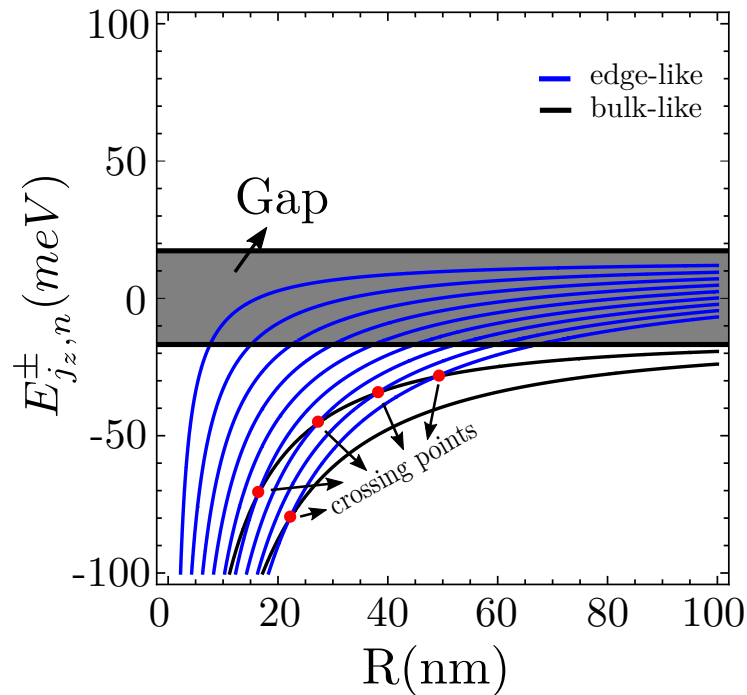


Figure 35 – Few spin + non-trivial edge states with their nearest bulk valence level $j_z^o = 1/2$ as a function of QD radius R . The red points indicate the degenerate crossing points where the number of the protected trivial edge states is decreased by one.

Source: By the author

Surprisingly, we show in this chapter that the geometrically protected helical edge states are also equivalent to the topologically ones from the point of view of transport properties such as the two terminal conductance \mathcal{G} at $T = 0$ K.

In the next chapter we will summarize all of our results results and provide an

outlook of our work.

7 CONCLUSION

In this thesis, we have studied two different, but related systems: i) the symmetric $\text{InAs}_{0.85}\text{Bi}_{0.15}/\text{AlSb}$ quantum wells and ii) the cylindrical $\text{InAs}_{0.85}\text{Bi}_{0.15}$ BHZ quantum dots in both topologically trivial and non-trivial regimes.

In the ordinary III-V InAs material, the addition of Bi with its resonant level in the InAs valence bands produces, through the idea behind the VBAC theory, an anti-crossing repulsion between these energy levels. For Bi concentrations $x > 0.15$, this repulsion leads to an inversion of the $\text{InAs}_{1-x}\text{Bi}_x$ bulk band ordering, supported by experimental evidence. Considering the symmetric $\text{InAs}_{1-x}\text{Bi}_x/\text{AlSb}$ QW, we show through a numerical diagonalization using the $\mathbf{k} \cdot \mathbf{p}$ approach for heterostructures, that similarly to the HgTe/CdTe QWs, our system also shows a subband inversion as a function of the well thickness, characterizing a 2D topological phase transition. For the symmetric $\text{InAs}_{0.85}\text{Bi}_{0.15}/\text{AlSb}$ QW, this topological phase transition happens at the critical thickness $d_c = 6.9$ nm. Therefore, we have predicted that the *InAs_{0.85}Bi_{0.15}/AlSb QW becomes a 2D topological insulator* for well widths $d > 6.9$ nm. Additionally, we find a large inverted gap ~ 30 meV for thickness $d = 8$ nm which should enable room temperature applications. We also calculate numerically the corresponding BHZ parameters of our 2D TI proposal for the topologically trivial regime with $d = 6$ nm and for the topologically non-trivial regime with $d = 8$ nm. In a future work we will also investigate the likely enhancement of the Rashba and Dresselhaus spin orbit couplings in $\text{InAs}_{0.85}\text{Bi}_{0.15}$ due to the inclusion of Bi atoms with their strong spin orbit coupling. Therefore, we anticipate that our 2D TI proposal should also be important for hosting Majorana fermions in topological superconducting wires.

The $\text{InAs}_{0.85}\text{Bi}_{0.15}$ BHZ QDs were defined here by a further cylindrical soft and hard wall confinements on $\text{InAs}_{0.85}\text{Bi}_{0.15}/\text{AlSb}$ QWs for both topological trivial and non-trivial regimes. We then solved their eigenvalue problems using the corresponding calculated BHZ parameters. By using the modified Bessel functions, we found for the hard wall confinement, analytical formulas for the wave functions and circulating currents together with a transcendental equation determining all the discrete QD energy levels. For the topologically non-trivial $\text{InAs}_{0.85}\text{Bi}_{0.15}$ BHZ QDs, we obtained discrete helical edge states, i.e., single Kramers pairs at a given energy with spin-angular-momentum locking, protected against elastic scattering within the energy gap region. Interestingly and unexpectedly we found for the first time *helical edge states in non-topological* BHZ cylindrical QDs - similarly to the topological BHZ QDs. Surprisingly, these trivial edge states are *geometrically protected* due to the confinement in a wide range of parameters. Additionally, we have also calculated the circulating currents for the topologically trivial and non-trivial helical edge states, finding no substantial difference between them. We

also showed that the BHZ structure of the QD Hamiltonian is an important ingredient behind the appearance of these trivial helical edge states, which are absent in the ordinary InAs QDs.

We corroborate our findings by calculating transport properties, e.g., the two-terminal conductance, in both trivial and non-trivial regimes of our BHZ QDs coupled to leads. We showed that, when we only consider edge states as conducting states, both trivial and non-trivial BHZ QDs always exhibit a two-peak resonance profile as a function of the QD radius and the gate controlling their energy levels. On the other hand, when we consider – in both QDs regimes – edge and extended states coexisting as conducting QD energy levels, the two-terminal conductance exhibits one-peak resonance profile when the the edge and extended states become degenerate in energy. Hence, also from the quantum transport point of view, our InAsBi cylindrical QDs - both topologically trivial and non-trivial - are equivalent. To conclude, we have shown in this thesis that the *boundaries between topological trivial and non-trivial physical phenomena is “blurred” in BHZ QDs.*

REFERENCES

- 1 THOULESS, D. J. et al. Quantized hall conductance in a two-dimensional periodic potential. **Physical Review Letters**, v. 49, n. 6, p. 405, 1982.
- 2 KANE, C. L.; MELE, E. J. Quantum Spin hall effect in graphene. **Physical Review Letters**, v. 95, n. 22, p. 226801, 2005.
- 3 BERNEVIG, B. A.; ZHANG, S.-C. Quantum spin hall effect. **Physical Review Letters**, v. 96, n. 10, p. 106802, 2006.
- 4 HASAN, M. Z.; KANE, C. L. Colloquium: topological insulators. **Review of Modern Physics**, v. 82, n. 4, p. 3045–3067, 2010.
- 5 QI, X.-L.; ZHANG, S.-C. Topological insulators and superconductors. **Reviews of Modern Physics**, v. 83, n. 4, p. 1057, 2011.
- 6 MA, E. Y. et al. Unexpected edge conduction in mercury telluride quantum wells under broken time-reversal symmetry. **Nature Communications**, v. 6, 2015. doi:10.1038/ncomms8252.
- 7 KITAEV, A. Unpaired Majorana fermions in quantum wires. **Physics-Uspekhi**, v. 44, n. 10S, p. 131, 2000.
- 8 OREG, Y.; REFAEL, G.; OPPEN, F. von. Helical liquids and majorana bound states in quantum wires. **Physical Review Letters**, v. 105, n. 17, p. 177002, 2010.
- 9 VERNEK, E. et al. Subtle leakage of a Majorana mode into a quantum dot. **Physical Review B**, v. 89, n. 16, p. 165314, 2014.
- 10 ELLIOTT, S. R.; FRANZ, M. Colloquium: Majorana fermions in nuclear, particle, and solid-state physics. **Reviews of Modern Physics**, v. 87, n. 1, p. 137, 2015.
- 11 ALICEA, J. Majorana fermions in a tunable semiconductor device. **Physical Review B**, v. 81, n. 12, p. 125318, 2010.
- 12 ARMITAGE, N.; MELE, E.; VISHWANATH, A. Weyl and dirac semimetals in three-dimensional solids. **Reviews of Modern Physics**, v. 90, n. 1, p. 015001, 2018.
- 13 BERNEVIG, B. A.; HUGHES, T. L.; ZHANG, S.-C. Quantum spin hall effect and topological phase transition in HgTe quantum wells. **Science**, v. 314, n. 5806, p. 1757–1761, 2006.
- 14 LIU, C. et al. Quantum spin hall effect in inverted type-II semiconductors. **Physical Review Letters**, v. 100, n. 23, p. 236601, 2008.
- 15 KNEZ, I.; DU, R.-R.; SULLIVAN, G. Evidence for helical edge modes in inverted InAs/GaSb quantum wells. **Physical Review Letters**, v. 107, n. 13, p. 136603, 2011.
- 16 ERLINGSSON, S. I.; EGUES, J. C. All-electron topological insulator in InAs double wells. **Physical Review B**, v. 91, n. 3, p. 035312, 2015.

- 17 FU, L.; KANE, C. L. Topological insulators with inversion symmetry. **Physical Review B**, v. 76, n. 4, p. 045302, 2007.
- 18 XIA, Y. et al. Observation of a large-gap topological-insulator class with a single dirac cone on the surface. **Nature Physics**, v. 5, n. 6, p. 398, 2009.
- 19 CHEN, Y. et al. Experimental realization of a three-dimensional topological insulator, Bi_2Te_3 . **Science**, v. 325, n. 5937, p. 178–181, 2009.
- 20 ZHANG, T. et al. Experimental demonstration of topological surface states protected by time-reversal symmetry. **Physical Review Letters**, v. 103, n. 26, p. 266803, 2009.
- 21 HSIEH, D. et al. Observation of unconventional quantum spin textures in topological insulators. **Science**, v. 323, n. 5916, p. 919–922, 2009.
- 22 KÖNIG, M. et al. Quantum spin hall insulator state in HgTe quantum wells. **Science**, v. 318, n. 5851, p. 766–770, 2007.
- 23 CHANG, K.; LOU, W.-K. Helical quantum states in HgTe quantum dots with inverted band structures. **Physical Review Letters**, v. 106, n. 20, p. 206802, 2011.
- 24 KORKUSINSKI, M.; HAWRYLAK, P. Quantum strain sensor with a topological insulator HgTe quantum dot. **Scientific Reports**, v. 4, p. 4903, 2014. doi:10.1038/srep04903.
- 25 FERREIRA, G. J.; LOSS, D. Magnetically defined qubits on 3d topological insulators. **Physical Review Letters**, v. 111, n. 10, p. 106802, 2013.
- 26 PAUDEL, H. P.; LEUENBERGER, M. N. Three-dimensional topological insulator quantum dot for optically controlled quantum memory and quantum computing. **Physical Review B**, v. 88, n. 8, p. 085316, 2013.
- 27 ERTLER, C.; RAITH, M.; FABIAN, J. Gate-defined coupled quantum dots in topological insulators. **Physical Review B**, v. 89, n. 7, p. 075432, 2014.
- 28 KUNDU, A. et al. Energy spectrum and broken spin-surface locking in topological insulator quantum dots. **Physical Review B**, v. 83, n. 12, p. 125429, 2011.
- 29 LI, J. et al. Single-and few-electron states in topological-insulator quantum dots. **Physical Review B**, v. 90, n. 11, p. 115303, 2014.
- 30 QU, J.-X. et al. Robustness of edge states in topological quantum dots against global electric field. **Journal of Applied Physics**, v. 122, n. 3, p. 034307, 2017.
- 31 XU, H.; LAI, Y.-C. Reverse stark effect, anomalous optical transitions, and control of spin in topological insulator quantum dots. **Physical Review B**, v. 92, n. 19, p. 195120, 2015.
- 32 SUKHANOV, A. A. Electrically controlled crossing of energy levels in quantum dots in two-dimensional topological insulators. **Physica B: condensed matter**, v. 513, p. 1–6, 2017.
- 33 ZHANG, S.-N.; JIANG, H.; LIU, H. Numerical study of transport properties in topological insulator quantum dots under magnetic field. **Modern Physics Letters B**, v. 27, n. 14, p. 1350104, 2013.

-
- 34 HERATH, T. M.; HEWAGEEGANA, P.; APALKOV, V. A quantum dot in topological insulator nanofilm. **Journal of Physics: condensed matter**, v. 26, n. 11, p. 115302, 2014.
- 35 ASHCROFT, N. W.; MERMIN, N. D.; RODRIGUEZ, S. **Solid state physics**. Maryland: AAPT, 1978.
- 36 DRESSELHAUS, G. Spin-orbit coupling effects in zinc blende structures. **Physical Review**, v. 100, n. 2, p. 580, 1955.
- 37 DRESSELHAUS, M. S.; DRESSELHAUS, G.; JORIO, A. **Group theory: application to the physics of condensed matter**. Berlin: Springer-Verlag, 2007.
- 38 BASTARD, G. **Wave mechanics applied to semiconductor heterostructure**. Les Ulis Cedex: Les Edition de Physique, 1988.
- 39 YU, P. Y.; CARDONA, M. **Fundamentals of Semiconductors - physics and materials properties**. 3rd ed. Berlin: Springer-Verlag, 2010.
- 40 SAKURAI, J. J. **Advanced quantum mechanics**. Menlo Park, Calif.: Benjamin/Cummings, 1967.
- 41 WINKLER, R. **Spin-orbit coupling effects in two-dimensional electron and hole systems**. Berlin: Springer, 2003.
- 42 BIR, G.; PIKUS, G. **Symmetry and strain-induced effects in semiconductors**. New York: John Wiley, 1974. 484 p.
- 43 GREINER, W. **Relativistic quantum mechanics: wave equations**. Berlin: Springer, 2000.
- 44 RINDLER, W. **Relativity: special, general, and cosmological**. New York: Oxford University Press, 2006.
- 45 CALLAN, J. C. G. **Introduction to relativistic quantum mechanics**. Princeton: Princeton University Press, 1996.
- 46 DRESSELHAUS, G. Spin-orbit coupling effects in zincblende structures. **Physical Review**, v. 100, n. 2, p. 580–586, 1955.
- 47 BERCHENKO, N. N.; PASHKOVSKII, M. V. Mercury telluride—a zero-gap semiconductor. **Physics-Uspekhi**, v. 19, n. 6, p. 462–480, 1976.
- 48 CHU, J.; SHER, A. **Physics and properties of narrow gap semiconductors**. Berlin: Springer, 2008.
- 49 NABER, G. L.; NABER, G. L. **Topology, geometry, and gauge fields**. New York: Springer, 1997.
- 50 BORN, M.; FOCK, V. Beweis des adiabatenatzes. **Zeitschrift für Physik**, v. 51, n. 3-4, p. 165–180, 1928.
- 51 FRANZ, M.; MOLENKAMP, L. **Topological insulators**. Amsterdam: Elsevier, 2013. (Contemporary concepts of condensed matter science, v. 6).

- 52 SHEN, S.-Q. **Topological insulators: Dirac equation in condensed matters**. Berlin: Springer Science & Business Media, 2013. (Springer series in solid-state sciences, v. 174).
- 53 CHIU, C.-K. et al. Classification of topological quantum matter with symmetries. **Reviews of Modern Physics**, v. 88, n. 3, p. 035005, 2016.
- 54 NAKAHARA, M. **Geometry, topology and physics**. Boca Raton: CRC Press, 2003.
- 55 BERRY, M. V. Quantal phase factors accompanying adiabatic changes. **Proceedings of the Royal Society of London A**, v. 392, n. 1802, p. 45–57, 1984.
- 56 THOULESS, D. J. et al. Quantized hall conductance in a two-dimensional periodic potential. **Physical Review Letters**, v. 49, n. 6, p. 405, 1982.
- 57 QI, X.-L.; WU, Y.-S.; ZHANG, S.-C. General theorem relating the bulk topological number to edge states in two-dimensional insulators. **Physical Review B**, v. 74, n. 4, p. 045125, 2006.
- 58 ESSIN, A. M.; GURARIE, V. Bulk-boundary correspondence of topological insulators from their respective greens functions. **Physical Review B**, v. 84, n. 12, p. 125132, 2011.
- 59 FUKUI, T. et al. Bulk-edge correspondence for chern topological phases: a viewpoint from a generalized index theorem. **Journal of the Physical Society of Japan**, v. 81, n. 11, p. 114602, 2012.
- 60 BURT, M. G. The justification for applying the effective-mass approximation to microstructures. **Journal of Physics: condensed matter**, v. 4, n. 32, p. 6651, 1992.
- 61 _____. An exact formulation of the envelope function method for the determination of electronic states in semiconductor microstructures. **Semiconductor Science and Technology**, v. 2, n. 7, p. 460, 1987.
- 62 _____. A new effective-mass equation for microstructures. **Semiconductor Science and Technology**, v. 3, n. 12, p. 1224, 1988.
- 63 KANE, E. O. Energy band structure in p-type germanium and silicon. **Journal of Physics and Chemistry of Solids.**, v. 1, n. 1-2, p. 82–99, 1956.
- 64 LUTTINGER, J. M.; KOHN, W. Motion of electrons and holes in perturbed periodic fields. **Physical Review**, v. 97, n. 4, p. 869–883, 1955.
- 65 CANDIDO, D. R. **Relaxação de spin via D'yakonov-Perel' em poços quânticos com acoplamento spin-órbita intersub-banda**. 2013. 227 p. Dissertação (Mestrado em Ciências) — Instituto de Física de São Carlos, Universidade de São Paulo, São Carlos, 2013.
- 66 NOVIK, E. G. et al. Band structure of semimagnetic $Hg_{1-x}Mn_xTe$ quantum wells. **Physical Review B**, v. 72, n. 3, p. 035321, 2005.
- 67 CALSAVERINI, R. S. et al. Intersubband-induced spin-orbit interaction in quantum wells. **Physical Review B**, v. 78, n. 15, p. 155313, 2008.
- 68 MICHETTI, P. et al. Tunable quantum spin hall effect in double quantum wells. **Physical Review B**, v. 85, n. 12, p. 125309, 2012.

-
- 69 BREE, J. van et al. Spin-orbit-induced circulating currents in a semiconductor nanostructure. **Physical Review Letters**, v. 112, n. 18, p. 187201, 2014.
- 70 _____. Geometric and compositional influences on spin-orbit induced circulating currents in nanostructures. **Physical Review B**, v. 90, n. 16, p. 165306, 2014.
- 71 VURGAFTMAN, I.; MEYER, J. R.; RAM-MOHAN, L. R. Band parameters for III-V compound semiconductors and their alloys. **Journal of Applied Physics**, v. 89, n. 11, p. 5815–5875, 2001.
- 72 MICHETTI, P. et al. Helical edge states in multiple topological mass domains. **Semiconductor Science and Technology**, v. 27, n. 12, p. 124007, 2012.
- 73 ROTHE, D. et al. Fingerprint of different spin–orbit terms for spin transport in HgTe quantum wells. **New Journal of Physics**, v. 12, n. 6, p. 065012, 2010.
- 74 CANDIDO, D. R.; FLATTÉ, M.; EGUES, J. C. **Blurring the boundaries between topological and non-topological phenomena in dots**, 2018. Available from: <<https://arxiv.org/pdf/1803.02936.pdf>>. Accessible at: 23 Mar. 2018.
- 75 MA, K. et al. Organometallic vapor phase epitaxial growth and characterization of InAsBi and InAsSbBi. **Applied Physics Letters**, v. 55, n. 23, p. 2420–2422, 1989.
- 76 FANG, Z. et al. Photoluminescence of InAsBi and InAsSbBi grown by organometallic vapor phase epitaxy. **Journal of Applied Physics**, v. 68, n. 3, p. 1187–1191, 1990.
- 77 WEBSTER, P. T. et al. Molecular beam epitaxy using bismuth as a constituent in InAs and a surfactant in InAs/InAsSb superlattices. **Journal of Vacuum Science & Technology B**, v. 32, n. 2, p. 02C120, 2014.
- 78 SHAN, W. et al. Band anticrossing in GaInNAs alloys. **Physical Review Letters**, v. 82, n. 6, p. 1221, 1999.
- 79 WALUKIEWICZ, W. et al. Interaction of localized electronic states with the conduction band: Band anticrossing in II – VI semiconductor ternaries. **Physical Review Letters**, v. 85, n. 7, p. 1552, 2000.
- 80 WU, J.; WALUKIEWICZ, W.; HALLER, E. Band structure of highly mismatched semiconductor alloys: coherent potential approximation. **Physical Review B**, v. 65, n. 23, p. 233210, 2002.
- 81 WU, J.; SHAN, W.; WALUKIEWICZ, W. Band anticrossing in highly mismatched III – V semiconductor alloys. **Semiconductor Science and Technology**, v. 17, n. 8, p. 860, 2002.
- 82 ALBERI, K. et al. Valence band anticrossing in mismatched III – V semiconductor alloys. **Physical Review B**, v. 75, n. 4, p. 045203, 2007.
- 83 SAMAJDAR, D.; DHAR, S. Valence band structure of and alloy semiconductors calculated using valence band anticrossing model. **Scientific World Journal**, v. 2014, 2014. doi.org/10.1155/2014/704830.
- 84 HILL, R.; RICHARDSON, D. The variation of energy gap with composition in ZnS – Te alloys. **Journal of Physics C: solid state physics**, v. 6, n. 5, p. L115, 1973.

- 85 WU, J. et al. Origin of the large band-gap bowing in highly mismatched semiconductor alloys. **Physical Review B**, v. 67, n. 3, p. 035207, 2003.
- 86 WEYERS, M.; SATO, M.; ANDO, H. Red shift of photoluminescence and absorption in dilute GaAsN alloy layers. **Japanese Journal of Applied Physics**, v. 31, n. 7A, p. L853, 1992.
- 87 UESUGI, K.; MOROOKA, N.; SUEMUNE, I. Reexamination of N composition dependence of coherently grown GaNAs band gap energy with high-resolution x-ray diffraction mapping measurements. **Applied Physics Letters**, v. 74, n. 9, p. 1254–1256, 1999.
- 88 MALIKOVA, L.; POLLAK, F. H.; BHAT, R. Composition and temperature dependence of the direct band gap of GaAs_{1-x}N_x ($0 \leq x \leq 0.0232$) using contactless electroreflectance. **Journal of Electronic Materials**, v. 27, n. 5, p. 484–487, 1998.
- 89 BHAT, R. et al. Growth of GaAsN/GaAs, GaInAsN/GaAs and GaInAsN/GaAs quantum wells by low-pressure organometallic chemical vapor deposition. **Journal of Crystal Growth**, v. 195, n. 1-4, p. 427–437, 1998.
- 90 VECHTEN, J. V.; BERGSTRESSER, T. Electronic structures of semiconductor alloys. **Physical Review B**, v. 1, n. 8, p. 3351, 1970.
- 91 WEI, S.-H.; ZUNGER, A. Giant and composition-dependent optical bowing coefficient in GaAsN alloys. **Physical Review Letters**, v. 76, n. 4, p. 664, 1996.
- 92 JONES, E. et al. Band structure of In_xGa_{1-x}As_{1-y}N_y alloys and effects of pressure. **Physical Review B**, v. 60, n. 7, p. 4430, 1999.
- 93 MATTLA, T.; WEI, S.-H.; ZUNGER, A. Localization and anticrossing of electron levels in GaAs_{1-x}N_x alloys. **Physical Review B**, v. 60, n. 16, p. R11245, 1999.
- 94 WANG, L.-W. Large-scale local-density-approximation band gap-corrected GaAsN calculations. **Applied Physics Letters**, v. 78, n. 11, p. 1565–1567, 2001.
- 95 SZWACKI, N. G.; BOGUSŁAWSKI, P. GaAs: N vs GaAs: B alloys: symmetry-induced effects. **Physical Review B**, v. 64, n. 16, p. 161201, 2001.
- 96 AL-YACOUB, A.; BELLAICHE, L. Quantum mechanical effects in (Ga, In)(As, N) alloys. **Physical Review B**, v. 62, n. 16, p. 10847, 2000.
- 97 ZHANG, Y. et al. Scaling of band-gap reduction in heavily nitrogen doped GaAs. **Physical Review B**, v. 63, n. 16, p. 161303, 2001.
- 98 HETTERICH, M. et al. Electronic states and band alignment in GaInNAs/GaAs quantum-well structures with low nitrogen content. **Applied Physics Letters**, v. 76, n. 8, p. 1030–1032, 2000.
- 99 WU, J. et al. Effect of band anticrossing on the optical transitions in GaAs_{1-x}N_x/GaAs multiple quantum wells. **Physical Review B**, v. 64, n. 8, p. 085320, 2001.
- 100 SHAN, W. et al. Nature of the fundamental band gap in GaN_xP_{1-x} alloys. **Applied Physics Letters**, v. 76, n. 22, p. 3251–3253, 2000.

-
- 101 ANDERSON, P. W. Localized magnetic states in metals. **Physical Review**, v. 124, n. 1, p. 41, 1961.
- 102 ECONOMOU, E. N. **Green's functions in quantum physics**. Berlin: Springer, 1983. v. 3.
- 103 HAUG, H.; JAUHO, A.-P. **Quantum kinetics in transport and optics of semiconductors**. Berlin: Springer, 2008. v. 2.
- 104 BRUUS, H.; FLENSBERG, K. **Many-body quantum theory in condensed matter physics: an introduction**. Oxford: Oxford University Press, 2004.
- 105 MAHAN, G. D. **Many-particle physics**. Berlin: Springer Science & Business Media, 2013.
- 106 ZUBAREV, D. Double-time green functions in statistical physics. **Soviet Physics Uspekhi**, v. 3, n. 3, p. 320, 1960.
- 107 YONEZAWA, F.; MORIGAKI, K. Coherent potential approximation. basic concepts and applications. **Progress of Theoretical Physics Supplement**, v. 53, p. 1–76, 1973.
- 108 SHIBA, H. A reformulation of the coherent potential approximation and its applications. **Progress of Theoretical Physics**, v. 46, n. 1, p. 77–94, 1971.
- 109 ELLIOTT, R.; KRUMHANSL, J.; LEATH, P. The theory and properties of randomly disordered crystals and related physical systems. **Reviews of Modern Physics**, v. 46, n. 3, p. 465, 1974.
- 110 JAUHO, A.-P.; WINGREEN, N. S.; MEIR, Y. Time-dependent transport in interacting and noninteracting resonant-tunneling systems. **Physical Review B**, v. 50, n. 8, p. 5528, 1994.
- 111 MEIR, Y.; WINGREEN, N. S. Landauer formula for the current through an interacting electron region. **Physical Review Letters**, v. 68, n. 16, p. 2512, 1992.
- 112 JANOTTI, A.; WEI, S.-H.; ZHANG, S. Theoretical study of the effects of isovalent coalloying of Bi and N in GaAs. **Physical Review B**, v. 65, n. 11, p. 115203, 2002.
- 113 BARNETT, S. Direct E_0 energy gaps of bismuth-containing III – V alloys predicted using quantum dielectric theory. **Journal of Vacuum Science & Technology A: vacuum, surfaces, and films**, v. 5, n. 5, p. 2845–2848, 1987.
- 114 LAU, W. H.; OLESBERG, J.; FLATTE, M. E. **Electronic structures and electron spin decoherence in (001)-grown layered zinblende semiconductors**. 2004. Available from: <<https://arxiv.org/pdf/cond-mat/0406201.pdf>>. Accessible at: 23 Jan. 2017.
- 115 FANG, Z. et al. Photoluminescence of InSb, InAs, and InAsSb grown by organometallic vapor phase epitaxy. **Journal of Applied Physics**, v. 67, n. 11, p. 7034–7039, 1990.
- 116 WEBSTER, P. et al. Measurement of InAsSb bandgap energy and InAs/InAsSb band edge positions using spectroscopic ellipsometry and photoluminescence spectroscopy. **Journal of Applied Physics**, v. 118, n. 24, p. 245706, 2015.

- 117 ARFKEN, G.; WEBER, H.; HARRIS, F. **Mathematical methods for physicists**. 6th ed. Massachusetts: Elsevier Science, 2005.
- 118 NOETHER, E. Invariant variations problem. Available from: <<https://arxiv.org/pdf/cond-mat/0406201.pdf>>. Accessible at: 23 Jan. 2017.
- 119 TINKHAM, M. **Group theory and quantum mechanics**. New York: Courier Corporation, 2003.
- 120 LAX, M. **Symmetry principles in solid state and molecular physics**. New York: Courier Corporation, 1974.
- 121 KANE, E. O. Band structure of indium antimonide. **Journal of Physics and Chemistry of Solids**, v. 1, n. 4, p. 249, 1957.
- 122 _____. **Physics of III-V compounds**. New York: Academic Press, 1966. v.1.
- 123 SHABANI, J. et al. Two-dimensional epitaxial superconductor-semiconductor heterostructures: a platform for topological superconducting networks. **Physical Review B**, v. 93, n. 15, p. 155402, 2016.
- 124 DATTA, S. **Electronic transport in mesoscopic systems**. Cambridge: Cambridge University Press, 1997.
- 125 HANSON, R. et al. Spins in few-electron quantum dots. **Reviews of Modern Physics**, v. 79, n. 4, p. 1217, 2007.
- 126 KOUWENHOVEN, L. P.; SCHÖN, G.; SOHN, L. L. Introduction to mesoscopic electron transport. In: SOHN, L. L.; KOUWENHOVEN, L. P.; SCHÖN, G. (Ed.) **Mesoscopic electron transport**. Berlin: Springer, 1997. p. 1–44.
- 127 GUEVARA, M. L. D.; CLARO, F.; ORELLANA, P. A. Ghost fano resonance in a double quantum dot molecule attached to leads. **Physical Review B**, v. 67, n. 19, p. 195335, 2003.
- 128 DING, G.-H.; KIM, C. K.; NAHM, K. Fano resonance in electron transport through parallel double quantum dots in the kondo regime. **Physical Review B**, v. 71, n. 20, p. 205313, 2005.
- 129 LU, H.; LÜ, R.; ZHU, B.-f. Tunable fano effect in parallel-coupled double quantum dot system. **Physical Review B**, v. 71, n. 23, p. 235320, 2005.
- 130 CAMENZIND, L. C. et al. **Hyperfine-phonon spin relaxation in a single-electron GaAs quantum dot**. 2017. Available from: <<https://arxiv.org/pdf/1711.01474.pdf>>. Accessible at: 30 Dec. 2017.

Annex

ANNEX A – SUBMITTED ARTICLES

“Blurring the boundaries between topological and non-topological phenomena in dots” – arXiv:1803.02936 – Denis R. Candido, M. E. Flatté, and J. Carlos Egues

Manuscript submitted to PRL. We received two good reports. However, one of them does not recommend PRL. The Editor told us he will send the manuscript to a third Referee if requested because this “negative” report is not substantial. We have already re-submitted this manuscript after some revisions.

Blurring the boundaries between topological and non-topological phenomena in dots

Denis R. Candido,¹ M. E. Flatté,² and J. Carlos Egues^{1,3}

¹*Instituto de Física de São Carlos, Universidade de São Paulo, 13560-970, São Carlos, São Paulo, Brazil*

²*Department of Physics and Astronomy and Optical Science and Technology Center, University of Iowa, Iowa City, Iowa 52242, USA*

³*International Institute of Physics, Federal University of Rio Grande do Norte, 59078-970, P. O. Box 1613, Natal, Brazil*

(Dated: August 24, 2018)

We investigate the electronic and transport properties of topological and non-topological InAs_{0.85}Bi_{0.15} quantum dots (QDs) described by a ~ 30 meV gapped Bernevig-Hughes-Zhang (BHZ) model with cylindrical confinement, i.e., “BHZ dots”. Via modified Bessel functions, we analytically show that *non-topological* dots quite unexpectedly have discrete helical edge states, i.e., Kramers pairs with spin-angular-momentum locking similar to topological dots. These unusual non-topological edge states are geometrically protected due to confinement in a wide range of parameters thus remarkably contrasting the bulk-edge correspondence in TIs. Moreover, for a conduction window with four edge states, we find that the two-terminal conductance \mathcal{G} vs. the QD radius R and the gate V_g controlling its levels shows a double peak at $2e^2/h$ for both topological and trivial BHZ QDs. Our results blur the boundaries between topological and non-topological phenomena for conductance measurements in small systems such as QDs. This is in stark contrast to conductance measurements in 2D quantum spin Hall and trivial insulators. Bi-based BHZ dots should also prove important as hosts to room-temperature edge spin qubits.

Introduction.— Topological Insulators (TIs) are a new class of materials having the unusual property of being an insulator in bulk with robust gapless helical states localized near their edges (2D TIs) and surfaces (3D TIs) [1–4]. Following these pioneering works, a few other TI proposals [5–11] have been put forward with some experimental support [12, 13]. More recently, topological QDs with cylindrical confinement have been investigated [14–27]. Their spectra feature discrete helical edge states protected against non-magnetic scattering and showing spin-angular-momentum locking. These states are potentially important for spintronics [15, 16], quantum computation and other quantum technologies [14, 17, 18].

Here we demonstrate that *non-topological* QDs defined in InAsBi wells obeying the effective Bernevig-Hughes-Zhang model with cylindrical confinement — “BHZ dots” — feature helical edge states *geometrically protected* due to confinement, Fig. 1. This surprising result contrasts with the usual bulk-edge correspondence in TIs, as the non-topological dots here exhibit edge states with spin-angular-momentum locking similar to topological dots [14–25]. Interestingly, our quantum transport calculation shows that circulating currents [28, 29] (Fig. 2) and the two-terminal linear conductance \mathcal{G} [30] (vs. the dot radius R and the gate V_g controlling its levels, Fig. 3) of non-topological and topological QDs are essentially identical. More specifically, for BHZ dots with two Kramers pairs of edge states, \mathcal{G} shows double-peak resonances at $2e^2/h$, separated by a dip due to destructive interference in both regimes. When bulk and edge-state Kramers pairs coexist and are degenerate, both regimes show a single-peak resonance also at $\mathcal{G} = 2e^2/h$. Our findings blur the boundaries between topological and non-topological BHZ dots as for the appearance of protected helical edge states and conductance measurements.

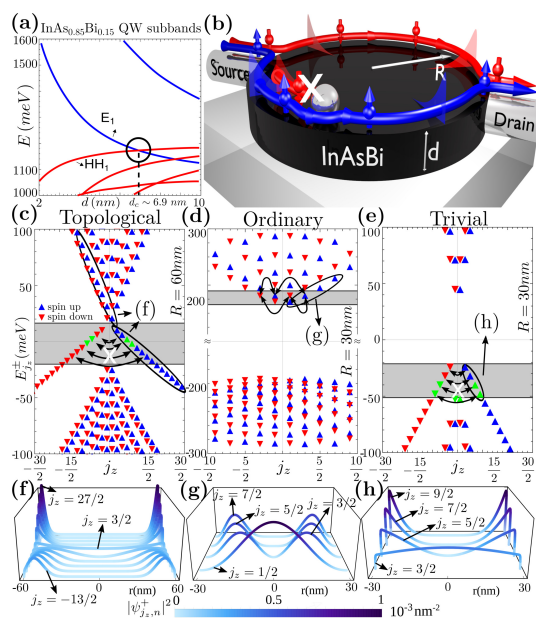


Figure 1. (a) InAs_{0.85}Bi_{0.15} QW subbands vs. the well thickness d . (b) Schematic of a cylindrical QD with helical edge states. Energy levels vs. the total angular momentum j_z for (c) a topological InAs_{0.85}Bi_{0.15} BHZ dot with $R = 60$ nm, (d) an ordinary (non-BHZ) InAs dot with $R = 30$ nm and (e) a trivial InAs_{0.85}Bi_{0.15} BHZ dot with $R = 30$ nm. The curved arrows denote the forbidden and allowed transitions. (f), (g) and (h): Probability densities $|\psi_{j_z, n}^+|^2$ for the edge states in (c) and (d) and bulk states (g) (see ellipses)

We also predict that InAs_{1-x}Bi_x/AlSb quantum wells (QWs) become 2D topological insulators for well widths $d > 6.9$ nm and $x = 0.15$, with large inverted subband gaps ~ 30 meV ($> k_B T$) that should enable room temperature applications, Fig. 1(a). Our BHZ dots are obtained by further confining these Bi-based wells with soft and hard walls. Our *analytical* QD eigenenergies and wave functions (Fig. 1) for both topological and non-topological regimes show that the helical edge states occur in a wide range of QD radii. Our findings also hold for HgTe-based systems (SM).

New 2D Topological Insulator: InAs_{0.85}Bi_{0.15}/AlSb.— The response of the electronic structure of InAs to the addition of the isoelectronic dopant Bi [31–33] is well described within valence band anticrossing theory [34–37]. Bi provides a resonant state within the valence band (complementary to the resonant state in the conduction band generated in the dilute nitrides such as GaAs_{1-x}N_x) which strongly pushes up the valence band edge of InAs as Bi is added. The small band gap of InAs allows it to close for approximately 7.3% of Bi [31–33], and for inversion of the conduction and valence bands similar to HgTe for larger Bi percentage. We determine the electronic states of a InAs_{1-x}Bi_x/AlSb QW grown on a GaSb substrate (SM, Sec. I) within a superlattice electronic structure calculation implemented within a fourteen bulk band basis [38] and obtain the zone-center [Γ point, Fig. 1(a)] quantum well states. From those we derive momentum matrix elements and the other parameters of the BHZ Hamiltonian. We obtain a crossing between the lowest conduction subbands $|E_1\pm\rangle$ and the highest valence subbands $|HH_1\pm\rangle$ at the critical well thickness $d_c = 6.9$ nm.

This crossing characterizes a topological phase transition between an ordinary insulator ($d < d_c$) and a 2D TI ($d > d_c$) with an inverted gap ~ 30 meV, Fig. 1(a).

Model Hamiltonian for a cylindrical BHZ dot.— We consider the BHZ Hamiltonian describing the low-energy physics of the $|E_1\pm\rangle$ and $|HH_1\pm\rangle$ subbands,

$$\mathcal{H}(\mathbf{k}) = \begin{pmatrix} H(\mathbf{k}) & 0 \\ 0 & H^*(-\mathbf{k}) \end{pmatrix}, \quad (1)$$

where $H(\mathbf{k}) = (C - Dk^2)\mathbf{1}_{2\times 2} + \mathbf{d} \cdot \boldsymbol{\sigma}$ and $\mathbf{d}(\mathbf{k}) = (Ak_x, -Ak_y, M - Bk^2)$. Here, \mathbf{k} is the in plane wave vector and $\boldsymbol{\sigma}$ are the Pauli matrices describing the pseudo-spin space. The parameters A, B, C, D, M , calculated within a superlattice $\mathbf{k}\cdot\mathbf{p}$ electronic structure calculation [38], depend on the QW thickness d and are given in Table (S1) of the SM for $d = 6$ nm ($x = 0.15$) and $d = 8$ nm ($x = 0.15$). We define our QDs by adding to Eq. (1) the in-plane cylindrical confinement [14–26]

$$V_c = \begin{pmatrix} V(r)\sigma_z & 0 \\ 0 & V(r)\sigma_z \end{pmatrix}, V(r) = \begin{cases} 0 & r < R \\ M_O - M & r > R, \end{cases} \quad (2)$$

where $M_O - M > 0$ defines the equal strength soft-wall barriers for electrons and holes [39]. Here we focus on the hard wall case ($M_O \rightarrow \infty$) as it is simpler analytically. In the SM we discuss the soft wall case, which qualitatively shows the same behavior.

BHZ dots: eigensolutions. We solve $[\mathcal{H}(\mathbf{k}) + V_c]\psi = \varepsilon\psi$ in polar coordinates: $k_x \pm ik_y = -i e^{\pm i\theta} \left(\frac{\partial}{\partial r} \pm \frac{1}{r} \frac{\partial}{\partial \theta} \right)$ and $k^2 = -\left(\partial_r^2 + \frac{1}{r} \partial_r + \frac{1}{r^2} \partial_\theta^2 \right)$. By imposing that $\psi(r, \theta) = 0$ at $r = R$, we obtain the transcendental equation for the discrete eigenenergies and eigenfunctions

$$\frac{\lambda_-^2(E_{j_z, n}^\pm) - \frac{E_{j_z, n}^\pm - C - M}{D + B} I_{j_z \mp \frac{1}{2}}[\lambda_+(E_{j_z, n}^\pm) R]}{\lambda_-(E_{j_z, n}^\pm)} = \frac{\lambda_+^2(E_{j_z, n}^\pm) - \frac{E_{j_z, n}^\pm - C - M}{D + B} I_{j_z \mp \frac{3}{2}}[\lambda_+(E_{j_z, n}^\pm) R]}{\lambda_+(E_{j_z, n}^\pm)}, \quad (3)$$

$$\psi_{j_z, n}^\pm(r, \theta) = \frac{N e^{i j_z \theta}}{\sqrt{2\pi}} \begin{bmatrix} \left(I_{j_z \mp \frac{1}{2}}(\lambda_+(E_{j_z, n}^\pm) r) - \frac{I_{j_z \mp \frac{1}{2}}(\lambda_+(E_{j_z, n}^\pm) R)}{I_{j_z \mp \frac{1}{2}}(\lambda_-(E_{j_z, n}^\pm) R)} I_{j_z \mp \frac{1}{2}}(\lambda_-(E_{j_z, n}^\pm) r) \right) e^{\mp i \frac{\theta}{2}} \\ \frac{(D+B)\lambda_+^2(E_{j_z, n}^\pm) - E_{j_z, n}^\pm + C + M}{\pm i A \lambda_+(E_{j_z, n}^\pm)} \left(I_{j_z \mp \frac{3}{2}}(\lambda_+(E_{j_z, n}^\pm) r) - \frac{I_{j_z \mp \frac{3}{2}}(\lambda_+(E_{j_z, n}^\pm) R)}{I_{j_z \mp \frac{3}{2}}(\lambda_-(E_{j_z, n}^\pm) R)} I_{j_z \mp \frac{3}{2}}(\lambda_-(E_{j_z, n}^\pm) r) \right) e^{\mp i \frac{3\theta}{2}} \end{bmatrix}. \quad (4)$$

Here $I_{j_z}(\lambda_\pm(E_{j_z, n}^\sigma) r)$ is the modified Bessel function of the first kind, N a normalization factor and $\lambda_\pm^2(E_{j_z, n}^\sigma) = -F \pm \sqrt{F^2 - Q^2}$ with $F = \frac{1}{2} \left(\frac{A^2}{(D+B)(D-B)} - \frac{E_{j_z, n}^\sigma - C - M}{D+B} - \frac{E_{j_z, n}^\sigma - C + M}{D-B} \right)$ and $Q^2 = \left(\frac{E_{j_z, n}^\sigma - C + M}{D-B} \right) \left(\frac{E_{j_z, n}^\sigma - C - M}{D+B} \right)$. The \pm signs in Eqs. (3)

and (4) label the “spin” subspaces in the BHZ model (i.e., its two 2×2 blocks) [40], and arise as the time reversal symmetry operator $\Theta = -i\sigma_y \otimes \mathbf{1}_{2 \times 2} K$ commutes with $\mathcal{H}(\mathbf{k})$ in Eq. (1). The ψ^\pm states in (4) form a Krammers pair, i.e., $\Theta \psi_{j_z, n}^+(r, \theta) = \psi_{-j_z, n}^-(r, \theta)$. The quantum number j_z corresponds to the z -component of the total angu-

lar momentum $\mathcal{J}_z = -i\hbar\partial_\theta + \hbar\sigma_z \otimes (\tau_0 - \frac{\tau_x}{2})$ that obeys $\mathcal{J}_z\psi_{j_z,n}^\pm(r,\theta) = \hbar j_z\psi_{j_z,n}^\pm(r,\theta)$, $j_z = \pm\frac{1}{2}, \pm\frac{3}{2}, \dots$. Incidentally, j_z also denotes the parity of the QD states defined via the inversion symmetry operator $\mathcal{I}(r,\theta) \rightarrow (r,\theta+\pi)$, satisfying $\mathcal{I}\psi_{j_z,n}^\pm(r,\theta) = (-1)^{j_z\mp\frac{3}{2}}\psi_{j_z,n}^\pm(r,\theta)$. Both \mathcal{J}_z and \mathcal{I} commute with the QD Hamiltonian. The quantum number n arises from the radial confinement of the dot; we index our energy spectrum such that for each j_z and $\sigma(=\pm)$, $n = 1, 2, 3, \dots$ ($n = -1, -2, -3, \dots$) for positive (negative) energies.

In Figs. 1(c), 1(d) and 1(e), we plot the InAs_{1-x}Bi_x dot energy levels [Eq. (3)] for *topological* ($x = 0.15$, $d = 8$ nm, $R = 60$ nm), *ordinary* ($x = 0$, $d = 6$ nm, $R = 30$ nm) and *trivial* ($x = 0.15$, $d = 6$ nm, $R = 30$ nm) cases, respectively. The *ordinary* InAs QD with its non-inverted large gap is considered here for comparison (SM, Sec. IV). Panels 1(f), 1(g) and 1(h) show the edge and bulk states grouped by the ellipses in 1(c), 1(d) and 1(e). To gain insight into the origin of the edges states in both topological and non-topological dots, next we look at Eq. (4) in the asymptotic limit $\lambda_r(E_{j_z,n}^\sigma)r \gg m \Rightarrow I_{j_z}[\lambda_r(E_{j_z,n}^\sigma)r] \rightarrow \exp[\lambda_r(E_{j_z,n}^\sigma)r]$ to leading order (this is the parameter range of our Bi-based dots, SM Sec. VI).

For topological BHZ dots ($M < 0$) with $M < E_{j_z,n}^\sigma < -M$, we find real $\lambda_\pm > 0 \Rightarrow \psi_{j_z,n}^\sigma \approx \hat{a}e^{\lambda_-r} + \hat{b}e^{\lambda_+r}$ [Eq. (4)], \hat{a}, \hat{b} complex spinors (SM, Sec. VI). This asymptotic form of $\psi_{j_z,n}^\sigma$ demonstrates its edge state character [Fig. 1(f)] as $\psi_{j_z,n}^\sigma$ peaks near $r = R$ [$\psi_{j_z,n}^\sigma(R) = 0$ for hard wall], similar to that of the 2D TIs. For $E_{j_z,n}^\sigma < M$ or $E_{j_z,n}^\sigma > -M$, edge and extended (“bulk”) states coexist.

Geometrically protected trivial edge states— For non-topological BHZ dots with $E_{j_z,n}^\sigma$ within the valence states [Fig. 1(e)] λ_- is purely imaginary, $\lambda_+ > 0$ and

$$\psi_{j_z,n}^\sigma \approx \begin{pmatrix} J_{j_z \pm \frac{1}{2}}(|\lambda_-|r) \\ J_{j_z \pm \frac{3}{2}}(|\lambda_-|r) \end{pmatrix} + \begin{pmatrix} c_+ \\ d_+ \end{pmatrix} e^{\lambda_+r}, \quad (5)$$

where c_+ and d_+ are complex amplitudes. The $J_m(|\lambda_-|r)$'s oscillate with r and have zeros at α_m^n [$J_m(\alpha_m^n) = 0$, $n = 0, 1, 2, 3, \dots$]. Here, however, they grow monotonically with r within the dot for $E_{j_z,n}^\sigma$ in the gray area of Fig. 1(e). This is due to $|\lambda_-|R < \alpha_m^1/2$ for the parameters of our Bi-based BHZ dot in the non-topological regime (SM, Sec. VI). Similarly to the topological dot case (previous paragraph), $\psi_{j_z,n}^\sigma$ in Eq. (5) peaks near $r = R$ and thus describes “edge-like” states [Fig. 1(h)]. The parameter λ_- controls the degree of localization of the trivial edge states (SM, Sec. VI). In addition, as the energies of extended and edge-like states depend differently on the dot radius R , we find that QD confinement precludes the coexistence of some of these states in our non-topological BHZ dots Fig. 1(e) (see also SM Sec. VII). That is, confinement gives rise to a single geometrically protected Kramers’ pair of dot states per energy within the gray area of Fig. 1(e). This holds for a

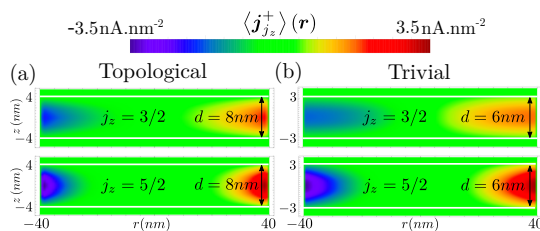


Figure 2. Spin-up circulating currents for topological (a) and trivial (b) edge states $j_z = \frac{3}{2}$ and $j_z = \frac{5}{2}$ within the gray area in Figs. 1(c) and 1(e). The topological and trivial circulating currents are essentially the same. The horizontal white lines delimit the QW barriers.

wide range of QD radii and BHZ parameters (e.g., those of HgTe/CdTe QDs, see also SM Secs. V, VI and VIII).

In contrast, ordinary cylindrical InAs QDs defined from InAs wells with parabolic subbands do not have protected edge-like states [Fig. 1(d), 1(g)]. These non-BHZ dots have the degeneracies $E_{j_z \mp \frac{1}{2}, n}^{E_{1\pm}} = E_{-j_z \pm \frac{1}{2}, n}^{E_{1\pm}}$ and $E_{j_z \mp \frac{3}{2}, n}^{HH_{1\pm}} = E_{-j_z \pm \frac{3}{2}, n}^{HH_{1\pm}}$ that allow for elastic scattering between these levels, thus precluding protection [43]. This picture still holds in the presence of spin-orbit and electron–heavy-hole mixing effects (SM, Sec. IV).

Circulating current densities: $\mathbf{j}(\mathbf{r})$. — We define $\mathbf{j}(\mathbf{r}) = \frac{e\hbar}{m_0} \text{Im} \{ \psi^\dagger(\mathbf{r}) \nabla \psi(\mathbf{r}) \}$, where the total QD wave function $\psi(\mathbf{r}) = \sum_i F_i(\mathbf{r}) u_i(\mathbf{r})$ is expressed as the sum of the product of the periodic part of the Bloch function $u_i(\mathbf{r})$ of band i at the Γ point and its respective envelope function $F_i(\mathbf{r})$. The average current over the unit cell is given by [28, 29] $\langle \mathbf{j} \rangle(\mathbf{r}) = \frac{e\hbar}{m_0} \text{Im} \sum_{i,j} \{ F_i^*(\mathbf{r}) F_j(\mathbf{r}) \langle u_i | \nabla | u_j \rangle + \delta_{ij} F_i^*(\mathbf{r}) \nabla F_j(\mathbf{r}) \}$. Using the wave function Eq. (4) (SM, Sec. IX), we find

$$\begin{aligned} \langle \mathbf{j}_{j_z,n}^\pm \rangle &= \pm e \frac{N^2}{2\pi} \left\{ \frac{\sqrt{2}P}{\hbar} |f_1^\pm(z)| |f_3^\pm(z)| I_{E_{1,n}^{\pm\frac{1}{2}}}(r) I_{HH_{1,n}^{\pm\frac{3}{2}}}(r) \right. \\ &\quad \pm \frac{\hbar}{r m_0} (j_z \mp \frac{1}{2}) \left[|f_1^\pm(z)|^2 + |f_4^\pm(z)|^2 \right] |I_{E_{1,n}^{\pm\frac{1}{2}}}(r)|^2 \\ &\quad \left. \pm \frac{\hbar}{r m_0} (j_z \mp \frac{3}{2}) |f_3^\pm(z)|^2 |I_{HH_{1,n}^{\pm\frac{3}{2}}}(r)|^2 \right\} \hat{\theta}, \quad (6) \end{aligned}$$

where m_0 is the bare electron mass and P is the Kane parameter [29, 44, 45] appearing due to the coupling between conduction and valence bands. Here, the first term is the “Bloch velocity” contribution to the average current as it stems from the periodic part of the Bloch function, while the second term is the contribution from the envelope function [28, 29]. Using $j_z \sim 1$, $P = 0.9055$ eV.nm [29] and $r \sim R = 40$ nm we estimate the ratio of the Bloch to envelope contributions $\left(\frac{\sqrt{2}P}{\hbar} \right) / \left(2 \times \frac{\hbar}{R m_0} \right) \sim 340$, thus showing we can neglect the envelope velocity part in agreement with Ref. [29] (see SM, Sec. IX for a detailed comparison). Since

$I_{E_1,n}^{j_z \mp \frac{1}{2}} = I_{E_1,n}^{-j_z \pm \frac{1}{2}}$ and $I_{HH_1,n}^{j_z \mp \frac{3}{2}} = I_{HH_1,n}^{-j_z \pm \frac{3}{2}}$, we find

$$\langle \mathbf{j}_{j_z,n}^{\pm} \rangle(\mathbf{r}) = -\langle \mathbf{j}_{-j_z,n}^{\mp} \rangle(\mathbf{r}), \quad (7)$$

which shows the helical nature of the edge-like states within the gray region in Figs. 1(c) and 1(e).

To compare the topological QD edge states and the edge-like states in the trivial QD, we plot Eq. (6) in Fig. 2 for the spin up QD levels $j_z = 3/2$ and $j_z = 5/2$ [see Figs. 1(c) and 1(e), gray area] with $R = 40\text{nm}$. Interestingly, although the $j_z = 3/2$ wave functions of both trivial and topological QDs are extended, their circulating currents are localized near the QD edges. This arises from the product of the upper and lower wave function components in Eq. (6). We find the highest current densities for the trivial edge-like states (due to the smaller d), Figs. 2(a), 2(b). However, the integrated current density over half of the cross section of the QD $I_{j_z,n}^{\pm} = \int d\mathbf{S} \cdot \langle \mathbf{j}_{j_z,n}^{\pm} \rangle = \int_0^R dr \int_{-\frac{d}{2}}^{\frac{d}{2}} dz |\langle \mathbf{j}_{j_z,n}^{\pm} \rangle| \sim 0.17 \mu\text{A}$ for both topological and trivial edge states to within 2%, i.e., it shows no significant difference.

Linear conductance. — To further compare the topological and trivial edge-like states, we calculate the two-terminal linear-response QD conductance \mathcal{G} (at $T = 0\text{K}$) [30] by coupling the dots to left (L) and right (R) leads, Fig. 1(b). Our Hamiltonian reads

$$\begin{aligned} \mathcal{H} = & \sum_i \varepsilon_i d_i^{\dagger} d_i + \sum_{k_{\alpha}, \alpha, \sigma} \varepsilon_{k_{\alpha}, \sigma} c_{k_{\alpha}, \sigma}^{\dagger} c_{k_{\alpha}, \sigma} + \sum_{i, k_{\alpha}, \alpha, \sigma} V_{k_{\alpha}, \sigma}^i d_i^{\dagger} c_{k_{\alpha}, \sigma} \\ & + \sum_{i \neq j} t_{ij} d_j^{\dagger} d_i + H.C., \end{aligned} \quad (8)$$

where d_i^{\dagger} creates an electron in the QD state $|i\rangle$ [Eq. (4)] with energy $\varepsilon_i = \varepsilon_i(R, V_g)$ [obtained from Eq. (3)], i denotes the set of QD quantum numbers j_z, \pm (or \uparrow, \downarrow [40]), and n (V_g is an additional gate controlling the dot levels with respect to the Fermi energy ε_F of the leads), and $c_{k_{\alpha}, \sigma}^{\dagger}$ creates an electron in the lead $\alpha = L, R$ with wave-vector k_{α} , energy $\varepsilon_{k_{\alpha}, \sigma}$ and spin component $\sigma = \uparrow, \downarrow$. The spin-conserving matrix element $V_{k_{\alpha}, \sigma}^i$ denotes the dot-lead coupling, while t_{ij} couples the dot levels. Next we focus on only four QD states with well-defined σ , as shown in Fig. 3(a). This can be achieved by tuning the conduction window and the QD levels via external gates.

Figures 3(b) and 3(c) show the QD conductance $\mathcal{G} = \mathcal{G}_{\uparrow} + \mathcal{G}_{\downarrow}$ for the four topological and trivial edge states with $j_z = \pm 7/2$ and $j_z = \pm 9/2$ [see green triangles in Figs. 1(c) and 1(e)], as a function of the QD radius R and the gate potential V_g . The radius R can be varied experimentally through an electrostatic confining potential [46]. The conductance for both the topological and trivial edge-like states show similar behaviors, i.e., double Lorentzian-like profiles centered approximately at the QD levels $\varepsilon_i(R, V_g)$, separated by a dip, and peaked at $2e^2/h$; this is clearly seen in the insets of Figs. 3(b) and

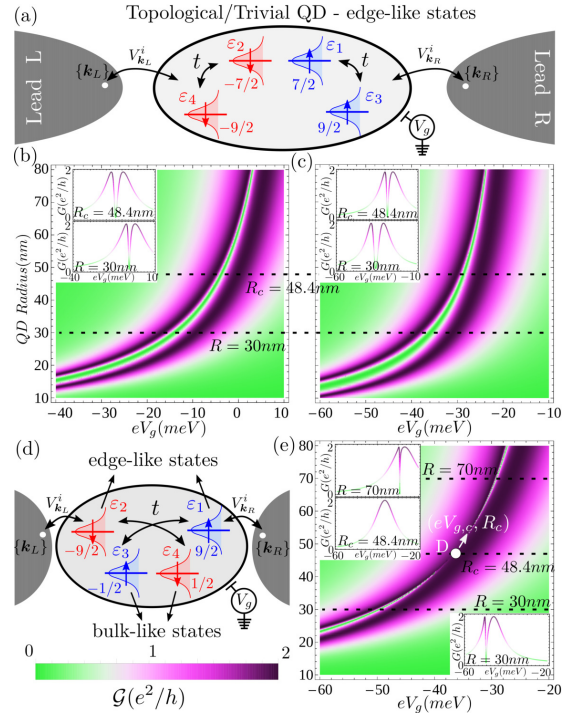


Figure 3. (a) Schematic QD Hamiltonian for the four topological and trivial edge states with $j_z = \pm 7/2$ and $j_z = \pm 9/2$. QD conductance \mathcal{G} at $T = 0\text{K}$ for the topological (b) and trivial (c) edge states in Fig. 3(a). (d) Same as (a) for the coexisting $j_z = \pm 1/2$ bulk and $j_z = \pm 9/2$ edge states and the corresponding \mathcal{G} for the trivial case (e). Here we use $t = 1 \text{ meV}$ and $\Gamma = 4 \text{ meV}$ (SM, Sec. X).

3(c) for two distinct R 's. The dip follows from a destructive interference between the two same-spin edge states in the overlapping tails of the broadened QD density of states. See SM (Sec. X) where the conductance \mathcal{G} is expressed as a sum of interfering amplitudes using Green functions [47].

Interestingly, bulk-like and edge-like valence edge states can coexist and even be degenerate in energy. In this case, our calculated conductances exhibit a crossover from a double-peak resonance for $R < R_c \text{ nm}$ and $V_g < V_{g,c}$ to a single-peak resonance at $R = R_c \text{ nm}$ and $V_g = V_{g,c}$ and back to a double-peak resonance for $R > R_c \text{ nm}$ and $V_g > V_{g,c}$. This is shown in Fig. 3(e) (and its insets) for a trivial QD, but a similar plot also holds for a topological QD. In the SM (Sec. X) we show that when the bulk and edge-state Kramers pairs obey $\varepsilon_{3(4)}(R, V_g) - \varepsilon_{1(2)}(R, V_g) = t \left(\frac{V^{3(4)}}{V^{1(2)}} - \frac{V^{1(2)}}{V^{3(4)}} \right)$, two of the transport channels are completely decoupled from the

leads and hence a single resonance (peaked $\mathcal{G} = 2e^2/h$) emerges. For the parameters in Fig. 3(e) this decoupling occurs when the two Kramers pairs (bulk and edge) become degenerate, i.e., $\varepsilon_{1(2)}(R_c, V_{g,c}) = \varepsilon_{3(4)}(R_c, V_{g,c})$ (incidentally, their protection is lost in this case).

Concluding remarks.— We have predicted that Bi-based InAs QWs can become room-temperature TIs (~ 30 meV) for well widths $d > 6.9$ nm. Our realistic $\mathbf{k}\cdot\mathbf{p}$ approach allows us to calculate the parameters of an effective BHZ model from which we can define cylindrical QDs via further confinement. By solving the BHZ QD eigenvalue equation analytically, we find quite surprisingly that both topological and non-topological BHZ QDs feature similar (i) protected helical edge states, (ii) circulating currents and (iii) two-terminal linear conductances \mathcal{G} exhibiting a two-peak resonance as a function of the QD radius and the gate V_g controlling its energy levels relative to the Fermi level of the leads. Hence our proposed cylindrical QDs – topological and non-topological – are equivalent from the standpoint of edge-state transport, in contrast with TIs. We expect that our work stimulate experimental research on this topic.

This work was supported by CNPq, CAPES, UFRN/MEC, FAPESP, PRP-USP/Q-NANO and the Center for Emergent Materials, an NSF MRSEC under Award No. DMR-1420451. We acknowledge the kind hospitality at the International Institute of Physics (IIP/UFRN), where part of this work was done and valuable discussions with Poliana H. Penteado and Joost van Bree. DRC also acknowledges useful discussions with Edson Vernek and Luis G. G. D. Silva.

-
- [1] C. L. Kane and E.J. Mele, Phys. Rev. Lett. **95**, 226801 (2005).
- [2] B. A. Bernevig, Taylor L. Hughes, Shou-Cheng Zhang, Science **314**, 1757, (2006).
- [3] M. König et. al., Science, **318**, 766, (2007).
- [4] M. Z. Hasan and C. L. Kane, Rev. Mod. Phys. **82**, 3045, (2010).
- [5] Chaoxing Liu, Taylor L. Hughes, Xiao-Liang Qi, Kang Wang, Shou-Cheng Zhang, Phys. Rev. Lett. **100**, 236601 (2008).
- [6] Y. Xia, et. al., Nature Phys. **5**, 398 (2009).
- [7] H. Zhang, et. al., Nature Phys. **5**, 438 (2009).
- [8] W. Feng, W. Zhu, H. H. Weiering, G. M. Stocks, Y. Yao, and D. Xiao, Phys. Rev. B **85**, 195114 (2012).
- [9] O. P Sushkov and A. H. Castro Neto, Phys. Rev. Lett. **110**, 186601 (2013).
- [10] D. Zhang, W. Lou, M. Miao, S. C. Zhang, and K. Chang, Phys. Rev. Lett. **111**, 156402 (2013).
- [11] S. I. Erlingsson, J. C. Egues, Phys. Rev. B **91**, 035312 (2015).
- [12] Ivan Knez, et. al., Phys. Rev. Lett. **107**, 136603 (2011).
- [13] Fabrizio Nichele, et. al., New. J. Phys. **18**, 083005 (2016).
- [14] K. Chang, Wen-Kai Lou, Phys. Rev. Lett. **106**, 206802 (2011).
- [15] M. Korkusinski, P. Hawrylak, Scientific Reports **4**, 4903 (2014).
- [16] G. J. Ferreira and D. Loss, Phys. Rev. Lett. **111**, 106802 (2013).
- [17] H. P. Paudel and M. N. Leuenberger, Phys. Rev. B. **88**, 085316 (2013).
- [18] C. Ertler, M. Raith and J. Fabian, Phys. Rev. B. **89**, 075432 (2014).
- [19] A. Kundu, A. Zazunov, A. L. Yeyati, T. Martin and R. Egger, Phys. Rev. B. **83**, 125429 (2011).
- [20] J. Li, et al., Phys. Rev. B. **90**, 115303 (2014).
- [21] J.-X. Qu, et al., J. Appl. Phys. **122**, 034307 (2017).
- [22] H. Xu and Y.C. Lai, Phys. Rev. B. **92**, 195120 (2015).
- [23] A. A. Sukhanov, Phys. B. Condens. Matter **513**, 1 (2017).
- [24] S.-N. Zhang, H. Jiang, and H. W. Liu, Mod. Phys. Lett. B **27**, 1350104 (2013).
- [25] T. M. Herath, P. Hewageegana and V. Apalkov, J. Phys. Condens. Matter **26**, 115302 (2014).
- [26] B. Scharf and I. Zutíć, Phys. Rev. B. **91**, 144505 (2015).
- [27] B. Messias de Resende, F. C. de Lima, R. H. Miwa, E. Vernek, and G. J. Ferreira, Phys. Rev. B. **96**, 161113(R) (2017).
- [28] J. van Bree, A. Yu. Silov, P. M. Koenraad and M. E. Flatté, Phys. Rev. B. **90**, 165306 (2014).
- [29] J. van Bree, A. Yu. Silov, P. M. Koenraad and M. E. Flatté, Phys. Rev. Lett. **112**, 187201 (2014).
- [30] Y. Meir, Ned S. Wingreen, Phys. Rev. Lett. **68**, 2512 (1992).
- [31] K. Ma, et. al., Appl. Phys. Lett. **55**, 2420 (1989)
- [32] Z. Fang, et. al., J. Appl. Phys. **68**, 1187 (1990)
- [33] P. T. Webster, et. al., J. Vac. Soc. & Tech. B **32**, 02C120-1 (2014).
- [34] W. Shan, et. al., Phys. Rev. Lett. **82**, 1221, (1999)
- [35] W. Walukiewicz, et. al., Phys. Rev. Lett. **85**, 1552, (2000)
- [36] J. Wu, W. Walukiewicz, and E. E. Haller, Phys. Rev. B, **65**, 233210, (2002)
- [37] K. Alberi, J. Wu, W. Walukiewicz, K. M. Yu, O. D. Dubon, S. P. Watkins, C. X. Wang, X. Liu, Y.-J. Cho, and J. Furdyna, Phys. Rev. B **75** 045203 (2007).
- [38] W. H. Lau, J. T. Olesberg and M. E. Flatté, cond-mat/0406201.
- [39] P. Michetti, P.H. Penteado, J.C. Egues, and P. Recher, Semicond. Sci. Technol. **27**, 124007 (2012).
- [40] Due to the mixing between spin up \uparrow and spin down \downarrow components within the $|E_{1\pm}\rangle$ subbands, the spin index \uparrow (\downarrow) is not a good quantum number within the BHZ subspace $+$ ($-$). However, we calculate $\langle j_z \pm | s_z | j_z \pm \rangle \simeq \pm \frac{\hbar}{2}$; hence it is an excellent approximation to identify the \pm subspace with \uparrow, \downarrow .
- [41] D. G. Rothe, R. W. Reinthaler, C-X Liu, L. W. Molenkamp, S-C Zhang and E. M. Hankiewicz, New J. Phys. **12**, 065012 (2010).
- [42] X.-L. Qi and S. C. Zhang, Rev. Mod. Phys. **83**, 1057, (2011).
- [43] J. I. Climente, et. al., New J. Phys. **15**, 093009 (2013).
- [44] E. O. Kane, J. Phys. Chem. Solids **1**, 249 (1957).
- [45] R. S. Calsaverini, E. Bernardes, J. C. Egues, and D. Loss, Phys. Rev. B **78**, 155313 (2008).
- [46] L. C. Camenzind, et. al., arXiv:cond-mat/1711.01474.
- [47] M. L. Ladrón de Guevara, F. Claro, and Pedro A. Orellana, Phys. Rev. B **67**, 195335 (2003); G.-H. Ding, C. K. Kim, and K. Nahm, Phys. Rev. B **71**, 205313 (2005); H. Lu, R. Lü, and B.-f. Zhu, Phys. Rev. B **71**, 235320

Supplemental Material

**Blurring the boundaries between topological and non-topological
phenomena in dots**

Denis R. Candido,¹ M. E. Flatté,² and J. Carlos Egues^{1,3}

¹*Instituto de Física de São Carlos, Universidade de São Paulo,
13560-970, São Carlos, São Paulo, Brazil*

²*Department of Physics and Astronomy and Optical Science and Technology Center,
University of Iowa, Iowa City, Iowa 52242, USA*

³*International Institute of Physics, Federal University of Rio Grande do Norte,
59078-970, P. O. Box 1613, Natal, Brazil*

(Dated: August 24, 2018)

I. InAs_{1-x}Bi_x QUANTUM WELLS: A NEW 2D TOPOLOGICAL INSULATOR.

The properties of III-V semiconductors doped with isoelectronic dopants that generate resonant states have been explored over the past fifteen years due to their dramatically smaller band gaps than the original host. The origin of this effect can be understood through the repulsion between the near-band-edge resonant state of the dopant and the band edge of the host. Dramatic changes in the band gap of GaAs through the addition of dilute nitrogen doping due to a resonant state in the conduction band, or through the addition of Bi due to a resonant state in the valence band, have been obtained. We use the experimentally obtained change in band gap of InAsBi of 58 meV/% Bi [1–3] for the electronic parameters of the bulk material. The resulting bulk material, sandwiched in a quantum well with symmetric AlSb barriers and grown on GaSb, is then studied using a superlattice electronic structure theory that has been applied to a broad range of narrow-gap semiconductor materials with inversion asymmetry and large spin-orbit interaction [4].

II. EFFECTIVE BHZ PARAMETERS FOR InAs_{0.85}Bi_{0.15}/AlSb QUANTUM WELLS.

The BHZ parameters A , B , C , D and M are obtained accordingly to Ref. [5] for our fourteen bulk band basis [4]. We calculate them for the a) topological trivial InAs_{0.85}Bi_{0.15} QW with $d = 6$ nm and b) topological non-trivial QW with $d = 8$ nm. The respective values of the BHZ parameters are given in Tab. I.

InAs _{1-x} Bi _x	d (nm)	A (meV.nm)	B (meV.nm ²)	C (meV)	D (meV.nm ²)	M (meV)
$x = 0.15$	6	543.2	-201.7	0	-180.0	16.1
$x = 0.15$	8	488.0	-339.3	0	-300.0	-15.5

Table I. Effective BHZ parameters for InAs_{1-x}Bi_x/AlSb QW with different well thicknesses (6 nm and 8 nm) and $x = 0.15$ of Bi concentration. For convenience we have chosen here $C = 0$ for all the cases.

III. BHZ SOFT-WALL ENERGY LEVELS FOR A CYLINDRICAL QD.

Here we derive a generalization of the transcendental equation [Eq. (3) in the main text] for the BHZ Hamiltonian with a cylindrical soft-wall confinement having equal conduction and valence

barriers $M_O - M$ given by [6]

$$V_c = \begin{pmatrix} V(r)\sigma_z & 0 \\ 0 & V(r)\sigma_z \end{pmatrix}, \quad V(r) = \begin{cases} 0 & r < R \\ M_O - M > 0 & r > R \end{cases} \quad (\text{S1})$$

For the inner region ($r < R$) we have the regularized modified Bessel functions at $r = 0$ (first kind)

$$\psi_{j_z, n}^{\pm, r < R}(r, \theta) = \sum_{\sigma=\pm} p_{j_z, n, \sigma}^{\pm} \left[\frac{I_{j_z \mp \frac{1}{2}}(\lambda_\sigma r) e^{i(j_z \mp \frac{1}{2})\theta}}{D_+ \lambda_\sigma^2 - E_{j_z, n}^{\pm} + C_+} I_{j_z \mp \frac{3}{2}}(\lambda_\sigma r) e^{i(j_z \mp \frac{3}{2})\theta} \right] = \sum_{\sigma=\pm} p_{j_z, n, \sigma}^{\pm} \left[\frac{I_{j_z \mp \frac{1}{2}}(\lambda_\sigma r) e^{i(j_z \mp \frac{1}{2})\theta}}{R_{j_z, n, \sigma}^{\pm} I_{j_z \mp \frac{3}{2}}(\lambda_\sigma r) e^{i(j_z \mp \frac{3}{2})\theta}} \right], \quad (\text{S2})$$

where $D_+ = D + B$, $C_+ = C + M$, $R_{j_z, n, \sigma}^{\pm} = \frac{(D_+ \lambda_\sigma^2 - E_{j_z, n}^{\pm} + C_+)}{iA(\pm \lambda_\sigma)}$, and the other parameters have been defined in the main text [see definitions below Eq. (4)]. For the outer region ($r > R$) we have the regularized modified Bessel at $r \rightarrow \infty$ (second kind)

$$\psi_{j_z, n}^{\pm, r > R}(r, \theta) = \sum_{\sigma=\pm} r_{j_z, n, \sigma}^{\pm} \left[\frac{K_{j_z \mp \frac{1}{2}}(\lambda_\sigma^O r) e^{i(j_z \mp \frac{1}{2})\theta}}{D_+ \lambda_\sigma^{O2} - E_{j_z, n}^{\pm} + C_+} K_{j_z \mp \frac{3}{2}}(\lambda_\sigma^O r) e^{i(j_z \mp \frac{3}{2})\theta} \right] = \sum_{\sigma=\pm} r_{j_z, n, \sigma}^{\pm} \left[\frac{K_{j_z \mp \frac{1}{2}}(\lambda_\sigma^O r) e^{i(j_z \mp \frac{1}{2})\theta}}{-R_{j_z, n, \sigma}^{O, \pm} K_{j_z \mp \frac{3}{2}}(\lambda_\sigma^O r) e^{i(j_z \mp \frac{3}{2})\theta}} \right], \quad (\text{S3})$$

with $\lambda_\sigma^O = \lambda_\sigma (M \rightarrow M^O)$ and $R_{j_z, n, \sigma}^{O, \pm} = R_{j_z, n, \sigma}^{\pm} (M \rightarrow M^O)$. To find the quantized energies of the system, we first need to match the continuity of 1) the wave function and 2) its derivative in the radial direction at $r = R$, yielding

$$\psi_{j_z, n}^{\pm, r < R}(r = R, \theta) = \psi_{j_z, n}^{\pm, r > R}(r = R, \theta), \quad (\text{S4})$$

$$\partial_r \psi_{j_z, n}^{\pm, r < R}(r = R, \theta) = \partial_r \psi_{j_z, n}^{\pm, r > R}(r = R, \theta). \quad (\text{S5})$$

Choosing $\theta = 0$, we combine Eqs. (S4) and (S5) in the following matrix equation

$$\begin{pmatrix} I_{j_z \mp \frac{1}{2}}(\lambda_+ R) & I_{j_z \mp \frac{1}{2}}(\lambda_- R) & K_{j_z \mp \frac{1}{2}}(\lambda_+^O R) & K_{j_z \mp \frac{1}{2}}(\lambda_-^O R) \\ R_{j_z, n, +}^{\pm} I_{j_z \mp \frac{3}{2}}(\lambda_+ R) & R_{j_z, n, -}^{\pm} I_{j_z \mp \frac{3}{2}}(\lambda_- R) & -R_{j_z, n, +}^{O, \pm} K_{j_z \mp \frac{3}{2}}(\lambda_+^O R) & -R_{j_z, n, -}^{O, \pm} K_{j_z \mp \frac{3}{2}}(\lambda_-^O R) \\ \partial_r I_{j_z \mp \frac{1}{2}}(\lambda_+ R) & \partial_r I_{j_z \mp \frac{1}{2}}(\lambda_- R) & \partial_r K_{j_z \mp \frac{1}{2}}(\lambda_+^O R) & \partial_r K_{j_z \mp \frac{1}{2}}(\lambda_-^O R) \\ R_{j_z, n, +}^{\pm} \partial_r I_{j_z \mp \frac{3}{2}}(\lambda_+ R) & R_{j_z, n, -}^{\pm} \partial_r I_{j_z \mp \frac{3}{2}}(\lambda_- R) & -R_{j_z, n, +}^{O, \pm} \partial_r I_{j_z \mp \frac{3}{2}}(\lambda_+^O R) & -R_{j_z, n, -}^{O, \pm} \partial_r I_{j_z \mp \frac{3}{2}}(\lambda_-^O R) \end{pmatrix} \begin{pmatrix} p_{j_z, n, +}^{\pm} \\ p_{j_z, n, -}^{\pm} \\ -r_{j_z, n, +}^{\pm} \\ -r_{j_z, n, -}^{\pm} \end{pmatrix} = 0, \quad (\text{S6})$$

whose determinant when set to zero determines all the non-trivial quantized energy levels for the soft wall case. We solve Eq. (S6) for a soft wall barrier $M_O = 2$ eV using the same set of BHZ

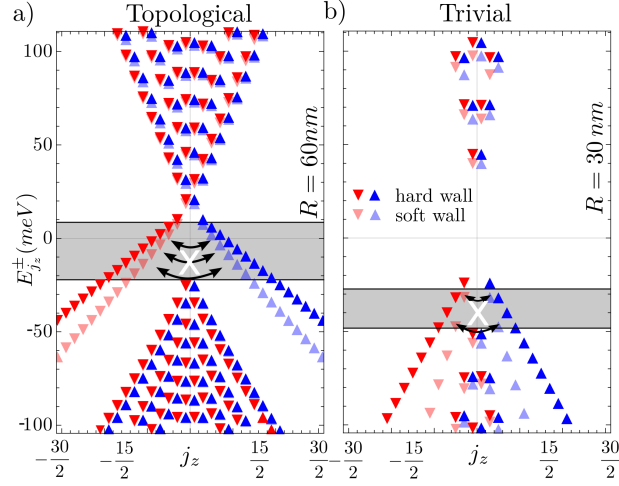


Figure S1. a) Topological QD energy levels as a function of the total angular momentum j_z for the soft ($M_O = 2 \text{ eV}$) and hard wall ($M_O \rightarrow \infty$) cases for $R = 60 \text{ nm}$. b) Same as a) but for a trivial QD with $R = 30 \text{ nm}$. The arrows denote forbidden transitions between spin up and spin down states of the BHZ blocks, blue and red symbol, respectively.

parameters and QD radii as that of Figs. 1(c) and 1(e) in the main text. We plot in Fig. (S1) both the soft and hard wall QD energy levels as a matter of comparison. The solid symbols represent the hard wall case, while the fading color symbols represent the soft wall case. We see that the bulk-like and the edge-like states of both the topological and trivial QDs behave similarly for soft wall confinement. The bulk-like levels are shifted by a small amount independent of j_z , while the edge states are shifted by a larger amount proportional to j_z . This follows from the edge states being more localized at the interface than the bulk states as we increase j_z . Therefore, the larger j_z is the more sensitive to the change from hard to soft wall the wave functions are, thus changing their corresponding energies. We emphasize that even in the presence of the soft wall confinement we still find protected trivial helical edge states within the energy range indicated by the gray area of Fig. (S1) b). We assume that $M_O = 2 \text{ eV}$ represents a realistic AISb soft wall barrier heterostructure. Although this choice gives just two Kramers pairs of *geometrically protected* trivial helical edge states, the soft wall barrier (possibly) modulated by tunable gates on our QWs could lead to a full control of the number of protected trivial helical edge states.

IV. ORDINARY InAs QD HAMILTONIAN.

In contrast to the topologically trivial and non-trivial InAsBi QWs, the ordinary InAs/AlSb QW with its large subband gap can be described approximately by decoupled parabolic dispersions using realistic effective masses. Thus we solve for the corresponding conduction and valence QD energy levels independently. The effective Hamiltonian for (the doubly-degenerate) lowest conduction $|C_{1\pm}\rangle$ (with energy E_{C_1}) and highest valence $|H_{1\pm}\rangle$ (with energy E_{H_1}) QW subbands reads

$$\mathcal{H}_{InAs} = \begin{bmatrix} \frac{\hbar^2}{2m_{C_1}} \mathbf{k}^2 + E_{C_1} & 0 & 0 & 0 \\ 0 & \frac{\hbar^2}{2m_{H_1}} \mathbf{k}^2 - E_{H_1} & 0 & 0 \\ 0 & 0 & \frac{\hbar^2}{2m_{C_1}} \mathbf{k}^2 + E_{C_1} & 0 \\ 0 & 0 & 0 & \frac{\hbar^2}{2m_{H_1}} \mathbf{k}^2 - E_{H_1} \end{bmatrix}. \quad (S7)$$

where realist $\mathbf{k}\cdot\mathbf{p}$ calculations [4] for the InAs/AlSb QW with thickness $d = 6$ nm yield effective masses $m_{C_1} = 0.0473 m_0$ and $m_{H_1} = -0.2163 m_0$ and $E_{C_1} - E_{H_1} = 401.4$ meV. The respective wave functions for cylindrical hard-wall confinement can be straightforwardly obtained

$$\psi_{j_z, n}^{C_{1\pm}}(r, \theta) = p_{j_z, n} I_{j_z \mp \frac{1}{2}}(\lambda_{C_1} r) e^{i(j_z \mp \frac{1}{2})\theta}, \quad (S8)$$

$$\psi_{j_z, n}^{H_{1\pm}}(r, \theta) = q_{j_z, n} I_{j_z \mp \frac{3}{2}}(\lambda_{H_1} r) e^{i(j_z \mp \frac{3}{2})\theta}, \quad (S9)$$

with $\lambda_{C_1} = \sqrt{\frac{E_{j_z, n}^{C_{1\pm}} - E_{C_1}}{-\frac{\hbar^2}{2m_{C_1}}}}$, $\lambda_{H_1} = \sqrt{\frac{E_{j_z, n}^{H_{1\pm}} + E_{H_1}}{-\frac{\hbar^2}{2m_{H_1}}}}$ and $p_{j_z, n}$, $q_{j_z, n}$ being the normalization factors. The energies are determined by imposing the vanishing of the above wave functions at $r = R$, yielding

$$E_{j_z, n}^{C_{1\pm}} = E_{C_1} + \frac{\hbar^2}{2m_{C_1}} \left(\frac{\alpha_{j_z \mp \frac{1}{2}}^n}{R} \right)^2, \quad (S10)$$

$$E_{j_z, n}^{H_{1\pm}} = -E_{H_1} + \frac{\hbar^2}{2m_{H_1}} \left(\frac{\alpha_{j_z \mp \frac{3}{2}}^n}{R} \right)^2, \quad (S11)$$

where $\alpha_{j_z \mp \frac{1}{2}}^n$ ($\alpha_{j_z \mp \frac{3}{2}}^n$) are the n^{th} -order zero of the modified Bessel function of order $j_z \mp \frac{1}{2}$ ($j_z \mp \frac{3}{2}$). Using now that the modified Bessel functions satisfy $I_{j_z \mp \frac{1}{2}}(\lambda r) = I_{-j_z \pm \frac{1}{2}}(\lambda r)$ and $I_{j_z \mp \frac{3}{2}}(\lambda r) =$

$I_{-j_z \pm \frac{3}{2}}(\lambda r)$, we find the following degeneracies

$$E_{j_z \mp \frac{1}{2}, n}^{C_{1\pm}} = E_{-j_z \pm \frac{1}{2}, n}^{C_{1\pm}}, \quad (\text{S12})$$

$$E_{j_z \mp \frac{3}{2}, n}^{H_{1\pm}} = E_{-j_z \pm \frac{3}{2}, n}^{H_{1\pm}}. \quad (\text{S13})$$

Together with the degeneracy due to time reversal symmetry, we find for each j_z level (with $j_z \neq \pm \frac{1}{2}$ for $C_{1\pm}$ and $j_z \neq \pm \frac{3}{2}$ for $H_{1\pm}$) the 4-fold degeneracies discussed in the main text

$$E_{j_z \mp \frac{1}{2}, n}^{C_{1\pm}} = E_{-(j_z \mp \frac{1}{2}), n}^{C_{1\mp}} = E_{-j_z \pm \frac{1}{2}, n}^{C_{1\pm}} = E_{-(-j_z \pm \frac{1}{2}), n}^{C_{1\mp}}, \quad (\text{S14})$$

$$E_{j_z \mp \frac{3}{2}, n}^{H_{1\pm}} = E_{-(j_z \mp \frac{3}{2}), n}^{H_{1\mp}} = E_{-j_z \pm \frac{3}{2}, n}^{H_{1\pm}} = E_{-(-j_z \pm \frac{3}{2}), n}^{H_{1\mp}}. \quad (\text{S15})$$

Additionally, the helical character in the ordinary InAs QD is also absent since the degenerate states Eqs. (S12) and (S13) have circulating currents with opposite propagation directions. Next we estimate the influence of the electron-hole mixing and the spin-orbit couplings of the Rashba and Dresselhaus types on the energy spectrum of ordinary InAs QDs. For completeness, in Sec. V we also assess the effect of the intrinsic bulk-inversion asymmetry (BIA) term on the Bi-based BHZ QD energy levels.

A. Ordinary InAs QD in the presence of C_1 - H_1 mixing

Here we investigate the influence of including the mixing between the $|C_{1\pm}\rangle$ and $|H_{1\pm}\rangle$ subbands in the effective InAs/AlSb QW Hamiltonian, Eq. (S7). We model this coupling through the $\pm A'k_{\pm}$ terms in the Hamiltonian

$$\mathcal{H}_{InAs}^{C_1-H_1} = \begin{bmatrix} \frac{\hbar^2}{2m_{C_1}} \mathbf{k}^2 + E_{C_1} & A'k_+ & 0 & 0 \\ A'k_- & \frac{\hbar^2}{2m_{H_1}} \mathbf{k}^2 - E_{H_1} & 0 & 0 \\ 0 & 0 & \frac{\hbar^2}{2m_{C_1}} \mathbf{k}^2 + E_{C_1} & -A'k_- \\ 0 & 0 & -A'k_+ & \frac{\hbar^2}{2m_{H_1}} \mathbf{k}^2 - E_{H_1} \end{bmatrix}. \quad (\text{S16})$$

The new energies thus read

$$E_{\pm} = \frac{E_{C_1} + E_{H_1}}{2} + \frac{\hbar^2}{4} \left(\frac{1}{m_{C_1}} + \frac{1}{m_{H_1}} \right) \mathbf{k}^2 \pm \sqrt{\left[\frac{E_{C_1} - E_{H_1}}{2} + \frac{\hbar^2}{4} \left(\frac{1}{m_{C_1}} - \frac{1}{m_{H_1}} \right) \mathbf{k}^2 \right]^2 + (A'\mathbf{k})^2}. \quad (\text{S17})$$

To obtain an estimate for the QD energies, we now make $|\mathbf{k}| \approx \frac{1}{R}$ in the above formula (the QD radius is a reasonable assumption for $|\mathbf{k}|$) and use simple perturbative expansion to find

$$\Delta E_{C_1-H_1}^{mix} \approx \frac{\left(\frac{A}{R}\right)^2}{E_{C_1} - E_{H_1}}. \quad (\text{S18})$$

Using $E_{C_1} - E_{H_1} = 401.4$ meV (Sec. IV), $A' \approx 300$ meV.nm (Tab. S1) and $R = 30$ nm, we obtain

$$\Delta E_{C_1-H_1}^{mix} \approx 1 \text{ meV}, \quad (\text{S19})$$

which is much smaller as compared to the energy separation of two conduction QD levels [Fig. 1d] in the main text].

B. Ordinary InAs QD in the presence of spin orbit Rashba term

Although our calculations (main text) were done by considering symmetric InAs/AlSb QWs, we can estimate the shift in the QD energy levels due to spin-orbit interaction by including the linear Rashba term [7, 8] arising from a possible structural inversion asymmetry (SIA). For simplicity, we only consider the Rashba term in the electron subspace. In this case our Hamiltonian reads

$$\mathcal{H}_{InAs}^{Rashba} = \begin{bmatrix} \frac{\hbar^2}{2m_{C_1}} \mathbf{k}^2 + E_{C_1} & 0 & -i\alpha k_- & 0 \\ 0 & \frac{\hbar^2}{2m_{H_1}} \mathbf{k}^2 - E_{H_1} & 0 & 0 \\ i\alpha k_+ & 0 & \frac{\hbar^2}{2m_{C_1}} \mathbf{k}^2 + E_{C_1} & 0 \\ 0 & 0 & 0 & \frac{\hbar^2}{2m_{H_1}} \mathbf{k}^2 - E_{H_1} \end{bmatrix}. \quad (\text{S20})$$

The new conduction energies are given by

$$E_{C_1,SIA}^\pm = E_{C_1} + \frac{\hbar^2 \mathbf{k}^2}{2m_{C_1}} \pm \alpha |\mathbf{k}|. \quad (\text{S21})$$

Using the realistic $\alpha = 28$ meV.nm [9] and again making $|\mathbf{k}| \approx \frac{1}{R}$ with $R = 30$ nm, we obtain the QD energy level shift due the Rashba spin orbit coupling

$$\Delta E_{C_1,SIA} \approx \frac{\alpha}{R} \rightarrow \Delta E_{C_1,SIA} \approx 0.9 \text{ meV}, \quad (\text{S22})$$

which is also small as compared to the energy separation of two conduction QD energy levels [c.f., Eq. (S19)].

C. Ordinary InAs QD in the presence of bulk inversion asymmetry term (BIA)

Now we take into account the influence of the intrinsic bulk inversion asymmetry (BIA) term [8], which arises from the lack of inversion symmetry in the Zincblende structure. Here we consider only the BIA term within the electron subspace. Using the leading order BIA terms [10, 11] in Eq. (S7) we obtain

$$\mathcal{H}_{InAs}^{BIA} = \begin{bmatrix} \frac{\hbar^2}{2m_{C_1}} \mathbf{k}^2 + E_{C_1} & 0 & -\beta k_+ & 0 \\ 0 & \frac{\hbar^2}{2m_{H_1}} \mathbf{k}^2 - E_{H_1} & 0 & 0 \\ -\beta k_- & 0 & \frac{\hbar^2}{2m_{C_1}} \mathbf{k}^2 + E_{C_1} & 0 \\ 0 & 0 & 0 & \frac{\hbar^2}{2m_{H_1}} \mathbf{k}^2 - E_{H_1} \end{bmatrix}, \quad (S23)$$

which has eigenvalues

$$E_{C_1, BIA}^\pm = E_{C_1} + \frac{\hbar^2 \mathbf{k}^2}{2m_{C_1}} \pm \beta |\mathbf{k}|. \quad (S24)$$

The linear Dresselhaus parameter for InAs/AlSb QW is typically $\beta \approx 5$ meV.nm [9]. Using then $|\mathbf{k}| \approx \frac{1}{R}$ with $R = 30$ nm, we obtain the following shift in the QD energy levels

$$\Delta E_{C_1, BIA} \approx \frac{\beta}{R} \rightarrow \Delta E_{C_1, BIA} \approx 0.17 \text{ meV}, \quad (S25)$$

which is also negligible.

V. TRIVIAL InAs_{0.85}Bi_{0.15} QD IN THE PRESENCE OF BIA

In our trivial InAs_{0.85}Bi_{0.15} QD case, the presence of the BIA terms should be more important as compared to the previous case (ordinary InAs QD). The reason lies in the fact that the Bi-based compounds have larger spin-orbit interaction thus possibly enhancing the strength of the

BIA terms. In leading order, the BHZ Hamiltonian with BIA reads [12]

$$\mathcal{H}_{\text{InAsBi}}^{\text{BIA}} = C - D\mathbf{k}^2 + \begin{bmatrix} M - B\mathbf{k}^2 & Ak_+ & 0 & -\Delta_{\text{BIA}} \\ Ak_- & -M + B\mathbf{k}^2 & \Delta_{\text{BIA}} & 0 \\ 0 & \Delta_{\text{BIA}} & M - B\mathbf{k}^2 & -Ak_- \\ -\Delta_{\text{BIA}} & 0 & -Ak_+ & -M + B\mathbf{k}^2 \end{bmatrix}, \quad (\text{S26})$$

with eigenenergies given by [6]

$$E_{\text{BHZ}}^{\pm, s=\pm}(\mathbf{k}, \Delta_{\text{BIA}}) = C - D\mathbf{k}^2 \pm \sqrt{(A|\mathbf{k}| + s\Delta)^2 + (M - B\mathbf{k}^2)^2}. \quad (\text{S27})$$

Using the parameters on Tab. S1, assuming $|\mathbf{k}| \approx \frac{1}{R}$ with $R = 30$ nm, and $\Delta_{\text{BIA}} = 4$ meV (twice the value of HgTe/CdTe [12]) we estimate the energy shift in, e.g., the valence levels, as

$$E_{\text{BHZ}}^{-, s=\pm}\left(\frac{1}{R}, \Delta_{\text{BIA}}\right) - E_{\text{BHZ}}^{-, s=\pm}\left(\frac{1}{R}, \Delta_{\text{BIA}} = 0\right) \approx 2\text{meV}, \quad (\text{S28})$$

leading to small energy level shift as compared to the QD energy separation. A similar estimate also holds for the topological InAs_{0.85}Bi_{0.15} QD.

VI. THE ORIGIN OF THE EDGE STATES IN THE TRIVIAL InAsBi BHZ QDS.

In this section we show qualitatively that the reason behind the appearance of the edge states in the *trivial* InAsBi BHZ QDs is the 2×2 structure of BHZ model with a large linear-k ‘‘A term’’ as compared to the BHZ gap $2M$. We show that in this case the BHZ model supports wave functions localized at the QD edge – even in the *trivial* regime.

As already shown in the main text, the wave functions for both trivial and non-trivial BHZ QDs [Eq. (4) in the main text] correspond to linear combinations of the modified Bessel functions of the first kind $I_m[\lambda_\tau(E_{j_z, n}^\sigma)r]$, with $\lambda_{\tau=\pm}^2(E_{j_z, n}^\sigma) = -F + \tau\sqrt{F^2 - Q^2}$ and F, Q already defined in the main text. For *real* and large arguments such as $\lambda_\tau(E_{j_z, n}^\sigma)r \gg m$, these modified Bessel functions are well described by the following exponential asymptotic form [13]

$$I_m[\lambda_\tau(E_{j_z, n}^\sigma)r] \approx \frac{e^{\lambda_\tau(E_{j_z, n}^\sigma)r}}{\sqrt{2\pi\lambda_\tau(E_{j_z, n}^\sigma)r}} \left[1 - \frac{4m^2 - 1}{8\lambda_\tau(E_{j_z, n}^\sigma)r} + \dots \right]. \quad (\text{S29})$$

Topological InAsBi BHZ QDs. In this case both $\lambda_-(E_{j_z,n}^\sigma)$ and $\lambda_+(E_{j_z,n}^\sigma)$ [with $\lambda_\pm(E_{j_z,n}^\sigma)R \gg m$] assume only real values within the gap region $M < E_{j_z,n}^\sigma < -M$ with $M < 0$. Therefore, the leading order radial part of the wave function [Eq. (4) in the main text] for these states reads

$$\psi_{j_z}^\sigma(r) \approx \frac{1}{\sqrt{2\pi\lambda_+(E_{j_z,n}^\sigma)}r} \begin{pmatrix} u_+ \\ l_+ \end{pmatrix} e^{\lambda_+(E_{j_z,n}^\sigma)r} + \frac{1}{\sqrt{2\pi\lambda_-(E_{j_z,n}^\sigma)}r} \begin{pmatrix} u_- \\ l_- \end{pmatrix} e^{\lambda_-(E_{j_z,n}^\sigma)r}, \quad (\text{S30})$$

where u_\pm and l_\pm are complex constants that depend on the QD energy level $E_{j_z,n}^\sigma$. Since $\lambda_\pm(E_{j_z,n}^\sigma) > 0$, it is clear that Eq. (S30) – as expected – leads to wave functions with high probability densities near the QD edge, i.e., peaking near $r \approx R$ with $\psi_{j_z}^\sigma(R) = 0$ [Fig. 1(f)]. Note that Eq. (S30) resembles the usual helical edge-state wave functions of 2D TIs with one interface [Refs. [6, 12]]. In Fig. (S2) a) we plot for the topological $j_z = 5/2$ state within the ellipse in Fig. 1(c), the conduction component of the total wave function [Eq. (4)] and its two separate parts.

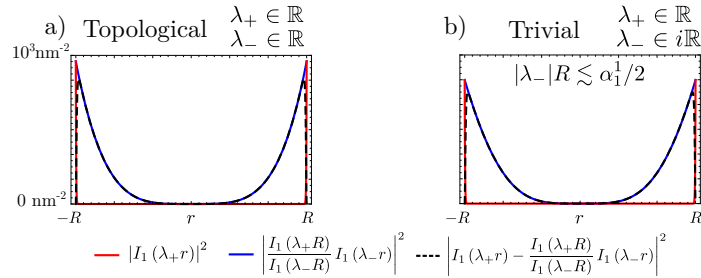


Figure S2. Plot of the larger wave function [Eq. (4)] component (dashed black line) with its two constituent functions $|I_1(\lambda_+ r)|^2$ (solid red line) and $\left| \frac{I_1(\lambda_+ R)}{I_1(\lambda_- R)} I_1(\lambda_- r) \right|^2$ (solid blue line) for the QD states within the ellipses: a) Topological QD state $j_z = \frac{5}{2}$ in Fig. 1(c) and b) Trivial QD state $j_z = \frac{5}{2}$ in Fig. 1(d).

Trivial InAsBi BHZ QDs. Unexpectedly, we find that $\lambda_-(E_{j_z,n}^\sigma)$ becomes purely imaginary, while $\lambda_+(E_{j_z,n}^\sigma)$ continues to assume *real* values [with $\lambda_+(E_{j_z,n}^\sigma)R \gg m$], for levels $E_{j_z,n}^\sigma$ lying in the valence states. Hence the modified Bessel function $I_m(\lambda_- r)$ with purely imaginary argument turn into the usual Bessel function $J_m(|\lambda_-|r)$, which oscillates between positive and negative values with an infinite number of zeros α_m^n , i.e., $J_m(\alpha_m^n) = 0$ with $n = 1, 2, 3, \dots$. Substituting Eq. (S29) into Eq. (4) (main text) and keeping only the leading order term, we obtain

$$\psi_{j_z}^\sigma(r) \approx \begin{pmatrix} cJ_{j_z \pm \frac{1}{2}}(|\lambda_-|r) \\ dJ_{j_z \pm \frac{3}{2}}(|\lambda_-|r) \end{pmatrix} + \frac{1}{\sqrt{2\pi\lambda_+ (E_{j_z,n}^\sigma)} r} \begin{pmatrix} u_+ \\ l_+ \end{pmatrix} e^{\lambda_+ (E_{j_z,n}^\sigma) r}, \quad (\text{S31})$$

corresponding to a linear combination of oscillatory and exponential functions. Here, c, d, u_+ and l_+ are complex constants that depend on the QD energy level $E_{j_z,n}^\sigma$.

Surprisingly, even though $J_m(|\lambda_-|r)$ in Eq. (S31) is an oscillatory function, we do find edge state wave functions [Fig. 1(h)] for the energy states grouped by the ellipse in Fig. 1(e) [trivial InAsBi BHZ QD]. This happens because these energy levels always satisfy $|\lambda_- (E_{j_z,n}^\sigma)| R < \alpha_m^1/2$, which implies that $J_{m \neq 0}(|\lambda_-|r)$ never oscillates but rather grows monotonically within the range $0 < r < R$ peaking near $r \approx R$ as $\psi_{j_z}^\sigma(R) = 0$, thus also contributing to the edge state character of $\psi_{j_z}^\sigma(r)$. This can be clearly seen in Fig. (S2) b) where we plot for the $j_z = \frac{5}{2}$ state within the ellipse in Fig. 1(e). More specifically, Fig. 1(e) shows the most relevant component (lower) of the wave function with its two Bessel functions $I_1(\lambda_+ r)$ and $J_1(|\lambda_-|r)$. Note, however, that the wave function of the highest valence level $m = 0$ ($j_z = 3/2$) within the ellipse in Fig. 1(h) is extended throughout the QD. This follows from $J_0(|\lambda_-|r)$ being the only Bessel function peaked at $r = 0$. Hence $\psi_{j_z}^\sigma(r)$ in Eq. (S31) becomes a linear combination of an edge wave function and a wave function centered at $r = 0$, which yields an extended pattern. [We note that all of these considerations are also valid for the HgTe/CdTe BHZ parameters as shown in Sec. VIII].

Ordinary InAs QDs. In stark contrast to the trivial InAsBi BHZ QDs here we do not find trivial edge states. As discussed in Sec. IV, the well-known ordinary InAs QD wave functions [Eqs. (S8) and (S9)] are given by the modified Bessel functions $I_{j_z} [\lambda_{C_1(H_1)} (E_{j_z,n}^{C_1(H_1)}) r]$, with $\lambda_{C_1(H_1)} (E_{j_z,n}^{C_1(H_1)}) = \sqrt{\frac{2m_{C_1(H_1)}}{\hbar^2} (E_{C_1(H_1)} - E_{j_z,n}^{C_1(H_1)})}$. They arise from the quadratic InAs QW Hamiltonian in Eq. (S7) which gives rise to parabolic dispersions [Sec. IV]. Differently from $\lambda_\tau (E_{j_z,n}^\sigma)$ for the BHZ QDs, here $\lambda_{C_1(H_1)} (E_{j_z,n}^{C_1(H_1)})$ always assume *purely imaginary* values for the valence and conduction levels of Fig. 1(d) thus yielding *only* oscillatory wave functions Fig. 1(g) (except for $j_z = 1/2$). This is analogous to the problem of a particle in an infinite well of width L with wave functions $\psi_n = \sqrt{\frac{2}{L}} \sin\left(\frac{n\pi}{L}z\right)$, $n = 1, 2, \dots$. Here, however, due to the cylindrical symmetry of our problem, we have Bessel functions instead of Sines.

From the above it is clear that the structure of the BHZ model underlying our InAsBi dots is a relevant ingredient producing the *trivial* edge states – similarly to the topological case. More specifically, for our BHZ parameters trivial edge states arise only when $|\lambda_- (E_{j_z,n}^\sigma)| R \lesssim \alpha_m^1/2$ so that

$J_{m \neq 0}(|\lambda_-|r)$ be a monotonic function for $0 < r < R$. For dot levels near the top of the valence states [grouped by the ellipse in Fig. 1(e)] we have $\lambda_-(E_{j_z, n}^\sigma) \approx \sqrt{\frac{2M}{A^2}(E_{j_z, n}^\sigma + M)}$. Hence the presence of trivial edge states in QDs is *controlled* by the strength of the factor $|\lambda_-|R \propto \sqrt{\frac{2M}{(A/R)^2}}$, where $2M$ is the subband gap and A/R is the coupling between the conduction and valence subbands assuming $k \sim 1/R$. As a consequence, trivial edge states appear in either InAsBi or HgTe QDs (as shown in Sec. VIII) but not in InAs/GaSb QDs. This follows from the small A term in InAs/GaSb dots as compared to InAsBi and HgTe cases, which in turn follows from the small overlap between the electron and hole envelope functions in type-II double QWs.

VII. PERSISTENCE OF THE GEOMETRICALLY PROTECTED TRIVIAL HELICAL EDGE STATES FOR INCREASING QD RADII.

We investigate here the persistence of the protected trivial helical edge-like states as a function of the QD radius R . Due to the distinct wave function character between the edge-like and bulk-like states, their energies behave differently as a function of the QD radius R . For the trivial edge-like states, the wave functions are more localized at the interface ($r = R$) with the corresponding eigenenergies not so sensitive to the QD size R . On the other hand, the bulk-like wave functions are extended through the whole QD and have very sensitive eigenenergies to R changes. Due to this different sensitivity to the QD radius, the energies of the edge-like and bulk-like states can cross each other as we increase R , thus destroying the robustness of the trivial edge-like states against scattering.

We plot in Fig. (S3) the energy levels as a function of R for the four spin up trivial helical edge-like energies $j_z = \frac{3}{2}, \frac{5}{2}, \frac{7}{2}, \frac{9}{2}$ in the gray area of Fig. 1(e) in the main text together with the nearest bulk-like energy level $j_z = \frac{1}{2}$ outside the gray area. The bulk-like energy level is more sensitive to the QD radius and cross the edge-like energy levels at $R_{c1} = 44$ nm and $R_{c2} = 106$ nm [see red points in Fig. (S3)], where the number of *geometrically protected* trivial helical edge states is decreased by one at each crossing. Although the number of *geometrically protected* trivial helical states have decreased, the four trivial helical edge states persist for a wide radius range $0 < R < 44$ nm. We emphasize that even for $R > 44$ nm, where we have just three pairs of protected trivial helical edge-like states, our main feature will still remain for a reasonable energy window. As for the topological QDs, we find that their bulk-like and edge-like states behave similarly to the ones of the trivial QDs. Thus we still have the similar energy crossing between

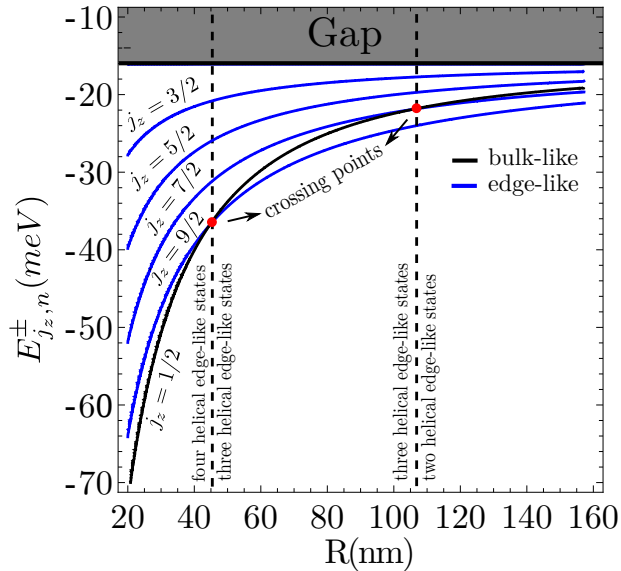


Figure S3. Trivial spin up edge-like energy levels $j_z = \frac{3}{2}, \frac{5}{2}, \frac{7}{2}, \frac{9}{2}$ within the gray area of Fig. 1(e) (main text) and their nearest bulk-like energy level $j_z = \frac{1}{2}$ plotted as function of the QD radius. The red dots indicate the crossing points where the number of the protected trivial edge states decreases by one.

bulk and edge states arising from their different sensitivity to the QD radius.

VIII. EXTENDED QD ENERGY LEVELS FOR DIFFERENT BHZ PARAMETER SETS

We plot in Fig. (S4) the QD energy levels for three different sets of HgTe/CdTe BHZ parameters given in Refs. [6, 12, 14]. Surprisingly, the existence of trivial helical edge states protected against elastic scattering holds, showing thus this is not a particular feature of our $\text{InAs}_{0.85}\text{Bi}_{0.15}$ QD. On the other hand, the number of protected trivial helical edge states within the gray area depends strongly on the BHZ parameters. We find that the smaller the difference $|D| - |B|$ with $D < 0$ ($D > 0$) is the larger the number of protected helical edge states in the valence (conduction) subspace are, thus enhancing the possibility of being experimentally controllable.

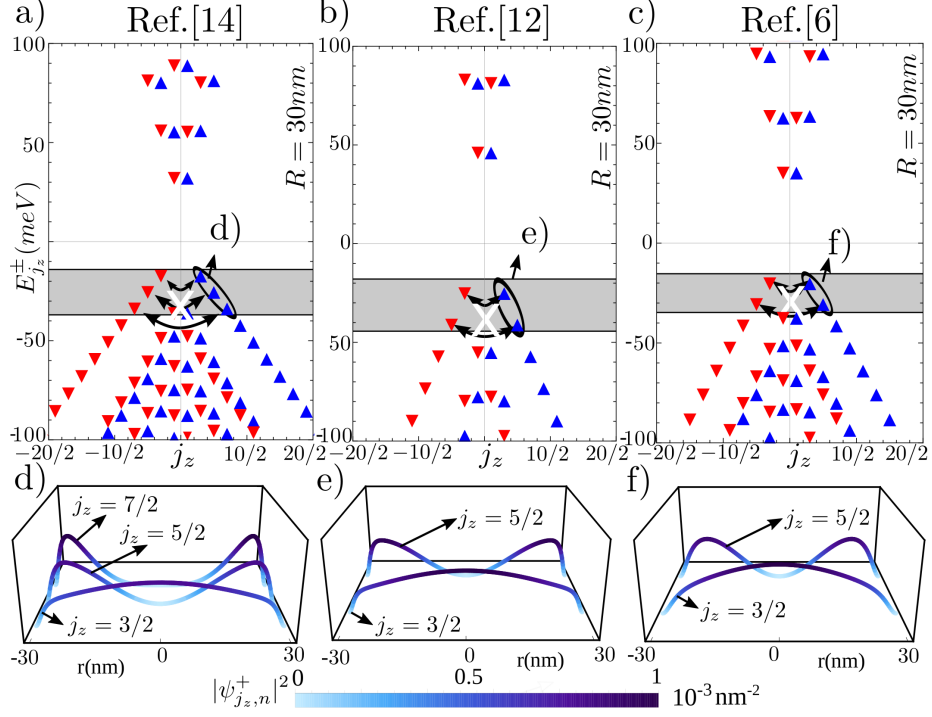


Figure S4. a) QD energy levels as a function of the total angular momentum j_z for the BHZ parameters of Ref. [14] with $R = 30$ nm; b) Same as a) for parameters from Ref. [12]. c) Same as a) for parameters from Ref. [6]. The arrows denote the forbidden transitions between spin up and down states of the BHZ blocks, blue and red triangles, respectively. d), e) and f): Probability density $|\psi_{j_z, n}^+|^2$ for the edge states grouped by the ellipses in a), b) and c)

IX. CIRCULATING CURRENT DENSITY

In this section we derive in details the circulating current formula Eq. (6) in the main text. For practical reasons, we write the total wave function Eq. (4) [main text] as

$$\psi_{j_z, n}^{\pm}(r, \theta, E_{j_z, n}^{\pm}) = \frac{N}{\sqrt{2\pi}} \left[I_{E_1}^{j_z \mp \frac{1}{2}, n}(r) e^{i(j_z \mp \frac{1}{2})\theta} \pm i I_{HH_1}^{j_z \mp \frac{1}{2}, n}(r) e^{i(j_z \mp \frac{1}{2})\theta} \right]^T, \quad (\text{S32})$$

with

$$I_{E_1}^{j_z \mp \frac{1}{2}, n}(r) = I_{j_z \mp \frac{1}{2}}(\lambda_+(E_{j_z, n}^{\pm})r) - \frac{I_{j_z \mp \frac{1}{2}}(\lambda_+(E_{j_z, n}^{\pm})R)}{I_{j_z \mp \frac{1}{2}}(\lambda_-(E_{j_z, n}^{\pm})R)} I_{j_z \mp \frac{1}{2}}(\lambda_-(E_{j_z, n}^{\pm})r), \quad (\text{S33})$$

$$I_{HH_1}^{j_z \mp \frac{3}{2}, n}(r) = \frac{D_+ \lambda_+^2 (E_{j_z, n}^\pm) - E_{j_z, n}^\pm + C_+}{\pm i A \lambda_+ (E_{j_z, n}^\pm)} \left(I_{j_z \mp \frac{3}{2}}(\lambda_+ (E_{j_z, n}^\pm) R) - \frac{I_{j_z \mp \frac{3}{2}}(\lambda_+ (E_{j_z, n}^\pm) R)}{I_{j_z \mp \frac{3}{2}}(\lambda_- (E_{j_z, n}^\pm) R)} I_{j_z \mp \frac{3}{2}}(\lambda_- (E_{j_z, n}^\pm) R) \right), \quad (\text{S34})$$

and N being the normalization factor. The wave function in Eq. (S32) is obtained within the BHZ model in the usual basis $|E_1 \pm\rangle, |HH_1 \pm\rangle, |E_1 \mp\rangle$ and $|HH_1 \mp\rangle$ defined by [5]

$$|E_1 \pm\rangle = f_1^\pm(z) \left| \Gamma_6 \pm \frac{1}{2} \right\rangle + f_4^\pm(z) \left| \Gamma_8 \pm \frac{1}{2} \right\rangle, \quad (\text{S35})$$

$$|HH_1 \pm\rangle = f_3^\pm(z) \left| \Gamma_8 \pm \frac{3}{2} \right\rangle, \quad (\text{S36})$$

where $f_i^\pm(z)$ are the QW envelope functions and $|\Gamma_i \pm\rangle$ are the periodic part of Bloch functions at Γ point $|u_{i=1,2,3,4,5,6}\rangle = \left\{ \left| \Gamma_6, \frac{1}{2} \right\rangle, \left| \Gamma_6, -\frac{1}{2} \right\rangle, \left| \Gamma_8, \frac{3}{2} \right\rangle, \left| \Gamma_8, \frac{1}{2} \right\rangle, \left| \Gamma_8, -\frac{1}{2} \right\rangle, \left| \Gamma_8, -\frac{3}{2} \right\rangle \right\}$ [5]. Using now Eqs. (S32)-(S36), we write the total wave function as

$$\psi_{j_z, n}^\pm = \frac{N}{\sqrt{2\pi}} \left[I_{E_1}^{j_z \mp \frac{1}{2}, n}(r) e^{i(j_z \mp \frac{1}{2})\theta} \left(f_1^\pm(z) \left| \Gamma_6, \pm \frac{1}{2} \right\rangle + f_4^\pm(z) \left| \Gamma_8, \pm \frac{1}{2} \right\rangle \right) \pm i I_{HH_1}^{j_z \mp \frac{3}{2}, n}(r) e^{i(j_z \mp \frac{3}{2})\theta} f_3^\pm(z) \left| \Gamma_8, \pm \frac{3}{2} \right\rangle \right], \quad (\text{S37})$$

Since now we have our wave function written as a product of envelope functions and the periodic parts of the Bloch functions at Γ point, $\psi_{j_z, n}^\pm(\mathbf{r}) = \sum_i F_{i, j_z, n}^\pm(r, \theta, z) u_i(\mathbf{r})$, we use the formula of the average (over the unit cell) current density [15, 16],

$$\langle \mathbf{j}_{j_z, n}^\pm \rangle(\mathbf{r}) = \frac{e\hbar}{m_0} \text{Im} \sum_{i, j} \left\{ F_{i, j_z, n}^* \mathbf{r} F_{j, j_z, n}(\mathbf{r}) \langle u_i | \nabla | u_j \rangle + \delta_{ij} F_{i, j_z, n}^* \mathbf{r} \nabla F_{j, j_z, n}(\mathbf{r}) \right\}, \quad (\text{S38})$$

to obtain the final formula for our problem,

$$\langle \mathbf{j}_{j_z, n}^\pm \rangle(\mathbf{r}) = \langle \mathbf{j}_{j_z, n}^\pm \rangle_b(\mathbf{r}) + \langle \mathbf{j}_{j_z, n}^\pm \rangle_e(\mathbf{r}), \quad (\text{S39})$$

where

$$\langle \mathbf{j}_{j_z, n}^\pm \rangle_b = \pm e N^2 \frac{\sqrt{2} P}{2\pi\hbar} |f_1^\pm(z)| |f_3^\pm(z)| I_{E_1}^{j_z \mp \frac{1}{2}, n}(r) I_{HH_1}^{j_z \mp \frac{3}{2}, n}(r) \hat{\theta}, \quad (\text{S40})$$

and

$$\langle \mathbf{j}_{j_z, n}^\pm \rangle_e = \frac{\hbar e N^2}{2\pi r m_0} \left\{ \left(j_z \mp \frac{1}{2} \right) \left[|f_1^\pm(z)|^2 + |f_4^\pm(z)|^2 \right] \left| I_{E_1}^{j_z \mp \frac{1}{2}, n}(r) \right|^2 + \left(j_z \mp \frac{3}{2} \right) |f_3^\pm(z)|^2 \left| I_{HH_1}^{j_z \mp \frac{3}{2}, n}(r) \right|^2 \right\} \hat{\theta}. \quad (\text{S41})$$

Here m_0 is the bare electron mass and P is the usual Kane parameter [7, 16, 17]. We emphasize that \mathbf{r} here denotes the center of the unit cell position (see Ref. [15, 16] for details). The first term $\langle \mathbf{j}_{j_z, n}^\pm \rangle_b$ is the ‘‘Bloch velocity’’ contribution to the average current as it stems from the periodic Bloch functions, while the second term $\langle \mathbf{j}_{j_z, n}^\pm \rangle_e$ is the contribution from the envelope functions. From Eqs. (S33) and (S34) we note that $I_{E_1}^{j_z \mp \frac{1}{2}, n}(\mathbf{r}) = I_{E_1}^{-j_z \pm \frac{1}{2}, n}(\mathbf{r})$ and $I_{HH_1}^{j_z \mp \frac{3}{2}, n}(\mathbf{r}) = I_{HH_1}^{-j_z \pm \frac{3}{2}, n}(\mathbf{r})$, yielding

$$\langle \mathbf{j}_{j_z, n}^\pm \rangle(\mathbf{r}) = -\langle \mathbf{j}_{-j_z, n}^\mp \rangle(\mathbf{r}), \quad (\text{S42})$$

which corresponds to the helical property of the QD levels, i.e., states with opposite j_z and spin (\pm) propagate in opposite angular directions.

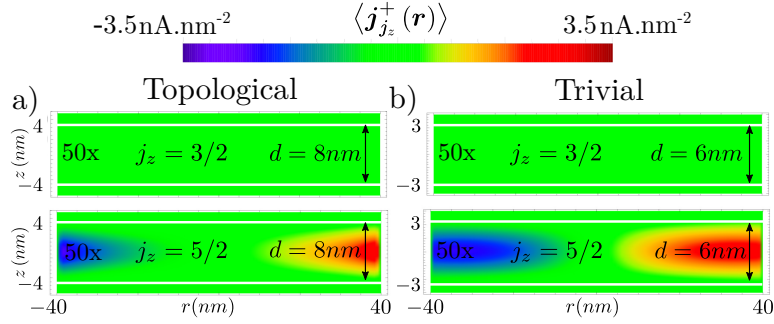


Figure S5. a) Spin-up envelope circulating current Eq. (S41) for the topological helical edge states $j_z = \frac{3}{2}$ and $j_z = \frac{5}{2}$ within the gray area of Fig. 1(c) (main text). b) Spin-up circulating current for the trivial helical edge states $j_z = \frac{3}{2}$ and $j_z = \frac{5}{2}$ within the gray area of Fig. 1(e) (main text). The solid white lines correspond to the soft-wall QW barriers.

A. Envelope contribution to the circulating current

We plot in Fig. (S5) the envelope function contribution $\langle \mathbf{j}_{j_z, n}^\pm \rangle_e$ to the circulating current for the spin up conduction levels of Fig. 2 (main text). All the density plots in Fig. (S5) were multiplied by a factor of 50 in order to compare them to the total circulating current density plotted in Fig. 2. The magnitude of the color bar here is the same as in Fig. 2. In accordance with Refs. [15, 16] here we obtain a small envelope current contribution. Interestingly, the envelope current contribution for $j_z = 3/2$ is negligible and cannot be visualized using the amplification of 50 times. This stems from the fact that 1) the spin-up $j_z = 3/2$ states are almost purely HH_1+ states, so the HH_1 wave function components, $I_{HH_1}^{j_z - \frac{3}{2}, n}(\mathbf{r})$, are larger than the E_1+ ones, $I_{E_1}^{j_z - \frac{1}{2}, n}(\mathbf{r})$, and 2) for spin up

$j_z = 3/2$ we have no envelope contribution from the HH_1+ subspace corresponding to the zero envelope orbital angular momentum $j_z - 3/2 = 0$. Using thus Eq. (S41) with 1) and 2) we find a negligible envelope circulating current.

B. Circulating current of the lowest $j_z = \frac{1}{2}$ conduction level in the ordinary InAs QD

Here we show that the circulating current for the lowest $j_z = \frac{1}{2}$ conduction level in the ordinary InAs QD [Fig. 1(d)] is very small as compared to currents of the trivial and topological InAsBi BHZ QDs in Fig. 2.

To calculate the circulating current of the ordinary InAs dot states we chose Hamiltonian Eq. (S16) which contains a mixing between electron and holes subspaces. For this Hamiltonian, we still have the circulating current given by an equation similar to Eq. (6) in the main text. Since we are interesting here in the spin up $j_z = \frac{1}{2}$ state with its zero envelope angular momentum, it is a good approximation to neglect the envelope contribution [Eq. (S41)] from the total circulating current, yielding

$$\left\langle \mathbf{J}_{j_z=\frac{1}{2},n=1}^+ \right\rangle \approx \frac{\sqrt{2}N^2P}{h} |f_1^\pm(z)| |f_3^\pm(z)| I_{C_1}^{0,1}(r) I_{H_1}^{-1,1}(r) \hat{\theta}, \quad (\text{S43})$$

where we recall that $I_{C_1}^{0,1}(r)$ and $I_{H_1}^{-1,1}(r)$ are the corresponding conduction and valence wave function components of Eq. (S32), respectively. For the energy of the lowest $j_z = \frac{1}{2}$ state, we have $E_{j_z=\frac{1}{2},n=1}^+ \approx M$, so that we can write

$$\mathcal{H}_{InAs}^{C_1-H_1} \begin{bmatrix} I_{C_1}^{0,1}(r) \\ I_{H_1}^{-1,1}(r) \end{bmatrix} \approx M \begin{bmatrix} I_{C_1}^{0,1}(r) \\ I_{H_1}^{-1,1}(r) \end{bmatrix}. \quad (\text{S44})$$

Using now $|\mathbf{k}| \approx \frac{1}{R}$, we find $\frac{\hbar^2}{2mc_1} \frac{1}{R^2} \ll E_{C_1}$ and $\frac{\hbar^2}{2m_{H_1}} \frac{1}{R^2} \ll E_{H_1}$. Hence, the above equation reads approximately

$$\begin{bmatrix} M & \frac{A}{R} \\ \frac{A}{R} & -M \end{bmatrix} \begin{bmatrix} I_{C_1}^{0,1}(r) \\ I_{H_1}^{-1,1}(r) \end{bmatrix} \approx M \begin{bmatrix} I_{C_1}^{0,1}(r) \\ I_{H_1}^{-1,1}(r) \end{bmatrix}. \quad (\text{S45})$$

From the second line of the above equation, we obtain the following relation between the conduction and valence components,

$$I_{H_1}^{-1,1}(r) \approx \frac{A/R}{2M} I_{C_1}^{0,1}(r). \quad (\text{S46})$$

Using the typical InAs parameters in Sec. IV we find $\frac{A/R}{2M} \ll 1$ thus yielding $I_{C_1}^{0,1}(r) \gg I_{H_1}^{-1,1}(r)$. As $I_{C_1}^{0,1}(r)$ and $I_{H_1}^{-1,1}(r)$ are normalized within the QD region, the product $I_{C_1}^{0,1}(r)I_{H_1}^{-1,1}(r)$ will be smaller as compared to the product $I_{E_1}^{1,1}(r)I_{HH_1}^{0,1}(r)$ arising from the highest $j_z = \frac{3}{2}$ valence state in the trivial InAsBi QD - since for the latter we find $\frac{A/R}{2M} \approx 0.5$. Therefore, even though the ordinary lowest $j_z = \pm\frac{1}{2}$ conduction states are protected, they do not carry a substantial circulating current as compared to the trivial BHZ QDs as seen in Fig. S6 (Note that the plot was multiplied by a factor of 100 in order to compare it with Fig. 2). Different from the other cases, here the circulating current peaks near the soft-wall QW barriers. This comes from the type-II structure of the double InAs/AlSb QW which yields a large overlap of the QW envelope functions around the QW barriers.

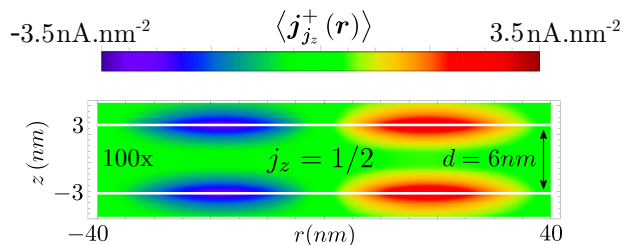


Figure S6. a) Spin-up circulating current Eq. (6) for lowest ordinary $j_z = \frac{1}{2}$ conducting state within the gray area of Fig. 1(d) (main text). The solid white lines correspond to the soft-wall QW barriers.

X. CONDUCTANCE CALCULATION

A. Conductance formula

We derive here the conductance within the linear regime through non-interacting QD levels coupled to left (L) and right (R) leads [18–21]. As already discussed in the main text, for the conductance calculations we consider two Kramers pairs, denoted by $|1\rangle = |j_z, \uparrow\rangle$, $|2\rangle = |-j_z, \downarrow\rangle$, $|3\rangle = |j'_z, \uparrow\rangle$ and $|4\rangle = |-j'_z, \downarrow\rangle$ with $\varepsilon_1 = \varepsilon_2$, $\varepsilon_3 = \varepsilon_4$, and $\varepsilon_i = \varepsilon_i(R, V_g)$. Although we have done the conductance calculation for the full Hamiltonian Eq. (8) in the main text (this result will be presented elsewhere), here we derive the conductance formula neglecting spin-flip processes as it is simpler analytically. The starting point is thus given by Eq. (8), which in the absence of spin-flip

processes, i.e., $t_{14} = t_{23} = V_{k_{\alpha\uparrow}}^{2(4)} = V_{k_{\alpha\downarrow}}^{1(3)} = 0$ yields the following spin block diagonal Hamiltonian

$$\begin{aligned}
 H = & \overbrace{\varepsilon_1 d_1^\dagger d_1 + \varepsilon_3 d_3^\dagger d_3 + \sum_{k_{\alpha\uparrow}, \alpha} \varepsilon_{k_{\alpha\uparrow}} c_{k_{\alpha\uparrow}}^\dagger c_{k_{\alpha\uparrow}} + \sum_{k_{\alpha\uparrow}, \alpha} (V_{k_{\alpha\uparrow}}^1 d_1^\dagger c_{k_{\alpha\uparrow}} + V_{k_{\alpha\uparrow}}^3 d_3^\dagger c_{k_{\alpha\uparrow}})}^{=H_\uparrow} + t_{13} d_1^\dagger d_3 + h.c. \\
 & + \overbrace{\varepsilon_2 d_2^\dagger d_2 + \varepsilon_4 d_4^\dagger d_4 + \sum_{k_{\alpha\downarrow}, \alpha} \varepsilon_{k_{\alpha\downarrow}} c_{k_{\alpha\downarrow}}^\dagger c_{k_{\alpha\downarrow}} + \sum_{k_{\alpha\downarrow}, \alpha} (V_{k_{\alpha\downarrow}}^2 d_2^\dagger c_{k_{\alpha\downarrow}} + V_{k_{\alpha\downarrow}}^4 d_4^\dagger c_{k_{\alpha\downarrow}})}^{=H_\downarrow} + t_{24} d_2^\dagger d_4 + h.c., \quad (S47)
 \end{aligned}$$

where the spin up Hamiltonian is represented schematically in Fig. (S7). Because we are neglecting spin flip processes, we can calculate the conductance formula for just one particular spin component and multiply it by a factor of two in order to account for both spin components.

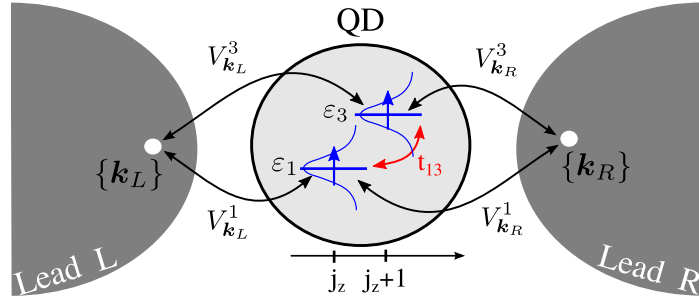


Figure S7. Schematic for the spin up QD Hamiltonian with levels $\varepsilon_1, \varepsilon_3$ coupled to each other through t_{13} and coupled to left and right leads through $V_{k_L\uparrow}^{1,3}$ and $V_{k_R\uparrow}^{1,3}$.

The equations of motion for the retarded spin up Green functions yield

$$\begin{pmatrix}
 E - \varepsilon_1 + i\eta - \sum_{\alpha}^{11} & 0 & 0 & -\sum_{\alpha}^{13} - t_{13}^* \\
 0 & E - \varepsilon_3 + i\eta - \sum_{\alpha}^{33} & -\sum_{\alpha}^{31} - t_{13} & 0 \\
 0 & -\sum_{\alpha}^{13} - t_{13}^* & E - \varepsilon_1 + i\eta - \sum_{\alpha}^{11} & 0 \\
 -\sum_{\alpha}^{31} - t_{13} & 0 & 0 & E - \varepsilon_3 + i\eta - \sum_{\alpha}^{33}
 \end{pmatrix}
 \begin{pmatrix}
 G_{11}^r(E) \\
 G_{33}^r(E) \\
 G_{13}^r(E) \\
 G_{31}^r(E)
 \end{pmatrix}
 =
 \begin{pmatrix}
 1 \\
 1 \\
 0 \\
 0
 \end{pmatrix}, \quad (S48)$$

with $\sum_{\alpha}^{l,m} = \sum_{k_{\alpha}, \alpha} \frac{V_{k_{\alpha\uparrow}}^l V_{k_{\alpha\uparrow}}^{m*}}{E - \varepsilon_{k_{\alpha\uparrow}} + i\eta}$, $\alpha = L, R$ and $l, m = 1, 3$. Using the Meir-Wingreen [18] results assuming 1) equal left and right density of states in the leads ($\rho_L = \rho_R$) and 2) equal spin-conserving coupling of the QD to left and right leads ($V_{k_L\uparrow}^l = V_{k_R\uparrow}^l$). We find that the spin up current in the

equilibrium regime reads

$$J_{\uparrow} = -\frac{e}{h} \int dE [f_L(E) - f_R(E)] \text{Im} \left[\text{tr} \left\{ \mathbf{\Gamma}^{L(R)} \mathbf{G}^r \right\} \right], \quad (\text{S49})$$

where $f_{L(R)}(E)$ is the Fermi-Dirac distribution of left (right) lead defined here as

$$f_L(E) = \frac{1}{\left(1 + e^{\frac{E-\mu_L}{k_B T}}\right)}, \quad f_R(E) = \frac{1}{\left(1 + e^{\frac{E-\mu_R}{k_B T}}\right)}, \quad (\text{S50})$$

where k_B is the Boltzmann constant, T is the temperature and $\mu_{L(R)}$ is the chemical potential of the left (right) lead. As for $\mathbf{\Gamma}^{L(R)}$ and \mathbf{G}^r , we have $(\mathbf{\Gamma}^{L(R)})_{lm} = \Gamma_{lm}^{L(R)} = 2\pi\rho_{L(R)} V_{k_{L(R)\uparrow}^l}^l V_{k_{L(R)\uparrow}^{m*}}$ and $(\mathbf{G}^r)_{lm} = G_{lm}^r$, or explicitly,

$$\mathbf{\Gamma}^L = 2\pi\rho_L \begin{pmatrix} V_{k_{L\uparrow}^1}^1 V_{k_{L\uparrow}^{1*}}^1 & V_{k_{L\uparrow}^1}^1 V_{k_{L\uparrow}^{3*}}^3 \\ V_{k_{L\uparrow}^3}^3 V_{k_{L\uparrow}^{1*}}^1 & V_{k_{L\uparrow}^3}^3 V_{k_{L\uparrow}^{3*}}^3 \end{pmatrix}, \quad \mathbf{G}^r = \begin{pmatrix} G_{11}^r(E) & G_{13}^r(E) \\ G_{31}^r(E) & G_{33}^r(E) \end{pmatrix}. \quad (\text{S51})$$

Within linear response, i.e., $\mu_L - \mu_R = -eV$ with $eV \ll \mu_{L,R}$, we write

$$f_L(E) - f_R(E) \approx (\mu_L - \mu_R) \left(-\frac{\partial f_0}{\partial E} \right) = (-eV) \left(-\frac{\partial f_0}{\partial E} \right), \quad (\text{S52})$$

where f_0 is the equilibrium Fermi function $f_0(E) = 1/(e^{\frac{E-\mu}{k_B T}} + 1)$ where we have taken the chemical potential as its $T = 0$ value, i.e., the Fermi energy $\mu = \varepsilon_F$. From Eq. (S49) the spin up conductance within linear response thus reads

$$\mathcal{G}_{\uparrow} = \left. \frac{dJ_{\uparrow}}{dV} \right|_{V=0} = \frac{e^2}{h} \int dE \text{Im} \left[\text{tr} \left\{ \mathbf{\Gamma}^{L(R)} \mathbf{G}^r \right\} \right] \left(-\frac{\partial f_0}{\partial E} \right). \quad (\text{S53})$$

Now we assume k -independent QD-lead couplings $V_{k_{L\uparrow}^l}^l = V_L^l$, together with the wide band limit [22] where the constant 2D density of states in the leads $\rho_{L(R)}$ is assumed to have an energy range much larger than the characteristic energies of our system, i.e., $\Delta\varepsilon_{L,R} \gg E$. We also assume the dependence of the QD energy levels on the gate V_g as $\varepsilon_i(R, V_g) = \varepsilon_i(R) - eV_g$. Thus, the spin

up conductance Eq. (S53) at $T = 0$ K reads

$$\mathcal{G}_\uparrow = \frac{e^2}{h} \frac{\left[\Gamma_3^L(\varepsilon_F - \varepsilon_1(R, V_g)) + \Gamma_1^L(\varepsilon_F - \varepsilon_3(R, V_g)) + 2t_{13}\Gamma_{13}^L \right]^2}{\left[(\varepsilon_F - \varepsilon_1(R, V_g))(\varepsilon_F - \varepsilon_3(R, V_g)) - t_{13}^2 \right]^2 + \left[\Gamma_3^L(\varepsilon_F - \varepsilon_1(R, V_g)) + \Gamma_1^L(\varepsilon_F - \varepsilon_3(R, V_g)) + 2t_{13}\Gamma_{13}^L \right]^2}, \quad (\text{S54})$$

which exhibits $\frac{e^2}{h}$ conductance peaks as a function of R and V_g [Figs. 3(b), (c) and (e) in the main text] when

$$\left[\varepsilon_F - \varepsilon_1(R, V_g) \right] \left[\varepsilon_F - \varepsilon_3(R, V_g) \right] - t_{13}^2 = 0. \quad (\text{S55})$$

We emphasize that the conductance formulas Eqs. (S53) and (S54) here correspond to a purely spin up conductance. Hence the total conductance follows

$$\mathcal{G} = \mathcal{G}_\uparrow + \mathcal{G}_\downarrow = 2\mathcal{G}_\uparrow. \quad (\text{S56})$$

The total QD conductance \mathcal{G} Eq. (S56) can also be written as

$$\mathcal{G} = \frac{2e^2}{h} \left\{ \pi\Gamma_1^L \rho_1(\varepsilon_F) + \pi\Gamma_3^L \rho_3(\varepsilon_F) \right\} - \frac{4e^2}{h} \Gamma_{13}^L \text{Im} [G_{13}^r(\varepsilon_F)], \quad (\text{S57})$$

where $\rho_i(\varepsilon_F) = -\frac{1}{\pi} \text{Im} \{G_{ii}(\varepsilon_F)\}$. The first two terms (always positive definite) correspond to the conductance via the two QD levels and the last one represents the interference term [19–21].

B. Diagonal QD level operators

The spin up QD Hamiltonian H_\uparrow [see Eq. (S47)] sketched in Fig. (S7) in the absence of coupling to the leads is given by

$$H_{QD} = \begin{pmatrix} d_1^\dagger & d_3^\dagger \end{pmatrix} \begin{pmatrix} \varepsilon_1 & t_{13} \\ t_{13} & \varepsilon_3 \end{pmatrix} \begin{pmatrix} d_1 \\ d_3 \end{pmatrix}, \quad (\text{S58})$$

and has the following diagonal form

$$H = \begin{pmatrix} d_+^\dagger & d_-^\dagger \end{pmatrix} \begin{pmatrix} \varepsilon_+ & 0 \\ 0 & \varepsilon_- \end{pmatrix} \begin{pmatrix} d_+ \\ d_- \end{pmatrix}, \quad (\text{S59})$$

with

$$d_+^\dagger = \frac{t_{13} d_1^\dagger + (\varepsilon_+ - \varepsilon_1) d_3^\dagger}{\sqrt{t_{13}^2 + (\varepsilon_+ - \varepsilon_1)^2}}, \quad d_-^\dagger = \frac{t_{13} d_1^\dagger + (\varepsilon_- - \varepsilon_1) d_3^\dagger}{\sqrt{t_{13}^2 + (\varepsilon_- - \varepsilon_1)^2}}, \quad (\text{S60})$$

and $\varepsilon_\pm = \frac{\varepsilon_1 + \varepsilon_3 \pm \sqrt{(\varepsilon_1 - \varepsilon_3)^2 + 4t_{13}^2}}{2}$. We rewrite now the Hamiltonian that couples the QD to the leads using the diagonal d_+, d_- operators, yielding

$$H_{\text{Lead-QD}} = \sum_{k_\alpha, \alpha} (V_{k_\alpha}^1 d_1^\dagger c_{k_\alpha} + V_{k_\alpha}^3 d_3^\dagger c_{k_\alpha}) + H.C \quad (\text{S61})$$

$$= \sum_{k_\alpha, \alpha} [V_{k_\alpha}^1 (\varepsilon_1 - \varepsilon_+) + t_{13} V_{k_\alpha}^3] \frac{\sqrt{(\varepsilon_1 - \varepsilon_-)^2 + t_{13}^2}}{(\varepsilon_- - \varepsilon_+) t_{13}} d_-^\dagger c_{k_\alpha} \\ - \sum_{k_\alpha, \alpha} [V_{k_\alpha}^1 (\varepsilon_1 - \varepsilon_-) + t_{13} V_{k_\alpha}^3] \frac{\sqrt{(\varepsilon_1 - \varepsilon_+)^2 + t_{13}^2}}{(\varepsilon_- - \varepsilon_+) t_{13}} d_+^\dagger c_{k_\alpha} + H.C \quad (\text{S62})$$

$$= \sum_{k_\alpha, \alpha} (V_{k_\alpha}^- d_-^\dagger c_{k_\alpha} + V_{k_\alpha}^+ d_+^\dagger c_{k_\alpha}) + H.C \quad (\text{S63})$$

We note that by tuning the QD parameters such that $\varepsilon_1(R_c, V_{g,c}) - \varepsilon_3(R_c, V_{g,c}) = t_{13} \left(\frac{V_{k_\alpha}^1}{V_{k_\alpha}^3} - \frac{V_{k_\alpha}^3}{V_{k_\alpha}^1} \right)$, we obtain $V_{k_\alpha}^1 (\varepsilon_1 - \varepsilon_+) + t_{13} V_{k_\alpha}^3 = 0$, thus decoupling the diagonal level d_- . As a consequence, we just see a single peak occurring in the conductance calculation Fig. 3(e) (main text) at $(R, V_g) = (R_c, V_{g,c})$.

C. Estimate for the hopping and broadening terms

A back of the envelope estimate for the couplings t_{ij} in the Hamiltonian Eq. (8) (main text) can be obtained from $t_{ij} = \int d\theta dr r \psi_i^\dagger V_{\text{pert}} \psi_j$. By taking $\psi_i = \psi_{j_z, n}^\sigma$ [Eq. (4), main text] and assuming $V_{\text{pert}} \approx 1$ meV (a typical value for, e.g., non-magnetic impurities [23]) we find $t_{13} = t_{24} = t \approx 1$ meV. Note that $t_{12} = t_{34} = 0$ due to time reversal symmetry. The broadening $\Gamma_{lm}^{L(R)}$ of the dot levels due to dot-lead coupling can range from tens of μeV to meV [24–26] for ordinary QDs. There are no level-broadening data for BHZ QDs. We assume $\Gamma = \Gamma_{lm}^{L(R)} = 4$ meV in our conductance calculation (Fig. 3, main text). Smaller Γ 's would make the resonances in \mathcal{G} narrower but would not change our findings. A detailed level broadening calculation for topological and non-topological BHZ QDs due to the leads is needed in the literature. This, however, is beyond

the scope of our present manuscript and should be addressed in a future work.

-
- [1] K. Ma, et. al., Appl. Phys. Lett. **55**, 2420 (1989)
 - [2] Z. Fang, et. al., J. Appl. Phys. **68**, 1187 (1990)
 - [3] P. T. Webster, et. al., J. Vac. Soc. & Tech. B **32**, 02C120-1 (2014).
 - [4] W. H. Lau, J. T. Olesberg and M. E. Flatté, cond-mat/0406201.
 - [5] B. Andrei Bernevig, Taylor L. Hughes, Shou-Cheng Zhang, Science **314**, 1757, (2006).
 - [6] P. Michetti, P.H. Penteado, J.C. Egues, and P. Recher, Semicond. Sci. Technol. **27**, 124007 (2012).
 - [7] R. S. Calsaverini, E. Bernardes, J. C. Egues, and D. Loss, Phys. Rev. B **78**, 155313 (2008).
 - [8] R. Winkler, *Spin-Orbit Coupling Effects in Two-Dimensional Electron and Hole Systems*, Springer Tracts in Modern Physics Vol. 191 (Springer, New York, 2003).
 - [9] J. Shabani, et. al., Phys. Rev. B **93**, 155402, (2016).
 - [10] J. Fu et. al., Phys. Rev. Lett. **91**, 075408, (2015).
 - [11] J. Fu et. al., Phys. Rev. Lett. **117**, 226401, (2016).
 - [12] X.-L. Qi and S. C. Zhang, Rev. Mod. Phys. **83**, 1057, (2011).
 - [13] P. Kasperkovitz, J. Math. Phys. **21**, 6 (1980).
 - [14] Rothe D. G., R. W. Reinthaler, C.-X. Liu, L. W. Molenkamp, S. C. Zhang, and E. M. Hankiewicz, New J. Phys. **12**, 065012, (2010).
 - [15] J. van Bree, A. Yu. Silov, P. M. Koenraad and M. E. Flatté, Phys. Rev. B. **90**, 165306 (2014).
 - [16] J. van Bree, A. Yu. Silov, P. M. Koenraad and M. E. Flatté, Phys. Rev. Lett. **112**, 187201 (2014).
 - [17] E. O. Kane, J. Phys. Chem. Solids **1**, 249 (1957).
 - [18] Y. Meir, Ned S. Wingreen, Phys. Rev. Lett. **68**, 16 (1992).
 - [19] M. L. Ladrn de Guevara, et. al., Phys. Rev. B **67**, 195335 (2003).
 - [20] G.-H. Ding, et. al., Phys. Rev. B **71**, 205313 (2005).
 - [21] H. Lu, et. al., Phys. Rev. B **71**, 235320 (2005).
 - [22] J. Antti-Pekka, N. S. Wingreen, and Y. Meir, Phys. Rev. B **50**, 5582 (1994).
 - [23] G. Bastard, *Wave mechanics applied to semiconductor heterostructures*. New York, NY (USA), John Wiley and Sons Inc. (1990).
 - [24] R. Hanson, et. al., Spins in few-electron quantum dots. Rev. Mod. Phys. **79**, 1217, (2007).
 - [25] S. Datta, *Electronic transport in mesoscopic systems*. Cambridge university press, (1997).

- [26] L. P. Kouwenhoven, et. al., *Mesoscopic electron transport*. Springer, Dordrecht, (1997).

ANNEX B – SUBMITTED ARTICLES

“Paradoxical extension of the edge states across the topological phase transition due to emergent approximate chiral symmetry in a quantum anomalous Hall system” – arXiv:1807.05111 – Denis R. Candido, Maxim Kharitonov, J. Carlos Egues, and Ewelina Hankiewicz.

We submitted the manuscript as a regular article in PRB; we received two very good reports, one recommending that the manuscript be published as a Rapid Communication.

Paradoxical extension of the edge states across the topological phase transition due to emergent approximate chiral symmetry in a quantum anomalous Hall system

Denis R. Cândido^{*1}, Maxim Kharitonov^{*2}, J. Carlos Egues¹, Ewelina M. Hankiewicz²

^{*}These authors contributed equally

¹Instituto de Física de São Carlos,
Universidade de São Paulo, 13560-970,
São Carlos, São Paulo, Brazil

²Institute for Theoretical Physics and Astrophysics,
University of Würzburg, 97074 Würzburg, Germany

We present a paradoxical finding that, in the vicinity of a topological phase transition in a quantum anomalous Hall system (Chern insulator), topology nearly always (except when the system obeys charge-conjugation symmetry) results in a significant extension of the edge-state structure beyond the minimal one required to satisfy the Chern numbers. The effect arises from the universal gapless linear-in-momentum Hamiltonian of the nodal semimetal describing the system right at the phase transition, whose form is enforced by the change of the Chern number. Its emergent approximate chiral symmetry results in an edge-state band in the vicinity of the node, in the region of momenta where such form is dominant. Upon opening the gap, this edge-state band is modified in the gap region, becoming “protected” (connected to the valence bulk band with one end and conduction band with the other) in the topologically nontrivial phase and “nonprotected” (connected to either the valence or conduction band with both ends) in the trivial phase. The edge-state band persists in the latter as long as the gap is small enough.

Introduction and main result. In quantum anomalous Hall (QAH) systems (also known as Chern insulators)^{1–4}, the topological Chern number C of an insulating phase defines, via bulk-boundary correspondence^{2,4}, the number of the edge-state bands that connect the valence and conduction bulk bands. This is the only characteristic of the edge states required by quantum Hall (QH) topology. Such states are *topologically protected* in the sense that they cannot disappear under continuous deformations of the Hamiltonian without closing the gap in the bulk spectrum.

One could define *minimal edge-state structures* that are *sufficient* to satisfy a given Chern number. In particular, in the topologically nontrivial (TnT) phase with $C = 1$, one topologically protected edge-state band, having minimal extent in momentum space just enough to connect the valence and conduction bands (for more common band structures, this is typically the region of momenta dominated by the bulk gap), is sufficient. In the topologically trivial (TT) phase with $C = 0$, no edge states at all are required. No edge states are also required at the topological phase transition (TPT) between the TT and TnT phases, when the gap closes and the system is a semimetal, since C is not even well-defined there.

In principle, *topologically nonprotected* edge-state bands that are connected to either the valence or conduction band with both ends could additionally exist. Also, topologically protected edge-state bands could extend beyond the gap region. Such additional edge-state structures are not required by QH topology, but neither are they prohibited.

In this work, we present a paradoxical finding that, in the vicinity of a TPT in QAH system, QH topology nearly always results in a significant extension of the edge-state structure beyond the minimal one required

to satisfy the Chern numbers, described above. This generic behavior is illustrated in Fig. 1 with the quadratic model, to be presented below, which describes one block of the Bernevig-Hughes-Zhang (BHZ) model⁵ of a quantum spin Hall (QSH) system^{5–7}. This behavior has previously been noticed⁸ in the BHZ model, but remained unexplained.

Applying the ideas recently formulated in Ref. 9, we show that this extension of the edge-state structure originates from the *emergent approximate chiral symmetry* of the universal gapless linear-in-momentum low-energy Hamiltonian of the nodal semimetal describing the system right at the TPT, which in its simplest form reads

$$\hat{H}_0(\mathbf{p}) = v(\tau_x p_x + \tau_y p_y), \quad (1)$$

where $\tau_{x,y}$ are Pauli matrices in the space defined below and v is the velocity of its linear spectrum $\pm v|\mathbf{p}|$, $\mathbf{p} = (p_x, p_y)$. This results in an edge-state band that exists [Fig. 1(b)] at the TPT on one side of the node (at least) in the region $|p_x| \lesssim p^*$ of momenta p_x along the $y = 0$ edge, where such *asymptotic form* of the Hamiltonian is dominant; p^* is the scale, where higher-order-in-momentum terms in the asymptotic expansion of the full Hamiltonian become comparable to the linear ones. Upon opening a small gap Δ , such that $p_\Delta = |\Delta|/v \ll p^*$, the edge-state band is modified only in the smaller region $|p_x| \lesssim p_\Delta$ dominated by the gap, in accord with QH topology. In the TT phase [$C = 0$, Fig. 1(a)], the edge-state band exists in the region $p_\Delta \lesssim |p_x| \lesssim p^*$ and remains topologically nonprotected, connected to the valence (in the case of quadratic model presented in Fig. 1) band with both ends without crossing the gap. In the TnT phase [$C = 1$, Fig. 1(c)], the edge-state band becomes topologically protected, connected to the valence band with one end and conduction band with the other,

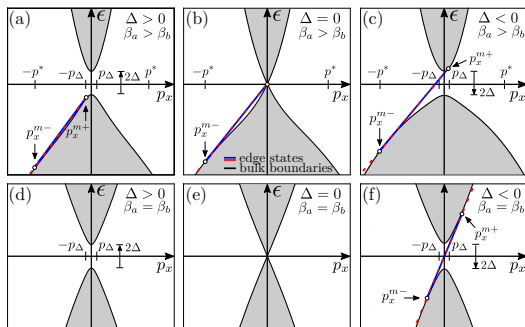


FIG. 1: Edge states (blue) of a quadratic model (6) and (7) of a QAH system in the vicinity ($p_\Delta \ll p^* \sim v/\sqrt{\beta_a\beta_b}$) of the TPT. At smaller momenta, the edge-state structure agrees with that (dashed red) of the low-energy linear model [Eqs. (2), (3), and (8), Fig. 2]. Grey-shaded regions denote the continua of bulk states. (a),(b),(c) Due to the approximate chiral symmetry of the linear model, in the general case $\beta_a \neq \beta_b$ of unequal curvatures $\beta_{a,b}$ of the conduction and valence bands, the edge-state structure is extended beyond the minimal one required to satisfy the Chern numbers. (d),(e),(f) Only in the exceptional case $\beta_a = \beta_b$, when the system obeys charge-conjugation symmetry, the minimal edge-state structure is realized. Graphs (a),(b),(c) are plotted for $\beta_a/\beta_b = 10$. Graphs (a),(c),(d),(f) are plotted for $\varkappa/p_\Delta = 3\sqrt{10}$.

crossing the gap in the region $|p_x| \lesssim p_\Delta$, but also extending well beyond it to the region $p_\Delta \lesssim |p_x| \lesssim p^*$.

Even though this extension of the edge-state structure is not topologically protected, it is *nearly always* present, i.e., for all forms of the low-energy model, except when it obeys charge-conjugation symmetry [Fig. 1(d),(e),(f)], which is an exceptional case that can likely be achieved only by accident or fine-tuning. Only in this case, the edge-state structure is minimal in the sense described above.

Our finding is quite paradoxical because the form (1) of the nodal semimetal Hamiltonian at the TPT is ultimately *enforced by QH topology*, to ensure the change of the Chern number across the TPT. This form, due to its approximate chiral symmetry, generates the extension of the edge-state structure, which is, however, not required to satisfy the Chern numbers in either the TT ($C = 0$) or TnT ($C = 1$) phase.

Low-energy Hamiltonian in the vicinity of a topological phase transition. We consider a QAH system¹, i.e., a 2D band insulator with broken time reversal symmetry, but no orbital effect of the magnetic field. Such system belongs to class A of the general classification scheme^{2,4} of topological systems and is characterized by an integer \mathbb{Z} bulk topological invariant well known as the Chern number.

We consider the vicinity of a TPT in a QAH system. At the phase transition, two electron states, to be de-

noted a and b , become degenerate at some point in the Brillouin zone, making the system gapless. The low-energy linear-in-momentum Hamiltonian for the wave function $\hat{\psi} = (\psi_a, \psi_b)^T$ in the subspace of these two states can be written in its simplest form as

$$\hat{H}(\mathbf{p}) = v(\tau_x p_x + \tau_y p_y) + \Delta \tau_z, \quad (2)$$

where $\tau_{x,y,z}$ are the Pauli matrices and $\mathbf{p} = (p_x, p_y)$ is the momentum *deviation* from the degeneracy point. In general, several additional terms could be present. In Supplemental Material (SM)¹⁰, we demonstrate that our findings for the simplest Hamiltonian $\hat{H}(\mathbf{p})$ presented below also hold for the most general form of the linear Hamiltonian.

The two insulating QAH phases correspond to two signs of the gap $\Delta \gtrless 0$ and have a difference $C_{\Delta < 0} - C_{\Delta > 0} = 1$ of the Chern numbers $C_{\Delta \gtrless 0}$; $\Delta = 0$ is the TPT point, where the system is gapless nodal semimetal, described by the Hamiltonian $\hat{H}_0(\mathbf{p}) = \hat{H}(\mathbf{p})|_{\Delta=0}$ [Eq. (1)]. We assume that one of the phases is TT with a zero Chern number, i.e., that possible full Chern numbers are $(C_{\Delta < 0}, C_{\Delta > 0}) = (1, 0)$ or $(0, -1)$.

The Hamiltonian (2) is valid at momenta $p = |\mathbf{p}| \lesssim p^*$ not exceeding the scale p^* defined above. Accordingly, the gap must also be small enough, so that $p_\Delta \lesssim p^*$.

General boundary condition. Next, we supplement the low-energy Hamiltonian $\hat{H}(\mathbf{p})$ [Eq. (2)] with the boundary condition (BC) of the most general form, describing termination of the sample, without any assumptions about the microscopic structure of the boundary. Such form is constrained by the only fundamental requirement that the probability current perpendicular to the boundary must vanish. Such BC has recently been derived¹¹ in Ref. 9 for the gapless Hamiltonian $\hat{H}_0(\mathbf{p})$ [Eq. (1)]. Since the current operator $\hat{\mathbf{j}} = \partial_{\mathbf{p}} \hat{H}(\mathbf{p}) = v(\tau_x, \tau_y)$ does not depend on Δ at all, the BC remains exactly the same for finite Δ . Throughout the paper, we consider the sample occupying the half-plane $y > 0$. The BC for the $y = 0$ edge¹² reads

$$\psi_a(x, y=0) \sin \frac{\theta}{2} - \psi_b(x, y=0) \cos \frac{\theta}{2} = 0. \quad (3)$$

All unique forms of the BC are parameterized by the angle θ covering the *full circle*, shown in Fig. 2(d).

Generic edge-state structure. The edge states for the Hamiltonian (2) and BC (3) can be calculated analytically and are shown in Fig. 2. All possible forms are parameterized by the angle θ and represent the generic edge-state structure in the vicinity of a TPT of QAH system, see also SM¹⁰. For every value of θ except $\pm \frac{\pi}{2}$ (to be discussed separately below), there exists *one* edge-state band

$$\mathcal{E}(p_x) = v p_x \sin \theta + \Delta \cos \theta \quad (4)$$

for any value of the gap Δ , at $p_x > p_x^m(\theta)$ for $\theta \in \Theta_a = (-\frac{\pi}{2}, \frac{\pi}{2})$ and at $p_x < p_x^m(\theta)$ for $\theta \in \Theta_b = (\frac{\pi}{2}, \frac{3\pi}{2})$. ($v p_x^m(\theta), \epsilon^m(\theta) = \Delta(\tan \theta, 1/\cos \theta)$ is the merging point

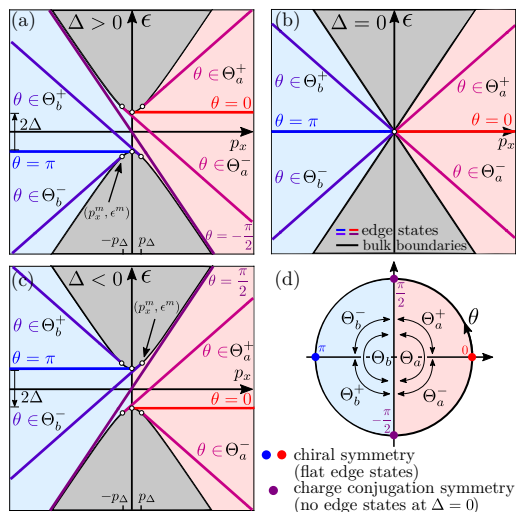


FIG. 2: Generic edge-state structure [Eq. (4)] in the vicinity of a TPT in a QAH system, calculated for the simplest form (2) of the low-energy linear-in-momentum Hamiltonian with the most general BC (3); see SM¹⁰ for the most general form of the Hamiltonian. Due to the approximate chiral symmetry of the model, for every value of the parameter θ of the BC (3) except $\pm\frac{\pi}{2}$, when the system satisfies charge-conjugation symmetry, the edge-state structure is extended at the TPT [$\Delta = 0$, (b)] and in both TT and TnT phases [$\Delta \gtrless 0$, (a),(c)] beyond the minimal one required to satisfy the Chern numbers. In (a),(b),(c), grey-shaded regions denote the continua of bulk states. (d) The circle of θ . The stability regions Θ_a and Θ_b were subdivided into the regions Θ_a^\pm and Θ_b^\pm , respectively, to indicate the location of the edge-state band in (a),(b),(c) for various values of θ .

of the edge-state dispersion relation (4) with the boundaries $\pm\sqrt{(vp_x)^2 + \Delta^2}$ of the continua of the bulk states.

Therefore, as the key property, the edge-state structure in the vicinity of the TPT in a QAH system is nearly always (i.e., for all $\theta \neq \pm\frac{\pi}{2}$) extended beyond the minimal one required to satisfy the Chern numbers. For the model (1) and (3) with $\Delta = 0$ [Fig. 2(b)], these edge states have recently been found and studied in Ref. 9. Applying the ideas expressed therein, below we demonstrate that this extension of the edge states can be explained in terms of *chiral symmetry*.

Edge states at the topological phase transition due to chiral symmetry. Chiral symmetry is one of the three main symmetries (along with time-reversal and charge-conjugation) that give rise to topological behavior^{2,4}. A bulk Hamiltonian $\hat{H}(\mathbf{p})$ satisfies chiral symmetry, if there exists a unitary operator \hat{S} under which it changes its sign, $\hat{S}\hat{H}(\mathbf{p})\hat{S}^\dagger = -\hat{H}(\mathbf{p})$.

In 2D, chiral symmetry allows⁴ for the existence of gapless topological semimetals with flat edge-state bands at zero energy $\epsilon = 0$. We notice that the gapless bulk Hamil-

tonian $\hat{H}_0(\mathbf{p})$ [Eq. (1)] at the TPT obeys chiral symmetry with $\hat{S} = \tau_z$. An important requirement for the topologically protected $\epsilon = 0$ edge states to exist is that the system *with an edge* must respect chiral symmetry. For a low-energy model, this means that not only the bulk Hamiltonian but also the BC must respect chiral symmetry^{9,10}. For the general BC (3), there are⁹ only two discrete cases

$$\psi_b(x, y = 0) = 0 \text{ or } \psi_a(x, y = 0) = 0 \quad (5)$$

with $\theta = 0$ or $\theta = \pi$, respectively, that obey chiral symmetry.

The model with the bulk Hamiltonian (1) and one of the BCs (5) represents a chiral-symmetric 2D topological semimetal. For each of the chiral-symmetric BCs (5), there is a flat edge-state band at $\epsilon = 0$ on one side of the node, for $p_x > 0$ and $p_x < 0$, respectively [Fig. 2(b)], ensured by the well-defined topological invariant of the node, the winding number 1.

The low-energy model of a QAH system in the vicinity of a TPT with the Hamiltonian (2) and BC (3) does not generally have exact chiral symmetry: in $\hat{H}(\mathbf{p})$, the gap term $\Delta\tau_z$ breaks chiral symmetry $\hat{S} = \tau_z$ and the BC generally differs from one of the chiral-symmetric forms (5). However, as demonstrated in Ref. 9, exact chiral symmetry is not required for the edge states induced by it to persist due to their *stability property*: upon breaking chiral symmetry, the edge-state bands depart from $\epsilon = 0$, but continue to persist as long as chiral-symmetric parts of the Hamiltonian and BCs are dominant. Accordingly, the concept of a *stability region* was introduced therein, as the region in the parameter space of chiral-asymmetric terms where the edge states persist.

At the TPT $\Delta = 0$ [Fig. 2(b)], the edge-state dispersion relation (4) reads⁹ $\mathcal{E}(p_x)|_{\Delta=0} = vp_x \sin\theta$. The circle of θ consists of two stability regions $\Theta_a = (-\frac{\pi}{2}, \frac{\pi}{2})$ and $\Theta_b = (\frac{\pi}{2}, \frac{3\pi}{2})$, for which the edge-state band is located at $p_x \gtrless 0$, respectively. The regions $\Theta_{a,b}$ contain the chiral-symmetric points $\theta = 0$ and $\theta = \pi$, respectively, corresponding to the BCs (5)¹³. As θ deviates from one of these points, the edge-state band deviates from $\epsilon = 0$ acquiring a finite slope. The edge-state band disappears by merging with the bulk bands only upon reaching $\theta = \pm\frac{\pi}{2}$ points. The stability regions $\Theta_{a,b}$ are thus separated only by two points $\theta = \pm\frac{\pi}{2}$ and the edge states persist even for significant deviations from chiral symmetry.

To summarize this part, right at the TPT of a QAH system, when the system is a nodal semimetal, an edge-state band [Fig. 2(b)] nearly always [i.e., for all values of the parameter θ in the BC (3), except $\pm\frac{\pi}{2}$] exists (at least) in the region $|p_x| \lesssim p^*$, where the linear terms of $\hat{H}_0(\mathbf{p})$ are dominant in the full Hamiltonian. This band can be attributed to the approximate chiral symmetry of the model (1) and (3). This band is not required by QH topology and is therefore an extension of the minimal edge-state structure.

Modification of the edge-state band by the gap. Introducing a small gap Δ , such that $p_\Delta \ll p^*$, modifies this

edge-state band only in the smaller region $|p_x| \lesssim p_\Delta$ dominated by the gap, in accord with QH topology. Indeed, as Figs. 2(a) and (c) show, in this region, the edge-state behavior is crucially sensitive to the sign of the gap, i.e., to which QAH phase the system is in. The numbers of the edge-state bands crossing the gap¹⁴ with the sign of their velocities $\partial_{p_x} \mathcal{E}(p_x) = v \sin \theta$ are: 0 and +1 for $\Delta \gtrless 0$, respectively, if $\theta \in (0, \pi)$; -1 and 0 for $\Delta \gtrless 0$, respectively, if $\theta \in (\pi, 2\pi)$. The difference of these numbers for $\Delta \gtrless 0$ at each value of θ is in full accord with the difference $C_{\Delta < 0} - C_{\Delta > 0} = 1$ of the Chern numbers, manifesting the bulk-boundary correspondence of a QAH system.

However, also for a finite gap, in the region $p_\Delta \lesssim |p_x| \lesssim p^*$, the edge states are still determined by the linear chiral-symmetric part $\hat{H}_0(\mathbf{p})$ [Eq. (1)] of the Hamiltonian $\hat{H}(\mathbf{p})$ [Eq. (2)], which is dominant there. As seen from Figs. 2(a),(b),(c), the edge-state structure in the region $p_\Delta \lesssim |p_x| \lesssim p^*$ is the same regardless of the presence of the gap and its sign and represents the extension beyond the minimal structure required to satisfy the Chern numbers.

The cases $\theta = \pm \frac{\pi}{2}$ of charge-conjugation symmetry. For $\theta = \pm \frac{\pi}{2}$, there is an edge-state band (4) only in one of the insulating phases $\Delta \lesgtr 0$, respectively, while there are no edge states at the TPT $\Delta = 0$ and in the other insulating phase $\Delta \gtrless 0$. Only in these cases of θ the minimal edge-state structure is realized. In SM¹⁰, we demonstrate that the bulk Hamiltonian $\hat{H}(\mathbf{p})$ [Eq. (2)] with the gap and the BC (3) at $\theta = \pm \frac{\pi}{2}$ satisfy charge-conjugation symmetry. Therefore, for $\theta = \pm \frac{\pi}{2}$, the system with an edge obeys charge-conjugation symmetry. Thus, interestingly, the only cases of the general BC (3), in which the edge states at the TPT $\Delta = 0$ [Fig. 2(b)] induced by chiral symmetry are absent, are the ones that have charge-conjugation symmetry. This can be understood as follows. For charge-conjugation symmetry, the edge-state spectrum has to satisfy $\mathcal{E}(p_x) = -\mathcal{E}(-p_x)$, which is incompatible with the property that chiral symmetry induces only one edge-state band on either side ($p_x > 0$ or $p_x < 0$) of a linear node.

Edge states of the quadratic model. Above, we have established the generic behavior of the edge states (Fig. 2) of a QAH system in the vicinity of a TPT using the universal low-energy model with the linear-in-momentum Hamiltonian, given by Eqs. (2) and (3) in its simplest form and in SM¹⁰ in its most general form. Any “full” model of a QAH system with an explicitly defined behavior at all momenta and properties of the boundary will asymptotically be described by this low-energy model in the vicinity of the TPT. The information about both the band structure of the bulk Hamiltonian away from the node and properties of the boundary will be fully contained in the BC of the low-energy model.

We demonstrate this point explicitly by considering the following QAH Hamiltonian

$$\hat{H}_2(\mathbf{p}) = \begin{pmatrix} \Delta + \beta_a p^2 & v p_- \\ v p_+ & -\Delta - \beta_b p^2 \end{pmatrix}, \quad p_\pm = p_x \pm i p_y, \quad (6)$$

with momenta taking all values up to infinity. One can recognize this model as one block of the BHZ model⁵. In addition to $\hat{H}(\mathbf{p})$ [Eq. (2)], this Hamiltonian contains diagonal quadratic terms $\beta_{a,b} p^2$ with the curvatures $\beta_{a,b} > 0$. These terms fully specify the topology, making the Chern number C well defined. The phases $\Delta \gtrless 0$ are TT and TnT with $C = 0, 1$, respectively. We consider “hard-wall” BCs¹⁵

$$\psi_a(x, y = 0) = 0, \quad \psi_b(x, y = 0) = 0 \quad (7)$$

for the Hamiltonian (6).

The linearized Hamiltonian $\hat{H}(\mathbf{p})$ is obtained from $\hat{H}_2(\mathbf{p})$ just by neglecting the quadratic terms. The BC of the form (3) for the linearized Hamiltonian is derived in SM¹⁰. As a result, the quadratic model of Eqs. (6) and (7) is described asymptotically in the vicinity of the TPT by the linear model of Eqs. (2) and (3), with the angle θ of the BC determined by the ratio of the curvatures as

$$\tan \frac{\theta}{2} = \sqrt{\beta_a / \beta_b}. \quad (8)$$

As β_a / β_b spans $(0, +\infty)$, the angle θ spans the half-circle $(0, \pi)$; i.e., in this particular model, only half of the possible forms of the general BC (3) can be realized. The BC (3) becomes chiral-symmetric [Eq. (5)] only asymptotically in the limits $\beta_a / \beta_b \rightarrow 0, +\infty$, i.e., for strong particle-hole asymmetry.

The edge states for the quadratic model of Eqs. (6) and (7) can actually be found analytically. It turns out that its *exact* edge-state spectrum is given¹⁶ by that (4) of the linear model with θ given by Eq. (8). For $\beta_a > \beta_b$, the exact edge-state band, shown in Fig. 1, exists in the interval $p_x^{m-} < p_x < p_x^{m+}$, where

$$p_x^{m\pm} = \frac{\varkappa \beta_a - \beta_b}{2 \beta_a + \beta_b} \left(-1 \pm \sqrt{1 - 8 \frac{\Delta \beta_a \beta_b (\beta_a + \beta_b)}{v^2 (\beta_a - \beta_b)^2}} \right) \quad (9)$$

with $\varkappa = v / \sqrt{\beta_a \beta_b}$ are the merging points with the bulk spectrum of Eq. (6). The merging points p_x^{m-} at larger momenta can be used to define the scale $p^* \equiv |p_x^{m-}|$ of validity of the linear model. For $p_\Delta \ll p^*$ and not too small $\beta_a - \beta_b$, $p_x^{m-} \approx -\varkappa \frac{\beta_a - \beta_b}{\beta_a + \beta_b} \sim \varkappa$.

We see that, indeed, for a small gap ($p_\Delta \ll p^*$), the exact edge-state behavior of the quadratic model at smaller momenta $|p_x| \ll p^*$ is in full accord with that of the linear model. For any value $\beta_a / \beta_b \neq 1$, the edge-state structure of the quadratic model in the vicinity of the TPT is extended beyond the minimal one, Figs. 1(a),(b),(c). Additionally, the well-defined merging point p_x^{m-} at larger momenta explicitly shows that the edge-state behavior is in agreement with QH topology. In the TnT [Fig. 1(c)] and TT [Fig. 1(a)] phase, the edge-state band is topologically protected and nonprotected, respectively. Upon increasing the gap in the TT phase, the merging points $p_x^{m\pm}$ come closer to each other and the edge-state band eventually disappears at $p_\Delta \sim \varkappa$. For $\beta_a = \beta_b$, Figs. 1(d),(e),(f), the quadratic model obeys

charge-conjugation symmetry¹⁰ and the edge states exist only in the TnT phase in the gap region, realizing the minimal edge-state structure.

Relation to real systems. Having demonstrated in SM the extension effect of the edge-state structure for the most general low-energy model, we expect it to be widespread in real QAH systems, and also in QSH systems, at least when coupling between the Kramers blocks is weak¹⁷. In SM, we demonstrate that the effect is quite

pronounced for the parameters of the BHZ model describing HgTe quantum wells.

Acknowledgements. M. K. and E. M. H. were supported by the German Science Foundation (DFG) via Grant No. SFB 1170 “ToCoTronics” and the ENB Graduate School on Topological Insulators. D. R. C. and J. C. E. were supported by CNPq, Capes, FAPESP, PRP-USP/Q-NANO and acknowledge useful discussions with P. H. Penteado.

-
- ¹ F. D. M. Haldane, Phys. Rev. Lett. 61, 2015 (1988).
² S. Ryu, A. Schnyder, A. Furusaki, and A. Ludwig, New J. Phys. 12, 065010 (2010).
³ M. Z. Hasan and C. L. Kane, Rev. Mod. Phys. 82, 3045 (2010).
⁴ C.-K. Chiu, J. C.Y. Teo, A. P. Schnyder, and S. Ryu, Rev. Mod. Phys. 88, 035005 (2016).
⁵ B. A. Bernevig, T. L. Hughes, and S. C. Zhang, Science 314, 1757 (2006).
⁶ C. L. Kane and E. J. Mele, Phys. Rev. Lett. 95, 226801 (2005).
⁷ M. König, S. Wiedmann, C. Brüne, A. Roth, H. Buhmann, L. Molenkamp, X.-L. Qi, S.-C. Zhang, Science 318 (5851), 766 (2007).
⁸ J. Li, R.-L. Chu, J. K. Jain, and S.-Q. Shen, Phys. Rev. Lett. 102, 136806 (2009).
⁹ M. Kharitonov, J.-B. Mayer, and E. M. Hankiewicz, Phys. Rev. Lett. 119, 266402 (2017).
¹⁰ See Supplemental Material at [URL], which includes Refs. 2,4, for the most general form of the low-energy linear-in-momentum model of the topological phase transition of a quantum anomalous Hall system and its analysis in terms of chiral and charge-conjugation symmetries and for the derivation of the low-energy boundary condition (3) from the quadratic model [Eqs. (6) and (7)].
¹¹ A mathematically equivalent result for a 1D gapped system was obtained earlier in M. T. Ahari, G. Ortiz, and B. Seradjeh, Am. J. Phys. 84, 858 (2016).
¹² Due to axial rotation symmetry of the Hamiltonian $\hat{H}(\mathbf{p})$ [Eq. (2)], the edge-state spectrum will be the same for any orientation of the edge.
¹³ The regions $\Theta_{a,b}$ are labelled according to the dominant character of the wave function, $|\psi_a| \gtrless |\psi_b|$, respectively.
¹⁴ We assume that the edge states eventually merge outside of the region $|p_x| \lesssim p^*$ of validity of the linear model with those bulk bands to which they are closest, as is the case, e.g., for the quadratic model (6) in Fig. 1.
¹⁵ Such BCs describe, for example, an interface with the TT phase of the model (6) with an infinite gap $\Delta \rightarrow +\infty$.
¹⁶ We believe this is an accidental property of this model, since, in general, agreement can be expected only *asymptotically*.
¹⁷ If a QSH system possesses additional reflection symmetry along the direction perpendicular to the quasi-2D sample, such as the original BHZ model⁵, then it decouples into two QAH systems and our results apply directly. If there is no exact reflection symmetry, our results should still apply at least when the effect of reflection-symmetry breaking is weak. Generalization of our approach to stronger coupling should be possible.

Supplemental Material: Paradoxical extension of the edge states across the topological phase transition due to emergent approximate chiral symmetry in a quantum anomalous Hall system

Maxim Kharitonov¹, Denis R. Cândido², J. Carlos Egues², Ewelina M. Hankiewicz¹

¹*Institute for Theoretical Physics and Astrophysics,
University of Würzburg, 97074 Würzburg, Germany*

²*Instituto de Física de São Carlos, Universidade de São Paulo, 13560-970, São Carlos, São Paulo, Brazil*

I. MOST GENERAL LINEAR MODEL

Here, we demonstrate that the main claim of the paper, that the edge-state structure in the vicinity of the TPT in a QAH system is nearly always significantly extended beyond the minimal one required to satisfy the Chern numbers, is valid not only for the simplest form (2) of the linear Hamiltonian, but also for its most general form.

A. General bulk Hamiltonian, convenient basis

The most general 2D Hamiltonian up to the linear order in momentum for a two-component wave function, describing the vicinity of a TPT of a QAH system with no assumed symmetries, has the form

$$\hat{H}(\mathbf{p}) = \sum_{\alpha=0,x,y,z} \tau_{\alpha}(\varepsilon_{\alpha} + v_{\alpha x}p_x + v_{\alpha y}p_y), \quad (\text{S1})$$

with 4 real energy parameters ε_{α} and 8 real velocity parameters $v_{\alpha x}$ and $v_{\alpha y}$, i.e., with 12 real parameters, out of which ε_0 at τ_0 is an inconsequential overall energy. Here, τ_{α} are the unity and Pauli matrices in the arbitrary initial basis of the two electron states and $p_{x,y}$ are the cartesian momentum components in the arbitrary initial coordinate basis¹. Additionally, the orientation of the edge relative to the initial coordinate axes is described by one angle. And so, the edge-state problem is described by 12 relevant parameters: 11 relevant parameters of the bulk Hamiltonian and the angle specifying the orientation of the edge.

There is freedom in the independent choice of the wave-function $\hat{\psi} = (\psi_a, \psi_b)^T$ and momentum $\mathbf{p} = (p_x, p_y)$ bases. The wave-function basis has 3 real parameters of the SU(2) transformation matrix \hat{U} ,

$$\hat{\psi} \rightarrow \hat{U}\hat{\psi}.$$

The momentum basis has one angle parameterizing the rotation matrix \hat{R} and 2 parameters $\mathbf{p}_0 = (p_{x0}, p_{y0})$ describing the choice of the origin,

$$\mathbf{p} \rightarrow \hat{R}\mathbf{p} + \mathbf{p}_0.$$

We exploit these 6 free real parameters to bring the most general Hamiltonian (S1) to the most convenient form for the analysis of the BC and edge-state problem.

First, we use the angle of the rotation matrix \hat{R} to orient the edge as $y = 0$. Next, we use 2 of the 3 parameters of the SU(2) matrix \hat{U} to bring the matrix at p_y momentum perpendicular to the edge $y = 0$ to the diagonal form (containing only $\tau_{0,z}$ and no $\tau_{x,y}$). After this, the Hamiltonian in this new basis takes the form

$$\hat{H}(\mathbf{p}) = \tau_0(v_{0x}p_x + v_{0y}p_y + \varepsilon_0) + \tau_z(v_{zx}p_x + v_{zy}p_y + \varepsilon_z) + \tau_x(v_{xx}p_x + \varepsilon_x) + \tau_y(v_{yx}p_x + \varepsilon_y).$$

(In order not to overcomplicate the notation and since we are interested only in the final convenient form of the Hamiltonian, we will preserve the same notation in all bases; this should not lead to confusion.) Next we use the remaining 3rd parameter of \hat{U} to eliminate the velocity v_{xx} , which brings the Hamiltonian to the form

$$\hat{H}(\mathbf{p}) = \tau_0(v_{0x}p_x + v_{0y}p_y + \varepsilon_0) + \tau_y(v_{yx}p_x + \varepsilon_y) + \tau_z(v_{zx}p_x + v_{zy}p_y + \varepsilon_z) + \tau_x\varepsilon_x.$$

Finally, by changing the origin \mathbf{p}_0 of the momentum basis, we eliminate two energies $\varepsilon_{y,z}$. Discarding also the inconsequential energy ε_0 at τ_0 , we arrive at the final desired form

$$\hat{H}(\mathbf{p}) = \tau_0(v_{0x}p_x + v_{0y}p_y) + \tau_y v_{yx}p_x + \tau_z(v_{zx}p_x + v_{zy}p_y) + \tau_x\Delta \quad (\text{S2})$$

of the Hamiltonian, where we denoted $\varepsilon_x \equiv \Delta$. It is characterized by 6 real parameters: 5 velocities and 1 energy Δ . The bulk spectrum of Eq. (S2) reads

$$\varepsilon_{\pm}(\mathbf{p}) = v_{0y}p_y + v_{0x}p_x \pm \sqrt{(v_{zy}p_y + v_{zx}p_x)^2 + (v_{yx}p_x)^2 + \Delta^2}. \quad (\text{S3})$$

Counting the degrees of freedom, we have used 6 available free parameters to represent the edge-state problem with the most general Hamiltonian (S1) with 11 substantial parameters and arbitrary edge orientation to that with the Hamiltonian (S2) with 6 parameters and $y = 0$ edge.

The simplest Hamiltonian

$$\hat{H}(\mathbf{p}) \rightarrow v(\tau_y p_x + \tau_z p_y) + \tau_x \Delta, \quad (\text{S4})$$

equivalent to Eq. (2) via an additional change of basis, is obtained from Eq. (S2) when $v_{0y}, v_{0x}, v_{zx} = 0$ and $v_{zy} = v_{xx} = v$.

B. General boundary condition

We now derive the most general form of the BC for the Hamiltonian (S2). Mathematically, such BC is a single linear homogeneous relation between the two components $\psi_{a,b}(x, y = 0)$ of the wave function at the edge $y = 0$; without loss of generality, it can be written as

$$e^{i\frac{\theta}{2}} \sin \frac{\theta}{2} \psi_a(x, y = 0) - e^{-i\frac{\theta}{2}} \cos \frac{\theta}{2} \psi_b(x, y = 0) = 0, \quad (\text{S5})$$

parameterized by two real angles θ and ϕ .

The BC must only satisfy the fundamental constraint that the current perpendicular to the edge vanishes at the edge. For the Hamiltonian (S2), the operator of the current perpendicular to the $y = 0$ edge reads

$$\hat{j}_y = \partial_{p_y} \hat{H}(p_x, p_y) = \tau_z v_{zy} + \tau_0 v_{0y}.$$

It is given by the matrix at p_y in Eq. (S2), which has conveniently been made diagonal.

Demanding that for any wave function satisfying Eq. (S5) the current $\hat{\psi}^\dagger(x, y = 0) \hat{j}_y \hat{\psi}(x, y = 0) = 0$ vanish, we obtain that the angle $\theta \equiv \theta_v \in (0; \pi)$ in Eq. (S5) is fixed by the velocity parameters of the bulk Hamiltonian as

$$\cos \theta_v = -\frac{v_{0y}}{v_{zy}}, \quad (\text{S6})$$

while the angle ϕ may be arbitrary².

And so, the most general form of the BC for the $y = 0$ edge for the most general linear Hamiltonian represented in the form (S2) reads

$$e^{i\frac{\phi}{2}} \sin \frac{\theta_v}{2} \psi_a(x, y = 0) - e^{-i\frac{\phi}{2}} \cos \frac{\theta_v}{2} \psi_b(x, y = 0) = 0. \quad (\text{S7})$$

All unique forms of the BC are parameterized by the angle ϕ covering the *full circle*, similar to the angle θ in Eq. (3).

C. Edge states and chiral and charge-conjugation symmetries

The edge states for the Hamiltonian (S2) and BC (S7) for the sample occupying the $y > 0$ half plane can be straightforwardly found. For every value of ϕ except $\pm \frac{\pi}{2}$, there exists one edge-state band

$$\mathcal{E}(p_x) = (v_{0x} + v_{zx} \cos \theta_v + v_{yx} \sin \theta_v \sin \phi) p_x + \Delta \sin \theta_v \cos \phi \quad (\text{S8})$$

for any value of the gap Δ , located at $p_x > p_x^m(\phi)$ for $\phi \in (-\frac{\pi}{2}, \frac{\pi}{2})$ and at $p_x < p_x^m(\phi)$ and for $\phi \in (\frac{\pi}{2}, \frac{3\pi}{2})$. Here,

$$p_x^m(\phi) = \frac{\Delta}{v_{yx}} \tan \phi, \quad \varepsilon^m(\phi) = \frac{\Delta}{v_{yx} \cos \phi} [v_{yx} \sin \theta_v + (v_{0x} + v_{zx} \cos \theta_v) \sin \phi]$$

are the momentum and energy, at which the edge-state spectrum $\mathcal{E}(p_x)$ merges with the boundaries

$$\varepsilon_{+x}(p_x) = \min_{p_y} \varepsilon_+(p_x, p_y), \quad \varepsilon_{-x}(p_x) = \max_{p_y} \varepsilon_-(p_x, p_y)$$

of the continua of the bulk spectrum [Eq. (S3)], given by

$$\varepsilon_{\pm x}(p_x) = (v_{0x} + v_{zx} \cos \theta_v) p_x \pm \sqrt{(v_{yx} p_x)^2 + \Delta^2} \sin \theta_v. \quad (\text{S9})$$

Therefore, for the most general form of the linear model [Eqs. (S2) and (S7)], the edge-state structure in the vicinity of the TPT in a QAH system is nearly always (i.e., for all $\phi \neq \pm \frac{\pi}{2}$) extended beyond the minimal one required to satisfy the Chern numbers. As with the simplest Hamiltonian (2), below we analyze and explain this behavior in terms of chiral and charge-conjugation symmetries, also providing some additional details.

A bulk Hamiltonian satisfies chiral symmetry^{3,4}, if there exists a *unitary* operation

$$\mathcal{S}[\hat{\psi}](\mathbf{r}) = \hat{S}\hat{\psi}(\mathbf{r}) \quad (\text{S10})$$

on the wave function $\hat{\psi}(\mathbf{r}) = (\psi_a(\mathbf{r}), \psi_b(\mathbf{r}))^T$, where \hat{S} is a unitary matrix and $\mathbf{r} = (x, y)$ is a radius vector, under which the Hamiltonian changes its sign; in momentum space, for $\hat{\psi}(\mathbf{p}) = \int d\mathbf{r} e^{-i\mathbf{p}\mathbf{r}} \hat{\psi}(\mathbf{r})$, this reads

$$\mathcal{S}[\hat{\mathcal{H}}](\mathbf{p}) = \hat{S}\hat{\mathcal{H}}(\mathbf{p})\hat{S}^\dagger = -\hat{\mathcal{H}}(\mathbf{p}). \quad (\text{S11})$$

We notice that the part

$$\hat{H}_0(\mathbf{p}) = \tau_y v_{yx} p_x + \tau_z (v_{zx} p_x + v_{zy} p_y) \quad (\text{S12})$$

of the Hamiltonian $\hat{H}(\mathbf{p})$ [Eq. (S2)] (with $v_{0x}, v_{0y}, \Delta = 0$) satisfies chiral symmetry with

$$\hat{S} = \tau_x,$$

while the velocity $\tau_0(v_{0x} p_x + v_{0y} p_y)$ and gap $\tau_x \Delta$ terms break such chiral symmetry.

Similarly, a bulk Hamiltonian satisfies charge-conjugation symmetry^{3,4}, if there exists an *anti-unitary* operation

$$\mathcal{C}[\hat{\psi}](\mathbf{r}) = \hat{C}\hat{\psi}^*(\mathbf{r})$$

on the wave function, where \hat{C} is a unitary matrix and * denotes complex conjugation, under which the Hamiltonian changes its sign; in momentum space, this reads

$$\mathcal{C}[\hat{\mathcal{H}}](\mathbf{p}) = \hat{C}\hat{\mathcal{H}}^*(-\mathbf{p})\hat{C}^\dagger = -\hat{\mathcal{H}}(\mathbf{p}). \quad (\text{S13})$$

We notice that the *whole* Hamiltonian $\hat{H}(\mathbf{p})$ [Eq. (S2)] satisfies charge conjugation symmetry with

$$\hat{C} = \tau_z$$

and $\mathcal{C}^2 = +1$.

Next, we analyze the BC (S7) in terms of symmetries. Chiral symmetry of the BC means that if a wave function $\hat{\psi}(\mathbf{r}) = (\psi_a(\mathbf{r}), \psi_b(\mathbf{r}))^T$ satisfies the BC, then the wave function $\mathcal{S}[\hat{\psi}](\mathbf{r}) = (\psi_b(\mathbf{r}), \psi_a(\mathbf{r}))^T$ transformed by the chiral symmetry operator (S10) also satisfies the same BC. Substituting $\mathcal{S}[\hat{\psi}](\mathbf{r})$ into the BC (S7), we obtain

$$e^{+i\frac{\phi}{2}} \sin \frac{\theta_v}{2} \psi_b(x, y = 0) - e^{-i\frac{\phi}{2}} \cos \frac{\theta_v}{2} \psi_a(x, y = 0) = 0.$$

This condition is identical to Eq. (S7) only if $\theta_v = \frac{\pi}{2}$, i.e., $v_{0y} = 0$ [Eq. (S6)], and

$$\phi = 0 \text{ or } \pi.$$

Therefore,

$$\psi_a(x, y = 0) \mp \psi_b(x, y = 0) = 0, \quad (\text{S14})$$

respectively, are the only two chiral-symmetric forms of the BC (S7), possible only when $v_{0y} = 0$.

So, the chiral-symmetric Hamiltonian $\hat{H}_0(\mathbf{p})$ [Eq. (S12)] with one of the chiral-symmetric BCs (S14) represents a 2D chiral-symmetric semimetal with an edge. Due to the well-defined winding number 1, such semimetal exhibits flat edge-state bands that are topologically protected by chiral symmetry⁴. Indeed, it follows from Eq. (S8) that in this case the edge-state band $\mathcal{E}(p_x) \equiv 0$ is flat and located at $p_x > 0$ for $\phi = 0$ and at $p_x < 0$ for $\phi = \pi$.

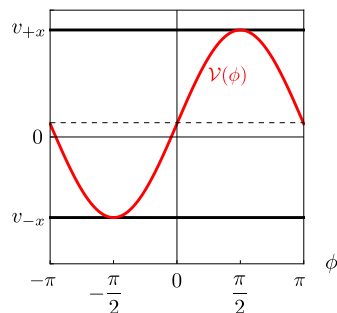


FIG. S1: The velocity $\mathcal{V}(\phi)$ [Eq. (S15)] of the edge-state band (S8) at the TPT $\Delta = 0$ of the most general linear Hamiltonian $\hat{H}(\mathbf{p})$ [Eq. (S2)] as a function of the angle parameter ϕ of the general BC (S7). The edge-state band exists at $p_x > 0$ for $\phi \in (-\frac{\pi}{2}, \frac{\pi}{2})$ and at $p_x < 0$ for $\phi \in (\frac{\pi}{2}, \frac{3\pi}{2})$, i.e., for every value of ϕ except $\pm\frac{\pi}{2}$, when the system obeys charge-conjugation symmetry. At $\phi = \pm\frac{\pi}{2}$, the band merges with the boundaries of the continua of the bulk spectrum, characterized by the velocities $v_{\pm x}$ [Eq. (S16)]. This edge-state band at the TPT can be attributed to approximate chiral symmetry of the linear model. It is not required by QH topology and thus represents an extension of the edge-state structure beyond the minimal one required to satisfy the Chern numbers. The graph is plotted for the velocity parameters $(v_{0x}, v_{0y}, v_{zx}, v_{zy})/v_{yx} = (\frac{1}{6}, \frac{1}{12}, \frac{1}{6}, \frac{1}{2})$.

The remaining gap $\tau_x\Delta$ and velocity $\tau_0(v_{0x}p_x + v_{0y}p_y)$ terms in the bulk Hamiltonian $\hat{H}(\mathbf{p})$ [Eq. (S2)] and the deviations of the angle ϕ of the BC (S7) from 0 or π break chiral symmetry. Nonetheless, the edge-state band (S8) persists. At the TPT $\Delta = 0$, when the system is gapless, the edge-state band exists for any values of v_{0x} and v_{0y} and any value of $\phi \neq \pm\frac{\pi}{2}$: the velocity

$$\mathcal{V}(\phi) = \partial_{p_x}\mathcal{E}(p_x) = v_{0x} + v_{zx}\cos\theta_v + v_{yx}\sin\theta_v\sin\phi \quad (\text{S15})$$

of the edge-state band (S8) is always between the velocities

$$v_{\pm x} = \partial_{p_x}\varepsilon_{\pm x}(p_x)|_{\Delta=0} = v_{0x} + v_{zx}\cos\theta_v \pm |v_{yx}|\sin\theta_v \quad (\text{S16})$$

of the dispersion relations (S9) determining the boundaries of the continua of the bulk spectrum, $\mathcal{V}(\phi) \in [v_{-x}, v_{+x}]$, reaching them only at $\phi = \pm\frac{\pi}{2}$, as shown in Fig. S1.

The values $\phi = \pm\frac{\pi}{2}$ are actually special symmetry-wise. As with chiral symmetry, a BC is charge-conjugation-symmetric if the transformed wave function $\mathcal{C}[\hat{\psi}](\mathbf{r}) = (\psi_a^*(\mathbf{r}), -\psi_b^*(\mathbf{r}))^T$ also satisfies the same BC. Substituting $\mathcal{C}[\hat{\psi}](\mathbf{r})$ into the BC (S7), we obtain

$$e^{-i\frac{\phi}{2}}\sin\frac{\theta_v}{2}\psi_a(x, y=0) + e^{+i\frac{\phi}{2}}\cos\frac{\theta_v}{2}\psi_b(x, y=0) = 0,$$

which is identical to Eq. (S7) only if

$$\phi = \pm\frac{\pi}{2}.$$

Therefore,

$$e^{\pm i\frac{\pi}{4}}\sin\frac{\theta_v}{2}\psi_a(x, y=0) - e^{\mp i\frac{\pi}{4}}\cos\frac{\theta_v}{2}\psi_b(x, y=0) = 0,$$

respectively, are the only two charge-conjugation-symmetric forms of the BC (S7). Thus, as with the simplest Hamiltonian (2)⁵, for the most general form (S2) of the linear Hamiltonian, the only cases of the general BC (S7), in which the edge-state band at the TPT $\Delta = 0$ induced by chiral symmetry is absent, are the ones that have charge-conjugation symmetry. The intervals $\phi \in (-\frac{\pi}{2}, \frac{\pi}{2})$ and $\phi \in (\frac{\pi}{2}, \frac{3\pi}{2})$, separated by the points $\phi = \pm\frac{\pi}{2}$, are the stability regions of the chiral-symmetric cases $\phi = 0, \pi$.

The above-described edge-state band induced by chiral symmetry at the TPT is not required by QH topology. Therefore, it represents the extension of the edge-state structure at TPT and also in gapped TnT and TT phases: a finite gap modifies this edge-state band only in the momentum region dominated by the gap, as explained in the Main Text.

We have thus demonstrated with the most general form of the linear model [Eqs. (S2) and (S7)] that the main claim of the paper is completely general and not specific to the simplest form (1) of the bulk Hamiltonian considered in the Main Text: the edge-state structure in the vicinity of the TPT in a QAH system is nearly always significantly extended beyond the minimal one required to satisfy the Chern numbers.

II. QUADRATIC MODEL OF A QUANTUM ANOMALOUS HALL SYSTEM

Here, we present in more detail the properties of the quadratic model described by Eqs. (6) and (7).

A. Boundary condition for the linear model

Here, we derive the BC of the form (3) for the linear model (2) that asymptotically describes the quadratic model with the Hamiltonian (6) and BCs (7) in the vicinity of its TPT $\Delta = 0$. The systematic procedure is as follows. Let us first find the general solution to the Schrödinger equation

$$\hat{H}_2(p_x, \hat{p}_y)\hat{\psi}(y) = \epsilon\hat{\psi}(y)$$

right at the TPT $\Delta = 0$ for momentum $p_x = 0$ and energy $\epsilon = 0$ exactly at the node that contains no contributions growing into the bulk. We obtain

$$\hat{\psi}(y) = \begin{pmatrix} \psi_a \\ \psi_b \end{pmatrix} + Be^{-\varkappa y} \begin{pmatrix} \sqrt{\beta_b} \\ \sqrt{\beta_a} \end{pmatrix},$$

with the momentum scale

$$\varkappa = \frac{v}{\sqrt{\beta_a\beta_b}} \quad (\text{S17})$$

and three independent *constant* coefficients $\psi_{a,b}$ and B . Applying the BCs (7) to it and excluding B , we arrive at the constraint

$$\sqrt{\beta_a}\psi_a - \sqrt{\beta_b}\psi_b = 0. \quad (\text{S18})$$

The quantity \varkappa defines the validity scale of the low-energy model with the linear Hamiltonian (2): the momentum scales of interest $p_x, \epsilon/v, p_\Delta \ll \varkappa$ must be small. Accordingly, the wave function $\hat{\psi}(\mathbf{r}) = (\psi_a(\mathbf{r}), \psi_b(\mathbf{r}))^T$ of the linear Hamiltonian (2) must vary slowly at the spatial scale $1/\varkappa$. To the leading order, the relation (S18) will still apply to the components $\psi_{a,b} \rightarrow \psi_{a,b}(x, y = 0)$ of such wave function at the edge. Thus, the relation (S18) represent the BC of the form (3) with the angle θ determined by the ratio of the curvatures as expressed in Eq. (8).

B. Charge-conjugation symmetry

The quadratic Hamiltonian (6) satisfies charge-conjugation symmetry [Eq. (S13)] with $\hat{C} = \tau_x$ only if $\beta_a = \beta_b$. Its hard-wall BCs (7) also satisfy this symmetry. Only in this case the minimal edge-state structure required to satisfy the Chern numbers is realized, shown in Fig. 1(d),(e),(f).

C. Extension of the edge-state structure

Here, we discuss in more detail the effect of the extension of the edge-state structure beyond the minimal one required to satisfy the Chern numbers in the quadratic model of a QAH system described by Eqs. (6) and (7).

The model is described by four parameters, the gap Δ , velocity v , and curvatures $\beta_{a,b}$. We observe that instead of $\beta_{a,b}$ it is more physically insightful to consider the combinations

$$\beta = \sqrt{\beta_a\beta_b}, \quad t = \sqrt{\frac{\beta_a}{\beta_b}} \quad (\text{S19})$$

as independent parameters, in terms of which

$$\beta_a = \beta t, \quad \beta_b = \beta \frac{1}{t}.$$

This way, the geometric mean β sets the overall momentum \varkappa [Eq. (S17)] and energy

$$\epsilon = v\varkappa = \frac{v^2}{\beta} \quad (\text{S20})$$